WIND AND THERMAL COMFORT DESIGN FOR URBAN OPEN AND SEMI-OPEN STRUCTURES: WIND TUNNEL AND NUMERICAL STUDIES

LI WENXIN

PhD

The Hong Kong Polytechnic University

2026

The Hong Kong Polytechnic University

Department of Building Environment and Energy Engineering

Wind and Thermal Comfort Design for Urban Open and Semi-open Structures: Wind Tunnel and Numerical Studies

LI Wenxin

A thesis submitted in partial fulfilment of the requirements for the Degree of Doctor of Philosophy

August 2025

CERTIFICATE OF ORIGINALITY

I hereby declare that this thesis is my own work and that, to the best of my knowledge and belief, it reproduces no material previously published or written, nor material that has been accepted for the award of any other degree or diploma, except where due acknowledgement has been made in the text.

_____________(Signed)

___LI Wenxin__(Name of student)

ABSTRACT

Abstract of thesis entitled : Wind and thermal comfort design for urban open and semi-open structures: wind tunnel and numerical studies

Submitted by : LI Wenxin

For the degree of : Doctor of Philosophy

at The Hong Kong Polytechnic University in August 2025

Due to rapid global urbanization and heatwaves intensified by the Urban Heat Island (UHI) effect, densely populated cities face inadequate pedestrian-level ventilation, degraded air quality, and severe thermal discomfort. As a result, urbanites increasingly stay indoors and avoid outdoor activities, leading to a more sedentary lifestyle that contributes to higher obesity rates and negatively impacts human health. Open and semi-open spaces distributed in individual precincts are widely recognized as heat resilience hubs that are conducive to wind flow and improve thermal comfort. Exploring the characteristics of urban open and semi-open designs improves our understanding of building-wind interactions to support sustainable environment development. Besides building-induced flow changes, atmospheric boundary layer (ABL) conditions significantly influence pedestrian-level wind environments (PLWEs). Urban wind direction is often altered by hilly terrain. In cities with such topography, like Hong Kong and Chongqing, wind direction varies significantly with height, a factor overlooked in prior studies on urban open designs. This vertical wind direction twist creates a twisted wind profile (TWP), distinct from the conventional wind profile (CWP), which assumes constant wind direction with height. Thus, understanding how urban open and semi-open designs influence PLWEs and how twisted wind impacts both PLWEs and surrounding thermal comfort is essential.

This thesis provides a comprehensive analysis of the impacts of open or semi-open building designs on pedestrian-level wind and thermal comfort. In addition to time-averaged

velocity, turbulent statistics that influence wind comfort are also considered. The impact of twisted wind profiles (TWPs) on PLWEs and thermal comfort is further included. For buildings featuring open or semi-open designs, two representative layouts are the elevated (open) and arcade (semi-open) designs. The elevated design refers to the structures that are raised on pillars, creating activity and recreational areas for residents beneath. The arcade's design adopts a semi-enclosed structural arrangement, characterized by horizontally recessed spaces positioned beneath the building body. Although the effectiveness of improving urban wind comfort using a single elevated building has been verified, previous studies have primarily focused on mean wind velocities; there is a lack of knowledge regarding both time-averaged quantities and gust wind characteristics around irregular elevated buildings with urban arrays. Moreover, while open and semi-open designs have been shown to improve wind and thermal comfort, their impact on airflow under twisted wind conditions remains unclear and requires further study. Based on the identified research gaps, this thesis conducted four sub-studies as follows:

The first and second sub-work involve wind tunnel experiments investigating three-dimensional turbulent flow structures around a building group, which includes a high-rise unconventional elevated building located centrally. Additionally, the Computational fluid dynamics (CFD) simulation, including the Steady Reynolds-averaged Navier-Stokes (RANS) and Large eddy simulation (LES), is conducted on a single Arc-shaped elevated building to predict mean and gust wind effects, validated against the results of the wind tunnel experiments. The results indicate that a region of high mean and gust wind velocity was observed at the lateral and rear side of the central elevated building, indicating that elevated buildings can enhance PLWEs even in the presence of surrounding buildings. The Arc-shaped elevated building tends to generate a larger "Intolerable" area compared with V- and Rectangular-shaped buildings due to its curved surface. The wind impacts the convex portion of the building, leading to airflow divergence and facilitating downstream ventilation. The RANS models substantially underestimated the mean wind velocity in the side and wake regions of the building when compared to the wind tunnel experiment results, while these models agreed well with wind tunnel data on mean wind velocity in the upstream region. The LES simulation can accurately reproduce the mean wind velocity and reasonably estimate the rmse velocity components around the elevated building. The vortex shedding frequency around an elevated building exhibits a wider range compared to that around a non-elevated building, which indicates the vortex shedding phenomenon is more complex around elevated buildings.

The third sub-work investigated two tandem buildings with varying relative height differences (H_{UB}/H_{DB}) ranging from 3:1 to 0.33:1 and different elevated structure locations under CWP and TWP by wind tunnel experiment. The two twist vanes were mounted upstream of the center of the turntable to simulate the twisted wind profile (TWP) with two different angles (15° and 30°). The results show that the step-up building configurations ($H_{UB}<H_{DB}$) exhibit heightened sensitivity to twisted wind profiles, resulting in larger deviation angles (β) of downstream low wind velocity (DSLWV) zones. Step-down building configurations ($H_{UB}>H_{DB}$) are relatively insensitive to the twisted wind profile. The presence of elevated structures enhances sensitivity to the twisted wind effect, resulting in increased displacement of DFLWV regions relative to the building's central axis. The twisted wind reorients the "Sitting short" zone in alignment with the direction of incoming twist flow and concurrently enlarges the "Strolling" area on the opposing side. The twisted wind can diminish the thermal comfort surrounding the two tandem structures during summer while enhancing the thermal environment in winter. Based on the third sub-work, the fourth sub-work further explores the influence of twisted wind on semi-open structures and influential factors under solar heating. The steady RANS model with Standard $k-\varepsilon$ models with discrete ordinate (DO) radiation was applied. The results showed that weakened downwash flow caused by the twisted wind within the street canyon was insufficient to counteract the buoyancy-driven flow generated by solar radiation. This condition facilitated the escape of heated air from the lower levels of the street canyon. Increasing the arcade width may negatively impact thermal comfort under TWP. The cooling effect of twisted winds was more pronounced in shorter street canyons.

This thesis examines how irregular elevated buildings influence turbulent flow structures and interact with surrounding buildings, and evaluates the effectiveness of elevated and arcade designs in improving wind and thermal comfort in areas with frequent twisted flows. The findings of this study can help city planners create local comfortable outdoor spaces by minimizing thermal risk and enhancing wind and thermal comfort. Predicting reduced high-wind areas under TWPs may also help avoid unnecessary costs from corrective measures based on overestimated wind speeds near building corners under the conventional wind profile, thus supporting better urban design for sustainable and liveable environments.

PUBLICATIONS ARISING FROM THIS THESIS

Journal Publications

2024 **Li, W.,** Mak, C.M., Fu, Y., Cai, C., Tse, K.T., Niu, J. and Wong, S.H.Y. Pedestrian-level wind environment surrounding two tandem non-identical height elevated buildings under the influence of twisted wind flows. *Sustainable Cities and Society*, 112, p.105641.

2024 **Li, W.,** Mak, C. M., Fu, Y., Cai, C., Tse, K. T., & Niu, J. The impact of twisted wind on pedestrian comfort around two non-identical-height buildings in tandem arrangement: a wind tunnel study. *Building and Environment*, 262, 111847.

2024 **Li, W.,** Mak, C. M., Cai, C., Fu, Y., Tse, K. T., & Niu, J. Wind tunnel measurement of pedestrian-level gust wind flow and comfort around irregular elevated buildings within simplified urban arrays. *Building and Environment,* 256, 111487.

2025 **Li, W.,** Mak, C. M., Cai, C. Numerical evaluation of the effect of twist wind on pedestrian comfort surrounding semi-open structures and influential factors under solar heating. *Building Simulation*, 18, 1409-1433.

2025 **Li, W.,** Mak, C. M., Cai, C., Tse, K.T. Mean and turbulent wind characteristics around a high-rise elevated building with curved cross-sections: Wind tunnel experiments and numerical simulations. *Building and Environment*, 285, 113666.

Conference Publication

2025 **Li, W.,** Mak, C. M. Effects of twisted wind on outdoor air temperature and wind comfort under solar radiation. 6th International Conference on Building Energy and Environment (COBEE 2025), Eindhoven, Netherlands, July 6-10, 2025.

ACKNOWLEDGEMENTS

The present work presented in this thesis was financially supported by the Hong Kong Polytechnic University and the Research Grants Council of the Hong Kong Special Administrative Region, China (Project No. T22-504/21-R).

I would like to express my sincerest appreciation to my supervisor, Prof. Cheuk Ming Mak. He gave me lots of support financially and mentally. I could not have completed this thesis without his support. Prof. Mak, who guided me from being a novice in scientific research to becoming a researcher with practical experience, and I would like to express my sincere gratitude for his patient mentorship. His encouragement and support for students have also inspired me to continue my efforts.

I would like to express my sincere gratitude to Prof. Chenzhi Cai from Central South University for providing me with valuable and indispensable guidance in paper writing and experimental design, which has greatly contributed to the present research. I would also like to express my sincere gratitude to Prof. Kam Tim Tse for his invaluable guidance and support regarding the wind tunnel experiment. I would like to express my sincere gratitude to my colleagues in our research group: Dr. Lan Chen, Dr. Rong Xue, Dr. Xiujie Li, Dr. Lei Gao, Dr. Yunfei Fu, Mr. Supeng Deng, for their invaluable support and assistance during my life in Hong Kong. I would like to thank all the staff in the Aerodynamics and Acoustics Facility (AAF) at the Hong Kong University of Science and Technology for providing the experience and advice during the wind tunnel experiment. I would also like to express my sincere gratitude to the thesis examiners for their insightful feedback and helpful suggestions, which have greatly enhanced the overall quality of this research.

Finally, I would like to express my heartfelt gratitude to my beloved parents and boyfriend for their enduring love and care. Thank you for your selfless support and for always

standing by my side in every decision I have made. Now that I have grown up, I am determined to take care of and protect you in the years to come.

TABLE OF CONTENTS

LIST OF FIGURES

LIST OF TABLES

NOMENCLATURE

Abbreviations

ABL	Atmospheric boundary layer
BLWT	Boundary layer wind tunnel
CFD	Computational fluid dynamics
CWP	Conventional wind profile
CFL	Courant-Friedrichs-Lewy number
DO	Discrete ordinates model
DWVR	Downstream wind velocity region
DSLWV	Downstream low wind velocity zones
DA	Downstream areas
GCI	Grid convergence index
GF	Gust factor
GVR	Gust wind velocity ratio
GEM	Gust equivalent mean
LST	Local solar time
LES	Large Eddy Simulation
LWV	Low wind velocity
MVR	Mean wind velocity ratio
NFWVR	Near-field wind velocity region
NFLWV	Near-field low wind velocity region
OF	Occurrence frequencies
PLW	Pedestrian-level wind
PLWEs	Pedestrian-level wind environments

PISO	Pressure-implicit with splitting of operators
RTE	Radiative transfer equation
SVF	Sky view factor
SRANS	Steady Reynolds averaged Navier-Stokes
SA	Side areas
TKE	Turbulence kinetic energy
TWPs	Twisted wind profiles
TWP 13	Twisted wind profile with 13° twist angle
TWP 25	Twisted wind profile with 25° twist angle
UHI	Urban heat island
UA	Upstream areas
UWVR	Upstream wind velocity region
WCE	Water channel experiment
WT	Wind tunnel
WALE	Wall-adapting local eddy-viscosity

Symbols

A_P	Ground-level plot coverage of buildings
AR_{WA}	Area ratio of categorized wind comfort zone
A_{WA}	Area of categorized wind comfort zone
AR_{WC}	Area ratio of the target comfort zone
A_{WC}	Target comfort zone area
A_T	Area of interested research region
A_{LWV}	Area of low wind velocity
A_{HWV}	Area of high wind velocity

c	Scale parameter
C_s	Roughness constant
C_w	Default value of the WALE constant
C_μ	Model constant
D	Building depths (m)
DL	Downstream low-rise buildings
DM	Downstream medium-rise buildings
DH	Downstream high-rise buildings
d	Elevated core depths (m)
f	Frequency
F_s	Safety factor
F_1	Blending function
$FAC2$	Fraction of predictions within a factor of two of observation
FB	Fraction bias
H	Building heights (m)
h_c	Heat transfer coefficients [W/(m^{2}K)]
h	Elevated heights (m)
H_{UB}	Upstream building heights (m)
H_{DB}	Downstream building heights (m)
h	Elevated core heights (m)
h_E	Ekman height
I	Turbulent intensity
I_r	Radiation intensity
k_s	Sand grain roughness height

k	Shape parameter
K_{2m}	Normalized wind velocity ratio at 2 m
$K_{pcl,ave}$	Average *K* value along the passage center line
K_p	Normalized wind velocity ratio at the center of the two buildings
K_{p_GEM}	Gust Equivalent Mean wind velocity ratio at the center of the two buildings
K_{WT}	Normalized wind velocity ratio in the wind tunnel
K_{WC}	Normalized wind velocity ratio at the specific climate
K_i	Short-wave radiation flux densities
L_u	Turbulence length scale
L_i	Long-wave radiation flux densities
L	Street length (m)
LES_{IQ}	LES index of resolution quality
MVR_w	MVR value with a specific architectural
MVR_{wo}	MVR value without a specific architectural
$NMSE$	Normalized mean square error
T	Gust duration
T_L	Local temperature
T_a	Air temperature
T_g	Window length
T_f	Floor temperature
T_{mrt}	Mean radiation temperature
TI	Turbulence intensity
t^*	Non-dimensional sampling time

ΔT	Samling lengths
u, v, w	Velocity components in x,y z directions
z_0	Roughness length [m]
z_{ref}	Reference height [m]
PET	Physiological equivalent temperature [°C]
P_{exce}	Maximum allowed exceedance probabilities
p	Pressure
$\bar{p}$	Filtered pressure
P_k, P_b	Turbulence production term due to mean velocity shear and buoyancy
Q_T	Heat production
q_r	Radiative heat flux
q	Hit rate
R_e	Reynolds number
RH	Relative humidity
R_b	Richardson number
$RMSE$	Root mean square error
R	Pearson correlation coefficient
$\vec{r}$	Position vector
r	Linear grid refinement
$\vec{s}$	Direction vector
$\overrightarrow{s'}$	Scattering direction vector
n	Refractive index
S_u	Power spectrum density
$\overline{u'^2}$	Reynolds stresses in the streamwise direction

u^*	Friction velocity
u_i	Air velocity of the *i*-axis
u_j	Air velocity of the *j*-axis
$\overline{U}$	Mean wind velocity
$\overline{U_{\iota,2m}}$	Mean wind velocity at the location i of the height of 2 m
$\overline{U_{\iota,2m,absence}}$	Mean wind velocity at the same location i without any obstructions.
U_{ref}	Reference velocity
U_g	Gust wind velocity
$\overline{U}_{m_{max}}^{T_g}$	Maximum moving average velocity of T_g
U_m^T	Time-average velocity of the T
U_{thr}	Wind velocity thresholds
U_{GEM}	Gust Equivalent Mean wind velocities
U_{150}	Wind velocity at 150 m height
$u_{i,rmse}$	rmse velocity components of u
$v_{i,rmse}$	rmse velocity components of v
$\overline{v'^2}$	Reynolds stresses in the lateral direction
V_{air}	Airflow velocity
v_g	Gradient wind velocity components
$\overline{w'^2}$	Reynolds stresses in the vertical direction
W	Building widths (m)
w	Elevated core widths (m)
W_i	Directional-dependent weighting factor

Δx	Mesh length
X_F	Reattachment length behind the building (m)
Z_{dsp}	Height of the downstream stagnation point

Greeks

α	Power-law exponent
α_k	Absorption coefficients of the clothed human body in the short-wave radiation domain
α_1	Absorption coefficients of the clothed human body in the long-wave radiation domain
ε	Turbulence dissipation rate (m^2/s^3)
κ	Von Karman constant
ρ	Density (kg/m^3)
υ	Kinetic viscosity (m^2/s)
σ	Stefan-Boltzmann constant
σ_u	Standard deviation of wind velocity
σ_s	Scattering coefficient
λ_P	Planar area ratio
λ_F	Frontal area density
φ	Approaching wind direction
θ	Twist angle
$\theta_{(z)}$	Twist angle along the vertical height
θ_0	Twist angle measured at the lowest height
β	Deviation angle

Φ	Phase function
Ω'	Solid angle
μ_t	Turbulent eddy viscosity
δ_{ij}	Kronecker delta
τ_{ij}	Subgrid-scale model stress tensor
υ	Molecular viscosity
υ_{sgs}	Turbulence viscosity

CHAPTER 1. INTRODUCTION

1.1 Research background and motivation

Owing to the accelerating urbanization process, an increasing number of buildings are being constructed at greater heights, resulting in a more compact urban layout and deteriorated wind and thermal comfort caused by poor ventilation (Tse et al., 2017). Unfavourable outdoor wind and thermal environments may prompt individuals to stay indoors for prolonged periods, particularly in densely populated urban areas such as Hong Kong and Tokyo, thereby fostering unhealthy lifestyles and increasing energy consumption for air conditioning (Chen and Mak, 2021). Moreover, Heatwaves intensified by the Urban Heat Island (UHI) effect significantly degrade urban thermal comfort, leading to the emergence of localised outdoor comfort hubs, such as elevated and arcade designs, in high-density cities with hot and humid summers. These design strategies are increasingly adopted due to their synergistic benefits in providing shading and enhancing downwash. By employing a microclimate design methodology based on wind and thermal simulations and experiments, both thermal and wind comfort can be maximized, while the risk of thermal stress is minimized. Therefore, conducting a comprehensive analysis of the flow field around diverse building shapes and configurations is of paramount importance for creating a more comfortable outdoor urban environment (Blocken et al., 2016).

Sustainable urban design improves pedestrian wind and thermal comfort. The elevated building, where the main structure is supported by pillars, has been proven to enhance ventilation at the pedestrian level (Figure 1.1 (a)). Liu et al. (2017) utilized Detached eddy simulation (DES) to investigate the flow field around an elevated building and concluded that URANS performs no better than SRANS while requiring more computational resources. Liu et al. (2019) employed LES simulations to investigate the influence of surrounding buildings on elevated buildings and discovered that elevated buildings can enhance ventilation even when surrounded by other structures. Gao et al. (2022) utilized PIV to examine the flow field surrounding multiple elevated tall buildings, revealing that the elevation can reduce the drag effect acting on the structures. Modern buildings are generally irregular in shape and exhibit diverse configurations and layouts. The wind environment near elevated buildings may be significantly altered by surrounding structures. Therefore, the impact of irregular high-rise elevated buildings on PLWEs, as well as the flow interactions between elevated buildings and adjacent building blocks, warrants further investigation to enhance PLWEs. Despite numerous investigations into evaluating the flow field around elevated buildings, the turbulent statistics, including turbulent kinetic energy, normal components of Reynolds stress, and instantaneous velocity components, have not been systematically investigated. The arcade design (Figure 1.1 (b)), characterized its semi-open structure or horizontal recesses beneath the main building body (Hang et al., 2024; Juan et al., 2017), has been demonstrated to enhance outdoor wind and thermal comfort while mitigating the UHI effect by providing a thoroughfare for pedestrians and offering a commercial space for commissaries to conduct business (Li et al., 2022). Juan et al. (2017) used CFD simulation to investigate the flow behavior with and without the arcade design and concluded that a wider arcade design was preferable for enhancing PLWEs. Li et al. (2022) conducted a study on the impact of setback dimensions on pedestrian comfort, demonstrating that an increased horizontal setback elevates wind velocity on the leeward side while reducing it on the windward side. However, most previous studies have focused on the effects of arcade design on urban microclimate under isothermal conditions. The thermal impact of solar radiation has been acknowledged as a crucial factor influencing flow patterns in urban areas, the integration of solar-responsive strategies into building configuration presents a significant challenge for professionals in the field of urban design (Yang et al., 2021). Therefore, it is essential to consider the impact of solar radiation when addressing urban microclimate issues.

(a) (b)

Figure 1.1. Schematics of (a) Elevated design (taken by another author) (Zhang et al., 2017) and (b) Arcade design (Internet figure).

In addition to the effect of building shapes on PLWEs, ensuring an accurate replication of the atmospheric boundary layer (ABL) in wind tunnel experiments is imperative to attain precise results (Tse et al., 2017). Considerable research efforts have been devoted to replicating ABL with a constant wind direction along the height of the layer; however, the variation of wind directions along the height was confirmed and documented in the literature (Mendenhall, 1967; Taylor, 1916). The turning of wind directions along the height is attributed to the combined effects of the Earth's rotation, the friction of the Earth's surface, and pressure gradient forces (A. Peña, 2014). The effects of wind turning have been observed by a series of field measurement studies (Liu et al., 2018; Mendenhall, 1967; Shu et al., 2018). Tse et al. (2016) summarized the wind twist angle of 256 measured wind profiles in Hong Kong and observed a larger twist angle at lower altitudes near the ground, indicating that deviations in wind directions are not only influenced by the Ekman spiral in the ABL but also by wind environments. Therefore, evaluating the impact of twisted wind flow at the pedestrian level in Hong Kong holds considerable importance. The accurate assessment of the wind environment under topography-induced twisted wind profiles is crucial for mountainous regions with complex meteorological conditions like Hong Kong, where hilly terrain is the primary factor causing such profiles (Figure 1.2). Therefore, an investigation into the impact of twisted wind on pedestrian comfort in various building configurations is essential.

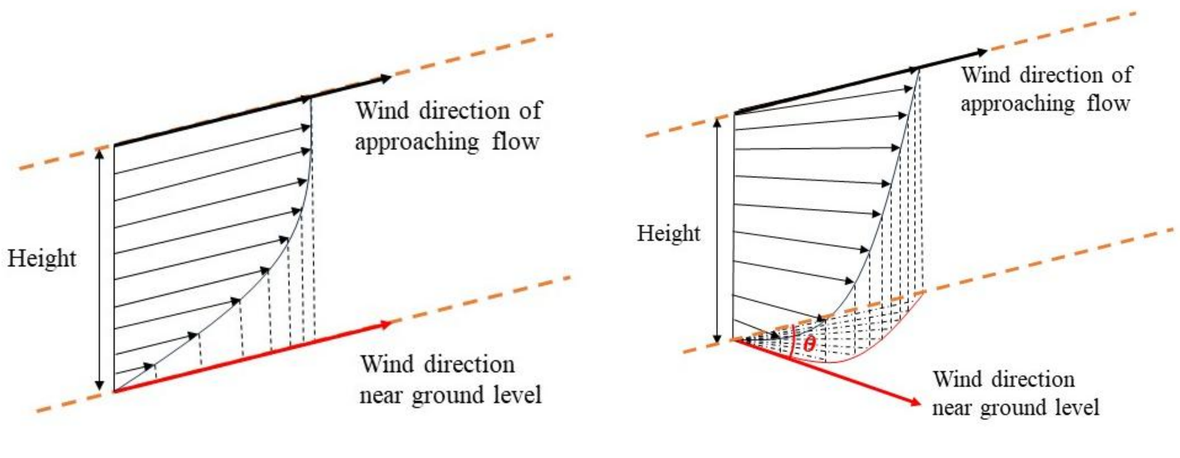

(a) CWP (b) TWP

Figure 1.2. Schematics of (a) Conventional wind profile (CWP) and (b) Twisted wind profile (TWP) (Tse et al., 2016).

The application of wind tunnel tests and Computational fluid dynamics (CFD) simulations has been recognized as two powerful methods to address a wide range of urban microclimate issues, including wind comfort and air quality (Blocken et al., 2016; Chew and Norford, 2018). These two methods are often used in conjunction for the prediction and assessment of PLWEs. Wind tunnel experiments are capable of controlling boundary conditions and providing reliable data for CFD validation, particularly for the validation of inflow flow properties and building geometries, which is a key aspect in ensuring the accuracy of CFD simulations. For example, Tominaga and Shirzadi (2021) conducted wind tunnel experiments to explore the effect of high-rise buildings on the PLWs around a building group, and the results showed obvious wind environment changes around the surrounding street canyon owing to the complex flow interactions generated by high-rise buildings. Tsang et al. (2012) revealed the effects of building dimensions, separation, and podium on PLWs through a wind tunnel test and pointed out that narrow building spacing was against the PLWs. Based on the validation with the reliable wind tunnel experiments, CFD has become an effective method to evaluate the outdoor microclimate by offering a detailed visualization of the flow field (Liu and Niu, 2016). Choosing appropriate turbulence modelling approaches is essential in CFD simulations, as various turbulence models have distinct impacts on the accuracy of the simulated flow field (Yang et al., 2023; Sudirman et al., 2025; Tominaga and Shirzadi, 2021). RANS and LES represent two primary turbulence modeling approaches utilized for the calculation of airflow characteristics in urban environments (Zheng and Yang, 2021; Yang et al., 2023). RANS have been extensively utilized in microclimate evaluation owing to their relatively short computational time and modest hardware requirements (Tominaga and Stathopoulos, 2009). RANS with the RNG $k-\varepsilon$ model and the SST $k-\omega$ model are popular in assessing airflows in urban areas; however, RANS models still exhibit certain limitations, such as over-predicting the reattachment length behind the building and failing to resolve flow variables (Caciolo et al., 2012). LES focuses on resolving large eddies to accurately capture transient processes while modeling small eddies using subgrid-scale models, which incurs relatively higher computational costs (Tominaga and Stathopoulos, 2012). For example, Zeng and Yang (2021) compared the SRANS and LES in simulating wind flow in a street canyon and found that the standard $k-\varepsilon$ (SKE) turbulence model demonstrated the best agreement with the wind tunnel data. Shirzadi and Tominaga (2022) investigated the accuracy of RANS and LES in predicting the mean and turbulent flow characteristics around a high-rise building surrounded by low-rise buildings and found that the performance of LES and RANS models was similar in high velocity regions. Wang and You (2024) investigated the wind speed distribution in real urban layouts using both RANS and LES models. They found that the RNG $k-\varepsilon$ model and SST $k-\omega$ model yield comparable predictions for mean wind velocity, whereas LES demonstrated superior performance in estimating wind speed. To sum up, the SRANS models, especially the RNG $k-\varepsilon$ model and SST $k-\omega$ model, can accurately capture airflows to a reasonable extent but exhibit limitations in complex turbulence modelling. In contrast, LES is able to resolve small-scale turbulence, yet it demands substantial computational resources. Therefore, it is crucial to investigate whether replacing the LES model with the RANS model is suitable for simulating the flow field around elevated buildings and systematically evaluate and compare the performance differences among these turbulence modelling approaches.

1.2 Research aim, objectives, and significance

Due to the limited research on three-dimensional turbulent flow structures around buildings with open or semi-open structures, and their behaviour under a twisted wind profile, this thesis aims to systematically investigate the PLWEs around a single elevated building and its performance when surrounded by other structures. In addition to its behaviour under conventional wind profiles, the differences in wind and thermal environments surrounding elevated and arcade buildings under conventional and twisted wind profiles are examined. In alignment with the research objective, this thesis is structured around the following research questions:

1. How do irregular elevated buildings ("V" shape, "Arc" shape) within the urban arrays affect the time-averaged velocities and the turbulent statistics, i.e., the turbulent kinetic energy, gust factor (GF), compared to a rectangular elevated building? And how does the elevated building influence PLWEs under both weak and windy conditions?
2. How does the single "Arc" shaped elevated building affect the time-averaged and gust wind environment compared to the non-elevated building? And how applicable are various turbulence modelling approaches for accurately simulating airflow dynamics in such geometries?

3. How do the non-identical-height elevated buildings in tandem arrangement affect the PLWEs under both CWP and TWP? And how does the ventilation performance of elevated buildings differ in hilly areas compared to flat areas?
4. How does the twisted wind affect the wind and thermal comfort around the street canyon with arcade design under realistic solar heating? And how do arcade design dimensions and street parameters impact wind and thermal comfort under CWP and TWP?

This study involves wind tunnel experiments and CFD simulations to investigate the PLWEs and gust characteristics around buildings with open or semi-open structures, as well as their performance under both conventional and twisted wind profiles. Figure 1.3 presents an overview of the present research. Task 1 addresses Research Questions (1) and (2), focusing on the three-dimensional turbulence structure around a single elevated building and assessing the influence of surrounding buildings. Tasks 2 and 3 address Research Questions (3) and (4), respectively, focusing on the effects of twisted wind on wind and thermal comfort surrounding the elevated and arcade buildings. The present study provides references about the impact of open and semi-open structures on the general flow structure and pedestrian wind environment, and offers valuable recommendations for urban planners on implementing elevated structures in hilly urban areas prone to frequent twist flows.

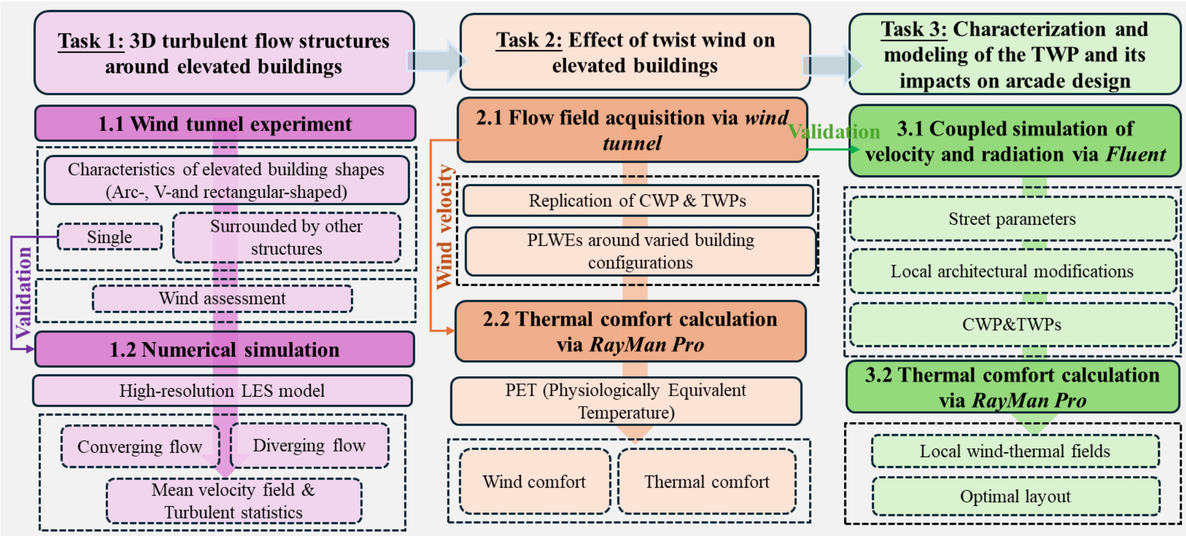

Figure 1.3. The outline of the research content.

1.3 Outline of the thesis

The present chapter outlines the research background and motivation for the current study. Based on the identified research gap, the chapter further elaborates on the research aim, outlines, and significance. The subsequent chapters of this thesis are structured as follows:

CHAPTER 2 presents a comprehensive literature review covering PLW and thermal comfort, flow fields around fully open and semi-open buildings, turbulence models, and wind tunnel experiments utilized in this thesis.

CHAPTER 3 assesses the pedestrian-level gust wind flow and comfort around irregular elevated buildings within simplified urban arrays through wind tunnel experiments.

CHAPTER 4 investigates the mean and turbulent wind characteristics around a high-rise elevated building with curved cross-sections using CFD simulations and wind tunnel experiments.

CHAPTER 5 presents the results of the PLWEs surrounding two tandem non-identical height elevated buildings under the influence of twisted wind flows, as investigated through wind tunnel experiments.

CHAPTER 6 examines the impact of twisted wind on pedestrian comfort around semi-open structures and the influential factors under solar heating, as analyzed through CFD simulations.

CHAPTER 7 summarizes the key contributions and findings of the present research and offers guidance for future academic investigations.

CHAPTER 2. LITERATURE REVIEW

2.1 Pedestrian level wind environment

The aerodynamic interference between buildings can alter the outdoor wind environment at the pedestrian level and may deteriorate pedestrian-level wind (PLW) comfort (Tominaga and Shirzadi, 2021). The pedestrian-level wind environments (PLWEs) generally refer to the wind velocity at pedestrian-level heights, typically ranging from 1.5 m to 2 m. Pervading tall buildings in cities tends to bring high-velocity wind from the upper level to the near-ground level and may create uncomfortable or even dangerous wind comfort conditions near building corners (Melbourne, 1971). Therefore, the effect of varied building shapes and layouts on PLW comfort has attracted increasing attention from worldwide researchers (Sheng et al., 2018), such as building heights (Chen and Mak, 2021; Tse et al., 2017), building disposition (Hang and Li, 2010), building permeability (Yuan and Ng, 2012; Du et al., 2018). PLW comfort assessments are typically based on statistical meteorological data, aerodynamic information, and predefined criteria. Statistical meteorological data are typically obtained from weather stations and integrated with wind comfort standards to assess the conditions of wind comfort (Blocken et al., 2016). Wind comfort criteria typically define threshold wind speeds (U_{THR}) for the effective wind speeds (U_e) and specify the maximum allowable exceedance probability (P), as expressed in the Equation (2.1). The wind conditions around the buildings are generally obtained from wind tunnel tests or numerical simulations with CFD.

$$U_e = U + k\sigma_u \tag{2.1}$$

where U is the mean wind velocity, k is the peak factor (usually has the value between 1 and 4) (Lawson, 1978), and σ_u is the RMS value of the wind velocity fluctuation.

According to the threshold wind velocities and the maximum allowable exceedance probability, several distinct wind comfort criteria have been established, each corresponding to specific wind conditions under both weak (Du et al., 2017; Tse et al., 2017) and strong wind regimes (Melbourne, 1978; Soligo, 1993; Willemsen and Wisse, 2007). These criteria were categorised based on various outdoor activities, such as sitting, strolling, and walking. The discrepancies among various wind comfort standards have been documented in previous studies (Bottema, 2000; Holger Koss, 2006). For instance, although the wind criteria proposed by Isyumov & Davenport and Lawson & Penwarden are similar in their use of the Beaufort scale and exceedance probability to classify outdoor activities (N. Isyumov and Davenport, 1975; Lawson, 1978), the Beaufort value specified by Isyumov & Davenport is higher than that defined by Lawson. The Melbourne criteria (1978) were established based on peak gust wind velocity and exceedance probability for various categories of outdoor activities (Melbourne, 1978). The Soligo criterion was formulated based on the mean wind velocity and the statistical likelihood of threshold exceedance, with a 20% exceedance probability applied uniformly across all activity categories (Soligo, 1993). Furthermore, wind assessments under weak wind conditions were proposed by previous researchers and are specifically designed for urban environments characterized by low-wind conditions, such as Hong Kong (Du et al., 2017). The wind assessment criteria were proposed on a seasonal basis, and the overall mean wind velocity ratio (*OMVR*) was adopted as the threshold wind velocity parameter.

Urban geometry is a more controllable factor than others, such as building materials and urban greening, and directly influences outdoor wind comfort. Many previous studies have focused on the effects of single building shapes (Memon et al., 2010; Hang et al., 2012; Yuan and Ng, 2012), street canyon (Gu et al., 2011; Xiaomin et al., 2006; Tang et al., 2023), and urban density on PLWEs (Li et al., 2020; Xu and Gao, 2022). For example, Lin et al. (2025) mentioned that the building height significantly alters PLW velocity fields, though its effect on turbulent kinetic energy (TKE) is less apparent. Peng et al. (2021) studied street canyon ventilation under various building forms and recommended avoiding buildings aligned parallel to streets for improved airflow. Li et al. (2020) systematically studied the impact of building array frontal area density (λ_F) on pedestrian-level thermal comfort and airflow, finding that increased density leads to a steady decrease in air velocity. Moreover, urban heterogeneity, including variations in building height and layout, plays a key role in the microclimate issue due to its non-uniform structure in real urban environments (Amorim et al., 2013). Irregular building shapes and non-uniform arrangements create complex flow patterns that impact wind comfort, promoting further research in this area (Li et al., 2020). Nevertheless, the effect of non-identical building layouts is often neglected (Li et al., 2020), and uniform building models fail to capture the flow structure in non-uniform building models (Gu et al., 2011). Numerous studies have investigated asymmetrical architectural designs intended to improve ventilation performance, as detailed in Table 2.1.

Table 2.1. Studies on the microclimate problems in the asymmetrical building configurations with and without an elevated structure. Source: the authors.

Reference	Methods	Urban geometry parameters	Elevated structure	Main conclusion
Reiminger et al., 2020	CFD	Aspect ratios of up-down buildings; Aspect ratio of street width to the windward building height.	No	The mean concentrations increased as building height disparities became more pronounced and decreased with narrower street widths.
Chew and Norford, 2018	WCE+CFD	Canyon aspect ratio, void deck height	No	The influence of variations in the canyon aspect ratio on wind enhancement was found to be less significant compared to variations in the void deck height.

Li et al., 2020	CFD	Aspect ratios of up-down buildings	No	The change in the height of the lower building caused a slight modification to the flow pattern within the step-up canyon.
Chen and Mak, 2021	CFD	Aspect ratios of up-down buildings	Yes	Uneven building height can improve PLWEs in the interest precinct.
Addepalli and Pardyjak, 2013	WT	Aspect ratios of up-down buildings, along-wind length	No	The flow along the vertical symmetry plane is shielded from the lateral flow at large building widths, resulting in a stable counter-rotating vortex pair within the canyon.
Freidooni et al., 2021	CFD	Gap spacing, aspect ratios of up-down buildings	No	A minimal gap of 3 is recommended for better PLW conditions.
Tang et al., 2023	CFD	Characteristics of trees, step-up, and step-down canyon	No	The ventilation performance of neighboring canyons varies greatly due to the non-uniform arrangement of street canyons.
Wen et al., 2022	CFD	Standard deviation of the building height	No	The increase in building height standard deviation enhances canopy ventilation, but the pronounced asymmetry of the building reduces interior ventilation capacity for step-up layouts.
Sin et al., 2023	CFD	Aspect ratios of up-down buildings	Yes	The ventilation capacity of asymmetric canyons increases with elevated height.

Note: WT=Wind tunnel; CFD=Computational fluid dynamics; WCE=Water channel experiment.

2.2 Thermal environment

The thermal comfort level is jointly determined by the outdoor thermal environment, human physiological status, and human adaptation, and the thermal environment is considered the primary determinant of thermal comfort when human physiological status and adaptive capacity are held constant (Ji et al., 2022). Air temperature, humidity, and wind velocity exhibit a strong correlation with the outdoor thermal environment. Furthermore, air temperature and solar radiation magnitude are the primary determinants of steady outdoor thermal comfort levels in hot-summer and cold-winter climates (Liu et al., 2016). Several indices are used for assessing outdoor thermal comfort, including the Predicted Mean Vote (*PMV*), which is calculated based on four environmental parameters (Fanger, 1970); the New Standard Effective Temperature (*SET**), defined as the equivalent temperature of an isothermal environment at 50% relative humidity (*RH*) (Gagge, 1986); the Physiological Equivalent Temperature (*PET*), determined as the air temperature at which core and skin temperatures match those under the evaluated conditions during thermal balance (Höppe, 1999); and the Universal Thermal Climate Index (*UTCI*), which is based on principles of thermophysiology, medicine, and environmental science (Fiala et al., 2012).

There are several methods for assessing thermal comfort, such as on-site measurements (Du et al., 2017; Liu et al., 2016), wind tunnel tests (Uehara, 2000), and numerical simulations (Li et al., 2022; Abd Elraouf et al., 2022). Most previous field studies have focused on measuring air temperature, humidity, wind speed, and direction, with more measurements conducted at the neighborhood rather than city scale (Yang et al., 2023). For example, Du et al. (2017) used on-site monitoring for obtaining environment parameters around the lift-up design in Hong Kong and found that the lift-up design can effectively improve the pedestrian level thermal comfort. Chen et al. (2024) investigated the thermal comfort around the elevated walkways through on-site measurement and found that they increased ground level PET by up to $2.7^{\circ}C$. Wind tunnel experiments face challenges in accounting for thermal buoyancy flow, with most laboratory studies focusing on the thermal conditions and radiation in urban street canyons. Lin et al. (2020) used particle image velocimetry (PIV) to study how different surface heating conditions affect the flow field in a wind tunnel and found that heat accumulates in various corners of the canyon walls under ground heating conditions. CFD simulations are widely used to explore urban microclimate issues due to their accessibility and flexibility. Li et al. (2020) combined the Rayman model with ANSYS Fluent to study how the frontal area density of building arrays affects thermal comfort and found that higher frontal area density increases PET over most sidewalks. Most previous studies focused on understanding the urban environment and identifying solutions to UHI issues. Lai et al. (2019) identified several strategies for improving thermal comfort, including urban geometry, vegetation, reflective surfaces, and water bodies. Modifying the geometry can change radiation, wind velocity, and air temperature, thereby significantly affecting thermal comfort (Chen et al., 2024). Thermal comfort improvement primarily involves reducing thermal radiation and increasing wind velocity (Niu et al., 2015), leading to the emergence of various shading types, such as overhangs (Middel et al., 2021), arcades (Li et al., 2025; Hang et al., 2024), elevated buildings (Du et al., 2017; Huang et al., 2020), walkways (Chen et al., 2024), and vegetation (Mohammadi et al., 2023). The shading elements are expected to reduce pedestrian heat stress by lowering solar radiation and cooling the surrounding temperature.

2.3 Building with open and semi-open designs

2.3.1 Elevated design

In metropolitan and densely populated cities such as Hong Kong, limited land resources have led to an increasing number of high-rise buildings, resulting in observed and addressed unfavourable wind and thermal environmental issues. Novel architectural designs have proven to be an effective way to improve PLW comfort, including building openings (van Druenen et al., 2019; Fan et al., 2017; Hang and Li, 2011; Hang and Li, 2010; Yuan and Ng, 2012), arcade design (Hang et al., 2013; Juan et al., 2017; Wen et al., 2017) and elevated buildings (Chen and Mak, 2021; Du et al., 2017; Zhang et al., 2018; Xia et al., 2015). Previous studies have mentioned the importance of single elevated buildings for improving PLW comfort in urban areas under weak wind conditions (Du et al., 2017; Zhang et al., 2017; Xia et al., 2015). Field measurements of the PLWEs have also been conducted (Zhang et al., 2023; Niu et al., 2015). Zhang et al. (2023) investigated the effects of the elevated ratio and elevated position on PLWEs through field measurements and numerical simulations, and found that the elevated position at both ends or in the middle can improve PLW significantly. Niu et al. (2015) found a higher wind velocity underneath an elevated building than in open space with surrounding buildings using field measurements. The CFD method is a popular alternative for PLW comfort evaluation in urban areas because of its relatively low cost and availability of whole-field flow data (Blocken et al., 2016). Chen and Mak (2021) investigated the PLW comfort around various unconventional elevated configurations through a CFD simulation and revealed the effects of the building width, wind incident angle, and surface discontinuity on the unfavourable wind comfort area size. Du et al. (2017) explored the effects of four elevated building configurations (“ — ”, “L”, “U”, and “□”) on PLW and concluded that elevated buildings can improve the wind environment in building surroundings. In addition to the field measurements and CFD simulations, the effectiveness of a single elevated building has also been validated through wind tunnel experiments. Zhang et al. (2017) measured the effects of aspect ratios and central core size of elevated buildings on pedestrian wind comfort near elevated buildings in a wind tunnel and proposed central core corner modifications for pedestrian wind comfort improvement. Xia et al. (2015) found that elevated buildings increase the mean wind velocity in the downstream region by approximately 3% – 11%. Tse et al. (2017) established a wind tunnel experimentation framework to evaluate the capacity of elevated building forms to improve PLWEs and revealed the relationship between the elevated core height and high and low wind velocity regions around elevated buildings. Although the effectiveness of improving urban wind comfort using a single elevated building has been verified, the wind environment near the elevated building may be altered dramatically by the surrounding buildings. Modern buildings are typically irregular and exhibit various configurations and layouts. Hence, the impact of an irregular high-rise elevated building on PLWEs and the flow interaction between elevated buildings and surrounding building blocks are worth exploring for PLWEs improvement.

2.3.2 Arcade design

The arcade design, characterized by a semi-open layout or horizontal setbacks beneath the main building body (Hang et al., 2024; Juan et al., 2017), has been demonstrated to enhance outdoor wind and thermal comfort while mitigating the UHI effect by providing a thoroughfare for pedestrians and offering a commercial space for commissaries to conduct business (Li et al., 2022). Hang et al. (2013) explored the effects of semi-open streets on the urban canopy layer and found that semi-open roofs significantly alter ventilation patterns and flow rates. Juan et al. (2017) used CFD simulation to investigate the flow behavior with and without the arcade design and concluded that a wider arcade design was preferable for enhancing PLWEs. Li et al. (2022) examined how the dimensions of setbacks influence pedestrian comfort and discovered that expanding the horizontal setback increased wind speed on the leeward side but reduced it on the windward side. Hang et al. (2024) investigated the effects of the arcade dimensions on pedestrian comfort under realistic solar radiation conditions and concluded that arcade heights have little influence on air temperature and wind velocity. The thermal impact of solar radiation has been acknowledged as a crucial factor influencing flow patterns in urban areas (Yang et al., 2021). The integration of solar-responsive strategies into building configuration presents a significant challenge for professionals in the field of urban design. The heat emitted from the building surfaces or the ground, resulting from solar radiation, elevates the air temperature between buildings compared to that outside and impacts air quality and ventilation in surrounding structures (Wang et al., 2014). The buoyancy effect should not be disregarded due to the temperature disparities between heated building surfaces and the ground (Li et al., 2021), as it serves as a crucial driving force for natural ventilation, particularly in low wind velocity conditions prevalent in densely populated cities such as Hong Kong. Therefore, it is essential to consider the impact of solar radiation when addressing urban microclimate issues.

2.4 Twisted wind

The utilization of wind tunnel experiments has emerged as a prominent methodology for investigating the impact of diverse building geometries on PLWEs. Ensuring an accurate replication of the ABL in wind tunnel experiments is imperative to attain precise results (Tse et al., 2017). Considerable research efforts have been devoted to replicating ABL with a constant wind direction along the height of the layer; however, the variation of wind directions along the height was confirmed and documented in the literature (Mendenhall, 1967; Taylor, 1916). The turning of wind directions along the height is attributed to the combined effects of the Earth’s rotation, the friction of the Earth's surface, and pressure gradient forces (A. Peña, 2014). The effects of wind turning have been observed by a series of field measurement research (Liu et al., 2018; Mendenhall, 1967; Shu et al., 2018). Mendenhall (1967) mentioned that the wind twist angle over land is approximately 20° influenced by horizontal temperature gradient and thermal stability. Liu et al. (2018) employed a wind profiler to measure wind velocities and directions in ABL up to a height of a thousand meters, revealing that within the first 1,000 m, wind twist angles can reach up from 5° to 40°. Shu et al. (2018) used a Doppler wind profiler to measure wind veering angle profiles under 800 m in Hong Kong and observed that wind direction turns by approximately 20° to 40° within the first 1,000 meters above ground. Tse et al. (2016) conducted a comprehensive analysis of wind twist angles obtained from 256 documented wind profiles collected in Hong Kong and observed a larger twist angle at lower altitudes near the ground, indicating that deviations in wind directions are not only influenced by the Ekman spiral in the ABL but also by wind environments. Based on the Ekman spiral (Ekman, 1905), the twist angle profile $\theta_{(z)}$ can be expressed as Equation (2.2) and lateral wind velocity $v_{(z)}$ can be expressed as Equation (2.3), where u_g and v_g denotes the components of the geostrophic wind velocity, h_E denotes the Ekman height.

$$\theta_{(z)} = \arctan(\frac{v_{(z)}}{u_{(z)}}) = \frac{v_g[1-e^{-\frac{z}{h_E}}\cos(\frac{z}{h_E})] + u_g e^{-\frac{z}{h_E}}\sin(\frac{z}{h_E})}{u_g[1-e^{-\frac{z}{h_E}}\cos(\frac{z}{h_E})] - v_g e^{-\frac{z}{h_E}}\sin(\frac{z}{h_E})} \tag{2.2}$$

$$v_{(z)} = u(z)\tan\theta \tag{2.3}$$

Therefore, assessing the impact of twisted wind flow at the pedestrian level in Hong Kong holds significant importance. As shown in Figure 1.2, a twisted wind profile refers to a situation where the wind di7%rection varies at different heights along the profile, which distinguishes it from a conventional wind profile characterized by constant wind directions (Yan et al., 2023). Extensive studies have been conducted on the wind environment under TWP (Tse et al., 2017; Tse et al., 2017; Tse et al., 2016; Liu et al., 2019; Tang et al., 2023; Yan et al., 2022; Yuan et al., 2023). Table 2.2 summarizes some representative research on the twisted wind effects of different parameters on pedestrian comfort. Tse et al. (2016) effectively employed wooden vanes to replicate twisted wind conditions within a boundary layer wind tunnel and found that twisted wind dramatically altered flow characteristics, resulting in an asymmetric distribution of wind velocity around buildings. Furthermore, the impact of twisted wind on isolated buildings and inter-building passages has been investigated and unveiled distinct influences of wind attack angles on airflow under both CWP and TWP (Tse et al., 2017; Tse et al., 2017). Weerasuriya et al. (2018) investigated the effect of wind veering on the outcomes of AVA and found significant variations in PLW velocity at locations with low building densities and previous studies have demonstrated that the mountainous topography in Hong Kong plays a significant role in the wind environments within urban areas (Tse et al., 2016; Zhang et al., 2021). The influence of twisted wind flows on the PLWEs, however, cannot be fully reflected in typical wind tunnel experiments that employ conventional wind profiles. The accurate assessment of the wind environment under topography-induced twisted wind profiles is crucial for mountainous regions with complex meteorological conditions like Hong Kong, where hilly terrain is considered to be the primary factor causing such profiles.

Table 2.2. Studies on the twisted wind effect between different parameters on pedestrian comfort. Source: the authors.

Reference	**Urban geometry factors**	**Building configurations**	**Methods**	**Main conclusion**
Tse et al., 2017	Aspect ratios (H/W)	Single building	WT	For wider buildings ($H<W$), the deviation of downstream far-field low-velocity wind zones was more significant.
Tse et al., 2017	Aspect ratios (H/W), Passage width (d)	Building array	WT	The wind velocities in the passage decreased as the twist angles increased.
Li et al., 2024	Height difference (H_{UB}/H_{DB})	Elevated building	WT	Elevated buildings were more sensitive to twisted wind compared to non-elevated buildings.

Li et al., 2024	Height difference (H_{UB}/H_{DB})	Two buildings in a tandem arrangement	WT	Step-down building configurations ($H_{UB}>H_{DB}$) were insensitive to the twisted wind profile.
Yuan et al., 2022	Horizontal homogeneity	Single building	CFD	The asymmetric flow field induced by TWP was affected by the twist angle and varied along the height.
Zhang et al., 2021	Building heights (H)	Real urban topology	CFD	The twisted wind flows exert a significant impact on the Air Ventilation Assessment (AVA) results.
Zhou et al., 2021	Building heights (H)	Single building	CFD	The wake deviation angle was determined by the incoming flow direction and the wake characteristics of the adjacent height.
Chen et al., 2023	Building heights (H)	Single building	CFD	The flow attachment on the left side gradually diminished as the degree of twist flow increases.
Feng et al., 2019	Aspect ratios (H/W)	Single building	CFD	The twisted wind induced inconsistencies in the wind directions at different vertical heights.

Note: WT=Wind tunnel; CFD=Computational Fluid Dynamics.

2.5 Wind tunnel and CFD simulations for pedestrian comfort assessment

Regarding the urban wind environment and thermal conditions, two primary methodologies are commonly employed for investigation: experimental approaches, encompassing wind tunnel testing and field measurements, and numerical simulations (Yang et al., 2023; Blocken et al., 2016). Wind tunnel experiments for assessing PLWEs can be conducted using low-cost measurement techniques such as hot-wire anemometry (Tominaga and Shirzadi, 2021), Irwin probes (Zhang et al., 2018; Du et al., 2017; Li et al., 2024), and Cobra probes (Li et al., 2024). Due to their high costs, Laser-Doppler Anemometry (LDA) and Particle Image Velocimetry (PIV) are less frequently employed in urban wind environment studies. The hot-wire anemometry (HWA) and Cobra probe exhibit high frequency response and are capable of measuring wind velocity components in the *x*-, *y*-, and *z*-directions, which contributes to their widespread use in studies of PLWEs. The Cobra Probe is a multi-hole pressure probe that provides dynamic three-component velocity measurements in real time for various turbulent flow conditions (Prohasky, 2014). The major drawbacks of these types of urban probes are their insensitivity to angular changes in velocity components normal to the wire axis, which limits their applicability in environments with high turbulence intensities (Durgin, 1992).

The Irwin probe is an omnidirectional sensor that measures wind velocity based on the differential pressure between the bottom of the sensor hole and the top of the sensor tube, with the velocity being calculated using a calibration formula (Irwin, 1981). The pressure difference between the sensor hole and the top of the sensor tube can be used to calculate wind velocity at pedestrian-level height. This relationship between the pressure difference Δp and the wind velocity u was established by Irwin (1981), as expressed in the Equation (2.4).

$$u = \alpha_1 + \beta_1 \sqrt{\Delta p} \tag{2.4}$$

where α_1 and β_1 are derived constants that are a function of the sensor dimensions and determined by comparison with reliable reference probes such as the Croba probe and hot-wire anemometer. In studies of PLWEs, Irwin probes are typically mounted at pedestrian-level height (1.5-2 m in the prototype) to rapidly measure wind velocity at a large number of locations. Another advantage of the Irwin probe is that it is less fragile compared to HWA. The drawback of the Irwin probe is that its low-frequency response may not be sufficient to capture adequate turbulent flow information. Additionally, it is unable to detect flow reversal. The use of Irwin probes for PLWEs studies has been reported by H. Wu, 1994; Tsang et al., 2012; Tse et al., 2017; Zhang et al., 2018.

A reliable and accurate wind tunnel study is essential for validating CFD simulations, particularly those involving ABL properties and building geometries. Many previous studies have employed wind tunnel experiments to investigate the flow regime around a single building (Tse et al., 2017; Tsang et al., 2012), and numerous simulations have used single-building configurations for validation (Murakami, 1993; K.B. Shah, 1997; Fu et al., 2024). Recently, an increasing number of researchers have focused on PLWEs around building arrays (Tominaga and Shirzadi, 2021; Tse et al., 2017), building arrangements (Gao et al., 2022), and real city areas (Fang et al., 2019; Flay et al., 2019), This is because the flow region around a building is often significantly influenced by surrounding structures, and the interactions affecting velocity fluctuations at the pedestrian level warrant further investigation. Additionally, although mean wind velocity is commonly used for validation in low-fidelity approaches such as steady RANS equations, measured turbulent fluctuation statistics are indispensable for high-fidelity approaches such as LES. Therefore, more turbulent statistics data obtained from wind tunnel experiments should be provided to improve transient turbulence simulations.

Owing to the rapid development of computational resources, CFD simulations have emerged and become one of the powerful approaches in wind-related studies (Blocken, 2015). CFD is often used in conjunction with wind tunnel experiments to obtain a comprehensive understanding of the flow field surrounding buildings. The turbulence model has a significant impact on the accuracy of the predicted flow field (Wang and You, 2024; Antoniou et al., 2019). RANS and LES are among the most widely used turbulence modelling approaches for urban wind environment studies (Zheng and Yang, 2021). For the governing equations of the steady

RANS approach, the following conservation equations are applied for incompressible fluids (Fluent, 2013):

$$\frac{\partial \overline{u_i}}{\partial x_i} = 0 \tag{2.5}$$

$$\frac{\partial(\rho \overline{u_i})}{\partial t} + \frac{\partial(\rho \overline{u_i}\,\overline{u_j})}{\partial x_j} = -\frac{\partial \overline{p}}{\partial x_i} + \frac{\partial \sigma_{ij}}{\partial x_j} + \frac{\partial \tau_{ij}}{\partial x_j} \tag{2.6}$$

$$\sigma_{ij} = \mu\left(\frac{\partial \overline{u_i}}{\partial x_j} + \frac{\partial \overline{u_j}}{\partial x_i}\right) - \frac{2}{3}\mu \frac{\partial \overline{u_l}}{\partial x_l}\delta_{ij} \tag{2.7}$$

$$\tau_{ij} = -\rho\overline{u_i^{'}u_j^{'}} \text{ for RANS} \tag{2.8}$$

$$\tau_{ij} = -\rho\overline{u_l u_j} + \rho\overline{u_i}\,\overline{u_j} \text{ for LES} \tag{2.9}$$

here, x_i and x_j are spatial coordinates; u_i, u_j and u_l are velocity components in different directions of Cartesian coordinates; ρ and $\overline{p}$ is the density and the mean pressure; μ is the dynamic viscosity; τ_{ij} is the Reynolds stresses; δ_{ij} is the Kronecker delta.

With regard to the RANS models, they are commonly employed in conjunction with two-equation turbulence closure models, including the standard $k-\varepsilon$ model, the realizable $k-\varepsilon$ model, and the renormalized group $k-\varepsilon$ model (Zhang et al., 2020). For the standard $k-\varepsilon$ model, the transport equation for k and ε may be expressed as:

$$u_i \frac{\partial k}{\partial x_i} = \frac{\partial}{\partial x_j}\left[\left(\mu + \frac{\mu_t}{\sigma_k}\right)\frac{\partial k}{\partial x_j}\right] + \frac{1}{\rho}(P_k + P_b) - \varepsilon \tag{2.10}$$

$$u_i \frac{\partial \varepsilon}{\partial x_i} = \frac{\partial}{\partial x_j}\left[\left(\mu + \frac{\mu_t}{\sigma_\varepsilon}\right)\frac{\partial \varepsilon}{\partial x_j}\right] + \frac{1}{\rho}C_1\frac{\varepsilon}{k}(P_k + P_b) - C_2\frac{\varepsilon^2}{k} \tag{2.11}$$

where, P_k and P_b is the turbulence production term due to the mean velocity shear and buoyancy; μ is the kinetic viscosity; μ_t is the turbulent eddy viscosity; C_1, C_2 and C_μ are the empirical constants at 1.44, 1.92, and 0.09 separately; σ_k and σ_ε are Parandtl numbers.

For the RNG $k-\varepsilon$ model, the turbulent viscosity was calculated by solving the two partial differential transport equations for turbulence kinetic energy (k) and dissipation (ε) based on Equations (2.12) and (2.13) (Yakhot, 1986).

$$\frac{\partial k}{\partial t}+\overline{u_j}\frac{\partial k}{\partial x_j}=\frac{1}{\rho}\frac{\partial}{\partial x_j}[\frac{\mu_t}{\sigma_k}\frac{\partial k}{\partial x_j}]+P_k-\varepsilon \tag{2.12}$$

$$\frac{\partial \varepsilon}{\partial t}+\overline{u_j}\frac{\partial \varepsilon}{\partial x_j}=\frac{1}{\rho}\frac{\partial}{\partial x_j}\left[\frac{\mu_t}{\sigma_\varepsilon}\frac{\partial \varepsilon}{\partial x_j}\right]+\frac{\varepsilon}{k}(C_{\varepsilon 1}P_k-C_{\varepsilon 2}\varepsilon) \tag{2.13}$$

where μ_t is the turbulent kinetic viscosity; P_k denotes the production term of k; $C_{\varepsilon 1}$, $C_{\varepsilon 2}$, σ_k, σ_ε, and C_μ are the values of the model constants.

The realizable $k-\varepsilon$ model consists of a new model dissipation rate equation and a new realizable eddy viscosity formulation, and the RLZ transport equation for ε (Lateb et al., 2013):

$$u_j\frac{\partial \varepsilon}{\partial x_j}=\frac{\partial}{\partial x_j}(\frac{\mu_t}{\sigma_\varepsilon}\frac{\partial \varepsilon}{\partial x_j})+C_1 S\varepsilon-C_2\frac{\varepsilon^2}{k+\sqrt{\mu\varepsilon}} \tag{2.14}$$

$$\eta=\frac{k}{\varepsilon}S \tag{2.15}$$

where $S=\sqrt{2S_{ij}S_{ij}}$ and S_{ij} is the velocity strain rate tensor.

CFD simulations can effectively model solar radiation, which is a significant factor influencing thermal comfort (Hang et al., 2024). An increasing number of CFD studies have incorporated the coupling of radiative transfer, and the radiative transfer equation (RTE) is defined as Equation (2.16) (Moemenbellah-Fard and Noori, 2020):

$$\frac{dI_r(r,s)}{ds}+(a+\sigma_s)I_r(r,s)=an^2\frac{\sigma T^4}{\pi}+\frac{\sigma_s}{4\pi}\int_0^{4\pi}I_r(r,s')\Phi(s,s')d\Omega' \tag{2.16}$$

here, I_r denotes the radiative intensity, r denotes the position, s denotes the direction, Ω represents the solid angle, Φ represents the phase function, σ_s is the scattering coefficient, a is the absorption coefficient, n is the refractive index. Several radiation models are widely utilized in urban thermal environment studies, such as P-1 (Toparlar et al., 2015), the discrete ordinate (DO) (Li et al., 2022), and Surface-to-Surface (S2S) (Chen et al., 2025) radiation models. The P-1 radiation model has been extensively employed in thermal environment studies due to its relatively lower computational resource requirements while maintaining accuracy in solving radiative heat transfer problems (Toparlar et al., 2015). The DO radiation model demonstrates high accuracy in resolving optical phenomena within systems characterized by complex geometries (Qu et al., 2012).

For the LES simulation, the Navier-Stokes equations are filtered to remove only the small turbulent eddies that are smaller than the filter size, which is typically set to the grid size. In LES, the small-scale flow motions are modelled, while the large-scale flow motions are directly resolved. The filtered variable is denoted as $\varphi(x) = \int_D \varphi(x^{'})G(x,x^{'})dx^{'}$, where D denotes the fluid domain and G denotes the filter function. Then, the LES equations are calculated by decomposing the solution variables:

$$\varphi = \varphi + \varphi^{'} \tag{2.17}$$

where φ presents the resolvable part and $\varphi^{'}$ is the subgrid-scale part. The filtered Navier-Stokes equations in LES are as follows:

$$\frac{\partial u_i}{\partial t} + u_j \frac{\partial u_i}{\partial x_j} = -\frac{1}{\rho}\frac{\partial p}{\partial x_i} + \frac{\partial}{\partial x_j}(2\nu s_{ij} - \overline{u_j^{'} u_i^{'}}) \tag{2.18}$$

where, u_i and p denotes the resolved velocity and pressure respectively, $u_i^{'}$ and $p^{'}$ denotes the subgrid-scale parts, $-\overline{u_j^{'}u_i^{'}}$ denotes the subgrid-scale stress and $\overline{s_{ij}}$ is the rate-of -strain tensor defined as $\overline{s_{ij}} = \frac{1}{2}(\frac{\partial u_i}{\partial x_j} + \frac{\partial u_j}{\partial x_i})$.

In LES simulations, subgrid-scale models are employed to approximate the effects of unresolved scales on the resolved flow field, and the Boussinesq hypothesis is commonly adopted:

$$\tau_{ij} - \frac{1}{3}\tau_{kk}\delta_{ij} = -2\mu_t s_{ij} \tag{2.19}$$

$$\tau_{ij} = u_i u_j - \overline{u_i u_j} \tag{2.20}$$

Here, μ_t denotes the subgrid-scale turbulent viscosity; τ_{kk} is the isotropic part of the subgrid-scale stresses. There are several SGS models that determine the μ_t : (a) the standard Smagorinsky-Lilly model; (b) the dynamic Smagorinsky-Lilly model; (c) the wall-adapting local eddy-viscosity model; and (d) the dynamic kinetic energy SGS model (Ai and Mak, 2015). LES is superior in resolving unsteady turbulent flows and capturing the nonlinear characteristics of wind flow around buildings. However, the computational resources required for LES are significantly greater than those needed for RANS. Additionally, LES requires inlet boundary conditions with time- and space-resolved data, as well as appropriate wall functions capable of introducing turbulence into the flow field. Moreover, the large number of output files generated poses a significant challenge to memory resources.

CHAPTER 3. Wind tunnel measurement of pedestrian-level gust wind flow and comfort around irregular elevated buildings within simplified urban arrays

3.1 Introduction

This chapter presents a wind tunnel study investigating the turbulent flow characteristics around two typical irregular elevated buildings (V-shaped and Arch-shaped) (Figure 3.1) and one traditional rectangular elevated building in Hong Kong among a group of low-rise buildings. Three different wind directions ($\varphi = 0^\circ$, 90°, and 180°) were investigated to examine the impact of wind flow on different parts of curved-shaped buildings (concave or convex) and their effects on pedestrian-level gust and mean wind velocities. The time-averaged characteristics and turbulence statistics of the wind velocity, including the TKE, gust factor, and the instantaneous velocity, have been analysed. Based on the measurement data, the PLW conditions of three elevated buildings within a simplified urban array with respect to different wind directions have been evaluated using the wind speed thresholds and maximum allowed exceedance probabilities in both weak and windy climates. This chapter aims to: (1) Investigate the flow characteristics of the flow field around two irregular elevated buildings with surrounding structures, in comparison to conventionally shaped elevated buildings; (2) Assess the turbulence statistics, especially gust wind and turbulence kinematic energy (TKE), around elevated buildings within urban environments (3) Reveal the disparities in flow field variations when winds impact the concave or convex sections of the building based on wind assessment criteria.

(a)

(b) (c)

Figure 3.1. (a) The elevated building (taken by another author) (Zhang et al., 2017) and two typical building shapes for (b) an Arc-shaped building and (c) a V-shaped building (snapshotted from Google map) in Hong Kong, China.

3.2 Experimental procedure

3.2.1 Building configuration and case description

Three types of elevated buildings with different shapes (V-shaped, Arc-shaped, and Rectangular-shaped) with the same 4.8 m-height elevated columns and a total height of 96 m are illustrated in Figure 3.2 (a) (Du et al., 2019). To reflect the actual layout of urban buildings, each elevated building was erected from a group of low-rise buildings to simulate a regular urban environment (Figure 3.2 (b)). A total of eight cubical buildings with dimensions of 40 m × 40 m × 40 m and a central elevated building were placed at the center of the turntable at planar area ratios of $\lambda_p = 0.25$, which represent urban areas of moderately dense configurations (Grimmond and Oke, 1999). The medium-density urban area is the most commonly used building layout for analyzing urban wind environments (Lin et al., 2014) and has been successfully employed in wind tunnel experiments (Tominaga and Shirzadi, 2021). The planar area ratio is defined as Equation (3.1):

$$\lambda_p = \frac{A_p}{A_T} \tag{3.1}$$

where λ_p represents the planar area ratio, A_p denotes the ground-level plot coverage of buildings, and A_T is the total ground coverage of the site under investigation. All the buildings were scaled by a factor of 1/200. Both the main body of the central elevated building and the surrounding blocks were made of high-density foam. As illustrated in Figure 3.2 (b), the interest precincts were 840 mm long and 840 mm wide in the scaled-down model, corresponding to 168 m long and 168 m wide in the prototype.

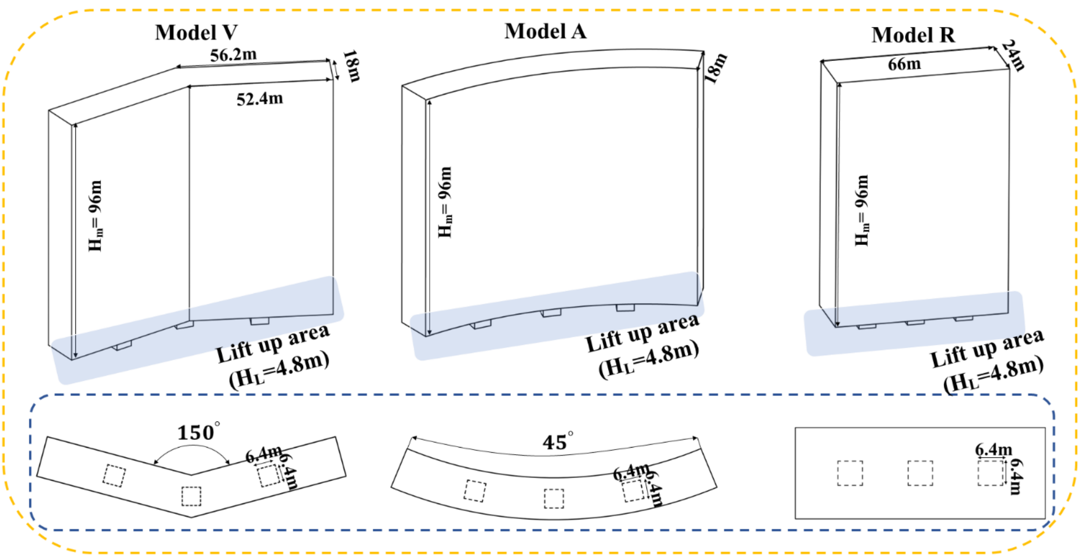

(a)

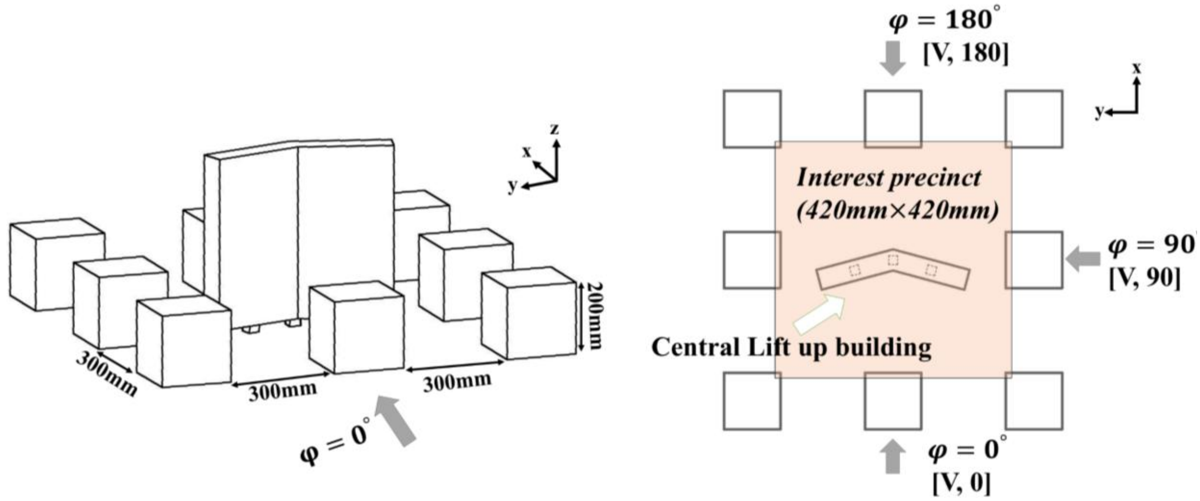

(b)

Figure 3.2. Schematics geometries of the elevated building models (a) three different elevated building shapes (in prototype), and (b) Test arrangement of V-shaped building and its interest precinct area.

The pedestrian-level winds with respect to these three elevated buildings under different wind directions ($\varphi = 0^{\circ}$, 90° and 180°) were measured. The approaching wind direction φ is defined as the angle between the wind direction and the coordinate axis x of the building plan. The nine cases with different building shapes and wind directions are listed in Table 3.1. It should be noted that Case [E] with open space in the middle of the array, rather than an elevated building, was set as the reference case.

Table 3.1. Test cases for elevated buildings.

Case name [model shape, wind direction]	Wind direction (degree)	Remarks
[A, 0]	0	
[A, 90]	90	Arc-shaped elevated building
[A, 180]	180	
[V, 0]	0	
[V, 90]	90	V-shaped elevated building
[V, 180]	180	

[R, 0]	0	Rectangular-shaped elevated building
[R, 90]	90	
[E]	0	Without a central elevated building

3.2.2 Wind tunnel setup

All wind tunnel experiments in this chapter have been performed in the Aerodynamics and Acoustics Facility (AAF) at the Hong Kong University of Science and Technology. The sizes of the test sections are 14.0 m, 2.5 m, and 2.0 m in the streamwise, spanwise, and vertical directions, corresponding to x, y, and z, respectively. The velocity components are denoted by u, v, and w. The building models were placed at the centre of a 1.8 m diameter turntable at the end of the test section. The ABL under natural wind conditions was simulated using the turbulence grid and floor roughness elements. The maximum blockage ratio was approximately 7%. Ratios up to 10% are sometimes used without correction in comparative or parametric studies, and as in our case, the relative differences between different cases remain valid. The mean wind speed profile in the ABL followed a power law with an exponent of approximately 0.2, which was adopted to simulate the suburban boundary condition corresponding to Terrain Category II (AS. NZS 1170.2, 2002). A TFI Series 100 Cobra probe was used to measure the ABL velocity and turbulence intensity profiles at the streamwise centreline of the test section. Figure 3.3 shows the measured mean wind velocity and turbulence intensity. The mean wind profile shown in Figure 3.3 (a) was normalised to the mean wind speed measured at the height of the central building (0.5 m). The measured errors were within 5%, ensuring confidence in the measurement data. The Reynolds number (R_e) calculated based on the height of the building H (0.5 m) and U_{ref} (7.5 m/s) was 2.65×10^5 ($R_{e,critical} = 5\times10^4$), thus, the flow conditions were independent of the Reynolds number (ASCE, 1999). By fitting the line to the velocity profile of the incident flow, the aerodynamic roughness length z_0 and ABL friction velocity u^* were obtained as 0.00049 m (0.098 m at full-scale) and 0.44 m/s, respectively. The velocity spectrum measured at the reference height is depicted in Figure 3.3 (b), demonstrating a good agreement with the Von Karman spectrum observed at the boundary layer height. The Von Karman spectrum can be described as follows (Biao et al., 2019):

$$\frac{fS_u}{\sigma_u^2} = \frac{4n}{(1+70.8n^2)^{5/6}} \tag{3.2}$$

where $n = fL_u / \overline{U}$, f is the frequency, L_u is the turbulence length scale, $\overline{U}$ is the mean wind velocity, S_u is the power spectrum density, and σ_u is the standard deviation of wind velocity.

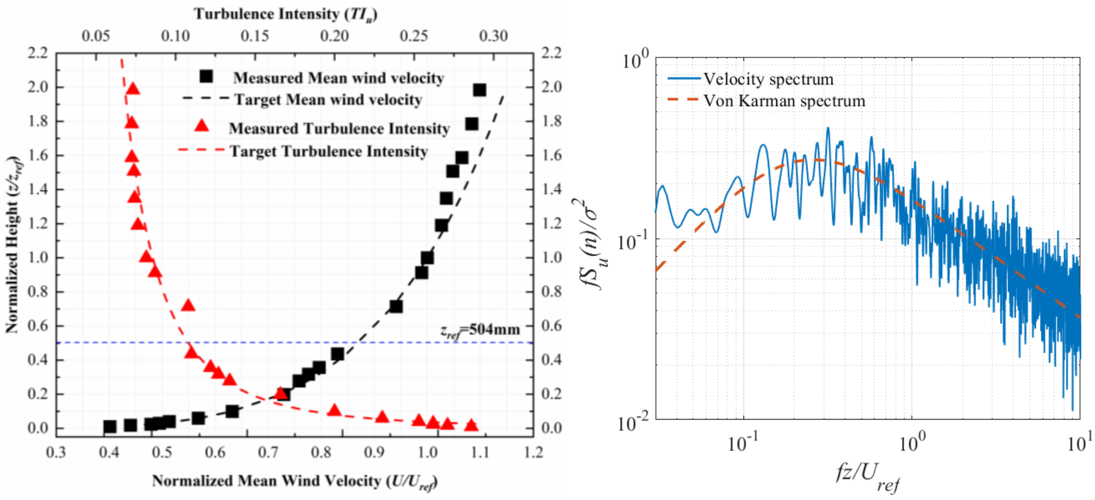

Figure 3.3. Vertical profiles of approaching flow (a) Normalized wind velocity and Turbulence Intensity profile, and (b) Longitudinal velocity spectrum at the reference height.

The wind velocities and directions at the pedestrian level were measured by the TFI Series 100 Cobra probe from TFI (Turbulent Flow Instrumentation Pty Ltd), and the Cobra probe was mounted on an ISEL transverse system to enable precise displacement control of the probe with an expected overall accuracy of 0.1 mm (Longo, 2012). When the turbulence intensity is lower than 30%, the wind velocity and wind direction measurement precisions of the probe are within $\pm 0.5ms^{-1}$, and the measurement precision for the wind direction is within $\pm 1^{\circ}$. The sampling frequency was 1,000 Hz, the sampling time was 30 s, and the length of each sampling data point was 30,000. The height of the reference point was 1 cm above the ground, corresponding to a height of 2 m in the prototype to represent pedestrian-level height. An overview of the wind tunnel setup and the detailed building model arrangements within the wind tunnel are shown in Figure 3.4 (a). The velocity measurement points are shown in Figure 3.4 (b), at approximately 100 points along the horizontal plane in each case.

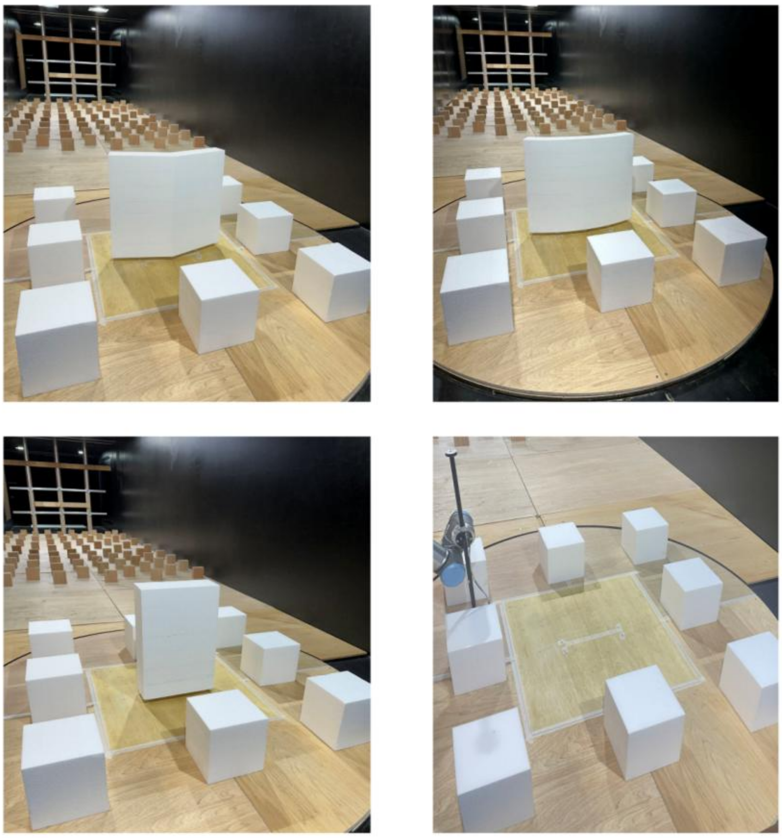

(a)

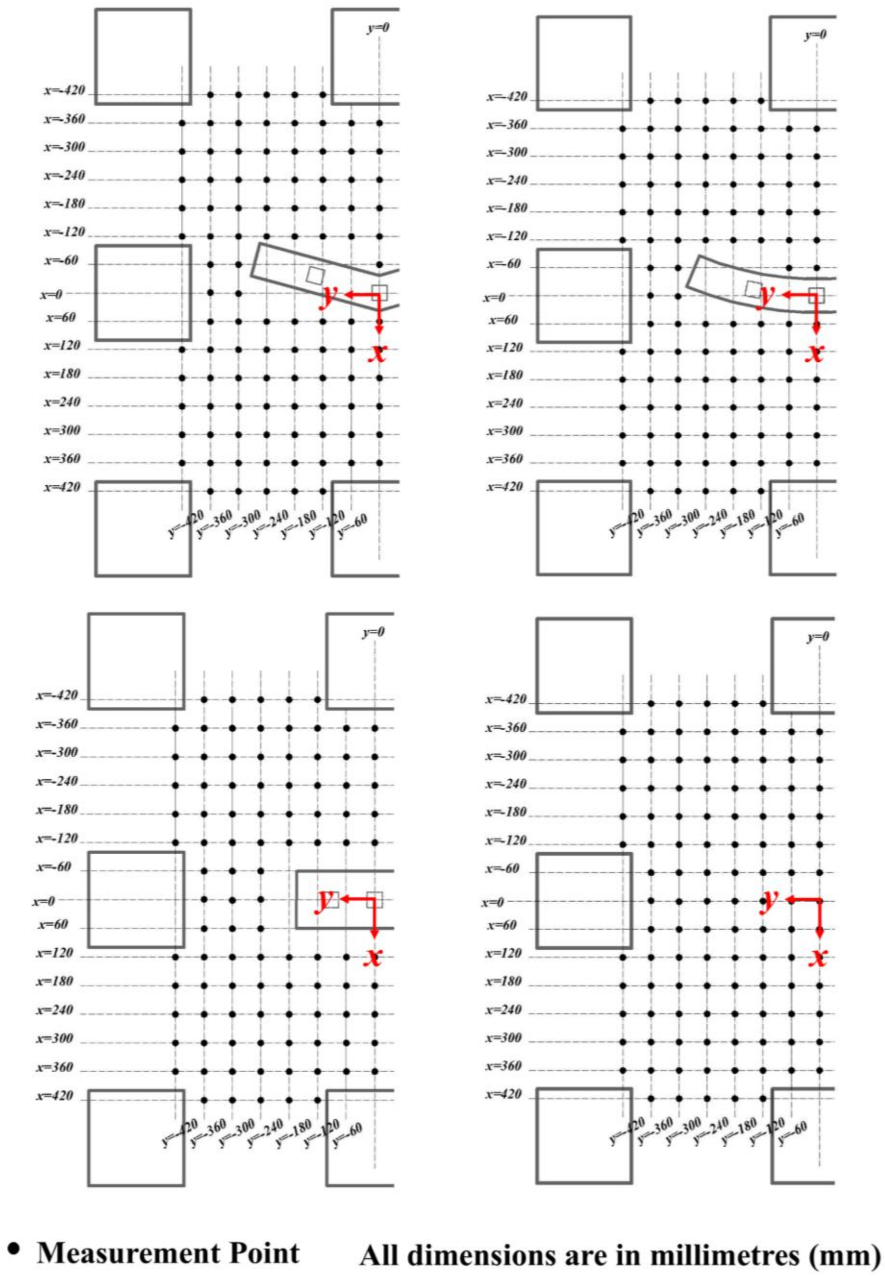

(b)

Figure 3.4. (a) Setup of wind tunnel experiments, and (b) Schematic of measurement points.

3.3 Wind parameters and wind comfort criteria

The mean wind velocity ratio (*MVR*) is a commonly used indicator for assessing PLW comfort (Chen and Mak, 2021). It is calculated as the ratio of the average wind speed at specific points of interest at pedestrian height ($\overline{U}$) to the average wind speed of the incoming flow at a reference height (U_{ref}), measured in the absence of any urban obstructions, which is given by Equation (3.3).

$$MVR = \frac{\overline{U}}{U_{ref}} \tag{3.3}$$

where the reference velocity U_{ref} is set as the velocity at the reference height without urban blocks from the wind profile in this chapter. The time-averaged velocity $\overline{U}$ was defined as $\sqrt{u^2 + v^2 + w^2}$.

Although the mean wind velocity is considered a significant index for assessing PLW comfort, the gust wind velocity can illustrate the maximum velocity that pedestrians might experience owing to an unsteady flow (Shirzadi and Tominaga, 2022). Thus, gust wind velocity can be regarded as a more significant index than mean wind velocity for revealing the effect of wind on pedestrians. (Zhong et al., 2022; Vita et al., 2020). The gust wind velocity is strongly related to the turbulent environment. Despite the existence of numerous wind comfort standards based on mean wind velocity at the pedestrian level, discomfort can still arise due to the occurrence of wind gusts at that height (Blocken et al., 2016). The importance of assessing gust winds around elevated buildings owing to excessive air movement has been addressed in Xia et al. (2015), particularly for subtropical cities where typhoons with high wind velocities occur frequently. This further demonstrates that high-rise elevated buildings may cause gust events at the pedestrian level even if the mean wind velocity magnitude remains within a reasonable range. It is necessary to assess both the mean and gust wind velocities to gain a comprehensive understanding of the effect of establishing an elevated building on PLWEs. Gust wind velocity can be measured directly through experiments and shows the maximum wind velocity that pedestrians may experience during a given period (Blocken et al., 2016). The gust wind velocity is characterized as Equation (3.4) (Melbourne, 1978).

$$U_g = \overline{U} \times (1 + GF \cdot I) \tag{3.4}$$

where U_g is the wind gust velocity, GF is the gust factor, and I is the turbulence intensity. For the calculation of the gust factor, the choice of gust duration originates from an anemometer, and the relationship between the length, velocity, and time scales, as referred to Lombardo (2021), as shown in the Equation (3.5):

$$L = \overline{U}T \tag{3.5}$$

where L denotes the length scale and T is the gust duration. Thus, the time scale of the prototype and scaled-down model is defined as the ratio between the geometric and velocity scales. The velocity scale is equal to 1 as the ratio between the full-scale reference velocity and the reference velocity in the wind tunnel, and the geometric scale is set at 1:200. In this chapter, the sample length T and gust duration T_g were set to 10 minutes and 3 s on a full scale; therefore, T and T_g could be converted to 3 s and 0.015 s on a reduced scale, respectively. The entire time series was divided into 10 segments of 3 s for each time segment. The gust factor is defined as the ratio between the peak moving average from the time-varying data for gust duration T_g and the time average velocity value over the total duration T (Tominaga and Shirzadi, 2021). The final gust factor can then be obtained by averaging the gust factors in all 10 segments, as follows:

$$GF = \frac{\overline{U}_{m\max}^{T_g}}{U_m^T} \tag{3.6}$$

where T_g is the gust duration, T is the sample length, $\overline{U}_{m\max}^{T_g}$ is the maximum moving average velocity of the T_g, and U_m^T is the time-averaged velocity of the T.

The present chapter selects two distinct wind climates, namely weak and windy climates, to assess the wind conditions surrounding irregular elevated buildings in urban environments. Weak climates were selected based on a relatively low ambient wind velocity to assess PLW comfort (Zhang et al., 2020). Recently, many PLW criteria have been proposed for different wind conditions, and the mean wind velocity is a vital assessment index for PLWEs (T.V. Lawson and Penwarden, 1975; N. Isyumov and Davenport, 1975; Soligo, 1993). The wind criteria proposed by Du et al. (2017) were used as a reference for the weak wind situation in Hong Kong, according to long-term wind speed measurements recorded at a reference elevation of 200 meters, where the wind speed was around 5 m/s with a 50% probability of being exceeded. The wind velocity within the range of 1.5 m/s to 7.6 m/s can be identified as acceptable for PLW comfort. Wind velocities of less than 1.5 m/s and larger than 7.6 m/s were considered unfavourable and dangerous, respectively. Thus, the acceptable *MVR* range for PLW comfort can be given from 0.2 to 1 according to the definition of *MVR*, as illustrated in the Equation (3.3). Table 3.2 describes the PLW comfort criteria adopted in this chapter based on five different wind comfort zones.

Table 3.2 Wind criteria used in this chapter under weak wind conditions (Du et al., 2017).

Category	Threshold wind velocity (m/s)	*MVR*	Activity description
Unfavourable	<1.5	<0.2	N/A
	<1.8	<0.24	Sitting Long
Acceptable	<3.6	<0.48	Siting Short
	<5.3	<0.71	Strolling
Tolerable	<7.6	<1.01	Walking fast
Intolerable	>7.6	>1.01	Not suitable for activities
Danger	>15	>2	Dangerous

For windy wind climates, because an elevated building might produce excessive wind flow beneath the building, there is a high probability that pedestrians will be exposed to high wind velocities, especially in windy climates. To assess the wind comfort at the pedestrian level in the street canyon for a windy climate, the wind comfort assessment criteria proposed by Lawson (T.V. Lawson and Penwarden, 1975), shown in Table 3.3, were adopted in this chapter. The wind assessment criteria consist of defined wind speed thresholds (U_{thr}, *m/s*) and maximum allowed exceedance probability (P_{exce}) ranges for different pedestrian activity categories. The relationships among the threshold wind velocity, maximum allowed exceedance probabilities, and appropriate activities are distinguished as follows: (2%) for sitting long, 3.6 (2%) for sitting short, 5.3 (2%) for strolling, and 7.6 (2%) for walking fast. When the maximum allowed exceedance probability is > 2% of the wind speed threshold at 7.6 m/s, the area is deemed intolerable (Zhong et al., 2022).

Table 3.3 Wind comfort criteria by Lawson (1978) (T.V. Lawson and Penwarden, 1975).

Activity	U_{thr}	Maximum P_{exce}	Description of activity
Sitting long	1.8 m/s	2 %	"Tolerable for covered areas"
Sitting short	3.6 m/s	2 %	"Tolerable for pedestrian stand around"
Strolling	5.3 m/s	2 %	"Tolerable for pedestrian walk-thru"
Waling fast	7.6 m/s	2 %	"Tolerable for roads, car parks"
Intolerable	>7.6	2%	"Not suitable for activities"

The statistical data of wind velocity were assumed to follow a two-parameter Weibull distribution (Du et al., 2017). The probability that the wind speed exceeds a given limit *V* associated with a specific wind climate is given by the $P_{exc}(V)$ as follows (Sanz-Andres and Cuerva, 2006):

$$P_{exc}(V) = 1 - F(x < V) = \exp[1 - \left(\frac{V}{c}\right)]^k \tag{3.7}$$

where k is the shape parameter, and c is the scale parameter.

The method adopted to estimate the parameters of the Weibull wind speed distribution follows the popular graphical method proposed by Seguro and Lambert (J.V.Seguro and Lambert, 2000). The k and c can be derived by plotting $\ln\{-\ln[1 - P(v < v_i)]\}$ versus $\ln_{vi}$ with a slope of k and a y-intercept of $-k \ln c$. The exceeding probabilities can then be obtained using the Equation (3.7). To comprehensively assess the spatial extent of each wind comfort zone,

AR_{WC}, the ratio of the area of different wind comfort category zones to the total area of the selected research region was defined as follows:

$$AR_{WC} = \frac{A_{WC}}{A_T} \tag{3.8}$$

where A_{WC} indicates the area of different wind comfort category regions, and A_T is the area of total interest precinct region. The areas of surrounding buildings and elevated columns were excluded from A_T.

3.4 Results and discussion

3.4.1 Modifications in the mean flow field

The distributions of the mean wind velocity near the central irregular elevated building with respect to the three different wind directions ($\varphi = 0^\circ$, 90° and 180°) over the horizontal plane (z=0.01 m) are shown in Figure 3.5. The approaching airflow in Case [E] (Figure 3.5 (i)) accelerated between the upwind buildings and was subsequently directed along the street canyon in a streamwise direction at high velocities with *MVR* values ranging from 0.6 to 0.8. The presence of dark blue zones, with *MVR* values below 0.4, was observed in front of the downwind buildings due to the downwash effects that induce flow recirculation at the pedestrian level. The addition of a central elevated building in the region led to a significant modification of the mean wind field, as depicted in Figure 3.5 (a)-(h). The primary modification lies in the establishment of the central elevated building, which effectively diminished the wake region of upwind buildings and amplified the downwash effect induced by the elevated building, thereby augmenting the wind velocities on both windward and lateral sides of downwind buildings. The *MVR* contour was compared with the measurement results by Tominaga and Shizadi (2021). Their study revealed that a recirculation flow with low wind velocities envelops the area behind the central high-rise structure due to the reverse flow induced by building and street flows. However, this phenomenon was not observed when a central high-rise building was substituted with an elevated alternative. In contrast, the region behind the elevated building experiences enhanced airflow due to the throughflow from the lifted section. This comparison also serves to illustrate that the elevated building can effectively improve ventilation in its rear vicinity.

For the test cases of wind direction $\varphi = 0^{\circ}$, a similar mean wind velocity distribution pattern could be seen among the three different elevated buildings, as shown in Figure 3.5 (a), (d), and (g). A relatively low wind velocity zone (*MVR*< 0.3) was observed in the frontal part of the central elevated building. The relatively stagnant flow area may have been induced by downwash flow from the high-rise elevated building. The intense downward airflow ahead of the central high-rise structure markedly redirected the movement of air along the street toward the sideways direction, generating an accelerated lateral corner stream (*MVR*>0.7). The complex interplay between the air movement around the high-rise structure and neighbouring street canyons formed an additional key element leading to areas of elevated wind speed. Moreover, another zone in the precinct of interest with a high wind velocity was found in the downstream region between the elevated columns of the elevated building at the rear side. This occurrence was attributed to the acceleration of wind velocity between the elevated columns by the throughflow from the elevated area. The wind velocity beneath the elevated building has been intensified, and the elevated section functions as a wind corridor, facilitating unobstructed airflow. The single elevated building has proven to be effective in improving air circulation at the pedestrian level (Zhang et al., 2017). In the present chapter, the presence of surrounding structures impeded the wind velocity at the corner side of the elevated building, resulting in constrained lateral acceleration. However, intricate interactions redirected this acceleration downstream, thereby enhancing ventilation downstream of the building group. The elevated buildings have the potential to enhance wind velocity, even in the presence of surrounding buildings. For the wind direction $\varphi = 180^{\circ}$ (Figure 3.5 (c), (f), and (g)), the distribution patterns of mean wind velocity around the central elevated building exhibited a remarkable similarity to the wind direction $\varphi = 0^{\circ}$; however, the overall magnitude of mean velocity was found to be larger than that observed at $\varphi = 0^{\circ}$, particularly in the downstream street region. The lateral regions and rear side of the central elevated building exhibited an expanded wind acceleration area due to the diverging flow induced by the Arc-shaped and V-shaped elevated building, thereby enhancing interaction with the surrounding street canyons. This divergence in airflow results in a greater magnitude of high-velocity airflow towards downstream streets, facilitating enhanced ventilation for buildings located downstream. The wind direction of $\varphi = 90^{\circ}$ within the precinct of interest is illustrated in Figure 3.5 (b), (e), and (h). A significant portion of the wind environment was characterized by decelerated wind velocities with *MVR*<0.6, exhibiting notably lower *MVR* magnitudes compared to the wind direction at $\varphi = 0^{\circ}$ and $\varphi = 180^{\circ}$. This phenomenon can be attributed to the absence of acceleration by the central elevated building, resulting in a direct upstream flow along the street and reduced wind interaction between the central building and its surroundings. The deflected flow partially recirculated into the streets but fails to sufficiently mobilize airflows at the pedestrian level, thereby impeding effective ventilation within the urban environment.

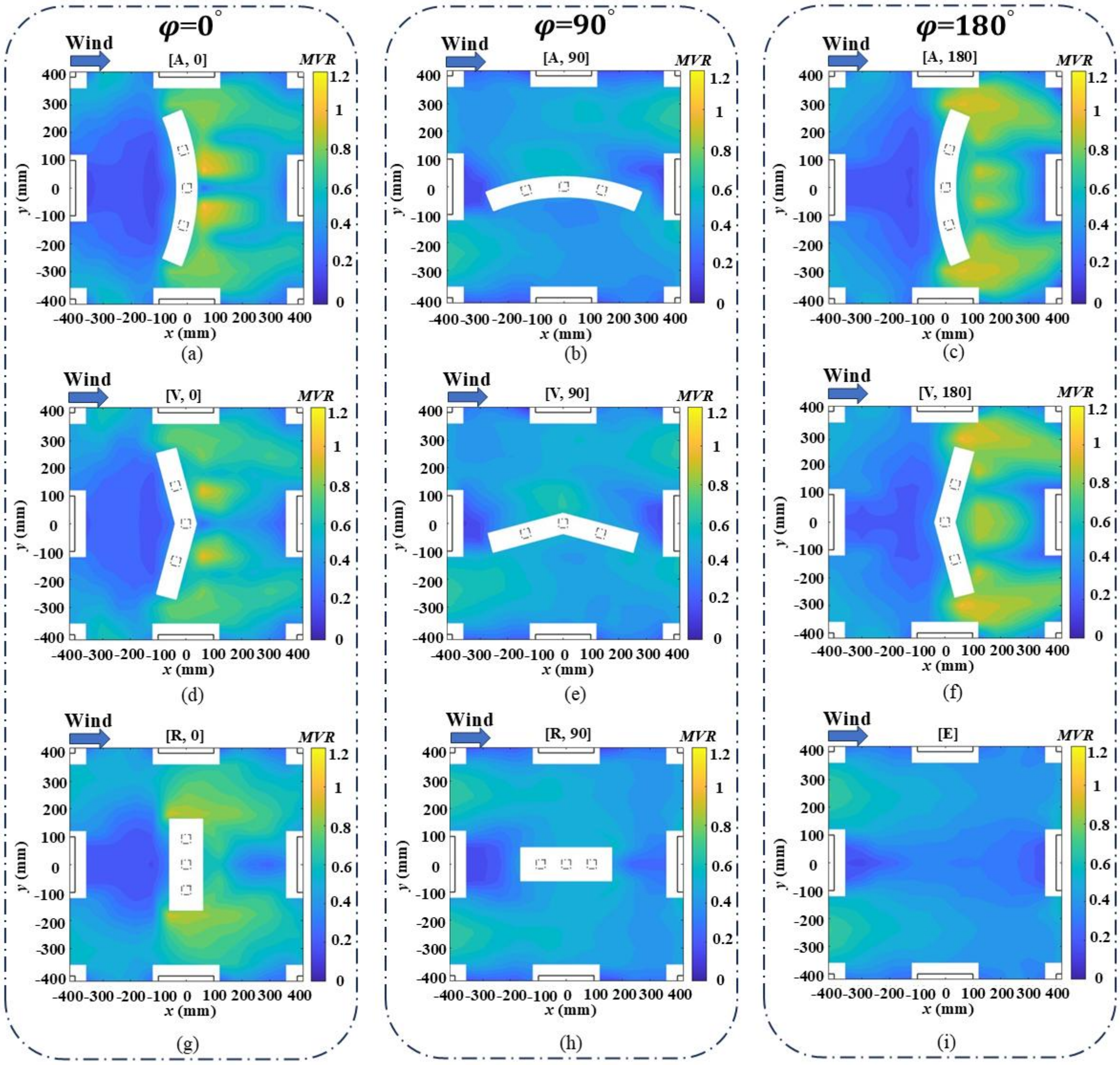

Figure 3.5. Pedestrian-level *MVR* distribution around irregular elevated buildings under three different wind directions: (a-c) Arc-shaped elevated building; (d-f) V-shaped elevated building; (g-h) Rectangular-shaped elevated building; (i) a central open case without the elevated building.

3.4.2 Modifications in the gust wind field

Pedestrian-level gust wind flow fields around an irregular elevated building with respect to different wind directions are shown in Figure 3.6. Similar to *MVR*, *GVR* is defined as the gust wind velocity magnitude normalised to the mean wind velocity at the reference height (U_g/U_{ref}). To further distinguish the magnitude of different gust wind regions, three *GVR* regions with different magnitude levels are defined as: low *GVR* region with *GVR*<0.5; medium *GVR* region with 0.5<*GVR*<1, and high *GVR* region with *GVR*>1. Overall, the *GVR* values remained within the range of 0-2 for all the test cases. The *GVR* distribution exhibited a pattern akin to that of the *MVR* distribution, with increased gust wind magnitude observed beside and behind the central elevated building. The windward corners of the elevated building exhibited the formation of intense separation layers, resulting in a localized area characterized by high gust wind velocities; therefore, the *GVR* value escalated to over 1.5 at the lateral sides and wake region of the central elevated building. When the wind flows to the convex part of the elevated building (wind direction of $\varphi = 180^{\circ}$), the *GVR* value was larger than that from the concave side of the elevated building (wind direction of $\varphi = 0^{\circ}$), as shown in Figure 3.6 (c), (f), and Figure 3.6 (a), and (d). The *GVR* distribution was uniform within the precinct of interest when the wind direction was $\varphi = 90^{\circ}$. In the central empty case (Figure 3.6 (i)), high *GVR* regions were observed on the lateral sides of the first-column buildings. Recirculation regions with reduced wind velocities were observed in front of the buildings in the third column, which resulted from the downward airflow caused by the buildings.

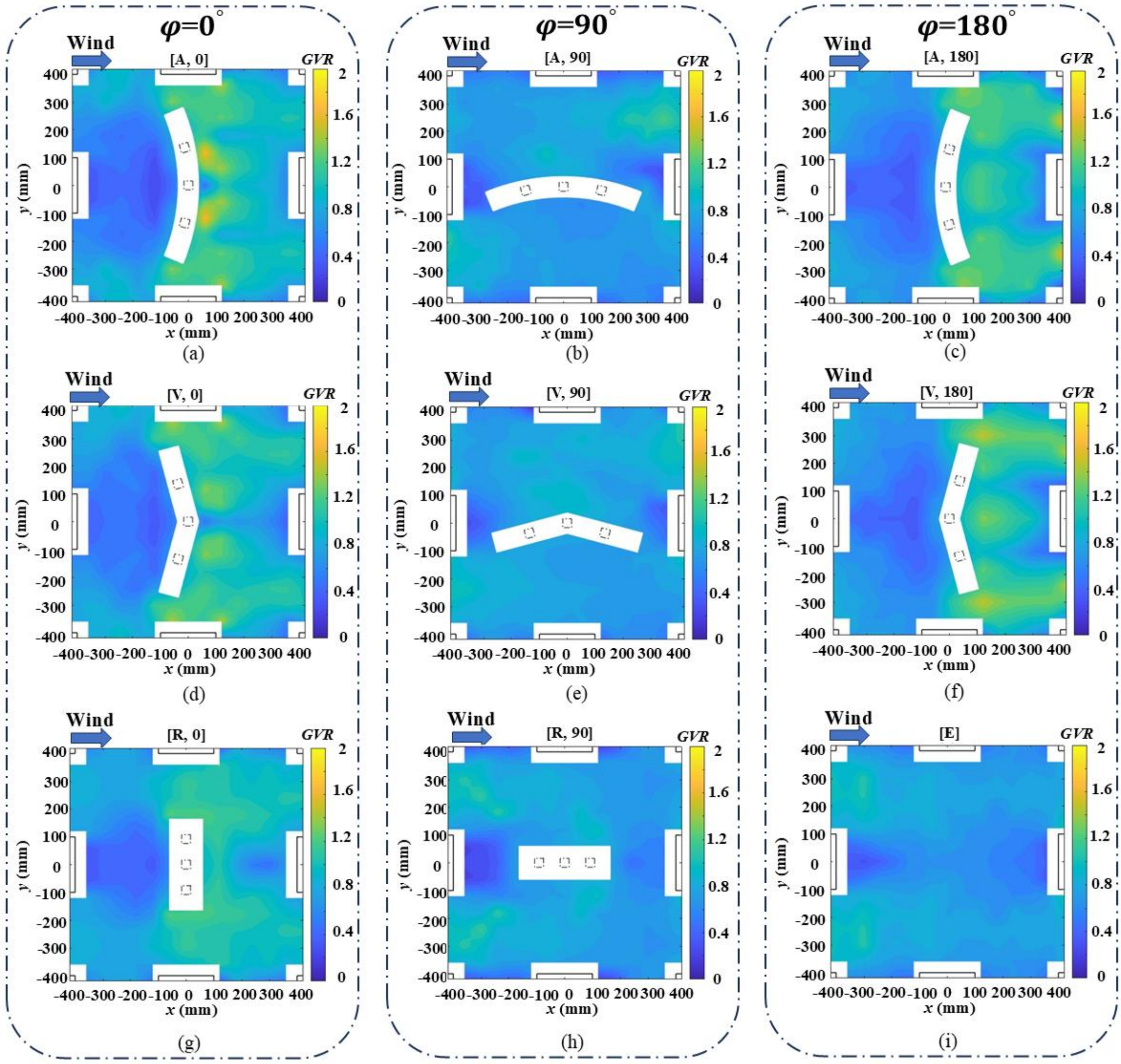

Figure 3.6. Pedestrian-level *GVR* distribution around irregular elevated buildings under three different wind directions: (a)-(c) Arc-shaped elevated buildings; (d)-(f) V-shaped elevated buildings; (g)-(h) Rectangular elevated buildings; (i) a central open case without the elevated building.

Figure 3.7 depicts area ratios of different *GVR* distribution contours for different test cases. In light of the wind direction of $\varphi = 0^{\circ}$, it can be found that the Rectangular-shaped elevated building occupied the largest high *GVR* region (34.16%) in comparison with the Arc-shaped (31.96%) and V-shaped (33.18%) elevated buildings. The coupling effects of both the lateral entrained wind and the Venturi effect yield two substantial high *GVR* regions at the side and rear regions around the elevated building. For the Arc- and V-shaped elevated buildings under wind directions of $\varphi = 0^{\circ}$ and $\varphi = 180^{\circ}$, the *GVR* regions exhibited no significant disparity due to the converging and diverging flow induced by the elevated building, except for the low *GVR* region in the V-shaped elevated building case. The proportion of the medium *GVR* region among all the test cases was more than 90% when the wind direction was $\varphi = 90^{\circ}$. However, the presence of an elevated building in the central open space results in a significant escalation of high *GVR* region proportion due to enhanced turbulence generation within the interest zone, as well as a conspicuous increase in the low *GVR* region proportion under wind directions of both $\varphi = 0^{\circ}$ and $\varphi = 180^{\circ}$. Whereas, there were no discernible alterations in the high *GVR* proportion between the elevated building cases and the central open space cases when the wind direction was set to be $\varphi = 90^{\circ}$.

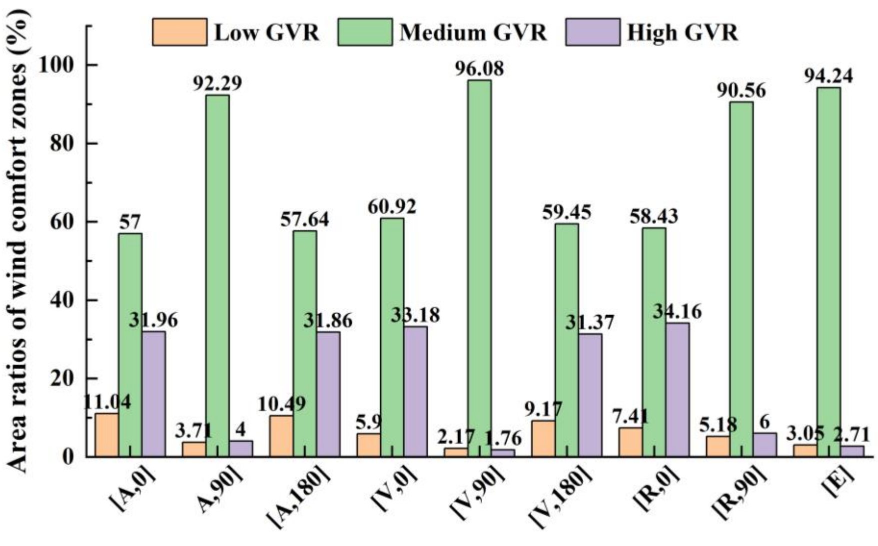

Figure 3.7. Area ratios of different *GVR* wind comfort zones.

3.4.3 Turbulent fluctuation components

The contours of the TKE with respect to different elevated buildings under varying wind directions are shown in Figure 3.8. Similar to the wind velocity contour, the concentration of high-TKE regions was predominantly observed in the lateral and downstream areas surrounding the central elevated structures. Notably, when considering the wind direction of $\varphi = 180^{\circ}$ ((Figure 3.8 (c) and (f)), it is evident that the high TKE region at the rear of the central elevated building exhibited relatively smaller dimensions compared to that observed for a wind direction of $\varphi = 0^{\circ}$ ((Figure 3.8 (a) and (d)). Conversely, for a wind direction of $\varphi = 90^{\circ}$ (as shown in Figure 3.8 (b), (e), and (h)), it can be noted that the TKE distributions of the Arc-, V-, and Rectangular-shaped elevated buildings were comparatively uniform. However, due to diverging flow patterns resulting from winds originating from $\varphi = 180^{\circ}$ ((Figure 3.8 (c) and (f)), a peak value of TKE near the downstream street was observed. This phenomenon can be attributed to the collision between flow recirculation among surrounding structures and the central elevated building, ultimately leading to the formation of an adjacent high-TKE zone.

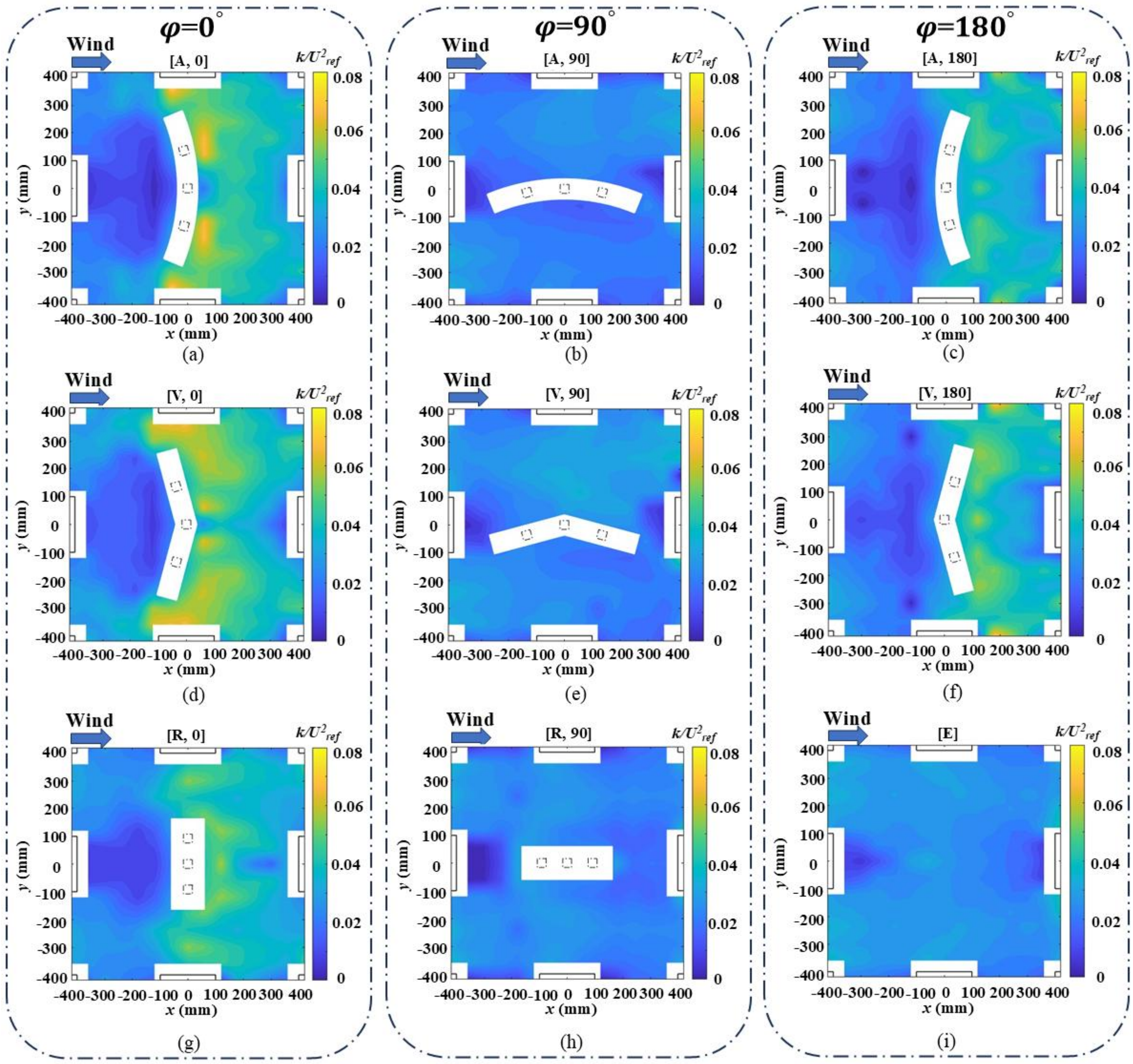

Figure 3.8. Contours of TKE for: (a)-(c) Arc-shaped elevated buildings; (d)-(f) V-shaped elevated buildings; (g)-(h) Rectangular elevated buildings; (i) a central open case without the elevated building.

3.4.4 Spatial occurrence frequencies of mean wind velocity and turbulence kinetic energy

The occurrence frequencies of both the normalized mean wind velocity magnitude and TKE over all the measurement points at the pedestrian-level plane with respect to the different test cases are shown in Figure 3.9. As indicated in Figure 3.9 (a)-(c), the highest OF values were observed when the wind direction was $\varphi = 90^{\circ}$, with a value of $U / U_{ref} \approx 0.45$. This particular velocity region was predominantly found near the central elevated building in most regions (Figure 3.5 (b), (e), and (h)). In contrast to the symmetrical distribution observed at a wind direction of $\varphi = 90^{\circ}$, characterized by a prominent peak, other wind directions exhibited a more uniform distribution within the study area, with distinct regions of high and low velocities. Regarding building shapes, the OF distribution of rectangular-shaped elevated buildings exhibited a narrower range with symmetric peaks at $U/U_{ref} \approx 0.5$, whereas the distributions in irregular-shaped buildings showed more pronounced variations in velocity regions. The presence of higher and lower velocity regions in irregular elevated buildings can be attributed to enhanced interaction between the central elevated structure and its surroundings, resulting from their unconventional shapes.

It can be observed from Figure 3.9 (d)-(f) that the occurrence frequency of the TKE showed similar trends to that of the mean wind velocity. The maximum normalised TKE (TKE/U_{ref}^2) values for the Arc-, V-, and Rectangular- shaped elevated buildings were approximately 0.08, 0.09, and 0.07, respectively. The peak of OF occurred at a wind direction of $\varphi = 90^{\circ}$ for all three building shapes, with a range between 0.02 and 0.03. In contrast, for the remaining wind directions ($\varphi = 0^{\circ}$ and $\varphi = 180^{\circ}$) relative to all three building shapes, the distribution of OF exhibited a more uniform pattern. The OF distribution in all three building shapes exhibited a skew towards large TKE values compared to Case [E], while irregular-shaped elevated buildings demonstrated a greater prevalence of regions with high TKE values when compared to rectangular-shaped elevated buildings. Stronger interactions between the central elevated building and the surrounding buildings lead to higher TKE regions.

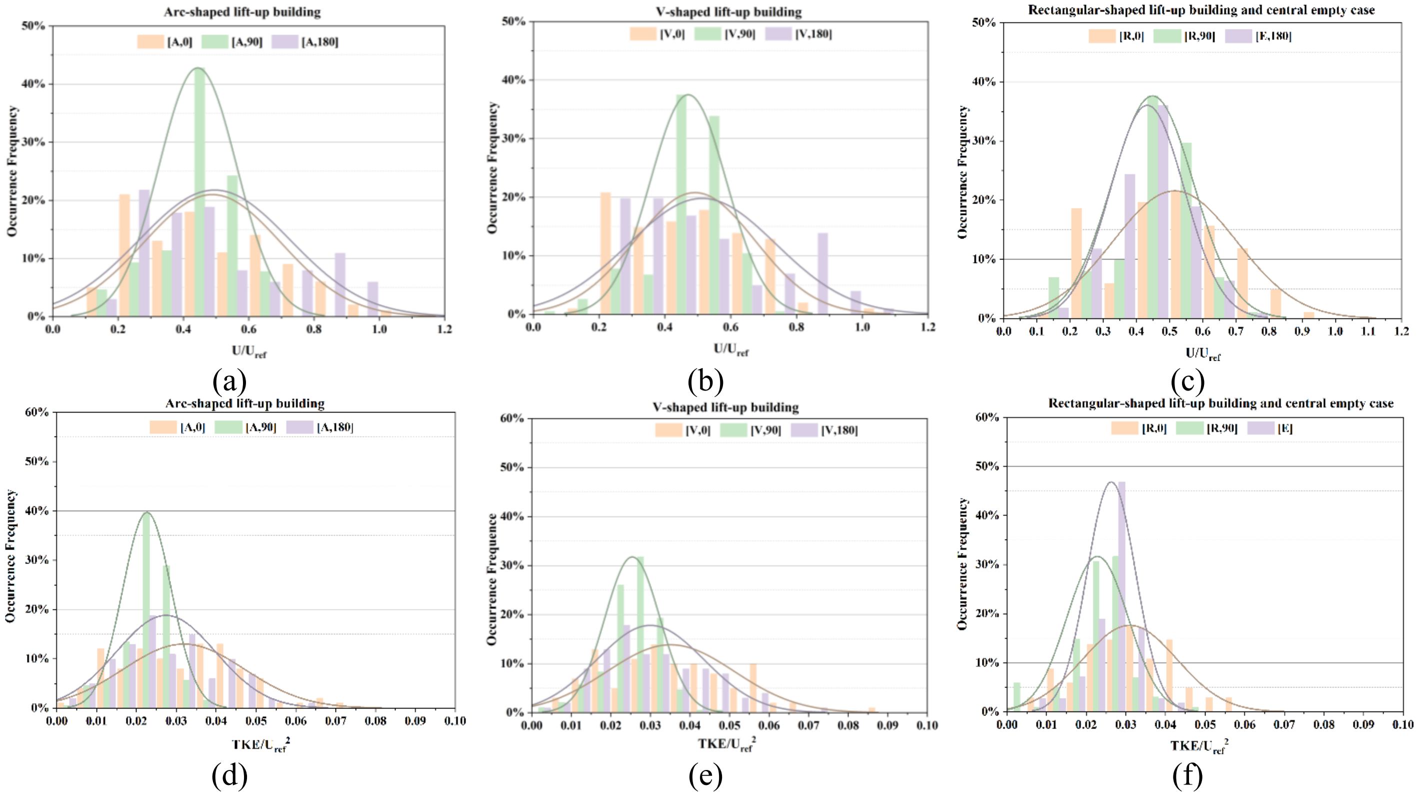

Figure 3.9. Occurrence Frequency of: (a)-(c): Mean wind velocity, and (d)-(f): Turbulence kinetic energy.

3.4.5 Wind comfort assessment under weak and windy wind conditions

The zones of wind comfort categories adjacent to the elevated buildings in weak wind conditions are illustrated in Figure 3.10. It can be observed that the proportion of “Unfavourable” regions with low wind velocities for pedestrians was relatively low, whereas a significant proportion was occupied by “Acceptable” regions. The wind comfort area near the Arc-shaped elevated building exhibited the largest "Unfavourable” wind conditions (3.34%), whereas minimal "Unfavourable” wind conditions were observed for the V-shaped (0.49%) and Rectangular-shaped (0.58%) elevated buildings.

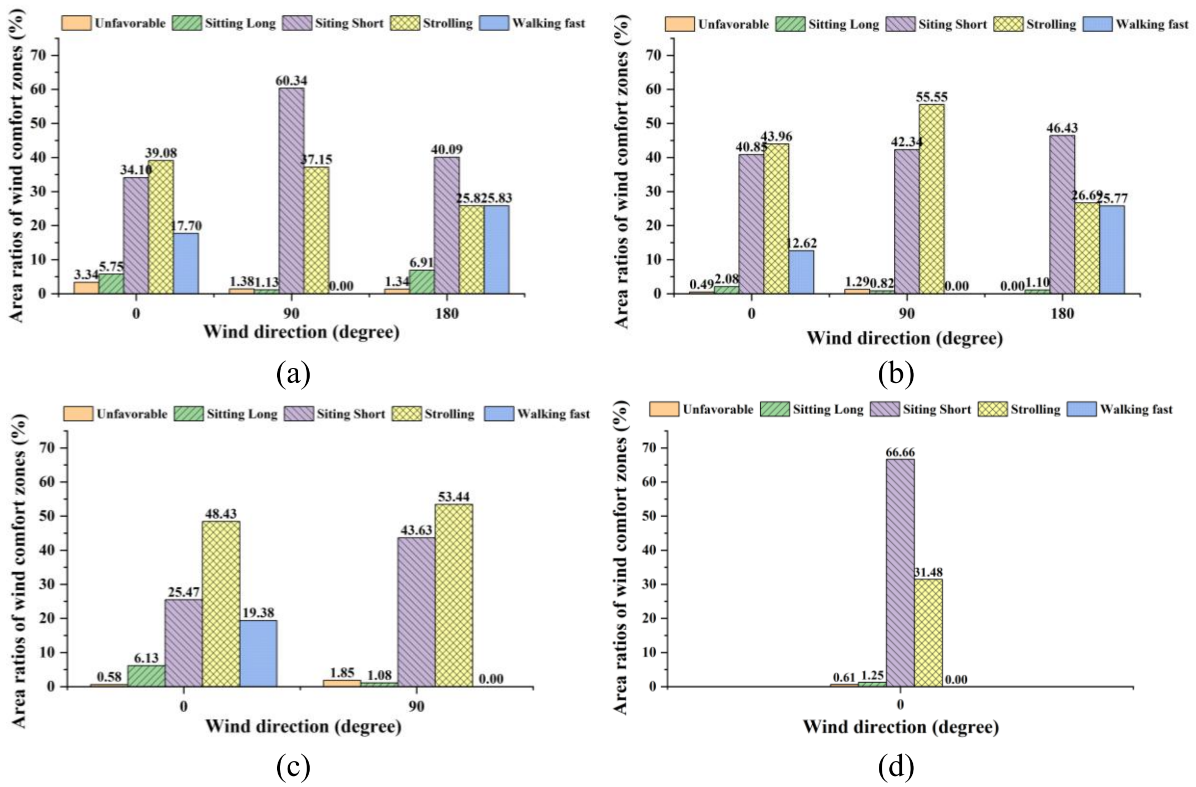

Figure 3.10. Area ratios of different wind comfort zones with respect to different elevated buildings: (a) Arc-shaped elevated building; (b) V-shaped elevated building; (c) Rectangular elevated building, and (d) a central open case without the elevated building.

Interestingly, the area categorised as "Walking fast" under the wind direction of $\varphi = 180^{\circ}$ was larger than the wind direction of $\varphi = 0^{\circ}$ for both Arc- and V-shaped elevated buildings. For instance, AR_{WC} near the Arc-shaped and V-shaped elevated buildings increased from 17.7% to 25.83% and 12.62% to 25.77%, respectively, as φ changed from 0° to 90° (Figure 3.10 (a) and (b)). The occurrence of this phenomenon is primarily attributed to the enlarged high-wind-velocity regions at the rear and lateral sides of the central elevated building, induced by diverging wind flows toward the building. Consequently, a greater extent of the area classified as “Sitting short” and “Sitting long” was observed in front of the elevated building in $\varphi = 0^{\circ}$ compared to that in $\varphi = 180^{\circ}$ due to the convergence of flow, resulting in relatively low-velocity regions. Owing to the unobstructed flow from the upstream to the downstream, bypassing the central elevated building without shedding, a larger “Acceptable” region and a smaller “Tolerable” area could be identified in the wind direction of $\varphi = 90^{\circ}$ in all building configurations. The area rated as "Tolerable” wind condition for Arc-, V-, and Rectangular-shaped elevated buildings with normal approaching wind directions ($\varphi = 0^{\circ}$ and $\varphi = 180^{\circ}$) notably increased compared to the central empty case (Case [E]), as shown in Figure 3.10. This crease can be due to the interaction between downwash flow caused by the elevated building and surrounding buildings, resulting in an augmentation of high-velocity regions downstream of the elevated building; however, this augmentation remains below the “Dangerous” limit of Hong Kong. In contrast, no significant alteration in the area rated as “Tolerable” wind condition was observed when the wind direction was $\varphi = 90^{\circ}$. The “Acceptable” wind comfort area remained relatively consistent for both the elevated building cases and empty cases under the wind direction of $\varphi = 90^{\circ}$. This may be the result of the counteraction effects of the shedding effect on the wind velocity decrease and the downwash flow effect on the wind velocity increase at the pedestrian level.

Figure 3.11 illustrates the PLW comfort condition assessment around the central elevated building with respect to different wind directions under windy climate conditions. Following the completion of the high-rise elevated building, PLW velocities intensified near the sides and back of the structure, causing a shift in the surrounding areas from “Sitting Long” and “Strolling” to wind discomfort with “Walking fast” and “Intolerable”. The elevated wind speeds rendered the surrounding area unsuitable for leisure activities such as “Sitting short” or “Sitting long”. Moreover, larger areas rated as “Intolerable” occur near elevated building, indicating the high vulnerability of pedestrians exposed to high-velocity flows near the high-rise elevated building. The frontal region of the central elevated building was conducive to

"Sitting short", whereas the remaining regions within the precinct of interest were suitable for "Strolling" and "Walking fast". The increase in the area rated as "Walking fast" for the elevated buildings was primarily attributed to a significant reduction in the areas designated for "Sitting short" in front of the building (Figure 3.11 (g)). For the wind direction at $\varphi = 90^{\circ}$ (Figure 3.11 (b), (e), and (h)), an "Intolerable" region was not observed due to the presence of relatively low wind velocity areas. In addition, the region suitable for "Walking fast" covers the majority of the street because the upstream flow can flow directly downstream without being obstructed by the central elevated building. The significant variations in the ratio of PLW comfort conditions for three elevated buildings in $\varphi = 0^{\circ}/180^{\circ}$ and $\varphi = 90^{\circ}$ can be attributed to the varying degrees of wind blockage caused by the building, with maximum blockage observed at $\varphi = 0^{\circ}/180^{\circ}$ and minimum at $\varphi = 90^{\circ}$, similar phenomena are also reported in the literature (Zhang et al., 2020).

To comprehensively assess the different PLW comfort zones around the different elevated buildings, Figure 3.12 shows the area ratios for the five different PLW comfort zones with respect to nine cases. The wind activity in the vicinity of the elevated building was relatively subdued, rendering the area in front of it suitable for "Siting short". This accounts for 21.78%, 22.34%, and 13.51% of the total area of Arc-, V-, and Rectangular-shaped elevated buildings at $\varphi = 0^{\circ}$, respectively. The lateral entrained winds and wind behind the elevated columns constituted the primary source of high wind velocities, creating areas conducive to "Walking fast" that account for 40.57%, 46.57%, and 50.83% of the street area for Arc-, V-, and Rectangular-shaped elevated buildings. Another striking feature of wind comfort near elevated buildings was high "Intolerable" areas reported in $\varphi = 180^{\circ}$ than that in $\varphi = 0^{\circ}$ (Figure 3.11 (c) and (a)). For instance, AR_{WC} near the Arch-shaped elevated building in windy climate increased from 11.72% to 19.27%, respectively, as φ changes from 90° to 180°. The increase in "Intolerable" areas might cause wind nuisance and discomfort to pedestrians at the side and rear of the buildings. In the wind direction of $\varphi = 90^{\circ}$, the "Strolling" area occupied the largest area for over 60% of the five distinct PLW comfort categories, with no "Intolerable" areas detected. Compared to Case [E], where the areas suitable for "Strolling" predominantly occupied the region near the elevated building (69.53%), all building shapes exerted varying degrees of influence on the wind environment surrounding the buildings. After establishing a high-rise elevated building amidst the cluster of buildings, the "Intolerable" and "Walking fast" wind conditions induced by more high-velocity regions increased, resulting in a constricted area for "Strolling" for wind direction $\varphi = 0^{\circ}$ and 180°. Comparatively, both the Arc- and V-shaped elevated buildings exhibited a reduction in "Acceptable" wind conditions when compared to the Rectangular building case. In essence, incorporating an elevated structure within this urban landscape amplified the average wind velocity while diminishing the region rated as "Acceptable" wind conditions within designated areas.

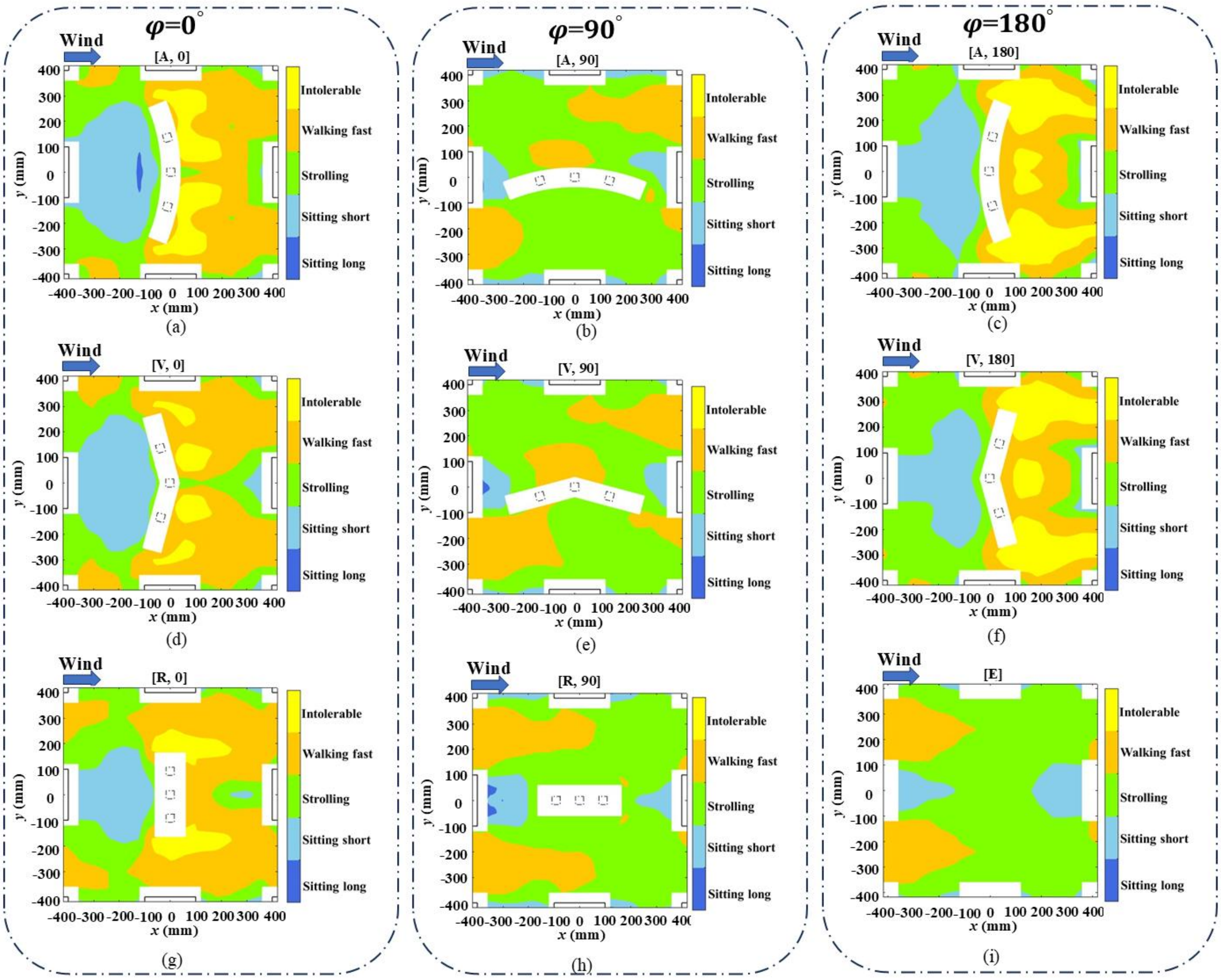

Figure 3.11. PLW comfort around irregular elevated buildings: (a)-(c) Arc-shaped; (d)-(f) V-shaped; (g)-(h) Rectangular-shaped; (i) a central open case without elevated building.

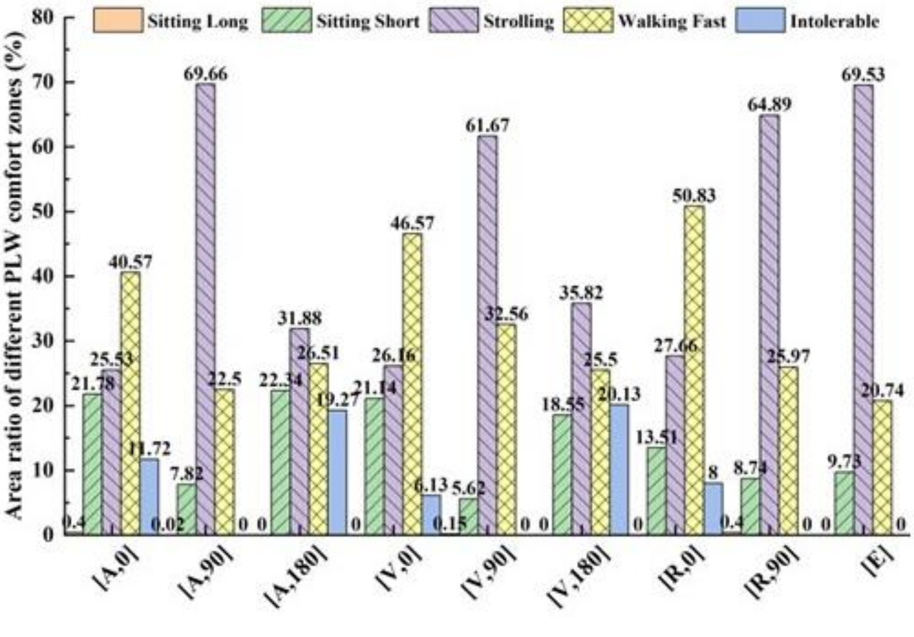

Figure 3.12. Area Ratio of different PLW comfort zones under windy wind conditions.

3.4.6 Influence of convex and concave architectural features on wind environment

To further explore the influence of flow caused by elevated buildings under normal approaching wind directions ($\varphi = 0^{\circ}$ and $\varphi = 180^{\circ}$), three wind velocity zones including upstream wind velocity area (UWVR), Near-field wind velocity area (NFWVR), and downstream wind velocity area (DWVR), and two flow divisions (Converging and Diverging flow) are indicated in Figure 3.13. According to Chen and Mak (2021), the converging flow can be described as a semi-open area on the windward side under an incoming wind to the concave part of the building, and the diverging flow can be described as a semi-open area on the leeward side under an incoming wind to the convex part of the building.

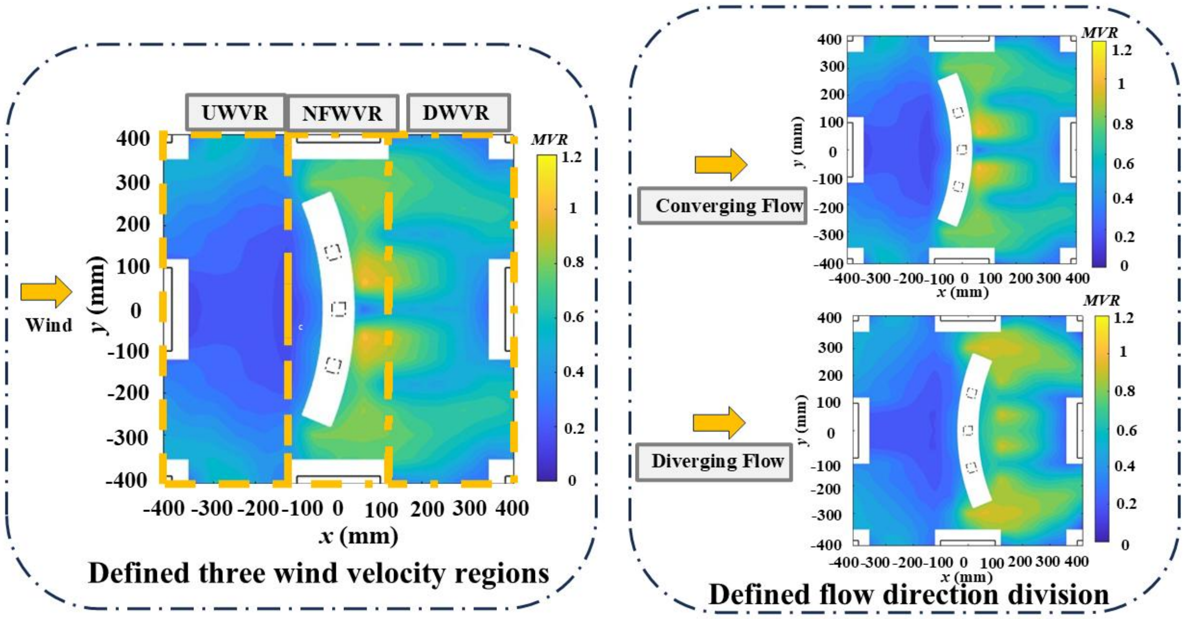

Figure 3.13. Defined three wind velocity zones and defined flow direction division (Arc-shaped elevated building as an example).

In order to provide a more comprehensive analysis of the wind conditions resulting from the concave and convex features of the buildings, a modified mean wind velocity change ratio (ΔMVR) was further employed to quantitively evaluate the impact of architectural design on the flow field at the pedestrian-level height between two scenarios (Du et al., 2017, Liu et al., 2019). The representation is as follows:

$$\Delta MVR = (MVR_w - MVR_{wo}) / MVR_{wo} \tag{3.9}$$

where the MVR_w and MVR_{wo} were the cases with and without a specific architectural design, respectively. A positive ΔMVR value indicated an amplification of local wind velocity, whereas a negative value indicated a reduction due to the architectural design. Figure 3.14 illustrates the ΔMVR distribution between the cases featuring open space and Arc- and V-shaped elevated buildings located at the center. When the wind blows towards the concave side of a building (Figure 3.14 (a) and (c)), there are more areas of low wind velocity at the front due to the trapping effect caused by the concavity, resulting in reduced flow activity. Consequently, less wind flows around the sides and back of the building, leading to lower wind velocities. Specifically, the lateral part of the elevated building exhibited increased wind amplification for positive ΔMVR (>1) values when subjected to diverging flow conditions (Figure 3.14 (b) and (d)). The underlying cause of this phenomenon can be attributed to the interaction between airflow and the convex structure of the building, resulting in a diversionary effect that significantly amplifies wind velocities at both sides and rear while concurrently leading to an increase in wind velocity at the front.

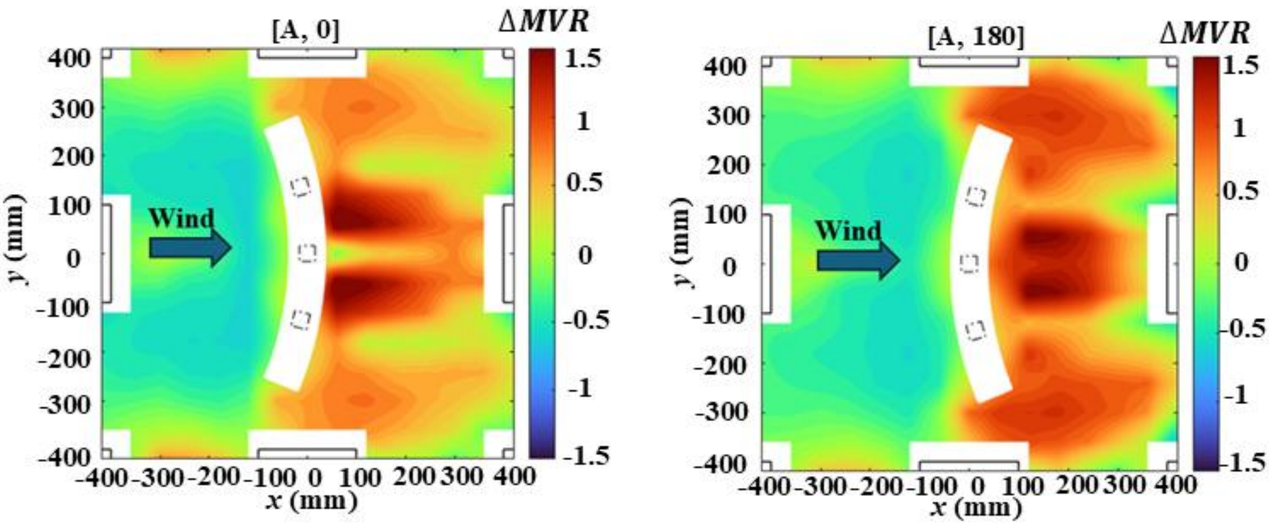

(a) (b)

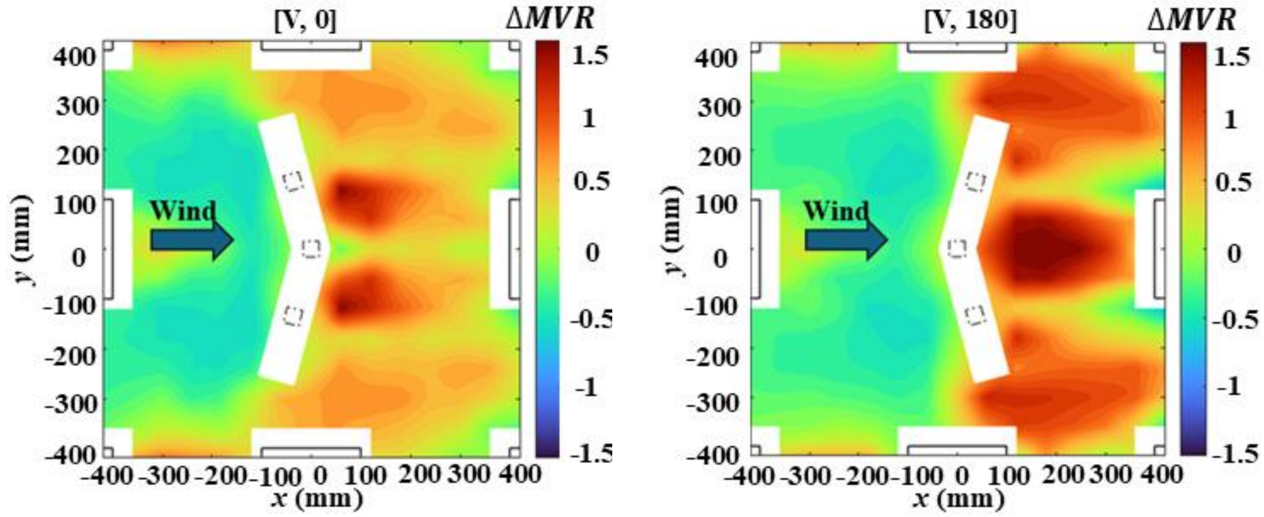

(c) (d)

Figure 3.14. Distribution of ΔMVR for the region near the (a) Arc-shaped and (c) V-shaped elevated building under converging flow; and (b) Arc-shaped and (d) V-shaped elevated building under diverging flow.

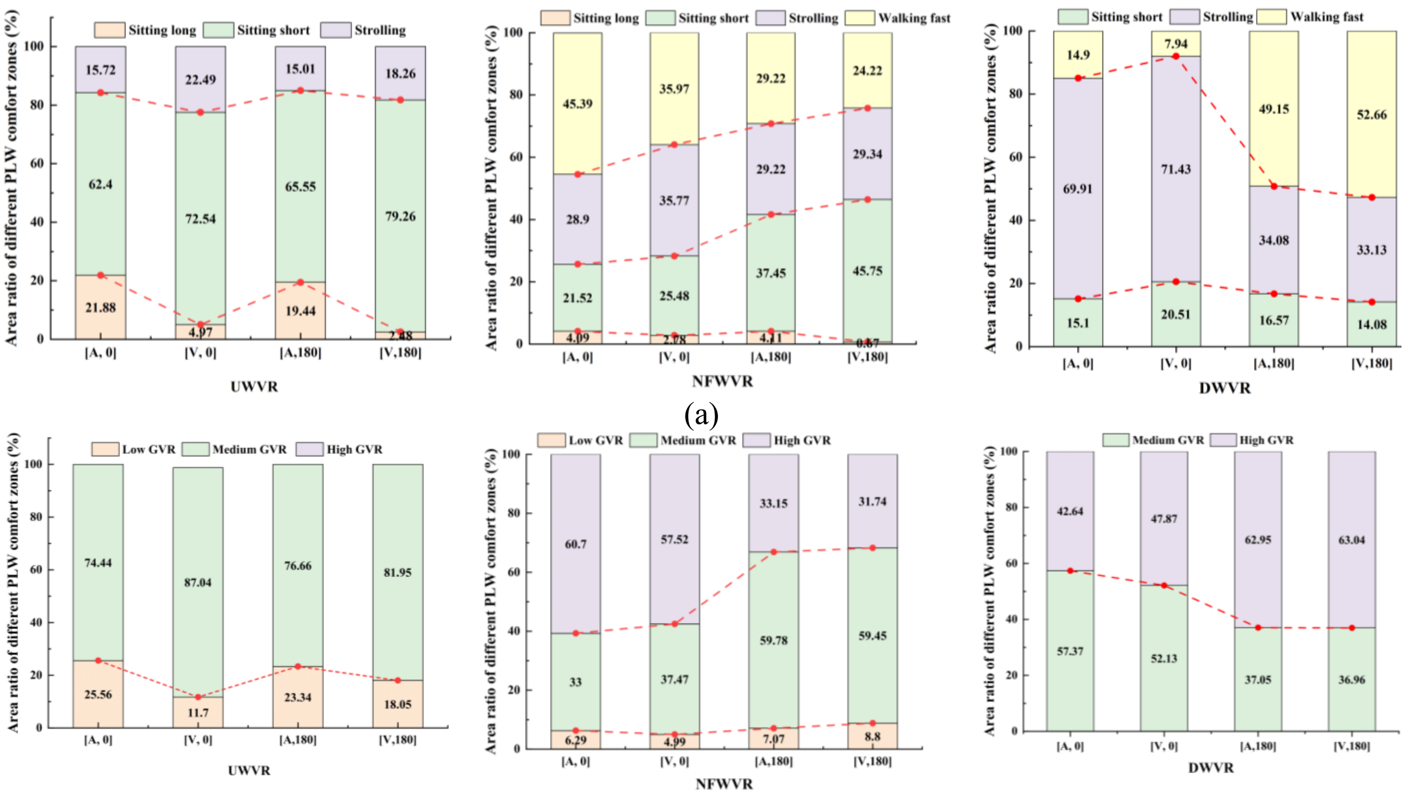

(a)

(b)

Figure 3.15. Area ratios of (a) *MVR* and (b) *GVR* comfort zones for three defined wind velocity zones.

The area ratios of the various wind conditions for these three wind velocity zones under both wind divisions were subsequently derived for *MVR*, as illustrated in Figure 3.15 (a). The Arc-shaped elevated building exhibited a larger area conducive to "Sitting long" compared to the V-shaped elevated building in the UWVR area under converging and diverging wind directions ($\varphi = 0^{\circ}$ and $\varphi = 180^{\circ}$). The low wind velocity observed in this region can be attributed to the recirculation flows occurring within the UWVR region (Tominaga and Shirzadi, 2021). However, this phenomenon was invisible when it came to NFWVR and DWVR areas. For acceptable wind conditions, no significant disparity was observed in the UWVR and DWVR areas for the Arc-shaped and V-shaped buildings, whereas the converging flow caused a more acceptable wind condition area than the diverging flow in the NFWVR area. The downstream cavity in the DWVR region exhibited higher wind velocities, particularly at the lateral entrained winds on both sides of the central building, where "Tolerable" wind conditions induced by corner streams were observed. For both irregular elevated buildings in DWVR, diverging flow results in more areas with "Tolerable" wind conditions compared with converging flow. However, no "Tolerable" wind condition area was identified in the UWVR, and the Arc- and V-shaped buildings did not exhibit significant differences in "Tolerable" wind conditions in the NFWVR and DWVR areas.

Figure 3.15 (b) demonstrates the area ratios of *GVR* comfort zones regarding Arc- and V-shaped buildings under converging and diverging flow in three wind velocity zones (UWVR, NFWVR, and DWVR area). The proportion of low and medium *GVR* regions exhibited comparable magnitude in the UWVR region for elevated buildings subjected to diverging or converging flows. However, in the NFWVR region, elevated buildings under diverging flow tend to generate a higher proportion of medium *GVR* regions, while no significant differences were observed in the low *GVR* region. The absence of a low *GVR* region in the DWVR area was conspicuous, while buildings subjected to diverging flow exhibited a propensity for generating an augmented high *GVR* region trailing behind the elevated structure. The influence of the convex and concave structures on the flow field was predominantly concentrated at the rear of the building, whereby wind blowing towards the convex part generated an expanded gust area behind while exerting minimal impact on its front façade.

3.5 Summary

To provide a comprehensive understanding of pedestrian-level gust wind flows and comfort around elevated buildings located in the middle of urban blocks, a series of wind tunnel experiments have been conducted in this chapter. The time-averaged characteristics and turbulence statistics of the wind velocity, including the TKE, gust factor, and gust wind velocity of the instantaneous velocity, have been analysed. The major results are as follows:

(1) The two irregular elevated buildings, in comparison to rectangular structures, demonstrated a higher concentration of accelerated areas in the lateral and rear regions of the central elevated building. This phenomenon can be attributed to the pronounced flow separation at the upwind corner and the formation of corner streams along the side of these distinctive architectural forms.

(2) The construction of the central elevated building resulted in an increase in the time-averaged velocity and led to an amplified high *GVR* region due to the complex interaction between downwash flow from the central building and lateral stream, as well as through flow. The elevated building is designed to cater to pedestrians' wind comfort needs while also providing an exquisite outdoor recreational space. The chapter presents compelling experimental evidence demonstrating that elevated buildings possess the capacity to augment wind velocity, even in the presence of surrounding structures.

(3) The architectural elements of concavity and convexity exerted a significant influence on wind patterns within specific regions. When wind encounters a convex structure,

the diverging flow facilitates the transportation of a larger volume of high-velocity upstream airflow towards the downstream building, thereby effectively enhancing downstream ventilation. Conversely, interaction with the concave portion confines wind movement and creates areas characterized by reduced airflow. Moreover, the disparity of concave and convex properties was primarily concentrated in the DWVR region.

(4) The wind assessment was conducted based on the Weibull distribution, revealing that the Arc-shaped elevated building exhibited a greater "Intolerable" area than V- and Rectangular-shaped building cases. Implementing aerodynamic modifications proves advantageous in controlling areas with extreme wind discomfort, encouraging winds from the convex side of both Arc- and V-shaped elevated buildings resulted in an amplification of "Intolerable" areas. The majority of areas in front of the elevated buildings were classified as "Sitting long", and the lateral and rear regions of the elevated buildings were classified as "Walking fast" and "Intolerable" areas.

CHAPTER 4. Mean and turbulent wind characteristics around a high-rise elevated building with curved cross-sections: Wind tunnel experiments and numerical simulations

4.1 Introduction

This chapter presents a study on the mean and turbulent wind characteristics around a C-shaped high-rise elevated building using wind tunnel experiments and CFD simulations. C-shaped high-rise elevated buildings are highly favoured for hotels and commercial use and are widely appreciated by architects for their distinctive appearance. However, research on the mean and gust wind flow fields surrounding C-shaped buildings remains insufficient. Also, this chapter aims to investigate whether replacing the LES model with the RANS model is suitable for simulating the flow field around elevated buildings and systematically evaluate and compare the performance differences among these turbulence modelling approaches. To fill the research gap, the objectives of the present chapter are: (1) to conduct a wind tunnel investigation of turbulent flow around a C-shaped elevated building, providing benchmark data for CFD studies; (2) to perform validation studies for 3D RANS (the Realizable $k-\varepsilon$ model (RLZ), the Renormalization group $k-\varepsilon$ model (RNG), the $k-\omega$ shear stress transport (SST) model) and LES models (Wall-Adapting Local Eddy-Viscosity model (WALE)) around C-shaped elevated building using wind tunnel experiment results and evaluate the applicability of different turbulence modelling approaches; (3) to investigate the impact of elevated sections on mean and gust wind velocities, the building geometry considered is representative of buildings in Hong Kong situated in a tropical climate.

4.2 Wind tunnel experiment

4.2.1 Wind tunnel experiment setup

The wind tunnel experiments were conducted in AAF at the Hong Kong University of Science and Technology. It is equipped with a turbulence grid positioned at the front and roughness elements installed upstream to generate the desired wind profile characterized by prescribed wind velocity and turbulence kinetic energy (TKE) (Figure 4.1 (b)). The wind velocity was normalized with the wind velocity at the reference height (H=0.5 m), and the reference wind velocity U_{ref} was 7.5 m/s. The Reynolds number is 4.5×10^5 and the normalized wind velocity and turbulence intensity (TI) profiles at the center of the turntable without models are plotted in Figure 4.2 (a), and the velocity spectrum at the reference height is in accordance with the Von Karman spectrum observed at the boundary layer height, as shown in Figure 4.2 (b). The C-shaped elevated building was modeled and fabricated at a scale of 1:200, as described in Figure 4.1 (a). The main body has a height of 480 mm, while the elevated column reaches a height of 24 mm (at model scale). Three elevated columns are arranged at the one-third points to support the main building.

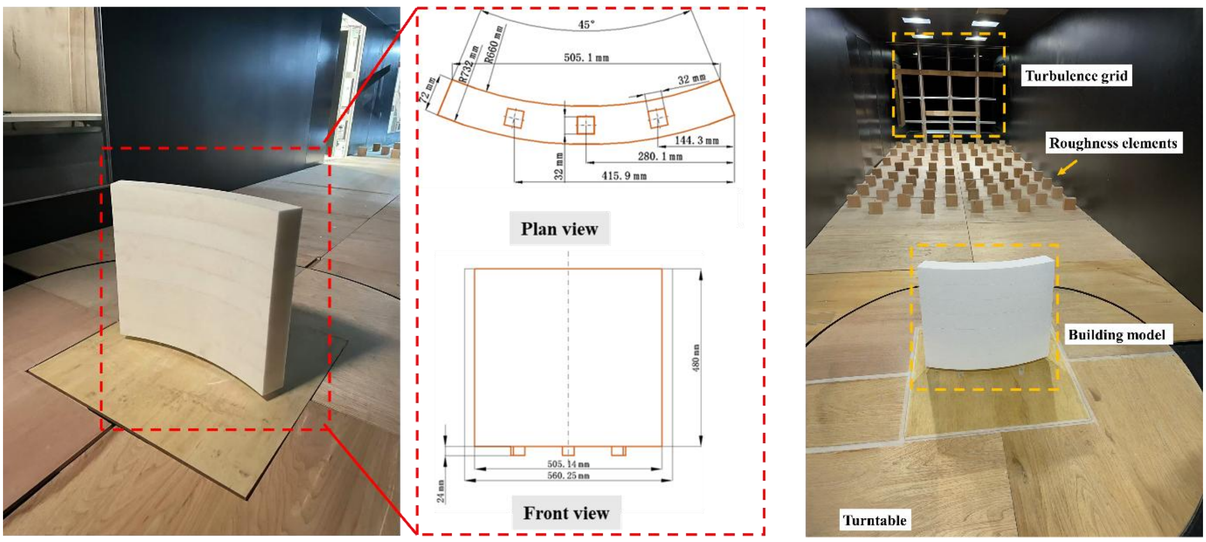

(a) (b)

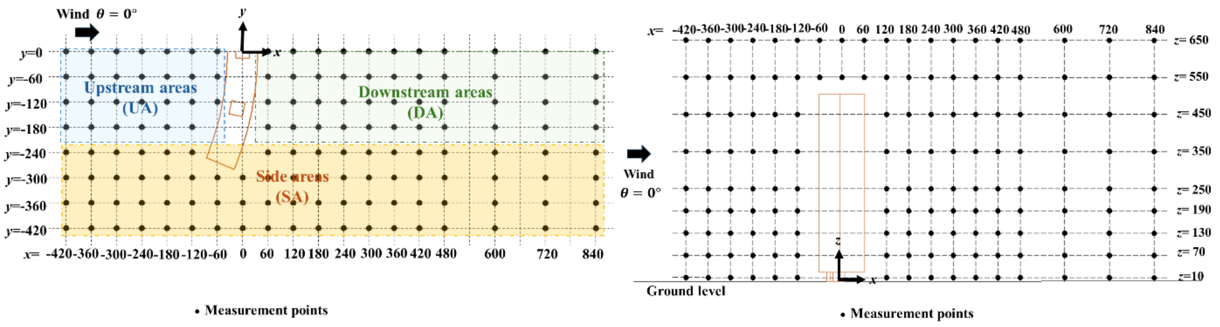

(c) (d)

Figure 4.1. (a) Building model, (b) Wind tunnel experiment setup photo, and the measurement points at (c) horizontal plane (z=0.01 m) and (d) vertical plane (y=0) (in millimeters).

4.2.2 Measurements

The wind velocity around the elevated C-shaped building was measured using a TFI series 100 Cobra probe, positioned point-by-point in both horizontal and vertical planes. Figure 4.1 (c)-(d) illustrates the spatial distribution of the measurement points established for velocity acquisition, encompassing a 420 mm region upstream and an 840 mm region downstream. This configuration ensured comprehensive coverage upstream, downstream, and laterally. The Cobra probe provides dynamic, 3-component velocity in real time and exhibits wind velocity measurement precision within 0.5 ms^{-1} and the measurement precision for wind direction within $\pm$ 1°, rendering it extensively employed in urban wind field analysis (Li et al., 2024; Du et al., 2017; Tse et al., 2017). The Cobra probe was mounted on the ISEL traverse system to ensure precise displacement of the probe, achieving an anticipated overall accuracy of 0.1 mm (Longo, 2012). The time series of wind velocity fields with a sampling rate of 1,000 Hz and a sampling length of 30 seconds was collected. The coordinates are defined as x, y, and z, while the instantaneous wind velocities in the streamwise (x-), lateral (y-), and vertical (z-) directions are denoted as u(t), v(t), and w(t), respectively. The turbulent kinetic energy (TKE) is defined as $k=(\overline{u'^2}+\overline{v'^2}+\overline{w'^2})/2$, where $\overline{u'^2}$, $\overline{v'^2}$, and $\overline{w'^2}$ are the Reynolds stresses in the x-, y-, and z- directions measured by the Cobra probe.

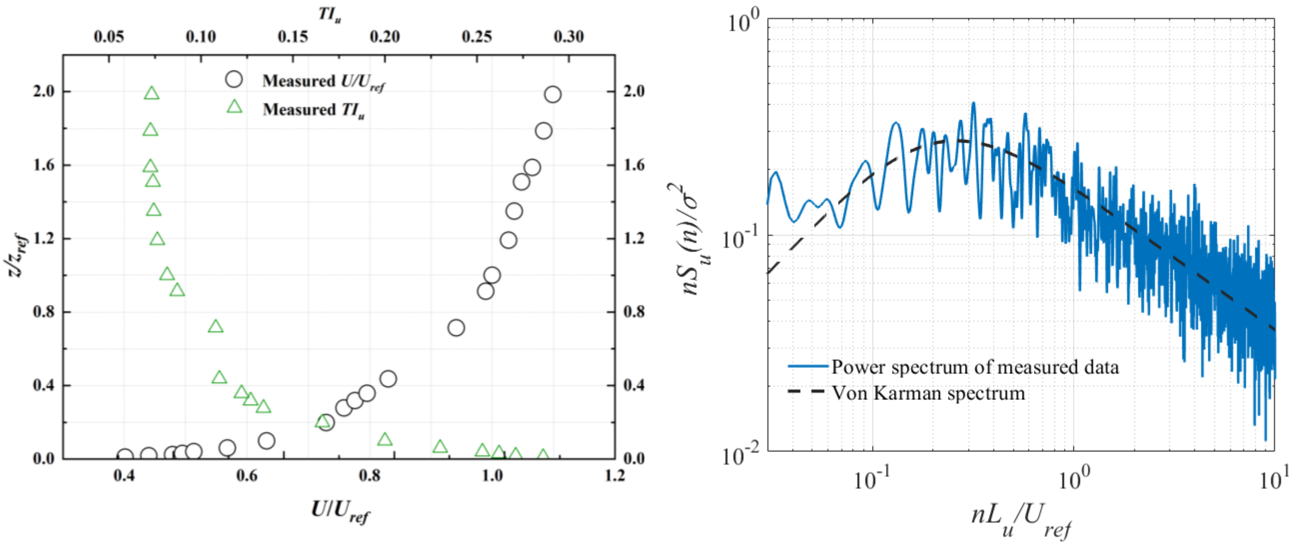

(a) (b)

Figure 4.2. Measured approaching wind flow properties for (a) Normalized wind velocity (*U*/*U*ref) and turbulence intensity (TI), and (b) Longitudinal velocity spectrum at the reference height.

4.3 CFD simulations: computational settings and parameters

4.3.1 Computational domain and grid

The computational study adheres to the same dimensions as the wind tunnel study, and the domain size and grid discretization conform to the best practice guidelines for CFD simulations (Tominaga et al., 2008). The distances from the domain's inlet, outlet, and lateral boundaries to the model boundaries are 5*H*, 15*H*, and 5*H,* respectively (Tominaga et al., 2008), and the blockage ratio was around 2%, which was smaller than the maximum allowable values (3%) based on the guidelines (Franke, 2011). The computational domain was discretized into hexahedral cells and developed using ANSYS ICEM CFD, with a mesh cell stretching ratio of 1.05 between adjacent cells to limit the communication error. For LES simulation, the entire mesh domain was divided into three subdomains: a fine inner domain for the area around the buildings Ω_1, a medium domain for transient areas Ω_2, and a coarse outer domain for areas far from the buildings Ω_3, to achieve a balance between low computational cost and high simulation accuracy. Specifically, for the inner domain near the building, the first cell height from the adjacent wall is 0.000042 m. The minimum element size was increased to 0.0035 m for the outer domain farther from the building (Figure 4.3 (b)).

Table 4.1. Cell element size for grid sensitivity check.

	Coarse	**Medium**	**Fine**	**Super-fine (LES)**
Minimum cell sizes (Around the buildings)	0.08	0.04	0.002	0.000042
Minimum cell sizes (Far from the buildings)	0.36	0.3	0.2	0.0035
Total cell numbers	2,504,000	3,213,960	5,236,740	11,054,994
y^+	>30	>30	4.2	<2

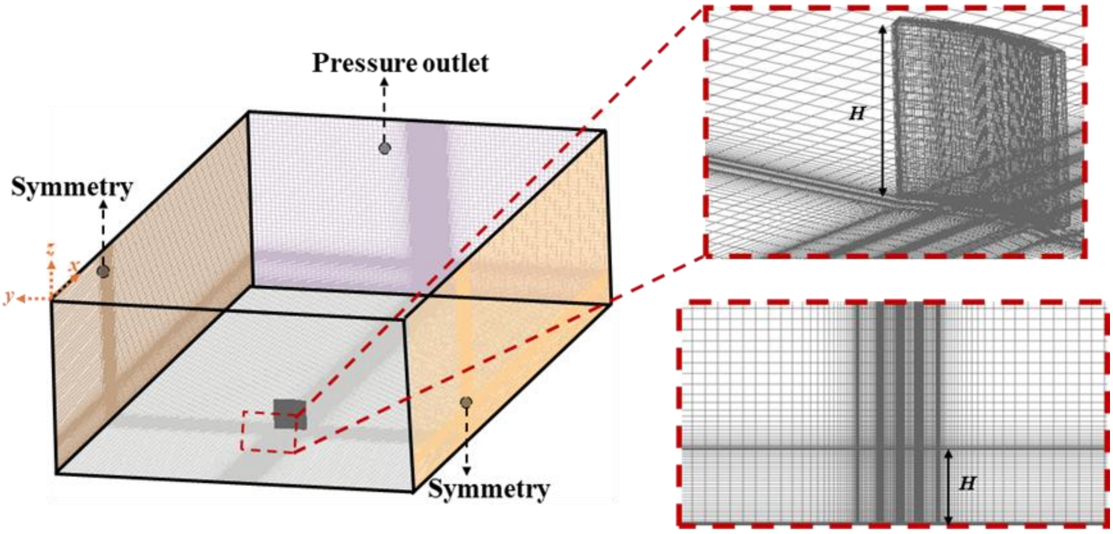

(a)

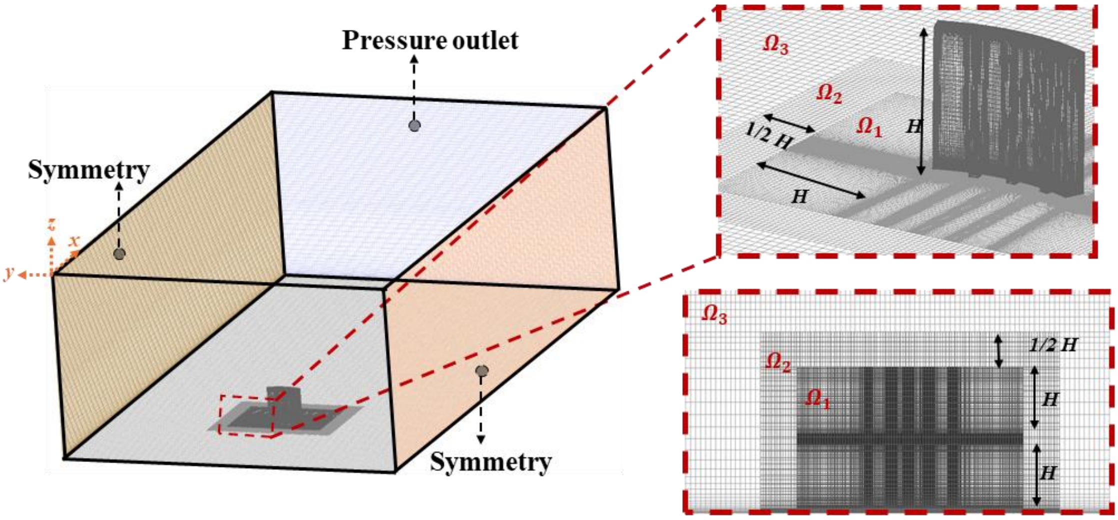

(b)

Figure 4.3. Computational domain and near building grid arrangement for (a) RANS and (b) LES.

19 LES and RANS cases (as listed in Table 4.2) were tested under various computational parameters. Three different Steady RANS models (SST $k-\omega$ model (SST), the realizable $k-\varepsilon$ model (RLZ), and the renormalization group (RNG) $k-\varepsilon$ model) were tested in the current chapter. Alphabet C represents the converging flow ($\varphi = 0^\circ$) and D represents the diverging flow ($\varphi = 180^\circ$) induced by the C-shaped elevated building. LES-blk served as the case for the C-shaped building without an elevated column, acting as the control building for comparison with the building that included an elevated column (Figure 4.4 (b)). Three different step sizes (Δt) of 0.05, 0.01, and 0.0002 s were employed to investigate their effects. Additionally, four different sampling lengths (ΔT) of 3, 6, 9, and 12 s were set to evaluate their respective influences. The non-dimensional sampling time t^* was defined as $t^* = \Delta T \times U_{ref} / H_{ref}$, where U_{ref} and H_{ref} is the reference velocity and height. The Courant-Friedrichs-Lewy number ($CFL = u\Delta t / \Delta x$), was employed to ensure the balance between the

spatial and temporal scales (Courant, 1967; Liu et al., 2019), where Δt is the time step, u is the velocity and Δx is the mesh length.

Table 4.2. Test cases and mesh arrangements for RANS and LES.

Case Name	Mesh numbers (million)	Min grid size (m)	Turbulence model	CFL	Time step	Sampling length	t^*	y^+
SST-C-1	2.5	0.08	SST $k-\omega$	-	-	-	-	>30
RLZ-C-1	2.5	0.08	RLZ $k-\varepsilon$	-	-	-	-	>30
RNG-C-1	2.5	0.08	RNG $k-\varepsilon$	-	-	-	-	>30
RNG-C-2	3.2	0.04	RNG $k-\varepsilon$	-	-	-	-	4.2
RNG-C-3	5.0	0.002	RNG $k-\varepsilon$	-	-	-	-	1.8
LES-C-1	11.0	0.00042	LES	5.61	0.005	12 s	172	<2
LES-C-2	11.0	0.00042	LES	1.53	0.001	12 s	172	<2
LES-C-3	11.0	0.00042	LES	0.86	0.0002	12 s	172	<2
LES-C-4	11.0	0.00042	LES	0.86	0.0002	3 s	43	<2
LES-C-5	11.0	0.00042	LES	0.85	0.0002	6 s	86	<2
LES-C-6	11.0	0.00042	LES	0.83	0.0002	9 s	129	<2
LES-D-1	11.2	0.00042	LES	5.69	0.005	12 s	172	<2
LES-D-2	11.2	0.00042	LES	1.57	0.001	12 s	172	<2
LES-D-3	11.2	0.00042	LES	0.89	0.0002	12 s	172	<2
LES-D-4	11.2	0.00042	LES	0.89	0.0002	3 s	172	<2
LES-D-5	11.2	0.00042	LES	0.88	0.0002	6 s	43	<2
LES-D-6	11.2	0.00042	LES	0.89	0.0002	9 s	86	<2
LES-C-blk	11.3	0.00042	LES	0.92	0.0002	12 s	172	<2
LES-D-blk	11.4	0.00042	LES	0.96	0.0002	12 s	172	<2

Notes: y^+=dimensionless distance between the wall-adjacent cell center and the wall.

4.3.2 Boundary conditions

For both RANS and LES, the profile of the approaching wind follows the profile measured in the wind tunnel experiment, with the longitudinal wind velocity (u) adhering to the logarithmic wind profile as defined in the Equation (4.1). The frictional velocity u^* was 0.44 m/s, and the dynamic roughness height z_0 was 0.00049 m derived from the fitting curves of the measured wind profile. The von Karman constant κ was 0.4187, and the model constant C_μ was 0.09. The homogeneity of the approach flow characteristics was ensured through a simulation in an empty domain, and Figure 4.4 (a) illustrates the comparison between the corresponding CFD wind profile results and the wind tunnel results. The velocity increased slightly with the distance from the inlet, while the turbulent kinetic energy (TKE) decreased with the distance from the inlet, remaining within the error range of the wind tunnel experiment results. The domain's ceiling and lateral surfaces were assigned symmetrical boundary conditions, the outlet was designed as a pressure outlet, and the ground and building surfaces were defined as no-slip boundaries.

$$u_{(z)} = \frac{u^*}{\kappa}\ln\left(\frac{z+z_0}{z_0}\right) \tag{4.1}$$

The turbulence kinetic energy (k) and turbulent kinetic energy dissipation rate (ε) are defined by the Equation (4.2) and Equation (4.3).

$$k_{(z)} \frac{3}{2}(I_{(z)}u_{(z)})^2 \tag{4.2}$$

$$\varepsilon_{(z)} = C_\mu^{1/2} k_{(z)} \frac{du_{(z)}}{dz} \tag{4.3}$$

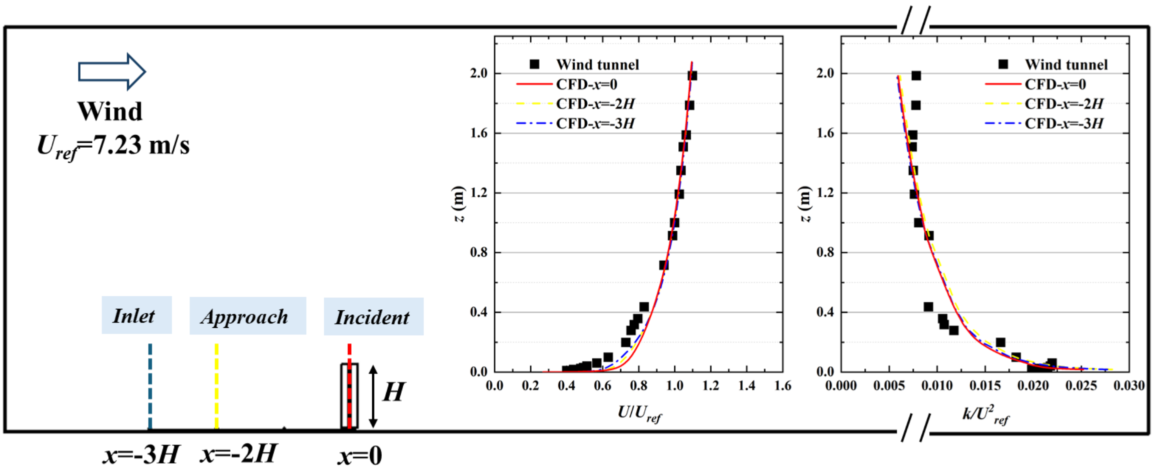

(a)

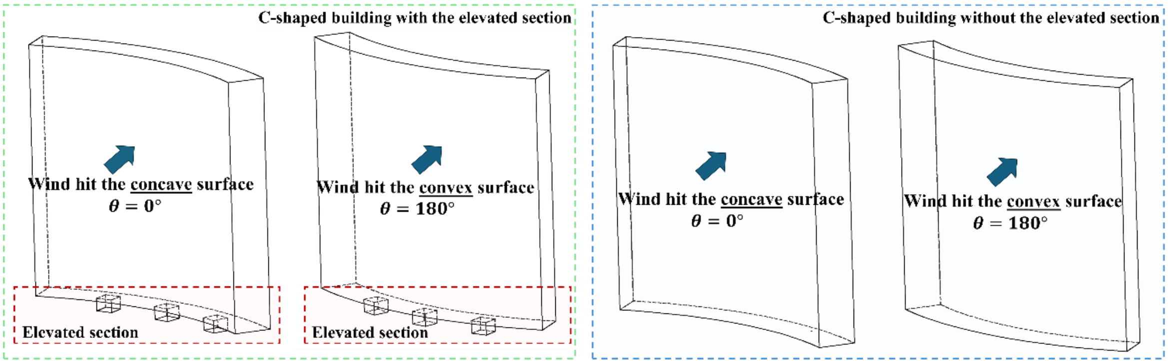

(b)

Figure 4.4. (a) Approach flow properties of U/U_{ref} and TKE at different domain locations and (b) Defined flow direction division and simulated cases.

4.3.3 Solver settings

ANSYS Fluent 19.0 was utilized to solve the governing equations for all the CFD simulations. In RANS scheme simulations, RNG $k-\varepsilon$ (RNG) (Yakhot, 1986), realizable $k-\varepsilon$ (RLZ) (Shih, 1995), and SST $k-\omega$ model (SST) (Tominaga, 2015) were employed to assess how RANS can model buildings with edge curvature. The RNG $k-\varepsilon$ model and SST $k-\omega$ model are considered the two most promising RANS methods for calculating airflows in urban areas (Tominaga and Stathopoulos, 2009; Wang and You, 2024), and the realizable $k-\varepsilon$ model demonstrates excellent performance in solving complex flows, including recirculation and rotation (Chen and Mak, 2021), which is a key issue in the present chapter. The SIMPLEC algorithm was chosen for pressure-velocity coupling, and the second-order discretization scheme utilized the convection terms of the governing equations. The governing equations employed in the steady RANS approach for incompressible fluid are as follows:

$$\frac{\partial \overline{u_i}}{\partial x_i} = 0 \tag{4.4}$$

where $\overline{u_i}$ and $\overline{u_j}$ denotes the component of the filtered velocity at the *i*th and *j*th directions, respectively. For the RNG $k-\varepsilon$ model, the turbulent viscosity was calculated by solving the two partial differential transport equations for turbulence kinetic energy (k) and dissipation (ε) based on Equation (4.5) and Equation (4.6) (Yakhot, 1986).

$$\frac{\partial k}{\partial t}+\overline{u_j}\frac{\partial k}{\partial x_j}=\frac{1}{\rho}\frac{\partial}{\partial x_j}[\frac{\upsilon_t}{\sigma_k}\frac{\partial k}{\partial x_j}]+P_k-\varepsilon \tag{4.5}$$

$$\frac{\partial \varepsilon}{\partial t}+\overline{u_j}\frac{\partial \varepsilon}{\partial x_j}=\frac{1}{\rho}\frac{\partial}{\partial x_j}\left[\frac{\upsilon_t}{\sigma_\varepsilon}\frac{\partial \varepsilon}{\partial x_j}\right]+\frac{\varepsilon}{k}(C_{\varepsilon 1}P_k-C_{\varepsilon 2}\varepsilon) \tag{4.6}$$

where υ_t is the turbulent kinetic viscosity; P_k denotes the production term of k; $C_{\varepsilon 1}$, $C_{\varepsilon 2}$, σ_k, σ_ε, and C_μ are the values of the model constants. For the SST $k-\omega$ model, the turbulence viscosity is calculated using the two partial differential transport equations (Equation (4.7) and Equation (4.8)) for k and dissipation rate (ω) (Menter, 1993):

$$u_i\frac{\partial k}{\partial x_i}=\frac{P_k}{\rho}-\beta^* k\omega+\frac{\partial}{\partial x_i}[(\upsilon+\sigma_k\upsilon_t)\frac{\partial k}{\partial x_i}] \tag{4.7}$$

$$u_i\frac{\partial \omega}{\partial x_i}=\alpha\frac{\omega}{k}\frac{P_k}{\rho}-\beta\omega^2+\frac{\partial}{\partial x_i}[(\upsilon+\sigma_\omega\upsilon_t)\frac{\partial \omega}{\partial x_i}]+2(1-F_1)\sigma_{\omega 2}\frac{1}{\omega}\frac{\partial k}{\partial x_i}\frac{\partial \omega}{\partial x_i} \tag{4.8}$$

where F_1 is the blending function; υ is the molecular viscosity; ρ is the flow density; P_k is the production limiter; σ_k, $\sigma_{\omega 2}$, σ_ω , β , β^* are model constants.

In the LES simulation, the PISO algorithm was employed, and second-order discretization schemes were adopted to solve the convection and viscous terms in the governing equations. The wall-adapting local eddy-viscosity (WALE) subgrid-scale (SGS) model was employed, as it has demonstrated success in numerical studies within urban environments (Ai and Mak, 2015). The random velocity fluctuations were superimposed on the mean wind velocity at the inlet using the vortex method, which incorporated 190 vortices (Dai et al., 2018). LES has the capability to filter flows based on the scale size of eddies and solves the governing equations for large eddies, and the filtered incompressible governing equations are shown in Equations (4.4)-(4.9) (Ai and Mak, 2015).

$$\frac{\partial(\rho\overline{u_i})}{\partial t}+\frac{\partial(\rho\overline{u_i u_j})}{\partial x_j}=\frac{\partial\sigma_{ij}}{\partial x_j}-\frac{\partial\overline{p}}{\partial x_j}-\frac{\partial\tau_{ij}}{\partial x_j} \tag{4.9}$$

where $\overline{p}$ is the filtered pressure, ρ is the density; τ_{ij} is the subgrid-scale model stress tensor.

The wall-adapting local eddy-viscosity (WALE) sub-grid scale model was adopted in the present chapter, and the SGS viscosity in this model is estimated by the following equation (Nicoud F, 1999):

$$v_{SGS}=(C_w\Delta)^2\frac{(S_{ij}^d S_{ij}^d)^{3/2}}{(\overline{S_{ij}}\,\overline{S_{ij}})^{5/2}+(S_{ij}^d S_{ij}^d)^{5/4}} \tag{4.10}$$

where $S_{ij}^d=\frac{1}{2}(\overline{g_{ij}}^2+\overline{g_{ji}}^2)-\frac{1}{3}\delta_{ij}\overline{g_{kk}}^2$, $\overline{g_{ij}}^2=\frac{\partial\overline{u_i}}{\partial x_j}$, C_w is the default value of the WALE constant.

4.4 Evaluation of computational parameters

This section evaluates the impact of various computational parameters, such as turbulence models, grid resolution, time steps, and sampling length, on wind flow characteristics and their alignment with wind tunnel experimental results.

4.4.1 Computational mesh resolution and sampling statistics

The mesh sensitivity tests were conducted for the RNG $k-\varepsilon$ model with three distinct mesh configurations (Coarse, Medium, and Fine), as tested in Table 4.1. Figure 4.5 illustrates the comparison of U/U_{ref} and k/U^2_{ref} values between Fine-Coarse, Medium-Coarse, and Medium-Fine grid settings. Specifically, for the coarse and medium meshes with y^+ values greater than 30, the standard wall function was applied, whereas for the fine mesh with y^+ values less than 5, the enhanced wall treatment was employed. A deviation of the U/U_{ref} and k/U^2_{ref} values exceeded 20% between medium and coarse grid arrangements, particularly at low wind velocity regions. The discrepancy between medium and fine grid arrangements is minimal, as evidenced by a smaller root mean square error (RMSE) of 0.02 between the two mesh settings, thereby demonstrating grid-independent results. Therefore, the medium mesh settings were employed for all the RANS simulations.

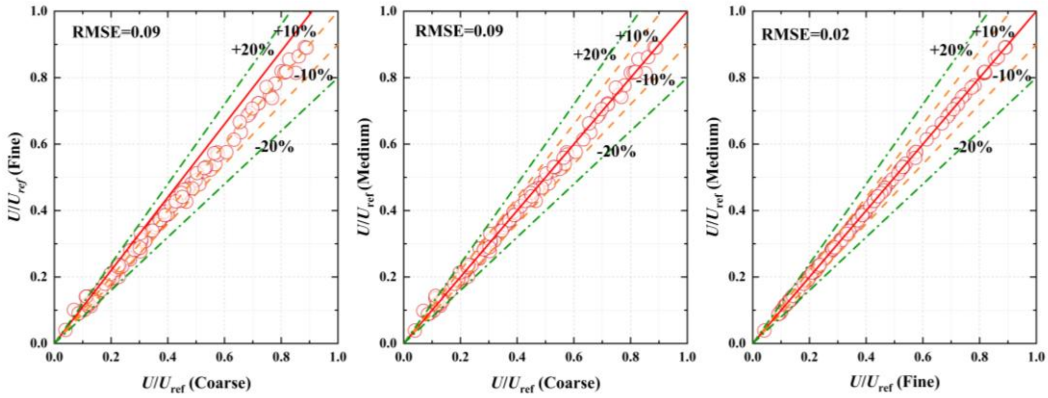

(a)

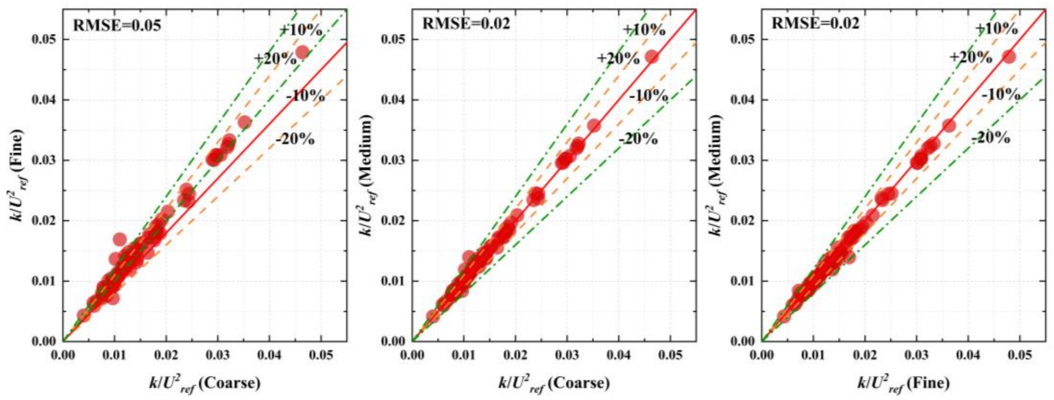

(b)

Figure 4.5. Comparison of (a) U/U_{ref} and (b) k/U^2_{ref} values for different mesh settings for RANS.

The mesh sensitivity of LES simulations was assessed using the resolved kinetic energy. To ensure adequate mesh quality in the simulation, the ratio of resolved kinetic energy to total kinetic energy should exceed 80% in regions of interest, as recommended by (Okaze et al., 2021). This requirement should be evaluated using the LES index of resolution quality (LES_{IQ}) proposed by I. B. Celik, (2005), as shown in the Equation (4.11):

$$LES_{IQ} = \frac{1}{1 + 0.05[\frac{\upsilon + \upsilon_{sgs}}{\upsilon}]^{0.53}} \tag{4.11}$$

where υ is the molecular viscosity, and υ_{sgs} is the turbulence viscosity. Figure 4.6 (a) and (b) illustrate the LES_{IQ} distribution under converging flows. The minimum LES_{IQ} value was approximately 82% near the building, while the majority of the other areas exceeded 90% and it can be concluded that the LES simulation resolved a sufficient amount of turbulent kinetic energy. Figure 4.6 (c) illustrates the power spectrum density (PSD) of wind velocity for P1, located upstream of the building. The LES and wind tunnel experiment results show consistency in the low-frequency range and successfully capture a portion of the inertial subrange.

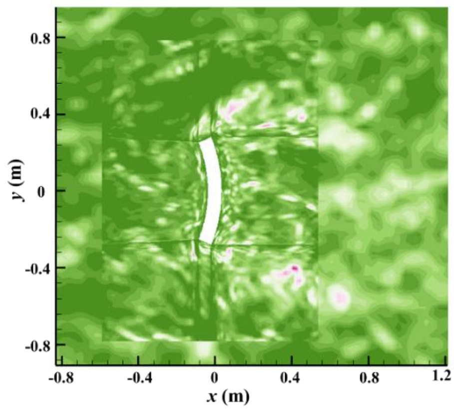

(a)

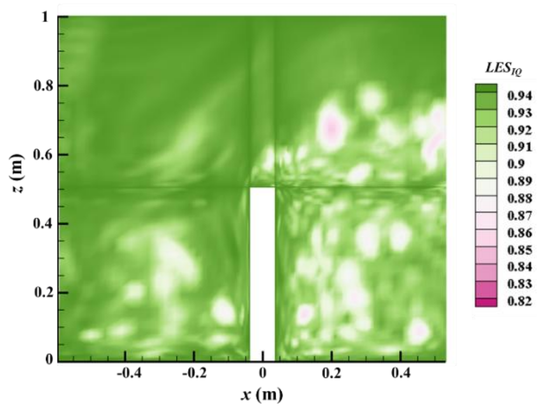

(b)

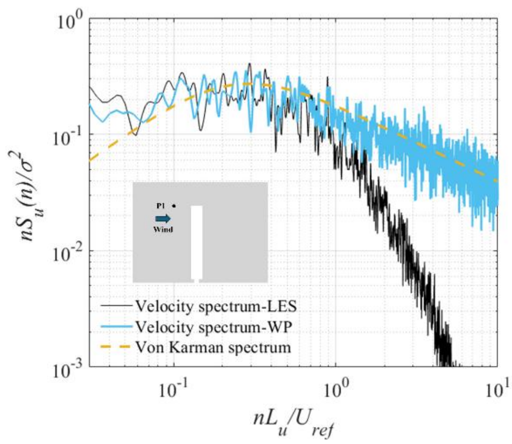

(c)

Figure 4.6. LES_{IQ} contour of control case at (a) pedestrian level plane (z=0.01 m), (b) central vertical plane (y=0), and (c) the normalized PSD at the building height upstream of the control building.

4.4.2 Effects of discretization of time step size and non-dimensional sampling time

In unsteady simulations, it is essential to choose the appropriate discretization time step Δt and non-dimensional sampling time t^* (Dai et al., 2018). Figure 4.7 (a)-(c) illustrates the differences in U/U_{ref} under various time steps (Δt) of 0.005, 0.001, and 0.0002 s. The results for Δt=0.005 s (LES-C-1) exhibited the largest deviation from the experimental data, while Δt=0.0002 s (LES-C-3) showed the closest agreement with the experimental data. Figure 4.7 (d)-(f) presents a comparison between the LES simulation results and the experimental data across various non-dimensional sampling times (t^*) ranging from 43 to 129. When the sampling time t^* was relatively short (<86), the U/U_{ref} measured in the elevated section was much lower than the experiment value, and the accuracy improved as t^* increased. The results of U/U_{ref} demonstrated negligible differences between t^*=129 and t^*=172, suggesting that 12 seconds was sufficiently long to generate a stable mean wind velocity for a C-shaped building. Figure 4.7 (g)-(m) illustrates the differences in TKE at various time step sizes and non-dimensional sampling times. The estimation of TKE was more sensitive to these parameters compared to wind velocity in LES simulations. Regarding the effect of time step size on TKE calculation, the results for Δt=0.005 s (LES-C-1) showed underestimation of TKE values near the building (-0.4 m<x<0.4 m) and overestimation of TKE values farther from the building (x>0.4 m) (Figure 4.7 (g)-(i)). This underscores the critical significance of selecting an appropriate time step to precisely capture the turbulence around the building, particularly in regions where highly turbulent downwash and ground-level vortices interact. The results of LES-C-4 exhibited slight underestimations of the TKE when compared to the wind tunnel data (Figure

4.7 (j)-(m)). In contrast, the differences between LES-C-3 and LES-C-6 were largely negligible. This indicates that the effect of t^* on wind velocity and TKE becomes increasingly negligible as t^* increases.

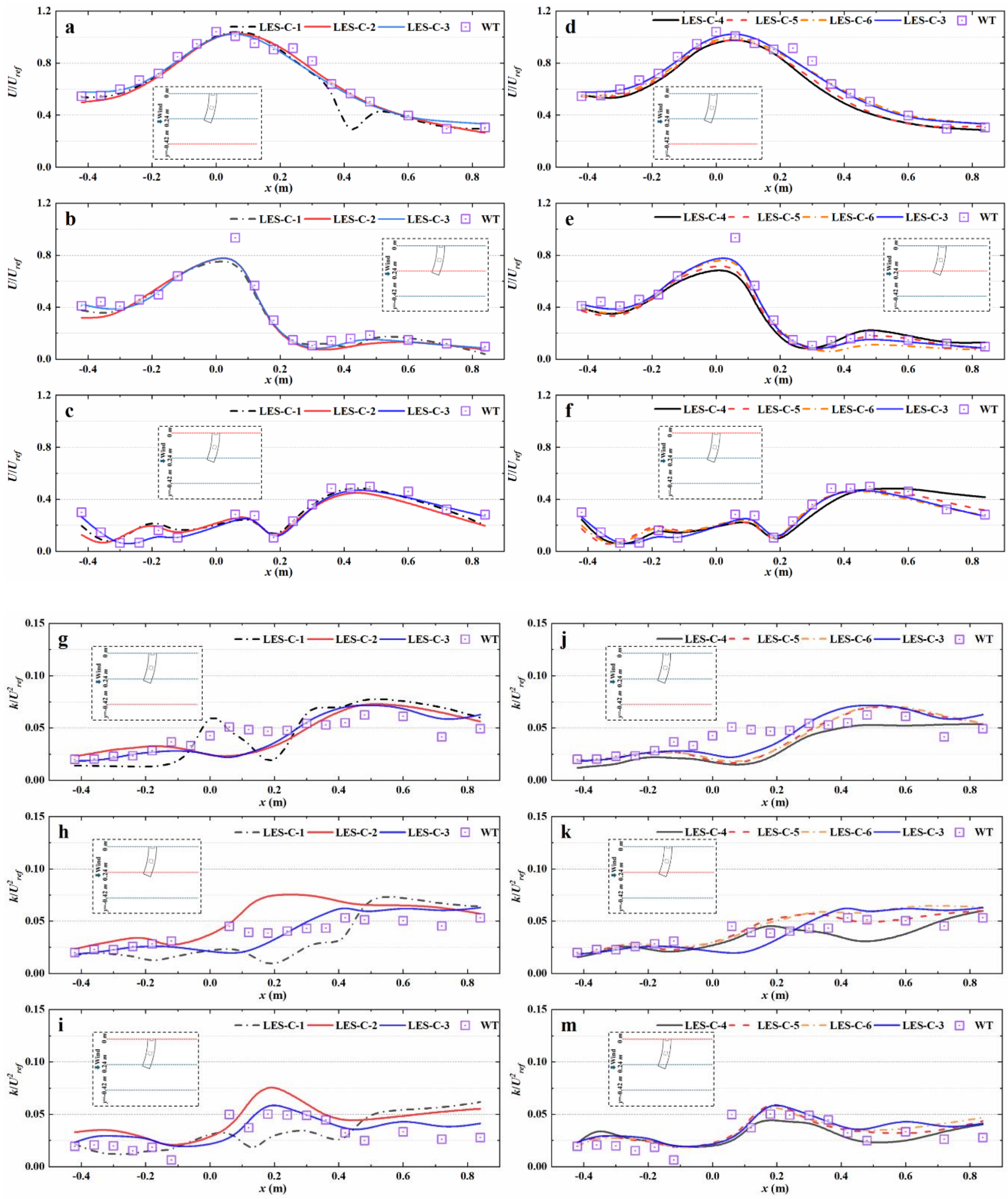

Figure 4.7. U/U_{ref} for LES cases with various time step sizes along: (a) y=-0.42 m; (b) y=-0.24 m, and (c) y=0 m; (d)-(f) Same as (a)-(c) but with various non-dimensional sampling

times and k/U^2_{ref} for LES cases with various time step sizes along: (g) y=-0.42 m; (h) y=-0.24 m, and (i) y=0 m; (j)-(m) Same as (g)-(i) but with various non-dimensional sampling times.

4.4.3 Comparison of RANS and LES models

Figure 4.8 illustrates the mean wind velocity and TKE distributions for side areas (SA), upstream areas (UA), and downstream areas (DA) of both the RANS and LES models. As the scatterplots shown in Figure 4.8 (a), all three RANS models provided a reasonable prediction of the wind velocity in the upstream areas, the predicted low wind velocities were comparable to the measurement data, with most data points deviating by less than 30%. Among these, the RNG turbulence model demonstrated superior performance in reproducing low wind velocities in the upstream areas in front of the building ($NMSE_{UA}$=0.06). However, the flow field reproduced by RANS tended to underestimate the high wind velocity in the side areas, with a deviation exceeding 20%, this underestimation was also evident in the downstream areas. Another notable feature was that the RANS model tended to overestimate the low wind velocity areas (U/U_{ref}<0.4) downstream. In contrast, the LES simulation yielded more accurate wind velocities around curved buildings, with the majority of deviations being within 10% when compared to the wind tunnel results. This further corroborates that LES outperformed RANS when modeling the flow field around buildings with curved surfaces, as demonstrated by the matrix presented in Table 4.4. Figure 4.8 (b) compares the predicted and measured TKE at z = 0.01 m near the C-shaped building. In terms of TKE agreement, LES performed better than RANS, the RANS models underestimated the TKE in downstream regions, with errors exceeding 20% when compared to experimental results, and significantly overestimated the TKE value in the low-velocity region upstream of the building, while the LES approach demonstrated a substantial improvement in predictive accuracy. A larger k/U^2_{ref} was observed in the separation regions and the area behind the elevated columns in LES. This phenomenon has been neglected by RANS models, as LES can accurately reproduce the periodic large-scale fluctuations behind the building, which RANS fails to capture (Tominaga and Stathopoulos, 2013).

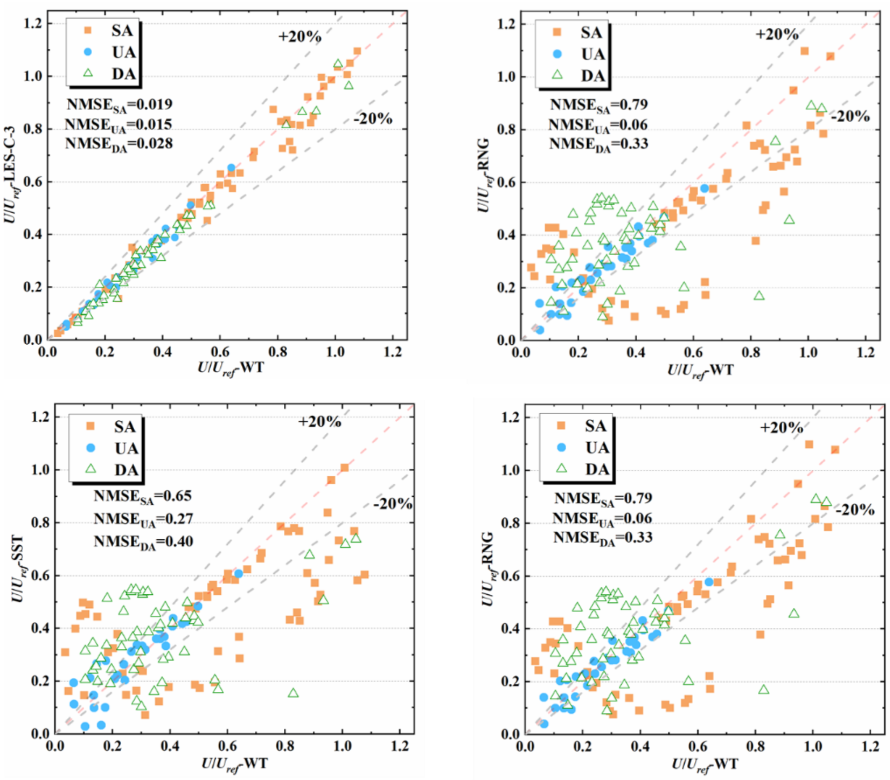

(a)

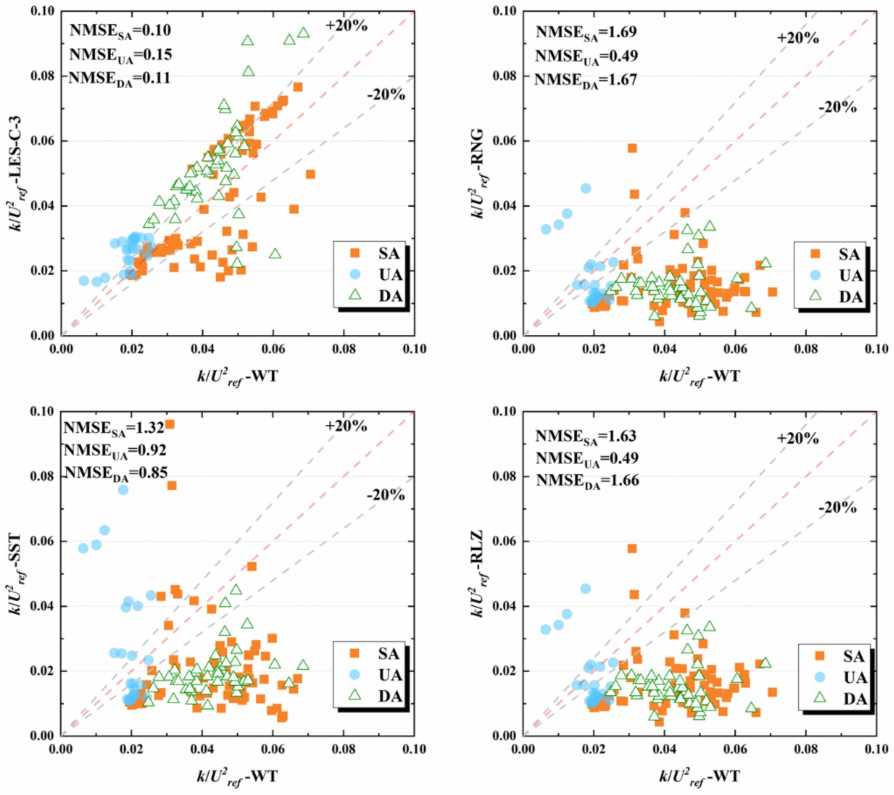

(b)

Figure 4.8. Scatter plot of (a) U/U_{ref} and (b) k/U^2_{ref} by the wind tunnel, RANS, and LES models.

Figure 4.9 (a) illustrates the U/U_{ref} contour at the pedestrian level for RANS and LES models, compared with the wind tunnel experiment. The wind velocity contours of the wind tunnel experiment were presented using cubic interpolation techniques (Tsang et al., 2012). Although the locations of the cores of the corner eddies predicted by the RANS model generally agree with those from wind tunnel experiments and LES, the RANS model predicted weaker corner eddies characterized by lower mean wind velocity magnitudes. It was found that the RANS approach has limitations in accurately predicting the position of the wake region. Specifically, the vortex core of the wake region predicted by RANS models significantly deviates from the results obtained through experiments and LES simulations, and the reattachment length behind the elevated building was overestimated by RANS models (Tominaga et al., 2008). Another feature of the flow pattern predicted by RANS and LES was that the intensity of the incoming jet through the elevated columns with relatively high velocities was underestimated by RANS models, whereas the area sizes affected by this incoming jet were overestimated by RANS models, extending the impacted regions to over 0.2 m behind the elevated building. The degree of outward inclination of the incoming jet in LES was estimated to be smaller and closer to the middle column, consistent with observations from the benchmark (Figure 4.9 (a)). Figure 4.9 (b) illustrates the spatial distribution of TKE at the pedestrian level. The discrepancies in TKE predicted by the RANS model were primarily attributed to the underestimation of TKE in the wake region behind the building and the overestimation of TKE in the elevated section located in front of the building. Furthermore, while the LES simulation predicted a more accurate TKE distribution in the wake region of the building, the LES also identified an additional high TKE region in front of the building that was not captured by the wind tunnel. This discrepancy might be attributed to the transverse flow around the Cobra probe.

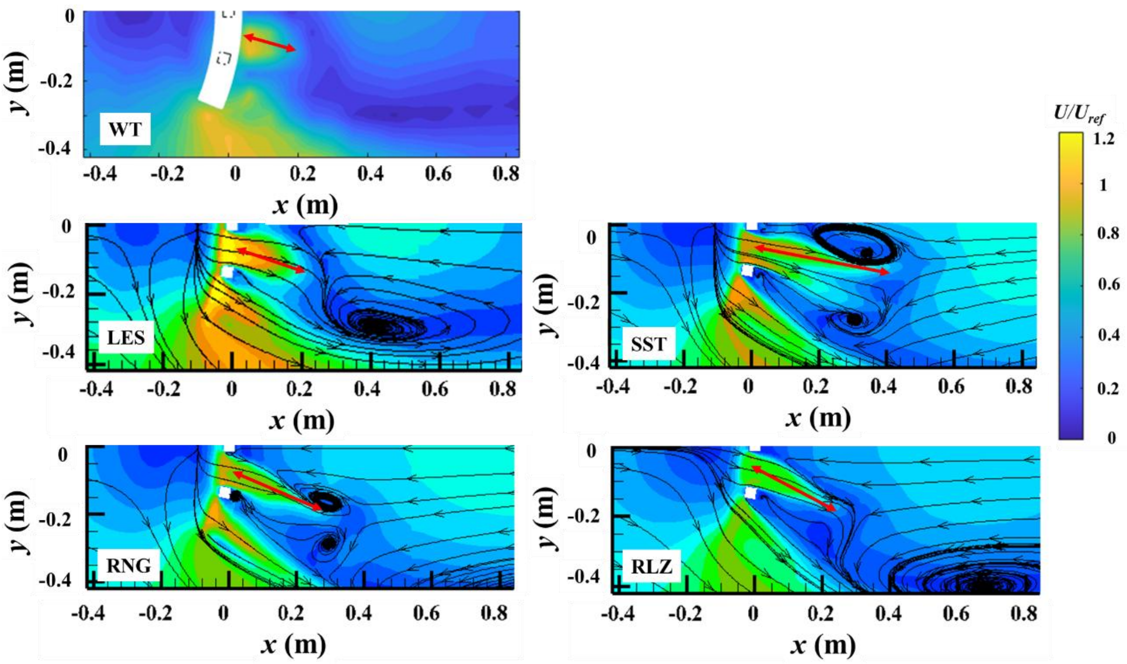

(a)

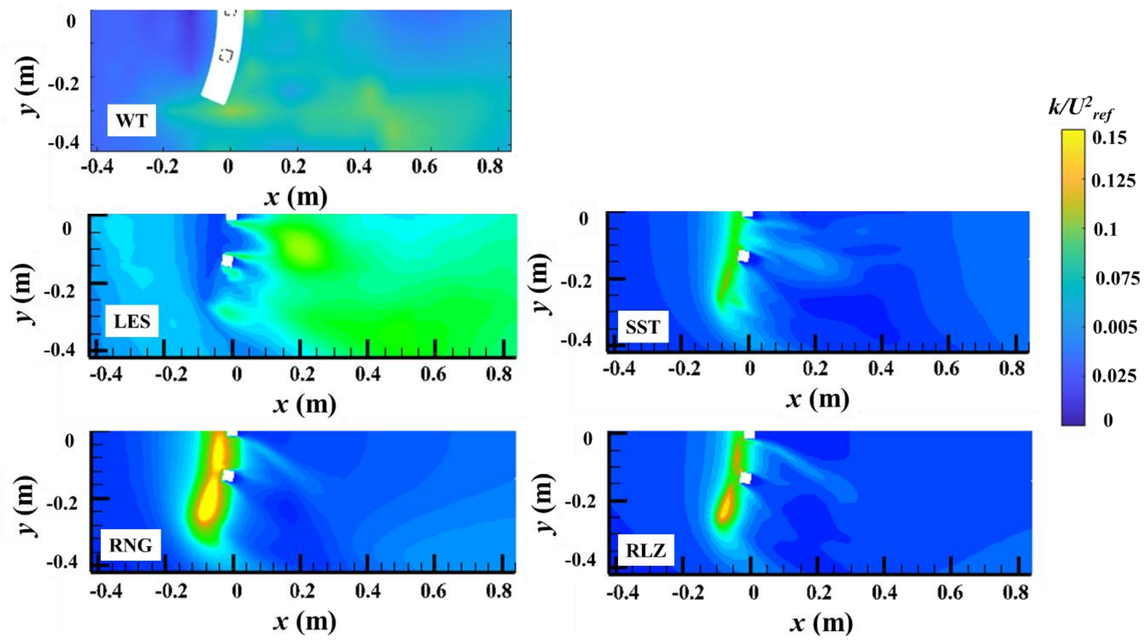

(b)

Figure 4.9. Comparison of (a) U/U_{ref} and (b) k/U^2_{ref} distribution over the horizontal plane (z=0.01 m) between wind tunnel, LES, and RANS models.

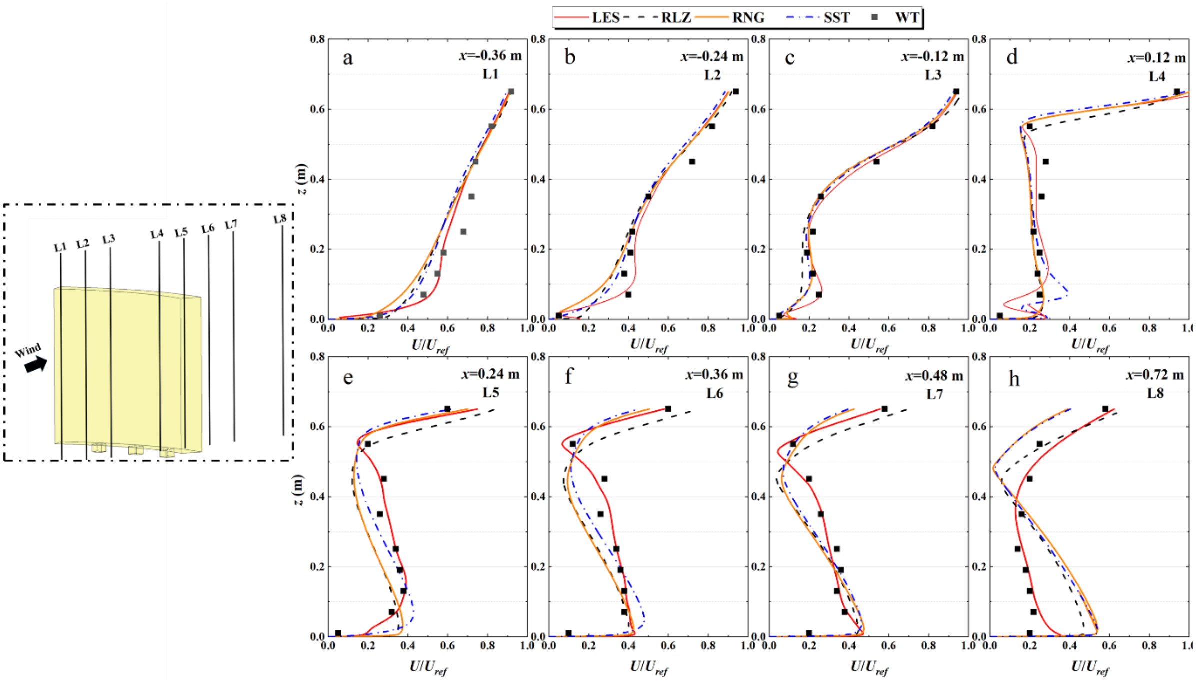

Figure 4.10. Comparison of U/U_{ref} distribution over vertical plane (y=0 m) between wind tunnel experiment results, LES, and RANS.

Figure 4.10 illustrates the comparison of U/U_{ref} across the central vertical plane (y=0) for RANS, LES, and wind tunnel experimental results. LES results demonstrated a strong correlation with experimental data, exhibiting smaller deviations compared to RANS, particularly in the region near the ground (z<0.2 m). RANS models underestimated the wind velocities near the ground and the separation flow at the roof height (z=0.5 m), particularly in the downstream region, where strong shear forces and high fluctuations were observed. In addition, among the RANS models, only the SST model successfully reproduced the near-ground vortex behind the building, whereas the RLZ and RNG models were unable to capture this feature (Figure 4.10 (d)). This was the reason why, at x=-0.12 m, where the near-ground vortex exists, the SST model exhibited a similar trend but with a smaller magnitude compared to the LES model. The wind velocity was consistently underpredicted by RANS models downstream of the building in the vertical direction, leading to a greater discrepancy compared to the upstream areas of the building. This can be attributed to the inherent limitations of the RANS model in accurately capturing TKE in recirculation regions influenced by transient fluctuations and eddies.

For the vertical central plane, the reattachment length behind the building (X_F) (the length of the flow recirculation zone downstream of the building (Liu and Niu, 2016) in the wake region and the height of the downstream stagnation point (Z_{dsp}) were compared for different turbulence models and the wind tunnel experiment (Table 4.3). SST, RLZ, and RNG models significantly overpredicted the X_F behind the building, resulting in an exaggerated recirculation zone. This outcome aligns with findings from a previous study that utilized RANS for a high-rise building model (Tominaga et al., 2008; Lin et al., 2021). While LES still slightly overestimated this length, it demonstrates much closer agreement with the benchmark. When the wind direction was oriented towards the convex side of the C-shaped building (LES-D-3), a longer reattachment length was observed in comparison to when the wind approached the concave side of the C-shaped building (LES-C-3). Additionally, the vortex near the ground behind the elevated building ascended (vortex N_d), and this effect became more pronounced under approaching wind conditions that induced diverging flows (LES-D-3). Consequently, Z_{dsp} increased from 0.2 m to 0.3 m as the wind direction shifted from 0° to 180°. Compared to non-elevated buildings, the downstream stagnation point (Z_{dsp}) shifted upward due to the pressure difference on the leeward side of the building and the elevated column.

Table 4.3. Comparison of reattachment length (X_F) and the height of the downstream stagnation point (Z_{dsp}).

Case	**Turbulence model**	X_F **(m)**	Z_{dsp}**(m)**
SST-C-1	SST $k-\omega$	1.8	0.18
RLZ-C-1	RLZ $k-\varepsilon$	1.7	0.05
RNG-C-1	RNG $k-\varepsilon$	2.0	0.1
LES-C-3	LES	1.15	0.2
Wind tunnel	-	1.1	0.2
LES-D-3	LES	1.25	0.3
LES-C-blk	LES	1.2	0.05
LES-D-blk	LES	1.2	0.08

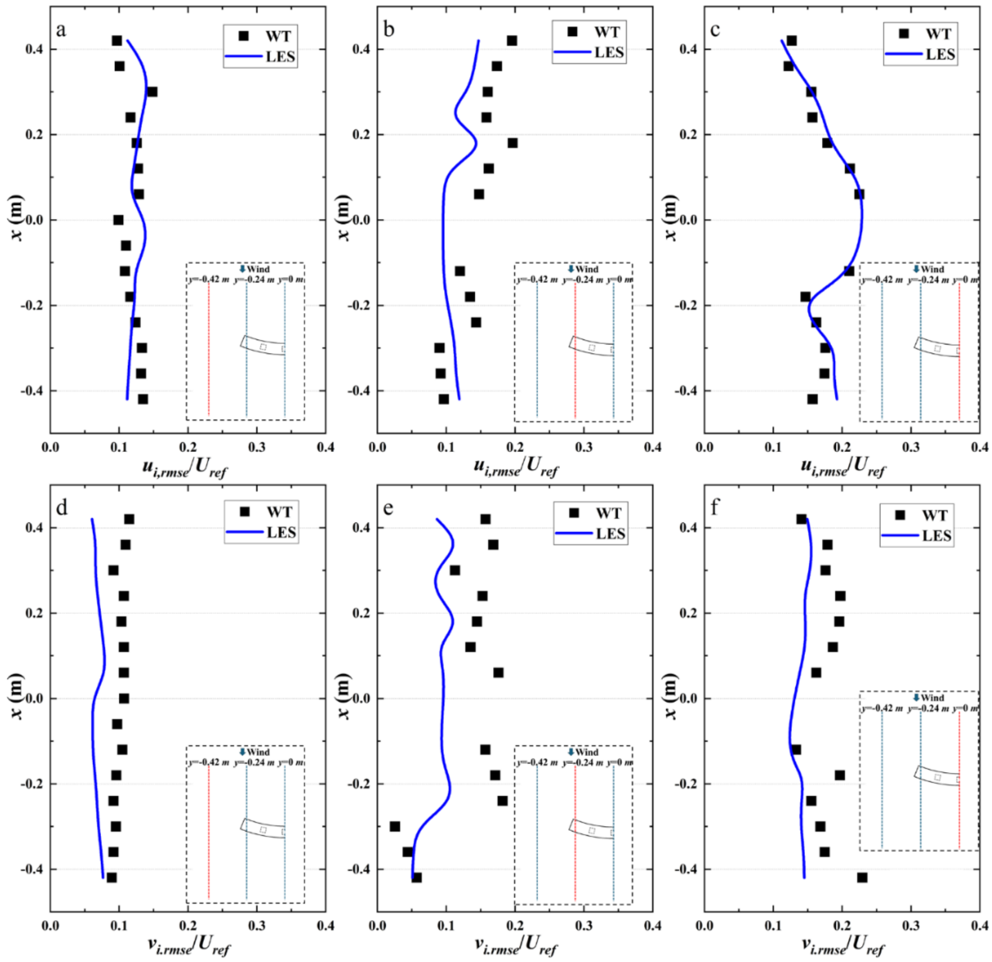

Figure 4.11. $u_{i,\ rmse}$ / U_{ref} from LES and wind tunnel data along three different horizontal lines: (a) y=-0.42 m; (b) y=-0.24 m; (c) y=0 m. (d)-(f) Same as (a)-(c) but for $v_{i,\ rmse}$ / U_{ref}.

In addition to the mean wind velocity, LES simulation demonstrates superior performance in predicting velocity components, such as the rmse velocity components ($u_{i,rmse}$ and $v_{i,rmse}$ as defined in the Equation (4.12) and Equation (4.13), where u_i and v_i are the velocity components in the streamwise and lateral directions respectively, $\overline{U}$ is the mean wind velocity, and n is the sampling time points) (Zheng and Yang, 2021). The comparison of the $u_{i,rmse}$ and $v_{i,rmse}$ from the LES simulations and the measured data from the wind tunnel experiment is illustrated in Figure 4.11. A good agreement of the $u_{i,rmse}$ was observed along three different lines, and LES slightly underpredicted the $v_{i,rmse}$ values at y=-0.24 m, where a pronounced outward flow occurred. Also, a discrepancy was observed in front of the building near the ground surface, which can be attributed to the influence of the traverse flow around the probe.

$$u_{i,rmse} = \sqrt{\frac{1}{n}\sum_{i=1}^{n}[(u_i - \overline{U})]^2} \tag{4.12}$$

$$v_{i,rmse} = \sqrt{\frac{1}{n}\sum_{i=1}^{n}[(v_i - \overline{V})]^2} \tag{4.13}$$

A quantitative evaluation of RAN and LES models for converging cases was conducted using validation metrics for normalized wind velocity and turbulence kinetic energy, considering all the measurement points. The validation metrics were factors of two observations (*FAC2*), fractional bias (*FB*), and normalized mean square error (*NMSE*) as the Equation (4.14)-(4.16). The validation metrics for the C-shaped building are presented in Table 4.4. For all turbulence models in velocity calculation, the *FAC2* values range between 0.8 and 1. The highest value was observed for LES-C-3 (1), while the lowest value corresponds to RNG $k-\varepsilon$ (0.8). For the TKE calculation at all measurement points around the building, the SST $k-\omega$ model produced the most accurate TKE values among all RANS models, as indicated by the lowest *FB* and highest *FAC2* values. It is noteworthy that the LES model yielded significantly more accurate TKE values than RANS models, even with relatively large time steps (LES-C-1). Moreover, the accuracy increased progressively with smaller time steps.

$$FAC2 = \frac{1}{n}\sum_{i=1}^{n} N_i \ with \ N_i = \begin{cases} 1, & for \ 0.5 < \frac{P_i}{M_i} < 2 \\ 0, & otherwise. \end{cases} \tag{4.14}$$

$$FB = \frac{2 \times ([P_i] - [M_i])}{[P_i] + [M_i]} \tag{4.15}$$

$$NMSE = \frac{\left[(M_i - P_i)^2\right]}{[M_i][P_i]} \quad (4.16)$$

where P_i and M_i are the predicted and measured values of the velocity and TKE, respectively; n is the data point number.

Table 4.4. Validation metric for the C-shaped building.

Metric	Velocity (U/U_{ref})			TKE (k/U^2_{ref})		
	NMSE	FB	FAC2	NMSE	FB	FAC2
Acceptance criterion	<4	(-0.3-0.3)	>0.5	<4	(-0.3-0.3)	>0.5
SST	0.33	-0.122	0.81	0.82	-0.46	0.47
RNG	0.32	-0.14	0.8	1.59	-0.78	0.34
RLZ	0.35	-0.09	0.82	1.59	-0.78	0.34
LES-C-1	0.129	-0.048	0.96	0.69	-0.35	0.7
LES-C-2	0.111	-0.07	0.83	0.17	0.20	0.96
LES-C-3	0.02	-0.088	1	0.13	0.01	0.96
LES-C-4	0.098	-0.1335	0.96	0.20	-0.14	0.9
LES-C-5	0.077	-0.137	0.98	0.13	-0.01	0.93
LES-C-6	0.056	-0.1	0.99	0.13	-0.01	0.94

4.5 Effects of the elevated section on wind flow patterns

This section evaluates the influence of the elevated section on wind flow patterns, including the time-averaged velocity field and turbulent statistics, using LES simulations. It adopts a time step of 0.0002 s and a sampling length of 12 s, with other numerical settings being identical to those described in Section 4.3.

4.5.1 Impact of the elevated section on instantaneous wind flow patterns

The time history of the velocity at six monitoring points for elevated and non-elevated high-rise buildings is illustrated in Figure 4.12. Two points, M1 (x/b =-2, y/b = 0) and M3 (x/b = -2, y/b =-2), were established on the windward side of the building. Two additional points, M2 (x/b = 2, y/b = 0) and M4 (x/b = 2, y/b = -2), were positioned on the leeward side.

Furthermore, two points, M5 (x/b = -2, y/b = -3) and M6 (x/b = 2, y/b = -3), were located near the corners of the building, where b is the building width. More pronounced fluctuations were observed at monitoring points 3-6 compared to monitoring points 1 and 2, under both elevated and non-elevated conditions. Compared to elevated conditions, non-elevated conditions tend to exhibit more fluctuations under both $\varphi = 0^\circ$ and $\varphi = 180^\circ$. The maximum U/U_{ref} values around the elevated building were significantly lower compared to those around the non-elevated building, with no distinct peak U/U_{ref} value observed. Specifically, the maximum values of U/U_{ref} were observed at t^* =20 for point M1 (U/U_{ref}=1.0) and at t^* =18 for point M4 (U/U_{ref} =1.4) under $\varphi = 0^\circ$ for a non-elevated building. Additionally, more fluctuations were observed when the wind interacted with the convex part of the building ($\varphi = 180^\circ$), indicating a higher likelihood of increased wind velocity that pedestrians may experience in a short period, thus enhancing the occurrence of gust wind (Figure 4.15 (b)-(c)).

Figure 4.12 describes the power spectrum density (PSD) of the velocity for elevated and non-elevated buildings. The PSD was derived from the fast Fourier transform (FFT) of the signal and describes the amplitude of the energy as a function of frequency, and the peak energy relates to the dominant vortex shedding frequency, the values of the PSD were normalized as $S_U^* = nS_U(n)/\sigma^2$, where U denotes the mean wind velocity and n denotes the frequency. The frequency n was normalized as $n^* = nb/\overline{U}$. Larger values of S_U^* were observed in the non-elevated case when n^*>1 for points M1 and M3, which were located at the windward side of the building. For elevated buildings, these values rapidly decayed in the same frequency range. This was because the vortex generated in the upstream elevated cavity (Vortex V_u) tended to weaken the backflow and the highly turbulent downwash. Meanwhile, the ground-level vortex formed in front of the non-elevated building played a significant role in generating the larger PSD at M1 and M3. For the wake regions behind the elevated building (M2), the velocity exhibited a peak when the n^* was 0.09. This peak was caused by the vortex shedding phenomenon originating from the building, and the peak energy was closely associated with the dominant vortex shedding frequency. The larger S_U^* values were observed for M2 and M4, located in the wake areas under the elevated building, compared with the non-elevated building. This can be attributed to the enhanced near-ground vortex behind the elevated building, which leads to highly turbulent regions in the wake areas. The monitoring points near the elevated building exhibit a wider Strouhal number range compared to those near the non-elevated building, indicating the vortex shedding frequency was broader for elevated buildings and the vortex shedding process in the elevated area was more complex compared to the podium area. For the points near the building corner (M6), the peaks of S_U^* were observed at approximately n^*=0.14 for the non-elevated building and 0.15 for the elevated building, respectively. The peak was attributed to the interaction between the incoming flow and the corner flow generated by the building. As for the effect of wind on the concave or convex parts of a building, larger S_U^* values were observed at points M1 and M3 located at the windward side of the building, when n^* less than 1 upon wind impacting the convex surface, compared to when the wind struck the concave surface, and these values decayed rapidly at high frequencies. The increase in S_U^* was attributed to the high turbulence downwash flow in front of the building and the enhanced backflow from the elevated columns. The peaks of n^* were larger when the wind impacted the convex surface when it struck the concave surface, suggesting that more organized turbulent fluctuations arise from the complex interaction between the separation flow and the downwash flow. No significant difference was observed for S_U^* values near the corners of the building (M5, M6) for $\varphi = 0^\circ$ and $\varphi = 180^\circ$.

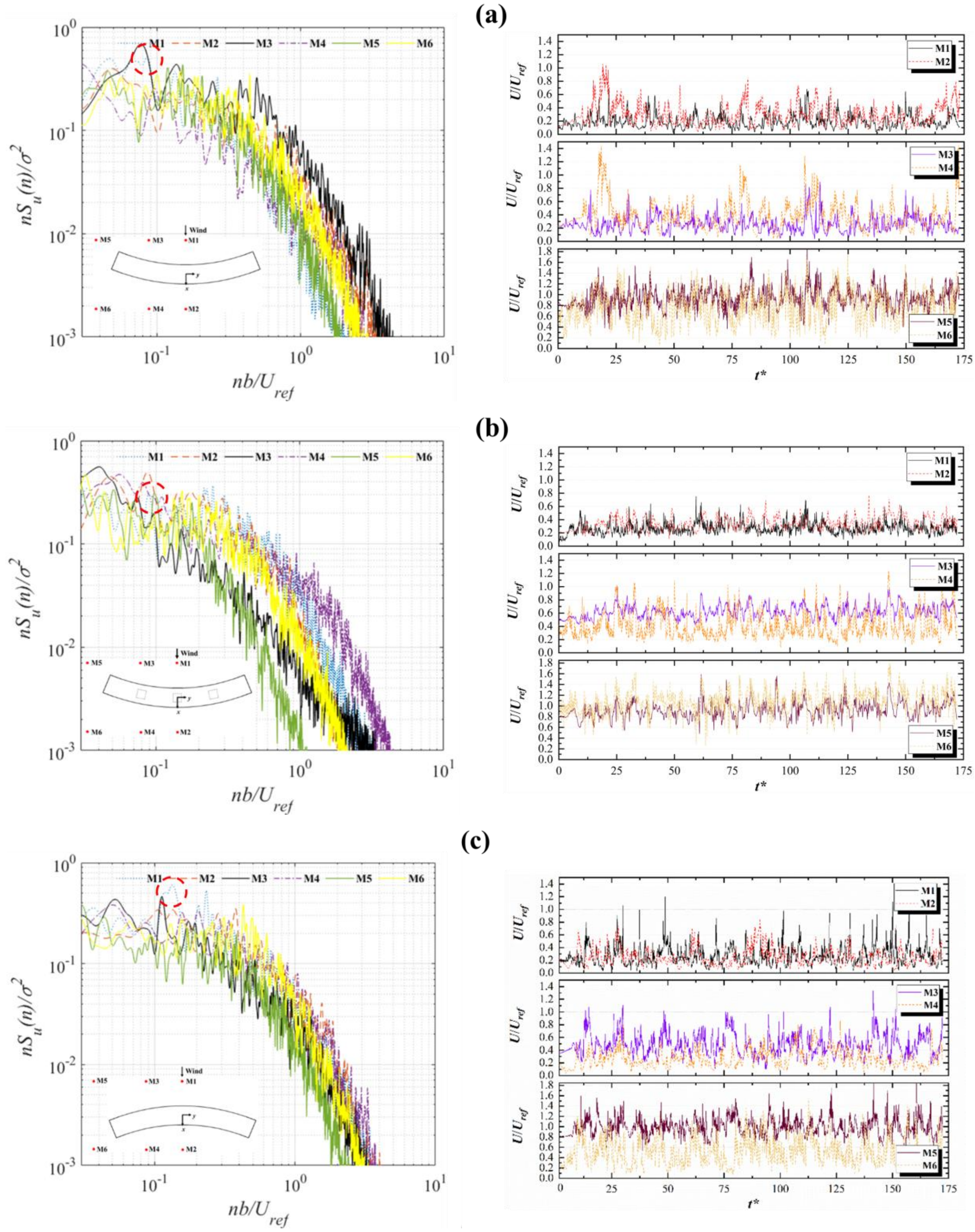
(a)
(b)
(c)
M1
M2
M3
M4
M5
M6
Wind
$nS_u(n)/\sigma^2$
nb/U_{ref}
U/U_{ref}
t*

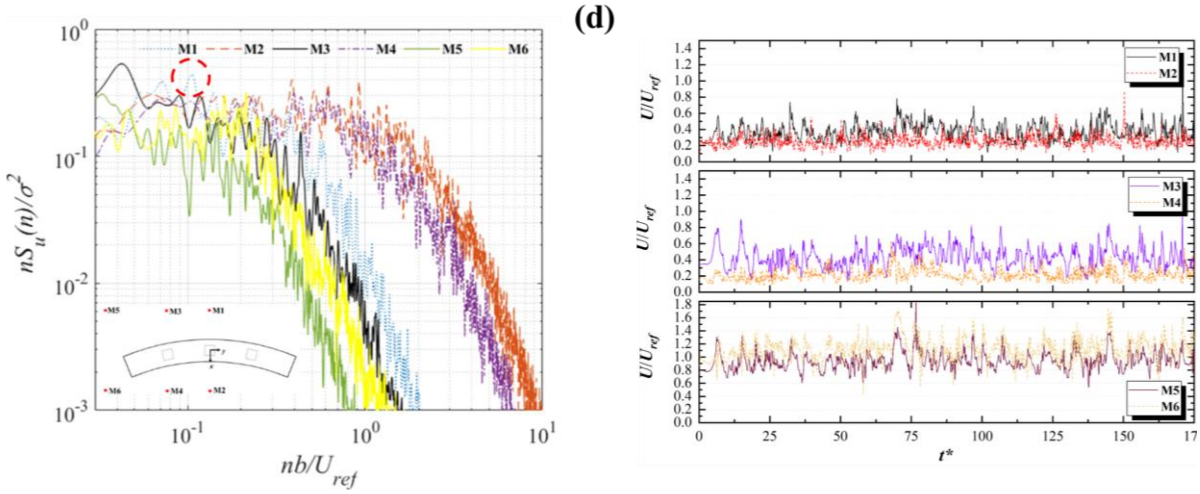

Figure 4.12. PSD of the velocity fluctuations and time history of U/U_{ref} at monitored points around elevated and non-elevated buildings under (a)-(b) $\varphi = 0^{\circ}$ and (c)-(d) $\varphi = 180^{\circ}$.

4.5.2 Impact of the elevated section on the PLW surrounding buildings

4.5.2.1 Mean wind velocity, vortex structure, and turbulent fluctuation components

Figure 4.13 (a)-(d) illustrates the comparison of vortex structures using time-averaged streamlines of the mean velocity field on the *x*-*z* plane (*y*=0 m) of the building, both with and without elevated sections. In general, in front of the building, the downwardly deflected flow generated a horseshoe vortex (1). Elevated buildings tended to reduce the intensity of the horseshoe vortex due to their smaller wind-exposed areas, and as a result, the horseshoe vortex became too weak to wrap around the building. When the wind strikes the convex portion of the building, the horseshoe intensity decreases (Figure 4.13 (c) and (d)). The principal vortex B_t (3) was located at the central position downstream of the trailing end, consistent with findings from previous studies (da Silva et al., 2020; Hassan et al., 2021). Two streamwise vortices (N_f (4) and N_u (5)) were observed in front of the non-elevated building along the *x*-axis, whereas these vortices were not observed for the elevated building. For elevated buildings, two vertices (V_u (7) and V_d (8)) merge at the elevated section. Wind penetrates the elevated section and strikes the elevated column; this flow swirls and thereby forms the vortex V_u. The formation of the vortex V_u led to the weaker backflow in front of the elevated building. This can be attributed to the horseshoe vortex being positioned closer to the windward side of the non-elevated building compared to that of an elevated building. This resulted in a slightly higher upstream stagnation point position for elevated buildings compared to non-elevated ones. Additionally, the downwash of the elevated building enters the elevated area and moves upward, thus forming the vortex V_d. The formation of the vortex V_d strengthened the intensity of vortex N_d (6), leading to a reduction in reverse flow. Figure 4.13 (e)-(h) shows the iso-surface of the turbulence structure around the building with and without the elevated section. The vortex shedding was observed on the side of both structures, where the flow separates at the separation point and forms a vortex shedding phenomenon. For the elevated building, a distinct and intensified tip vortex (B_t) was observed (Figure 4.13 (e)), which enhanced the reattachment phenomenon, consequently resulting in an increased height of the downstream stagnation point. The elevated building reduced the intensity of the horseshoe vortex (as indicated by the red rectangle), which was further amplified under $\varphi = 180^\circ$. The flow through the elevated structure interacts with the backflow induced by the tip vortex near ground level, thereby increasing turbulence at the bottom leeward side of the building compared to non-elevated buildings (Figure 4.13 (e) and (g)). The conical vortex was intensified by the presence of the elevated building and originated from the lower edge of the main structure, as indicated by the yellow rectangle in Figure 4.13 (e)-(h). It gradually shifted along the z-axis, eventually disappearing near the side walls of the elevated building. The large-scale vortex structures near the ground were broken down into smaller eddies and extended streamwise in both elevated and non-elevated buildings.

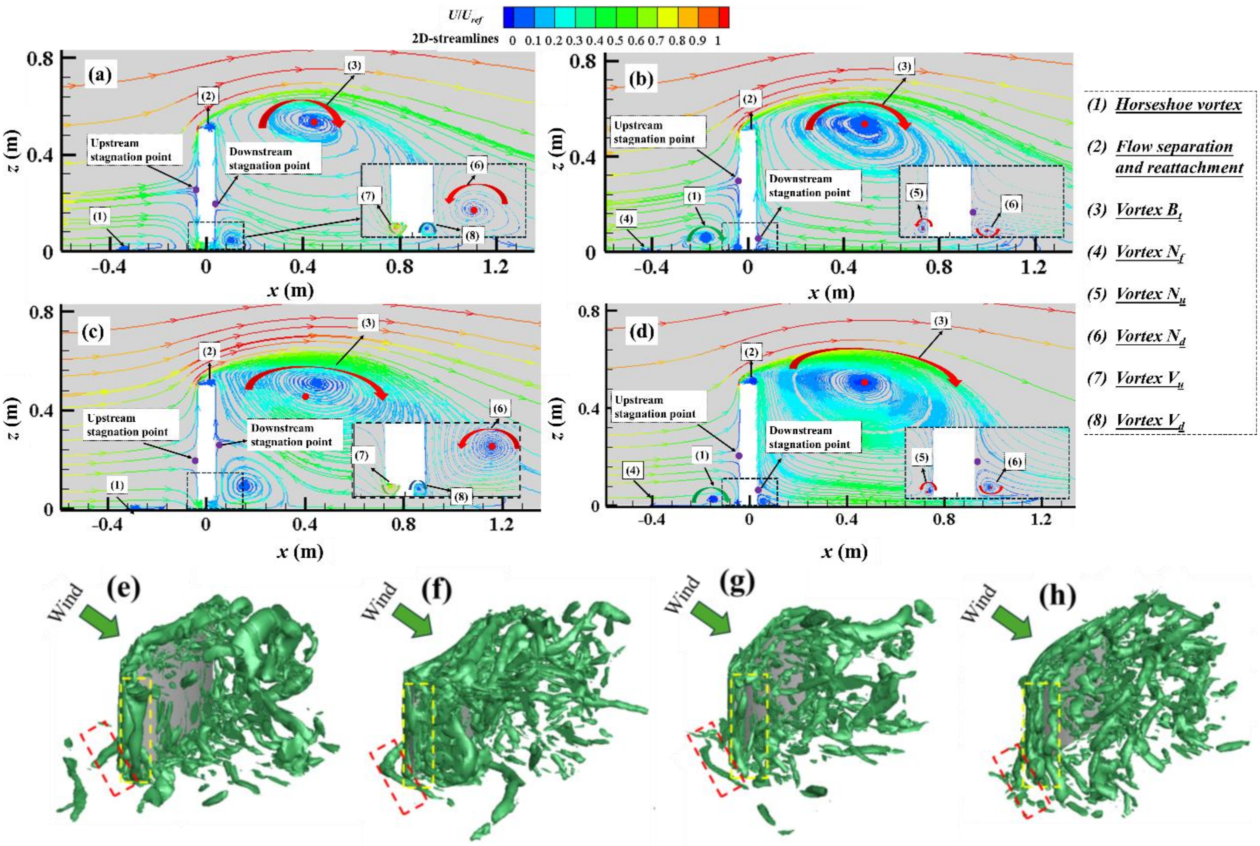

Figure 4.13. 2D streamlines of mean wind velocity of (a) elevated and (b) non-elevated building at the central vertical plane under $\varphi = 0^{\circ}$; Same as (c)-(d) but under $\varphi = 180^{\circ}$. The instantaneous vortex structure of (e) elevated and (f) non-elevated building under $\varphi = 0^{\circ}$; Same as (g)-(h) but under $\varphi = 180^{\circ}$.

Figure 4.14 illustrates the fluctuating velocity components in both streamwise (*x*-) and lateral directions (*y*-) across upstream regions (*x*=-0.2 and -0.1 m) and downstream regions (*x*=0.1, 0.2, 0.4, and 0.6 m). The presence of high-rise elevated buildings tended to generate lower instantaneous lateral flow (*v* component) near the structures. This was primarily due to the through-flow from the elevated columns tending to counteract the corner stream entering the wake areas. In comparison, the elevated building tended to generate a larger instantaneous streamwise flow (*u* component) compared to the non-elevated building in the region from *y*=0 to *y*=0-0.3 m near the building, and this phenomenon becomes minimal as the distance from the building increases. This also suggests that the instantaneous streamwise flow (v component) is more likely to be entrained on average near the building, with smaller fluctuations observed near the elevated building (Figure 4.12).

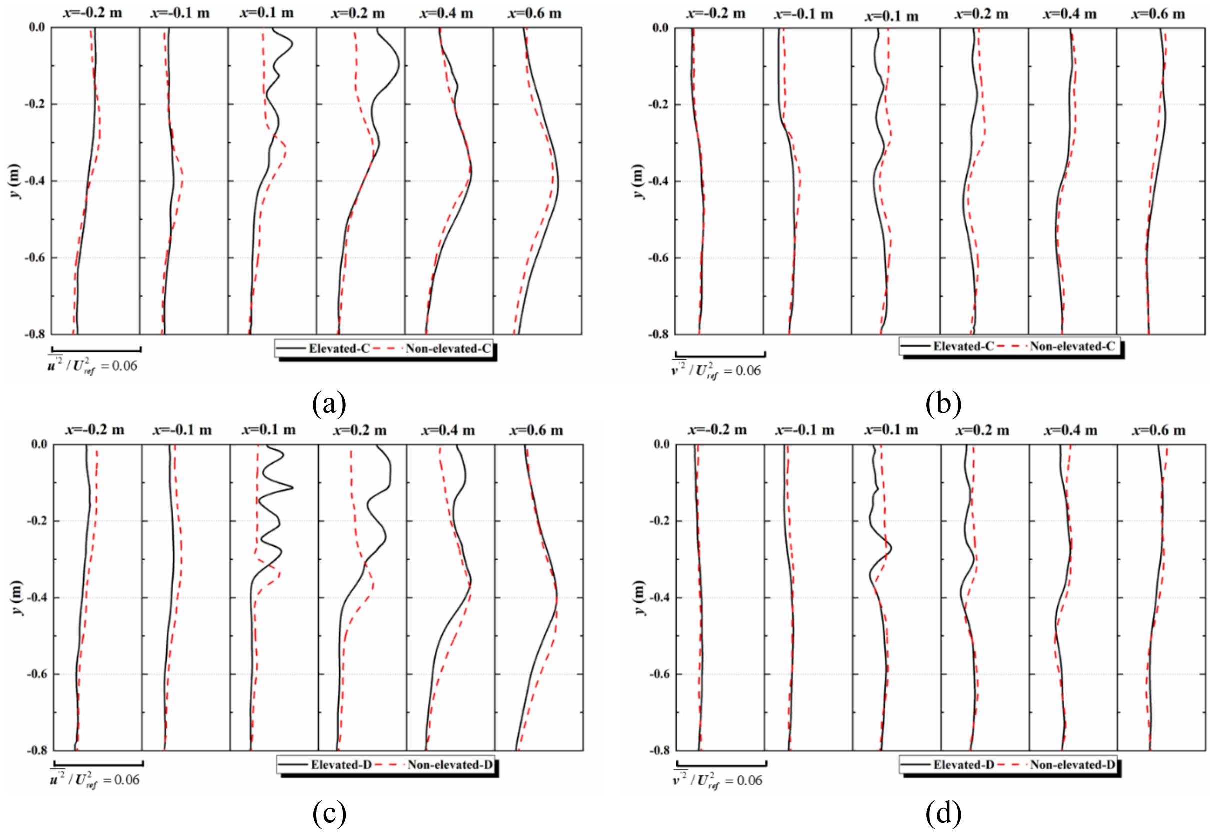

Figure 4.14. Profiles of fluctuating velocity components ($\overline{u'^2}$ and $\overline{v'^2}$) surrounding elevated and non-elevated buildings under (a)-(b) $\varphi = 0^\circ$ and (c)-(d) $\varphi = 180^\circ$.

4.5.2.2 Gust wind velocity and turbulence kinetic energy

When assessing the wind comfort near the target building, it is crucial to evaluate not only the mean wind velocity but also the peak gust wind velocity (Lin et al., 2025; Li et al., 2024). The gust wind velocity can be directly obtained from high-fidelity numerical simulations, such as LES, using the gust factor (*GF*). The gust factor (*GF*) is defined as the ratio of the maximum wind velocity within a specific time period to the mean wind velocity, as expressed in the Equation (4.17). In the present chapter, the sample length T and gust duration T_g were chosen as 10 min and 3 s in full scale, respectively. According to the relationship between the length, velocity, and time scale (Lombardo, 2021), these values correspond to 3 s and 0.015 s in reduced scale. After obtaining the gust factor (*GF*), the gust wind velocity (U_g) can be calculated by multiplying the gust factor and the mean wind velocity, as presented in the Equation (4.18).

$$GF = \frac{U^{T_g}_{xy,\max}}{\overline{U_{xy}}^{T}} \quad (4.17)$$

$$U_g = GF \times \overline{U} \quad (4.18)$$

where $U^{T_g}_{xy,\max}$ is the maximum moving average wind velocity of 0.015 s on a reduced scale; $\overline{U_{xy}}^{T}$ is the average velocity in 3 s on a reduced scale; $\overline{U}$ is the mean wind velocity.

The distribution of the TKE around the elevated and non-elevated buildings is illustrated in Figure 4.15 (a), where the black circle indicates the location of the peak TKE on the sides and downstream of the buildings. It can be observed that on the side of the building, the elevated structure tended to shift the peak TKE region downstream to 0.55 m, in contrast to the non-elevated building, where the peak TKE region was located closer to 0.4 m. Also, the location of the peak TKE showed little variation regardless of whether the flow impacted the concave or convex parts of the elevated building, while the magnitude was slightly higher when the wind struck the concave portion. The variation of the normalized maximum wind velocity (U_{max}/U_{ref}), gust wind velocity (U_g/U_{ref}), and average TKE (k_{ave}/U^2_{ref}) at converging and diverging wind conditions for elevated and non-elevated buildings is presented in Figure 4.15 (b)-(c). The results indicate that for both elevated and non-elevated high-rise buildings, the TKE value was significantly lower when the flow impacted the convex side of the building compared to when it struck the concave side, indicating a trend opposite to that of velocity. This suggests that areas with low wind velocity may also exhibit high TKE values due to the large turbulence. In addition, while the maximum wind velocity exhibited minimal variations across different cases, the gust wind velocity was significantly higher for elevated buildings compared to non-elevated buildings in side areas. Specifically, the U_g/U_{ref} for an elevated building was 40% greater than that for a non-elevated building. This shows that high-rise elevated buildings may cause strong peak winds at the pedestrian level near the structure in windy regions, and the impact of the elevated section on downstream areas was not significantly distinct (Figure 4.15 (c)).

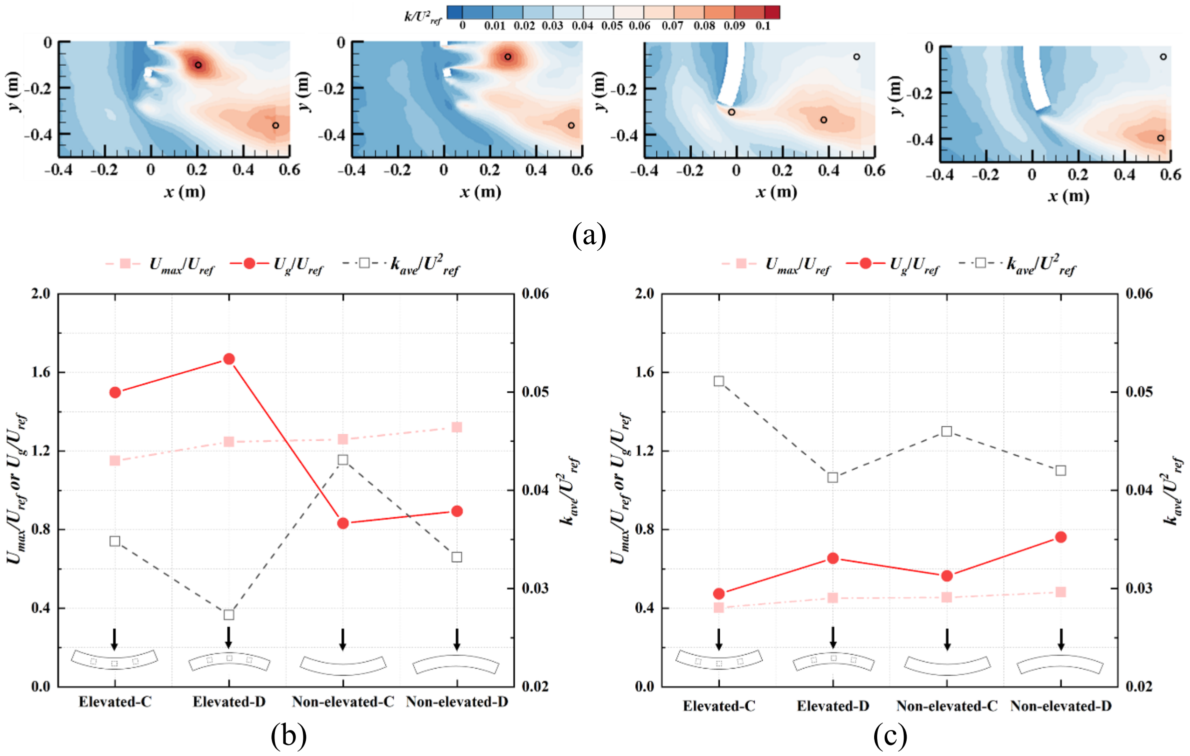

Figure 4.15. (a) TKE distributions at the pedestrian level; Variation of maximum wind velocity, gust wind velocity, and TKE in (b) side areas and (c) downstream areas surrounding elevated and non-elevated buildings under various wind directions.

4.6 Summary

In this chapter, a wind tunnel test was conducted on a typical high-rise building with a curved cross-section to investigate the wind velocity at the pedestrian level and serve as the benchmark for numerical simulation. Numerical results from RANS and LES models were validated using the data from wind tunnel experiments, and the applicability of various turbulence modeling approaches was compared. The building without the elevated section served as the control base, and the effects of the elevated section on time-averaged quantities and turbulent statistics were systematically investigated and discussed. The major outcomes of the research are as follows:

(1) The prediction of the mean wind velocity in the side and wake regions of the building by RANS models deviated from the wind tunnel experiment results, while these models demonstrated fairly good agreement with the wind tunnel data for the mean wind velocity in the upstream region. In the elevated region where vortices formed due to the reverse flow and backflow generated by the elevated column, the RANS model failed to reproduce the vortex V_d in the downstream elevated section and N_d behind the building, but only the SST model reasonably reproduced these vortices. The length of the jet flow generated between the elevated columns was overestimated by RANS models compared to experimental data, with discrepancies ranging from 1.5 to 2 times.
(2) The LES simulation can accurately reproduce the mean wind velocity and reasonably estimate the rmse velocity components around the elevated building. LES demonstrates superior capability in predicting the high TKE region surrounding the elevated building, particularly downstream of the building. The choice of time step is crucial for estimating the mean wind velocity and TKE around the building. Results obtained with relatively large time steps may underestimate the TKE near the building; however, even though LES with relatively larger times steps may not fully resolve all turbulent structures, its results are generally more accurate than those of RANS models.
(3) In the comparison of fluctuating characteristics of PLWEs surrounding elevated and non-elevated buildings, the vortex shedding frequency around elevated buildings exhibits a wider range compared to those around non-elevated buildings, indicating that

the interaction between the flow separation and vortex shedding is more complex surrounding elevated building. The elevated section resulted in a new upstream vortex (V_u), which weakened the backflow and consequently reduced the intensity of the horseshoe vortex in front of the building. This leads to a decrease in the highly turbulent downwash, resulting in the distinctive peaks of PSD being less pronounced in the windward areas of elevated buildings. The emergence of the downstream vortex (V_d) in the elevated downstream section led to a reduction in reverse flow, thereby weakening the near-ground vortex (N_d) and ultimately increasing the height of the downstream stagnation point (Z_{dsp}).

(4) The presence of high-rise elevated buildings tends to induce a significant increase in instantaneous streamwise flow (*u* component). These buildings exhibit reduced mean wind fluctuations, implying that the instantaneous lateral flow (*v* component) is more likely to be entrained on average near the building. The increase in the *u* component indicates that elevated building tends to laterally entrain high velocity streamwise flows into the wake region of the buildings, thereby reducing the size of the wake areas. The elevated building reduces the TKE on the side of the building as a result of the weakened corner stream magnitude, while increasing the TKE downstream of the building due to the collision between the jet flow from the elevated column and the downwash flows. In addition, while the mean wind velocity is higher when the wind strikes the convex part of the building, the TKE value is greater when the wind hits the concave part. This suggests that regions of high turbulence can also be observed in areas with low velocity, owing to the increased turbulence intensity.

CHAPTER 5. Pedestrian-level wind environment surrounding two tandem non-identical height buildings under twisted wind flows

5.1 Introduction

The wind environment at the pedestrian level in urban areas is a combination of various flow fields resulting from the complex interaction between incoming winds and surrounding structures. Due to the combined effects of the Earth's rotation, the friction of the Earth's surface, and pressure gradient forces, the twist of wind is observed, which significantly impacts pedestrian-level environments but has been largely overlooked in previous studies. Although the literature has demonstrated the effectiveness of enhancing ventilation through elevated building designs (Xia et al., 2015; Chen and Mak, 2021; Du et al., 2017; Tse et al., 2017; Zhang et al., 2017), the performance of such structures under the influence of twisted winds remains unclear. Based on this background, the primary focus of this chapter is to investigate the impact of twisted wind on PLWEs surrounding non-identical height elevated buildings, while simultaneously evaluating the performance and optimal locations for these elevated structures. A series of experiments was conducted in a boundary layer wind tunnel (BLWT) using models under conventional and twisted wind profiles. Based on wind velocity measurements obtained from a wind tunnel at pedestrian level (2 m), this chapter explores the flow field under CWP and TWPs. It further proposes relevant measures to enhance urban ventilation in mountainous areas with twisted winds, thereby providing valuable insights for urban planning.

5.2 Experiment Setup

5.2.1 Building Configuration and Case Description

5.2.1.1 Elevated building

The building models employed in this chapter consist of two buildings arranged in tandem, as this particular arrangement has been empirically demonstrated to accurately replicate the interaction between the two buildings (Gao et al., 2022; T.Stathopoulos, 1986). The selected building models exhibited varying relative building heights and the presence or absence of elevated structures, which are two influential parameters in the tandem arrangement of buildings in PLWEs, as listed in Table 5.1. The dimensions of the building were 120 m, 80 m, and 40 m in height (H), 40 m in width (W), and 20 m in depth (D) in full scale, as suggested by Tse et al. (2017). The height ratio between the upstream and downstream buildings (H_{UB}/H_{DB}) ranged from 3:1 to 0.33:1 to simulate the variations in building height in urban areas (Chen and Mak, 2021; Li et al., 2020). The elevated building featured an elevated core with dimensions of 6 m (h) × 20 m (w) × 10 m (d), occupying a plan area equivalent to 25% of the total building's plan area (Zhang et al., 2017). The elevated building featured an elevated core with dimensions of 6 m (h) × 20 m (w) × 10 m (d). The downstream models were categorized into three types: DL for downstream low-rise buildings; DM for downstream medium-rise buildings, and DH for downstream high-rise buildings. The passage width between the two buildings was 20 m. The height of the upstream building (H_{UB}) and downstream building (H_{DB}) varies, resulting in a vertical disparity that manifests as step-up and step-down scenarios (Figure 5.1 (b)). Each test case was evaluated under both conventional and twisted wind profiles.

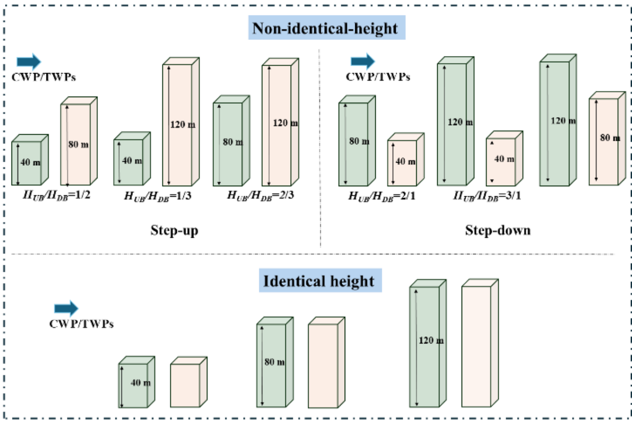

(a)

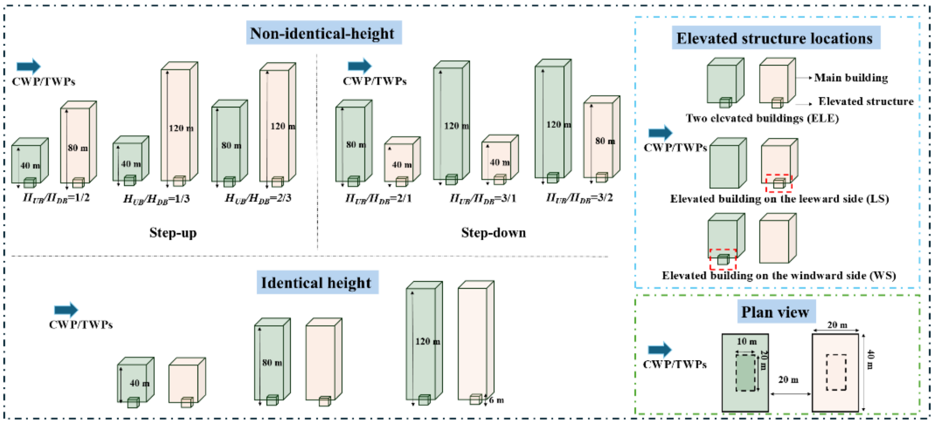

(b)

Figure 5.1. Schematic diagrams of (a) Non-elevated and (b) Elevated building models (in full scale).

Table 5.1. Summary of all elevated tested cases in the wind tunnel scale.

(a) Two elevated buildings in tandem arrangements (ELE)				
Case name [Model type, H_{UB}, ELE]	**Upstream building height (H_{UB})**		**Downstream building height (H_{DB})**	
	Main building height	**Elevated height**	**Main building height**	**Elevated height**
[DL, 200, ELE]	170 mm	30 mm	170 mm	30 mm
[DL, 400, ELE]	370 mm	30 mm	170 mm	30 mm
[DL, 600, ELE]	570 mm	30 mm	170 mm	30 mm
[DM, 200, ELE]	170 mm	30 mm	370 mm	30 mm
[DM, 400, ELE]	370 mm	30 mm	370 mm	30 mm
[DM, 600, ELE]	570 mm	30 mm	370 mm	30 mm

[DH, 200, ELE]	170 mm	30 mm	570 mm	30 mm
[DH, 400, ELE]	370 mm	30 mm	570 mm	30 mm
[DH, 600, ELE]	570 mm	30 mm	570 mm	30 mm

(b) The upstream building is elevated while the downstream building is not elevated (WS)

Case name [Model type, H_{UB}, WS]	**Upstream building height (H_{UB})**		**Downstream building height (H_{DB})**	
	Main building height	**Elevated height**	**Main building height**	**Elevated height**
[DL, 200, WS]	170 mm	30 mm	200 mm	0 mm
[DL, 400, WS]	370 mm	30 mm	200 mm	0 mm
[DL, 600, WS]	570 mm	30 mm	200 mm	0 mm
[DM, 200, WS]	170 mm	30 mm	400 mm	0 mm
[DM, 400, WS]	370 mm	30 mm	400 mm	0 mm
[DM, 600, WS]	570 mm	30 mm	400 mm	0 mm
[DH, 200, WS]	170 mm	30 mm	600 mm	0 mm
[DH, 400, WS]	370 mm	30 mm	600 mm	0 mm
[DH, 600, WS]	570 mm	30 mm	600 mm	0 mm

(c) The upstream building is elevated while the downstream building is not elevated (LS)

Case name [Model type, H_{UB}, LS]	**Upstream building height (H_{UB})**		**Downstream building height (H_{DB})**	
	Main building height	**Elevated height**	**Main building height**	**Elevated height**
[DL, 200, LS]	200 mm	0 mm	170 mm	30 mm
[DL, 400, LS]	200 mm	0 mm	370 mm	30 mm
[DL, 600, LS]	200 mm	0 mm	570 mm	30 mm
[DM, 200, LS]	400 mm	0 mm	170 mm	30 mm
[DM, 400, LS]	400 mm	0 mm	370 mm	30 mm
[DM, 600, LS]	400 mm	0 mm	570 mm	30 mm
[DH, 200, LS]	600 mm	0 mm	170 mm	30 mm
[DH, 400, LS]	600 mm	0 mm	370 mm	30 mm
[DH, 600, LS]	600 mm	0 mm	570 mm	30 mm

5.2.1.2 Non-elevated building

For the non-elevated building, the experiment utilized two tandem-arranged building models, featuring varying height differences between the structures. Rectangular buildings with varying aspect ratios [height (H)/width (W)] of 3:1, 2:1, and 1:1 have been selected to represent the predominant architectural characteristics observed in urban areas (Zhang et al., 2017; Tse et al., 2017). The planar dimensions of each building are 100 × 200 mm^2 [depth (D) × width (W)]. A height disparity between the upstream building (H_{UB}) and downstream building (H_{DB}) ranges between 3:1 and 0.33:1 to replicate the vertical variation in urban areas (Chen and Mak, 2021; Li et al., 2020; Park et al., 2019), with a separation distance of 100 mm between the two tandem buildings to simulate the closely spaced tall tandem buildings (Figure 5.1 (a)). This configuration is commonly observed in urban settings (Niegodajew et al., 2024) and numerous building clusters in Hong Kong exceed a height of 100 m and are positioned at a distance of less than one building width (To, 1995). All the tested building model dimensions are listed in Table 5.2. The test cases were categorized into three groups based on the vertical disparity between the two adjacent buildings: IH denotes a configuration with tandem buildings of identical height; SU represents a step-up building configuration, and SD signifies a step-down building configuration. Among the test cases, the building model had a maximum cross-sectional area of 0.12 m^2, which accounted for 2.4% of the cross-sectional area of the wind tunnel testing segment. The reduced scale model satisfies the requirement that the frontal area of the testing subject should not exceed 5% of the cross-sectional area of the wind tunnel testing section (Jeong et al., 2018; Engineers, 2012).

Table 5.2. Summary of all non-elevated test cases (in reduced scale).

(a) Identical-height building configuration				
Case name [Model type, H_{UB}]	**Upstream building height (H_{UB})**	**Downstream building height (H_{DB})**	H_{UB}/H_{DB}	**Remarks**
[IH, 200]	200 mm	200 mm	1/1	Identical-height building configuration
[IH, 400]	400 mm	400 mm	1/1	
[IH, 600]	600 mm	600 mm	1/1	
(b) Non-identical-height building configuration				
Case name (Model type, H_{UB}/H_{DB})	**Upstream building height (H_{UB})**	**Downstream building height (H_{DB})**	H_{UB}/H_{DB}	**Remarks**
[SU, 2/3]	400 mm	600 mm	2/3	Step-up building configuration
[SU, 1/3]	200 mm	600 mm	1/3	
[SU, 1/2]	200 mm	400 mm	1/2	
[SD, 3/2]	600 mm	400 mm	3/2	Step-down building configuration
[SD, 3/1]	600 mm	200 mm	3/1	
[SD, 2/1]	400 mm	200 mm	2/1	

5.2.2 Wind tunnel setup

5.2.2.1 Simulation of the twisted wind flows

The twist vanes were mounted upstream of the center of the turntable to simulate the wind profiles with required mean wind velocities, turbulence intensities, and yaw angles. Based on the Ekman spiral theory, the twisted angle is determined by the angle formed between the lateral and longitudinal components of the wind velocity, as the Equation (5.1).

$$\theta = \tan^{-1}(\frac{v}{u}) \tag{5.1}$$

It is important to mention that an excessive degree of twisting may result in undesired reflection of twisted flow off the wind tunnel wall (Chen et al., 2023), therefore, the maximum yaw angle chosen in this chapter was 30°. Two 1.3 m tall twist wooden vanes with twist angles of 15° and 30° were used to simulate 'low' and 'high' twisted wind conditions (Figure 5.2).

The maximum guiding angle was observed at the ground level, gradually decreasing to 0.9 m in height. To prevent the formation of undesirable eddies caused by vane edges reaching the test area on the turntable, a straight wooden board was utilized to account for the remaining 0.4 m of height. The production of the twist vanes follows the system proposed by Tse et al. (2017).

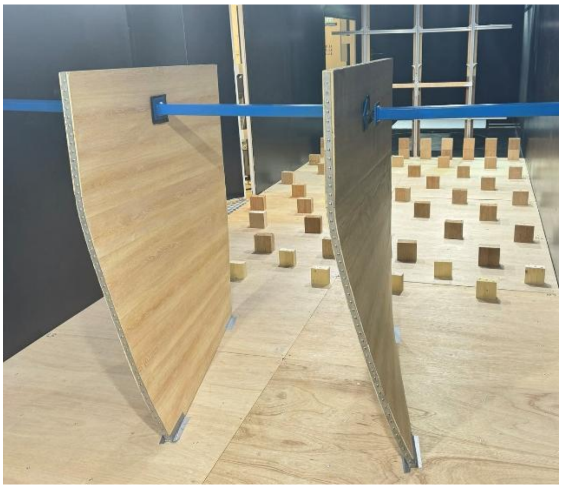

(a)

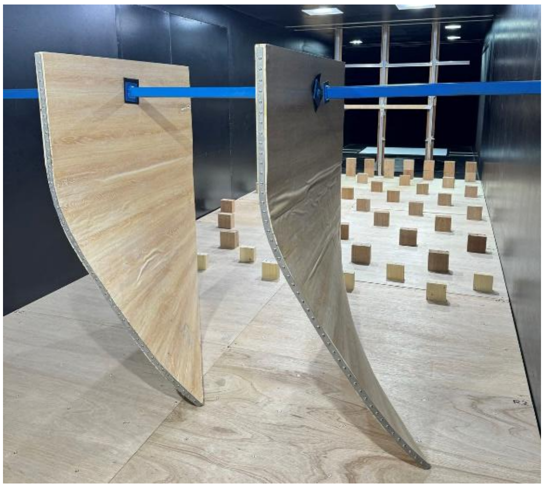

(b)

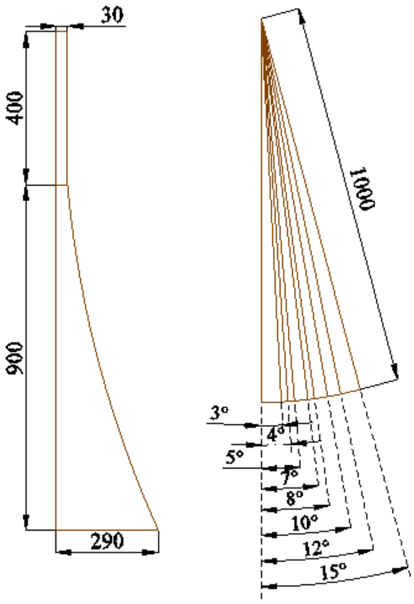

(c)

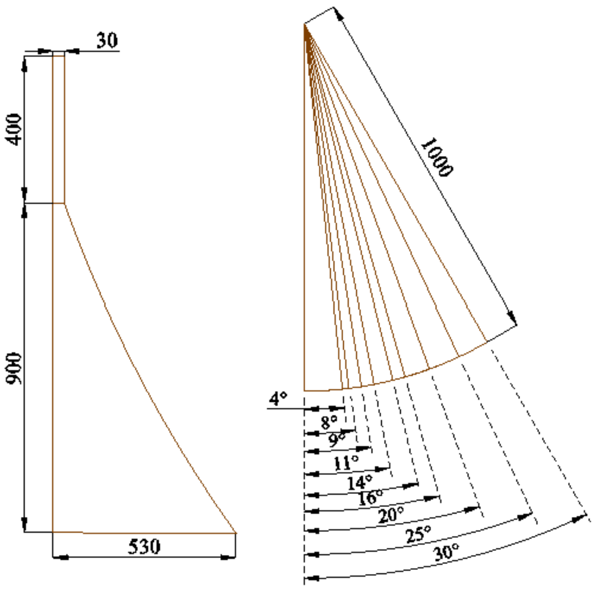

(d)

Figure 5.2. Two twist wooden vanes setup in the wind tunnel with maximum guide angles of (a) 15° and (b) 30° and the schematic diagram of twist vanes of (c) 15° and (d) 30°.

The placement of twisted vanes close to the inlet may impede the complete development of turbulence (Chen et al., 2023). Therefore, to accurately simulate the twisted winds, twist vanes were strategically positioned 3 m upstream of the centre of the turntable after conducting preliminary testing, as depicted in Figure 5.2. Two identical vanes were placed across the width of the wind tunnel to ensure stable and uniform flow properties within the designed test region. All the twist vanes were installed by screw rods for horizontal and vertical fixation. It is worth mentioning that the twisted wind profile was labeled as TWP while the conventional wind profile was labeled as CWP. The conventional wind profile and twisted wind profile were measured using a TFI Series 100 Cobra probe and transverse system, the Cobra probe can measure wind speeds within the 2 ms^{-1} to 100 ms^{-1} with an accuracy of $\pm$ 0.5 ms^{-1}. The vertical profiles of the time-averaged streamwise velocity (U/U_H) and turbulence intensity measured at the center of the turntable are illustrated in Figure 5.3 (a). The reproduced wind profiles (TWP 15 and TWP 30) exhibited similar mean wind velocity and turbulence intensity profiles with the conventional wind profile (CWP). The simulated profiles followed the power-law model with a coefficient of 0.15 and the wind velocity profiles are normalized using the mean wind velocity of 6.53 ms^{-1} at a height of 0.6 m, where the measured turbulence intensity is approximately 7% (Figure 5.3 (a)). The aerodynamic roughness length z_0 and friction velocity u^* of the wind tunnel were 0.00025 m and 0.37 m/s by logarithmic law curve fitting of the wind profile (Gromke et al., 2008). The building Reynolds number was 2.6×10^5 determined by H (0.6 m) and U_H (6.53 m/s). It is noteworthy that the twist angles measured at a height of 1 cm were found to be 13° and 25° at the center of the turntable, corresponding to twist vane angles of 15° and 30°, respectively (Figure 5.3 (b)). Therefore, the simulated twisted wind angles are referred to as TWP 13 and TWP 25 while the conventional wind profile is referred to as CWP. The velocity spectrum at heights equivalent to 200 mm, 400 mm, and 600 mm, as depicted in Figure 5.4, demonstrates an alignment with the Von Karman spectrum observed at the boundary layer height. Figure 5.5 illustrates the wind and turbulence intensity profiles observed at three distinct measurement locations within the measurement areas.

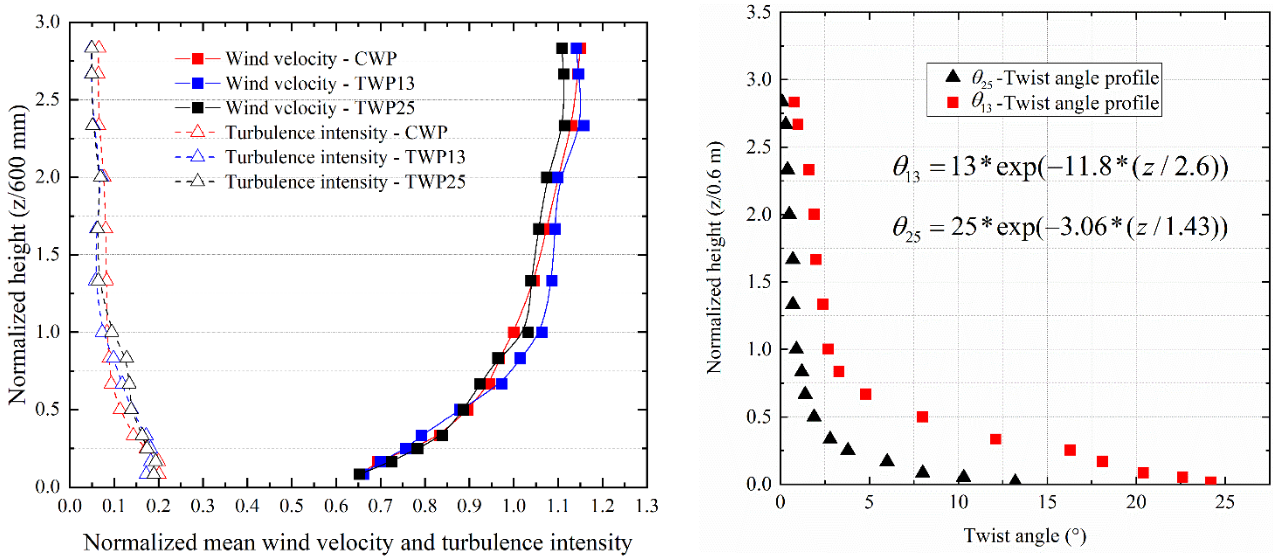

(a) (b)

Figure 5.3. (a) Wind velocity and turbulence intensity profiles and (b) Twist angle profiles.

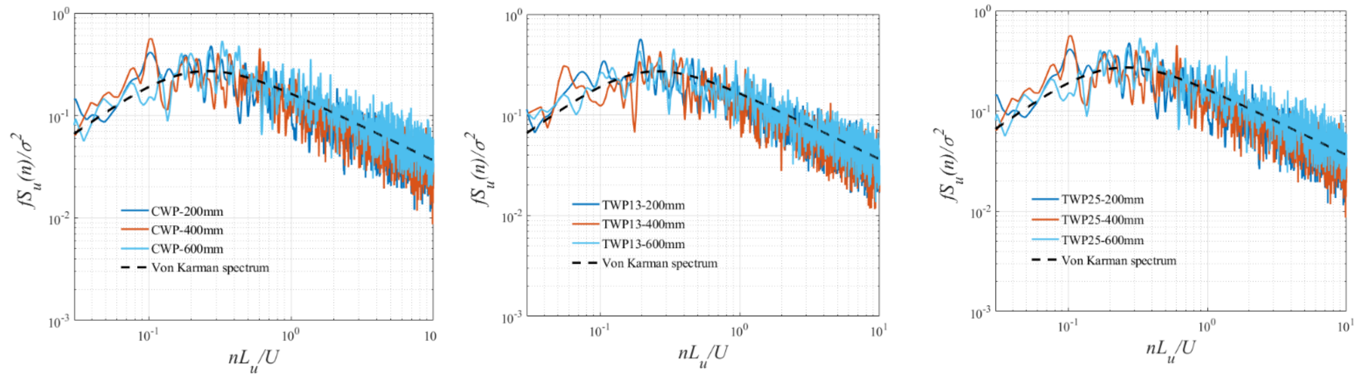

(a) (b) (c)

Figure 5.4. Longitudinal velocity spectra at different heights under (a) CWP, (b) TWP 13, and (c) TWP 25.

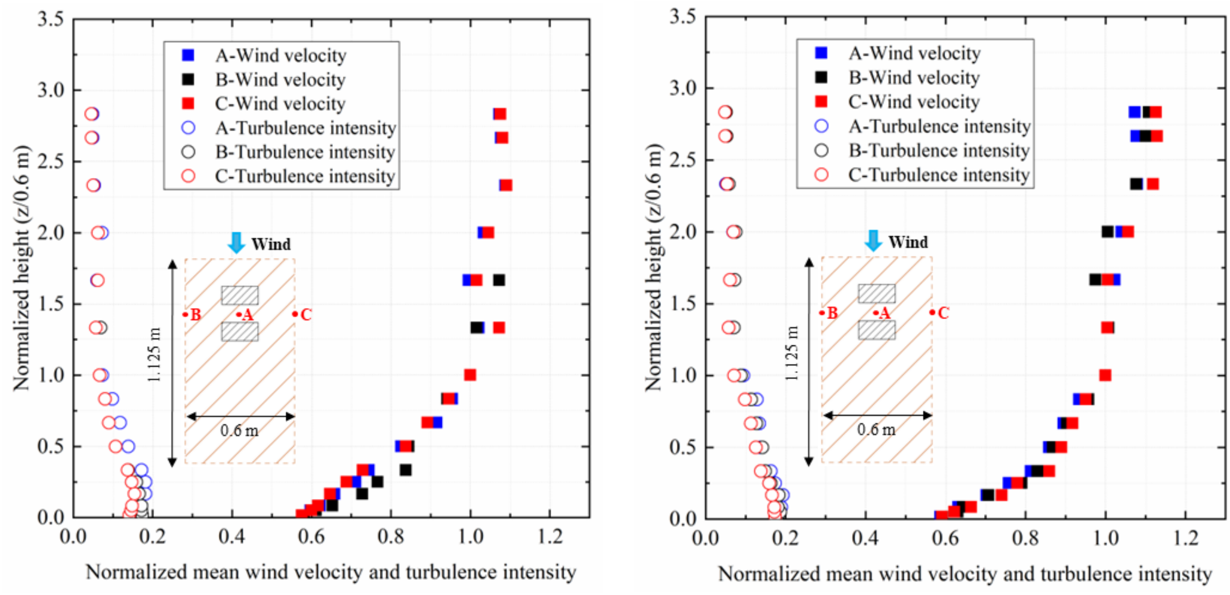

(a) (b)

Figure 5.5. Normalized wind velocity and turbulence intensity profiles at three locations for (a) TWP 13 and (b) TWP 25.

5.2.2.2 Measurements

For measurements of horizontal distributions of the wind velocity at the pedestrian level, the wind velocities at 1 cm above the ground of the wind tunnel were measured using 72 thermistor sensors (KANOMAX, Model 0965-07) at a sampling frequency of 10 Hz. Every velocity sensor was accompanied by a temperature compensator unit to rectify any potential influence of the temperature on the velocity measurements. These sensors have an accuracy of ±0.01 m/s within the range of 0-9.99 m/s and were connected to a multichannel system (KANOMAX, Model 1560). The acquired data was subsequently processed using KANOMAX data processing software. The discrete velocity measurements of the KANOMAX sensor were arranged in both longitudinal and lateral directions, which have been successfully employed in previous wind tunnel experiments to describe the flow field with high accuracy at pedestrian-level height (Tsang et al., 2012; Xia et al., 2015; Zhang et al., 2017). The KANOMAX thermistor sensors were calibrated using the wind velocity measured by the reference air velocity transducer (Air Velocity Transducer 8455 Series (TSI 8455-150-1)) prior to testing, with a deviation of less than 5% (Figure 5.6). The accuracy of the reference air velocity transducer was checked against the MKS AD06A Baratron® Differential Pressure Sensor in regular intervals. Figure 5.7 (a) demonstrates the arrangement of twist vanes, building models, and the corresponding measurement area. The arrangement of the KANOMAX sensor surrounding the two tandem buildings was determined based on the resolutions of measurement points, the capacity of experimental equipment, and operational stability. Figure 5.7 (b) shows the Kanomax sensor displacement around the buildings, the minimum separation distances along the longitudinal and transverse axes were established at 75 mm and 100 mm, respectively, which satisfied the minimum separation distances requirement proposed by Wu and Stathopoulos (1994) to reduce the interference effects of surrounding sensors. The sensor arrangement was positioned to extend 300 mm upstream, 825 mm downstream, and 300 mm from the center of the turntable on either side. This resulted in a total measurement area of 600 mm by 1125 mm with fine resolution near the building but gradually decreasing resolution downstream. The Kanomax measurement readings were taken for 120 seconds at a sampling frequency of 10 Hz to obtain statistically stationary values. The complete experiment setup, including the installation of vanes and a building model in the wind tunnel, is illustrated in Figure 5.7 (c). Regarding instrument accuracy, the Kanomax sensors typically have a tolerance of $\pm 1\%$ of the mean wind velocity. The combined uncertainty for the mean wind velocity is generally within $\pm 3\%$ of the mean wind velocity, accounting for instrument accuracy, calibration error, probe positioning, as well as environmental factors such as temperature and turbulence.

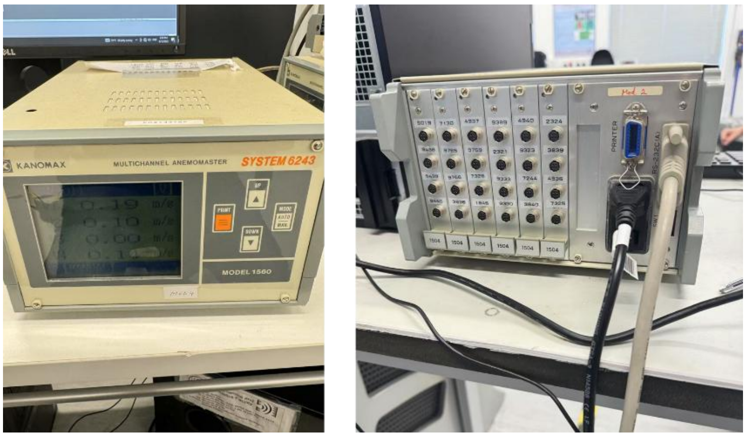

(a)

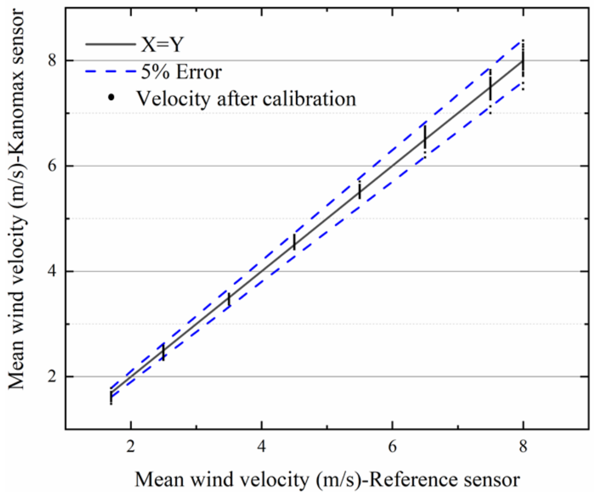

(b)

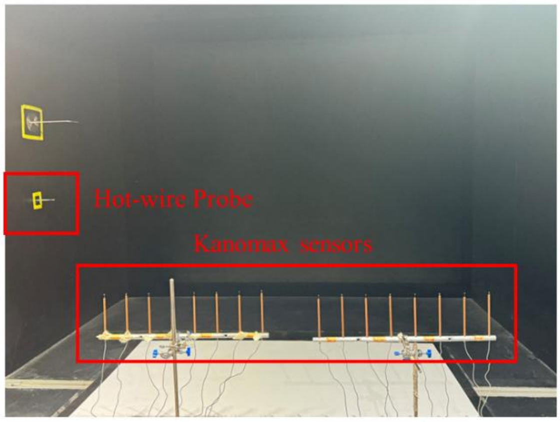

(c)

Figure 5.6. (a) Kanomax multi-channel data acquisition and Kanomax sensor calibrations for (b) Calibration results, (c) Calibration photos.

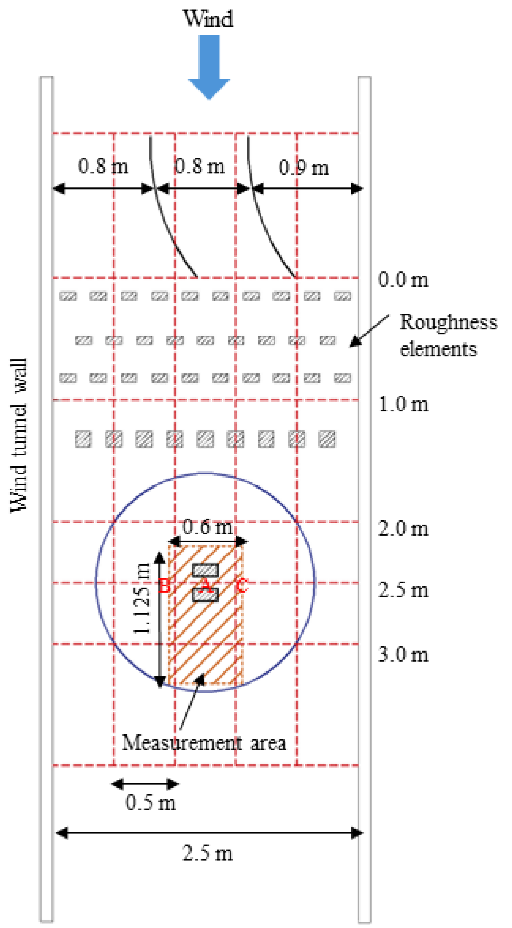

(a)

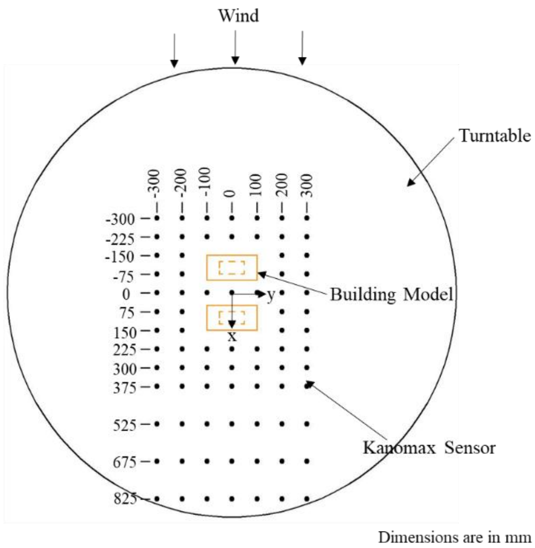

(b)

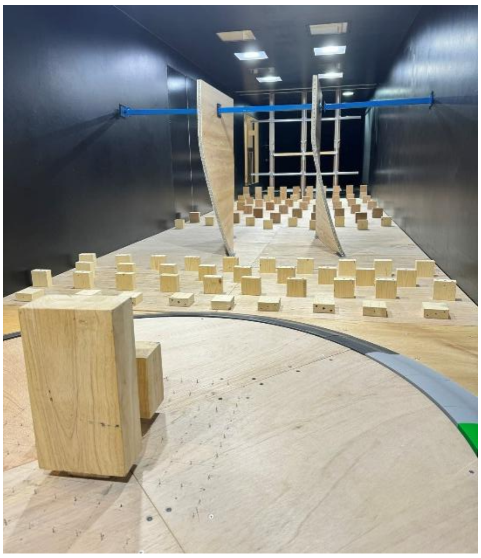

(c)

Figure 5.7. Schematics of (a) Arrangement of twist vane and measurement area, (b) Arrangement of Kanomax sensors surrounding the building models (Dimensions in mm), and (c) Experimental setup with twist vane system and building models.

5.3 Assessment method for wind and thermal comfort

The normalized wind velocity ratio *K*, defined as the ratio between the mean wind velocity at pedestrian-level height (2 m in full scale) and the mean wind velocity at the same location without the presence of a building model, has been effectively utilized to characterize the wind environment at the pedestrian level (Equation (5.2)) (Tse et al., 2017). Additionally, the PLW velocities measured in the wind tunnel were converted to the corresponding wind velocity in a specific wind climate based on the Equation (5.2) (Zhang et al., 2017; Zhang et al., 2020), taking into account the discrepancies between the simulated wind profile in the wind tunnel experiment and that from the specific weather climate.

$$\left.\begin{aligned}
K_{WT} &= \left(\frac{U_{2m}}{U_{2m,absence,WT}}\right)_{\alpha_{WT}} \\
K_{WC} &= \left(\frac{U_{2m}}{U_{ref}}\right) \\
K_{WC} &= \left(\frac{U_{2m}}{U_{2m,absence,WT}}\right)_{\alpha_{WT}} \times \left(\frac{U_{2m}}{U_{ref}}\right)_{\alpha_{WC}} \\
K_{WC} &= \left(\frac{U_{2m}}{U_{2m,absence,WT}}\right)_{\alpha_{WT}} \times \frac{U_G\left(\frac{2}{z_G}\right)^{\alpha_{WC}}}{U_G\left(\frac{H_{ref}}{z_G}\right)^{\alpha_{WC}}} \\
K_{WC} &= \left(\frac{U_{2m}}{U_{2m,absence,WT}}\right)_{\alpha_{WT}} \times \left(\frac{2}{H_{ref}}\right)^{\alpha_{WC}} \\
K_{WC} &= K_{WT} \times \left(\frac{2}{H_{ref}}\right)^{\alpha_{WC}}
\end{aligned}\right\} \qquad (5.2)$$

The normalized mean wind velocity in the wind tunnel and the specified wind climate, denoted as K_{WT} and K_{WC}, was calculated by considering both the wind velocity at 2 m and the wind velocity at the same location without the building models. U_{2m} is the mean wind velocity at 2 m (1 cm in experiment scale) and $U_{2m,absence,WT}$ is wind velocity at the same location without the building models. α_{WT} is the power-law exponent of the wind profile in the wind tunnel and α_{WC} is the power-law exponent of the wind profile from the specified wind climate. U_{ref} is the velocity at the reference height, and H_{ref} is the reference height, z_G is 500 m, which is considered as the gradient height in Hong Kong (Zhang et al., 2017), U_G is the mean wind velocity measured at 500 m. Similar to Chapter 3, the PLWEs surrounding the two tandem buildings were comprehensively evaluated by selecting two distinct wind climates, including both weak and windy climates. The converted wind velocities were subsequently utilized to evaluate the PLWEs surrounding two tandem buildings, based on the wind comfort criteria proposed by Zhang et al. (Zhang et al., 2017) for weak wind conditions (Table 5.3) and by Lawson (Lawson, 1978) for windy wind conditions (Table 3.3). The K_{200} is defined as the ratio between the mean wind velocity at pedestrian level and the mean wind velocity at 200 m. The area ratio (AR_{WC}) of the target comfort zone is defined to quantify the size of different wind comfort zones around two tandem buildings under CWP and TWPs, similar to the method described in Chapter 3 Equation (3.8).

Table 5.3. Wind comfort criteria proposed by Zhang et al. (Zhang et al., 2017).

Comfort level	Threshold velocity	K_{200}
Low wind velocity	<1.6	<0.3
Acceptable	1.6-3.5	0.3-0.7
High wind velocity	3.5-5	0.7-1
Unacceptable	>5	>1

The Physiological Equivalent Temperature (PET) is a widely employed thermal comfort index based on the Munich Energy-balance model for individuals (MEMI). Various PET values demonstrate different heat/cold stress and thermal perception levels. Du et al. (2017) proposed an integrated approach that combines the measured thermal parameters from on-site measurements and wind velocity data from the wind tunnel experiment to determine PET values. Chen and Mak (2021) successfully combined the wind velocity data from the CFD simulation and adopted thermal parameters from a Hong Kong university campus to evaluate the thermal comfort around two buildings. The subjective thermal perception range sets modified by Li and Matzarakis (2008) for subtropical Taiwan were adopted in this chapter (Table 5.4), considering the similar weather conditions shared between Taiwan and Hong Kong.

Table 5.4. Thermal sensations and PET classes for Taiwan (Lin and Matzarakis, 2008).

Thermal sensation	PET range for Taiwan ($^{\circ}C$)
Very cold	14<
Cold	14-18
Cool	18-22
Slightly cool	22-26
Neutral	26-30
Slightly warm	30-34
Warm	34-38
Hot	38-42
Very hot	>42

Table 5.5. Measured thermal parameters and personal data (Du et al., 2017).

	Sunny day in summer	Sunny day in winter
Thermal parameters		
Air temperature ($T_a, ^{\circ}C$)	32.8	25.4
Relative humidity ($RH, \%$)	86.7	55.2
Mean radiation temperature ($T_{mrt}, ^{\circ}C$)	58.6	52.5
Personal data		
Pedestrian age	35 years old	
Pedestrian height	175 cm	
Pedestrian weight	75 kg	
Internal heat production	69.8 W	
Closing level	0.3	0.7

The PET thermal analysis was performed using the RayMan Pro 3.1 software (Deevi and Chundeli, 2020; Ribeiro et al., 2022), with meteorological data employed as the input (air temperature, wind speed, relative humidity, and mean radiant temperature) (Liu et al., 2016). The wind velocity for PET calculation was determined by $K_{WC} \times U_{ref}$, where U_{ref} = 5 m/s is the reference wind velocity at 200 m over Hong Kong, and K_{WC} values could be converted from K_{WT} measured in the wind tunnel based on the Equation (5.2). The thermal parameters, including air temperature (T_a, $^\circ C$), relative humidity (RH, %), and mean radiation temperature (T_{mrt}, $^\circ C$) were obtained on the field survey from Du et al. (2017) that collected meteorological data from two sunny days in Hong Kong, as listed in Table 5.5.

5.4 Results and discussion

5.4.1 Modification of the flow field by twisted wind profile

The velocities need to be converted due to the disparity between the simulated wind profile in the wind tunnel experiment and that of the Waglan Island meteorological station, as the Equation (5.3) (Zhang et al., 2020). The power-law exponent (α) utilized in this chapter corresponds to the α value derived from the mean wind profile measured at Waglan Island, which is 0.15.

$$K = K_{2m} \times (2/200)^{\alpha} = K_{2m} \times 0.5 \tag{5.3}$$

To characterize the alteration of LWV and HWV area across various building configurations, the area percentage for LWV and HWV was estimated by calculating the area-weighted average of zones with *K*<0.3 and 0.7<*K*<1, respectively, relative to the total area of interest, as described in the Equation (5.4).

$$\left.\begin{aligned}\text{Area Percentage (AP)}_{LWV} &= \frac{A_{LWV}}{A_T} \times 100\% \\ \text{Area Percentage (AP)}_{HWV} &= \frac{A_{HWV}}{A_T} \times 100\%\end{aligned}\right\} \tag{5.4}$$

where A_{LWV} is the area of low wind velocity (K<0.3), A_{HWV} is the area of high wind velocity (0.7<K<1), and A_T is the total area of the research region (i.e., 0.6 m × 1.125 m).

The general flow field variation induced by CWP, TWP 13, and TWP 25 is depicted in Figure 5.8. Two low wind velocity zones are defined as the Upstream Low Wind Velocity (USLWV) zones and Downstream Low Wind Velocity (DSLWV) zones. Due to the narrow inter-building gaps (20 m), the downstream building becomes fully submerged in the wake of the upstream building, while the separated shear layer from the upstream building interacts with and initiates a downstream rolling motion along the sides of the downstream building. Notably, the upstream structure exhibits a significant amplification of wind velocity, whereas the downstream structure experiences negligible enhancement in wind velocity. The twisted wind profile induces an asymmetric flow field surrounding the central line, in contrast to the symmetrical flow field generated by conventional wind profiles. To be more precise, TWP results in an asymmetrical wind environment at the pedestrian level due to (1) the deviation of downstream low-wind velocity zones from the center line of the building, (2) the asymmetric distribution of corner stream with a noticeable presence of region with relatively higher wind velocity on the right side of the building, (3) the formation of regions with relatively lower wind velocities on the left side of the building.

The K value magnitude and distribution under both CWP and TWPs are influenced by the various locations of elevated structures (Figure 5.9), the WS case generates a larger area of LWV compared to ELE and LS cases due to the presence of downstream near-field low wind velocity (DNLWV) zones on the leeward side of the downstream building. When positioned downstream, elevated buildings can effectively eliminate these areas of low velocity (Figure 5.9). In contrast, the LS case yields a smaller LWV area due to the increased extent of the corner stream caused by the separated shear layer around the buildings, thereby impacting more surrounding areas compared to the ELE case. It is important to highlight that the space beneath the elevated building has been excluded from this chapter to ensure a fair comparison between these building configurations.

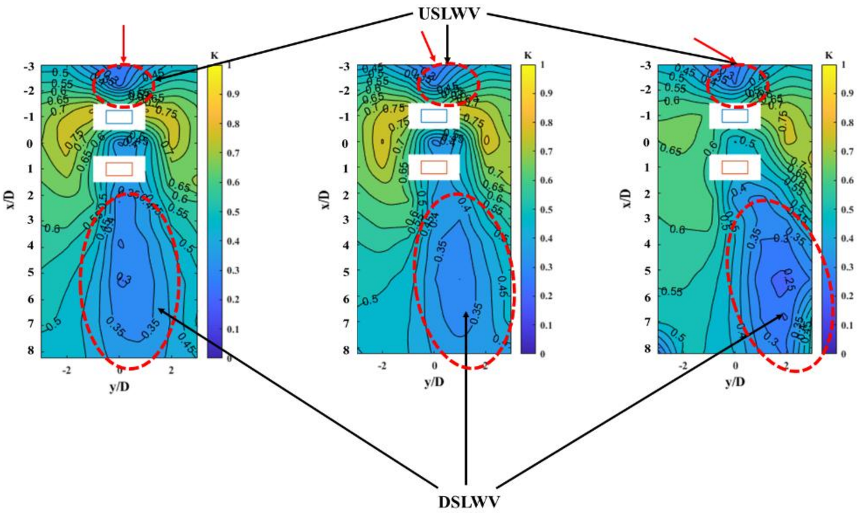

(a) (b) (c)

Figure 5.8. Distribution of *K* value around two 120 m buildings in tandem arrangement with 20 m building gaps in (a) CWP, (b) TWP 13, and (c) TWP 25.

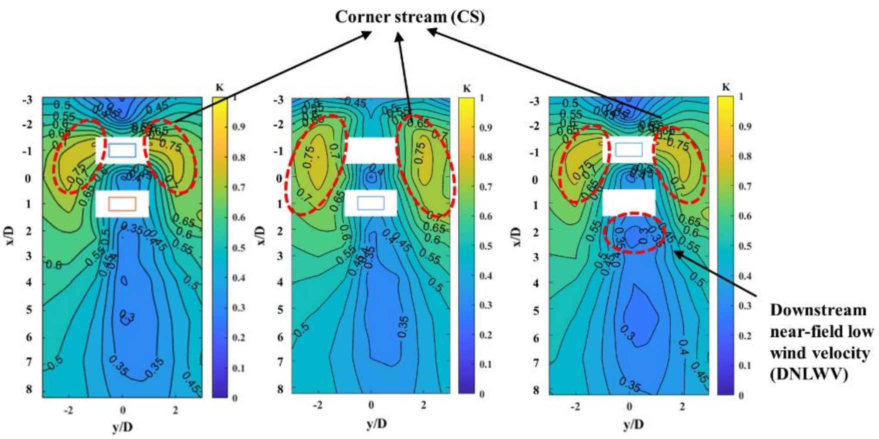

(a)

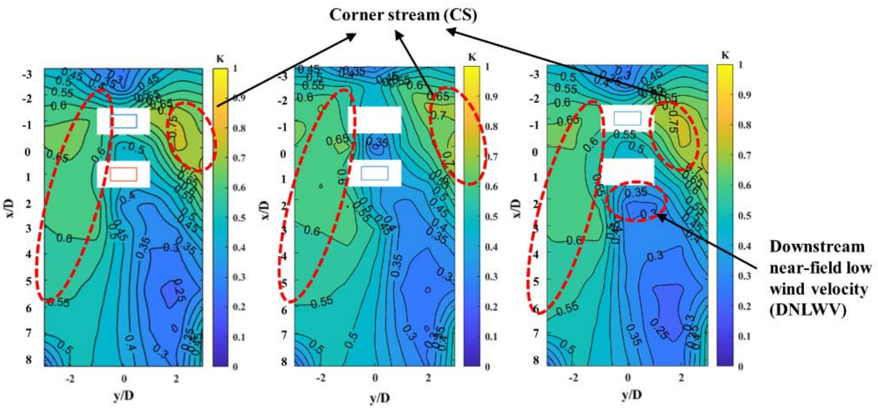

(b)

Figure 5.9. Distribution of *K* value around two buildings with 120 m height under (a) CWP and (b) TWP 25 for various elevated structure locations.

5.4.2 Variation of *K* values in the vicinity of two elevated buildings in tandem arrangement

5.4.2.1. Variation of *K* values with identical building height

Figure 5.10 demonstrates a strong correlation between building height and the variations in flow field features. The corner streams of a taller upstream building, for instance, exhibit a more pronounced magnitude compared to those of a shorter upstream building. Additionally, as the height of the building increases, the DSLWV region is displaced further from the downstream building due to the intensified vertical circulation resulting from taller structures. These circulations converge on the ground at a considerable distance away from the leeward side of the downstream building (Tse et al., 2017; Tsang et al., 2012). With the increase in building height, the upstream migration of the USLWV occurs due to intensified downwash flow, thereby amplifying wind velocity ahead of the structure. Another striking feature is that the velocity between two buildings increases as the building height increases, owing to the pronounced downwash effect caused by the upstream building. The aforementioned phenomena have been observed in both CWP and TWPs.

Apart from these common flow features caused by variations in height, the rightward twisting of the flow field becomes more pronounced when the building's height is low. The high-wind velocity region, resulting from the intense separation layer in front of the upstream elevated building, also deviated from the center line due to the twisted wind profile attacking the building at varying angles along the horizontal plane and deflecting flows of different magnitudes. With the anticlockwise twisted wind profile simulated in this chapter, a greater volume of wind as redirected toward the right side of the building compared to the left side. The separation layer on the right side is more prominently observed, while the corner stream on the left side exhibits a smaller magnitude yet exerts a larger influence over the surrounding regions in the area. The recirculation zone, characterized by low wind velocities, is closely associated with an unfavourable wind environment and a concentration area of pollutants. The deflection angle of the recirculation zone was reduced due to the presence of the downstream building, compared to isolated buildings (Zhou et al., 2021; Tse et al., 2017).

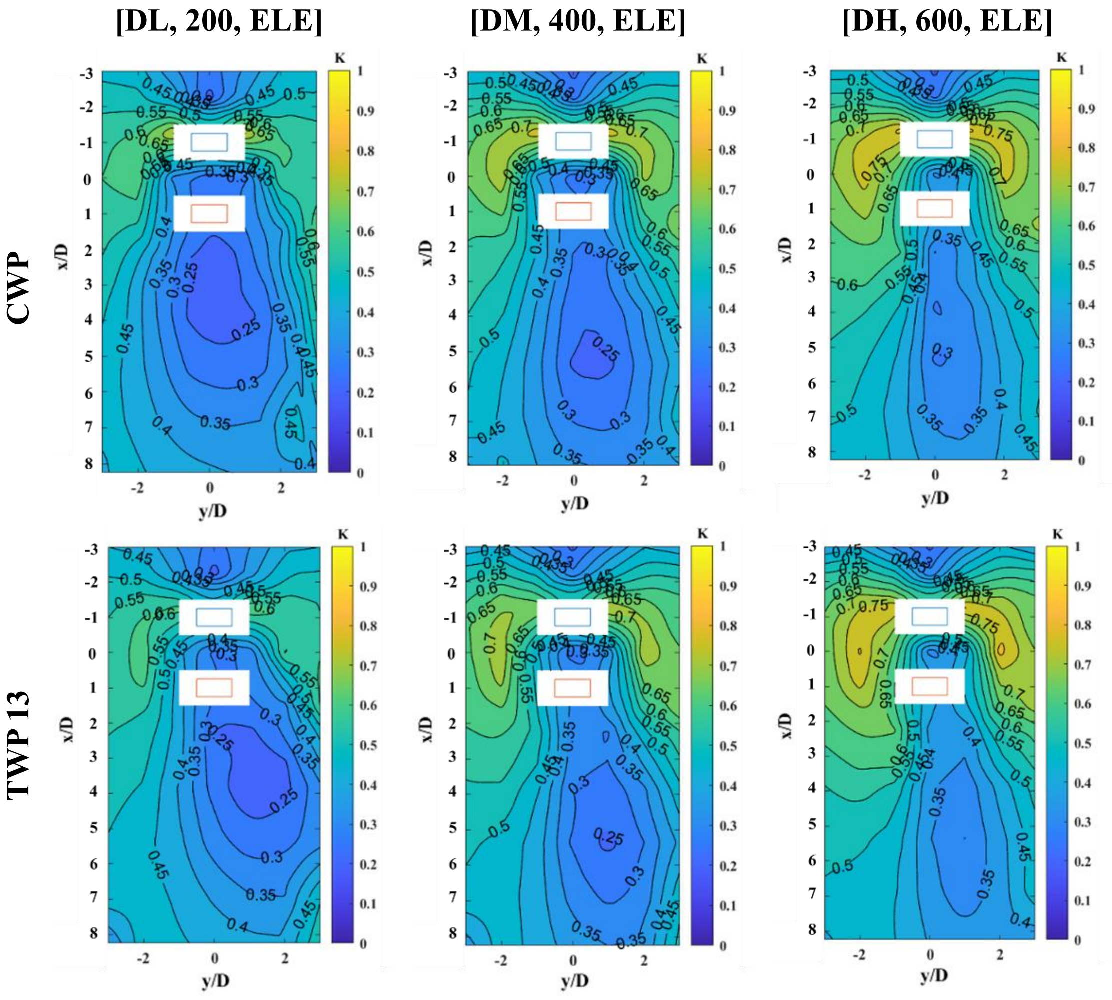

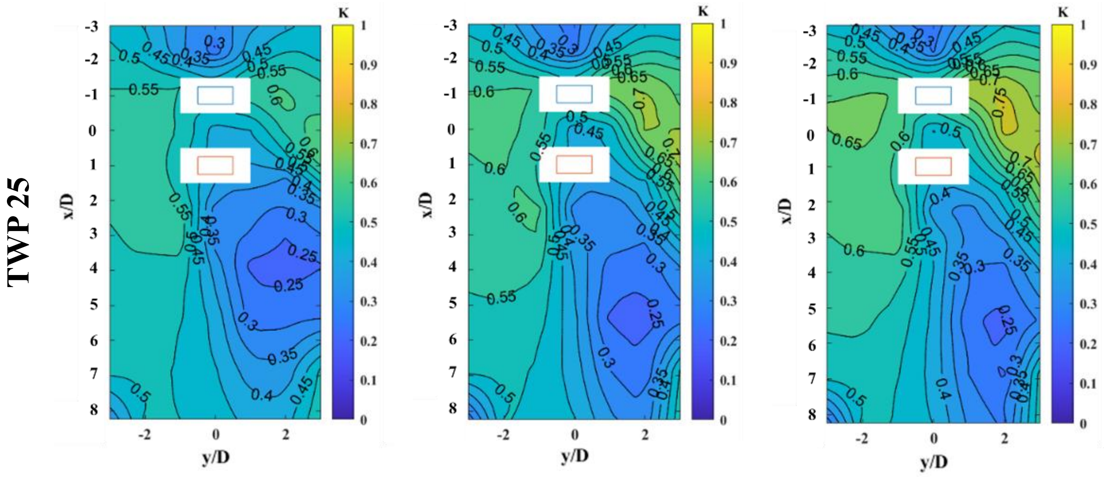

Figure 5.10. Distribution of *K* value near two elevated buildings in tandem arrangement.

5.4.2.2 Variation of *K* values with non-identical building height

Figure 5.11 illustrates the *K* value distribution for step-up and step-down elevated building configurations. The relative height between the two elevated buildings significantly affects the surrounding PLWEs. In the case of step-up building configurations ([DH, 400, ELE], [DH, 200, ELE], and [DM, 200, ELE]) shown in Figure 5.11, the *K* distribution exhibits distinct patterns compared to the two elevated buildings with identical heights. The wind velocity between buildings is primarily influenced by the height of the upstream building. Instead of manifesting at the corner of the upstream building (Figure 5.10), two distinct regions characterized by high wind velocities emerge within the interstitial space between the two buildings, with an increase in wind velocity observed as the relative height difference between them escalates. The interaction between these two regions of high wind velocity and the downstream elevated building generates a dynamic flow that traverses the elevated area beneath the structure, resulting in the formation of an additional two regions of heightened wind velocity behind the downstream structure. This occurrence is attributed to the obstruction of incoming wind by taller downstream buildings, resulting in a pronounced downwash flow through the gaps between two buildings. Consequently, when this flow interacts with the throughflow from upstream, it leads to significantly higher velocities at the gaps between buildings and on the leeward side of the downstream building. Conversely, the height of the downstream building influences the extent of the DSLWV area, as a higher downstream building results in an increased area of the DSLWV on the leeward side.

The K value distribution around the two buildings in step-down building configurations ([DM, 600, ELE], [DL, 600, ELE] and [DL, 400, ELE] (see Figure 5.12)), exhibits similarities to that of the two elevated buildings with identical heights (Figure 5.10), a high-velocity region is observed at the corner side of the upstream elevated building. In the case of a step-down building configuration with H_{UB}/H_{DB}=3/1, the downwash flow generated by the upstream building induces a vortex in the inter-building gaps, causing flow divergence within the lower region of the downstream building. As H_{DB} increased, minimal changes were observed in the wind velocity at the center of the two elevated buildings. This is analogous to the step-up structure, further demonstrating that the wind velocity between two buildings is primarily influenced by the height of the upstream building and less affected by the height of the downstream building. The step-up building configuration (Figure 5.11) leads to a shift of the two regions with high wind velocities towards to right side, resulting in an amplification of wind velocity at the right side of the building gaps while decreasing it at the left side. The discrepancy in K value between the left and right sides of the building gap becomes more pronounced under TWPs as the vertical disparity between the two tandem buildings increases. Specifically, the highest K value differences (ΔK) between the right and left sides of the corner stream around the upstream building are 0.3, 0.25, and 0.05 when H_{UB}/H_{DB} is 1/3, 1/2, and 1/1, respectively under TWP 25 ([DH, 200, ELE], [DM, 200, ELE] and [DL, 200, ELE]). The findings indicate that the impact of twisted wind on the wind field becomes more pronounced in the presence of height heterogeneity, resulting in an amplified discrepancy in wind velocities between the two ends of the building. In contrast to upstream flow features, DSLWV zones downstream of step-up building configurations are substantially shifted to the right side of the buildings due to the oblique wind incidence of TWPs. Moreover, as the wind turning angle increases, such as TWP 25, which exhibits the highest wind twist angle, a larger deviation of DSLWV is observed compared to TWP 13 for all models. The impact of TWPs on step-down building configurations exhibits a similar trend to that observed in the case of two elevated buildings with the same height (Figure 5.12). It is noteworthy that the ΔK between the left- and right-side corner streams remains constant at 0.1 when H_{UB}/H_{DB} is set to 3/1, 2/1, and 1/1, thereby demonstrating that variations in building height have minimal impact on the twisted wind phenomenon observed in step-down building configurations.

The variations of LWV and HWV wind condition areas for elevated buildings are illustrated quantitatively in Figure 5.13. The area of the LWV areas generated by TWPs is smaller than that in CWP, and this area continuously decreases with wind twists. The smaller low wind condition areas in TWPs can be attributed to the larger left-side corner stream areas, which expand due to wind twists. It is important to note that while the twisted wind displaces the high-velocity area (K>0.7) towards the right and reduces the wind velocity on the left side, velocities on the left side remain within the acceptable wind velocity range (0.3<K<0.7). However, due to their larger spatial extent compared to CWPs, the contribution of the left-side velocities to the overall LWV areas in TWPs is relatively less significant, thereby resulting in smaller low wind condition areas under TWPs. For wind conditions causing high wind velocities (K>0.7), both CWP and TWP 13 exhibit similar patterns of high wind velocity areas, while TWP 25 shows significantly lower areas associated with elevated wind velocities. The step-down building configuration demonstrates higher levels of high wind velocity conditions compared to the step-up building configuration. This analysis is consistent with the previous distribution of K values (Figure 5.11 (a) and (b)).

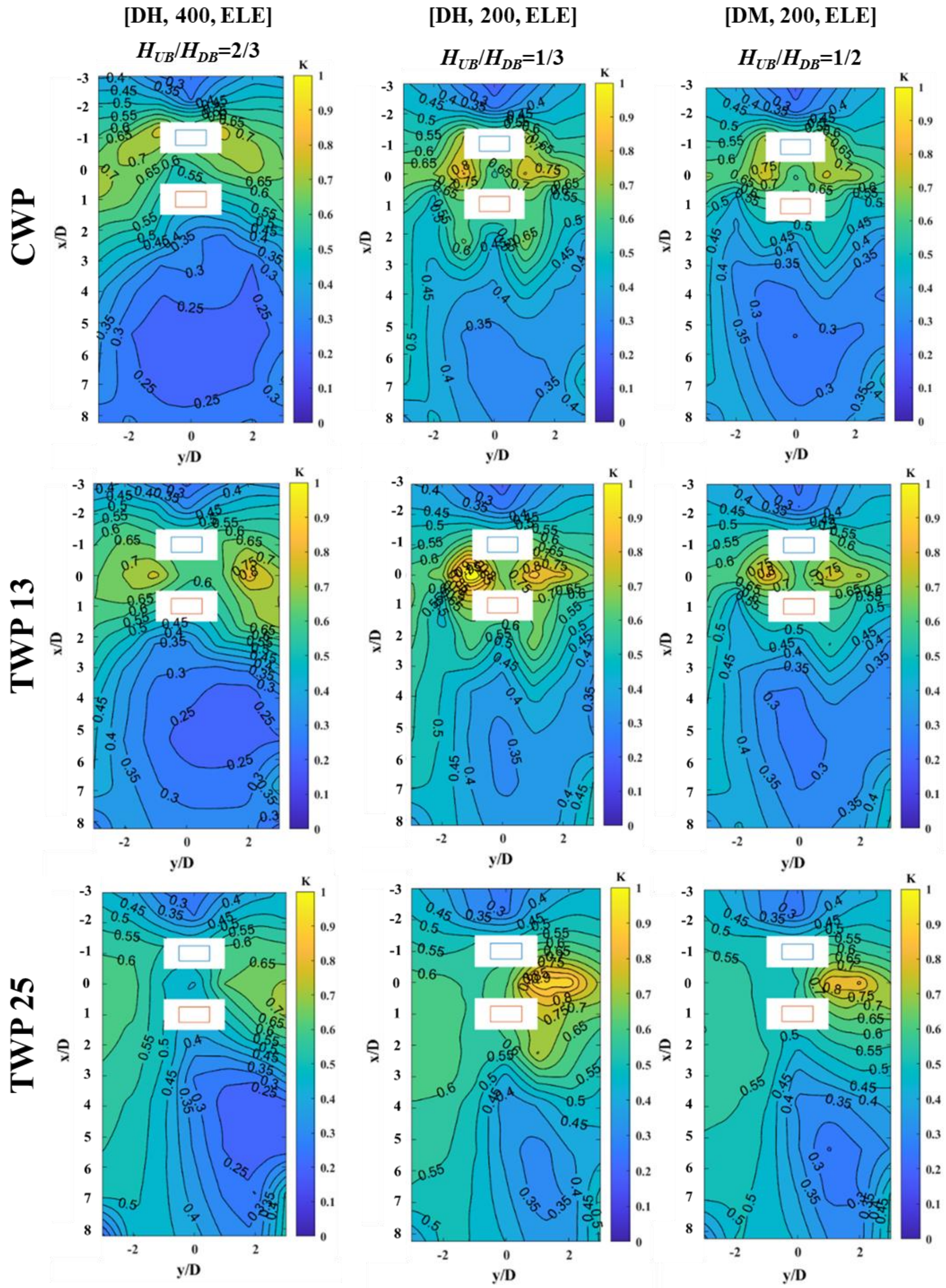

Figure 5.11. Distribution of *K* value near step-up tandem arrangement with non-identical building heights.

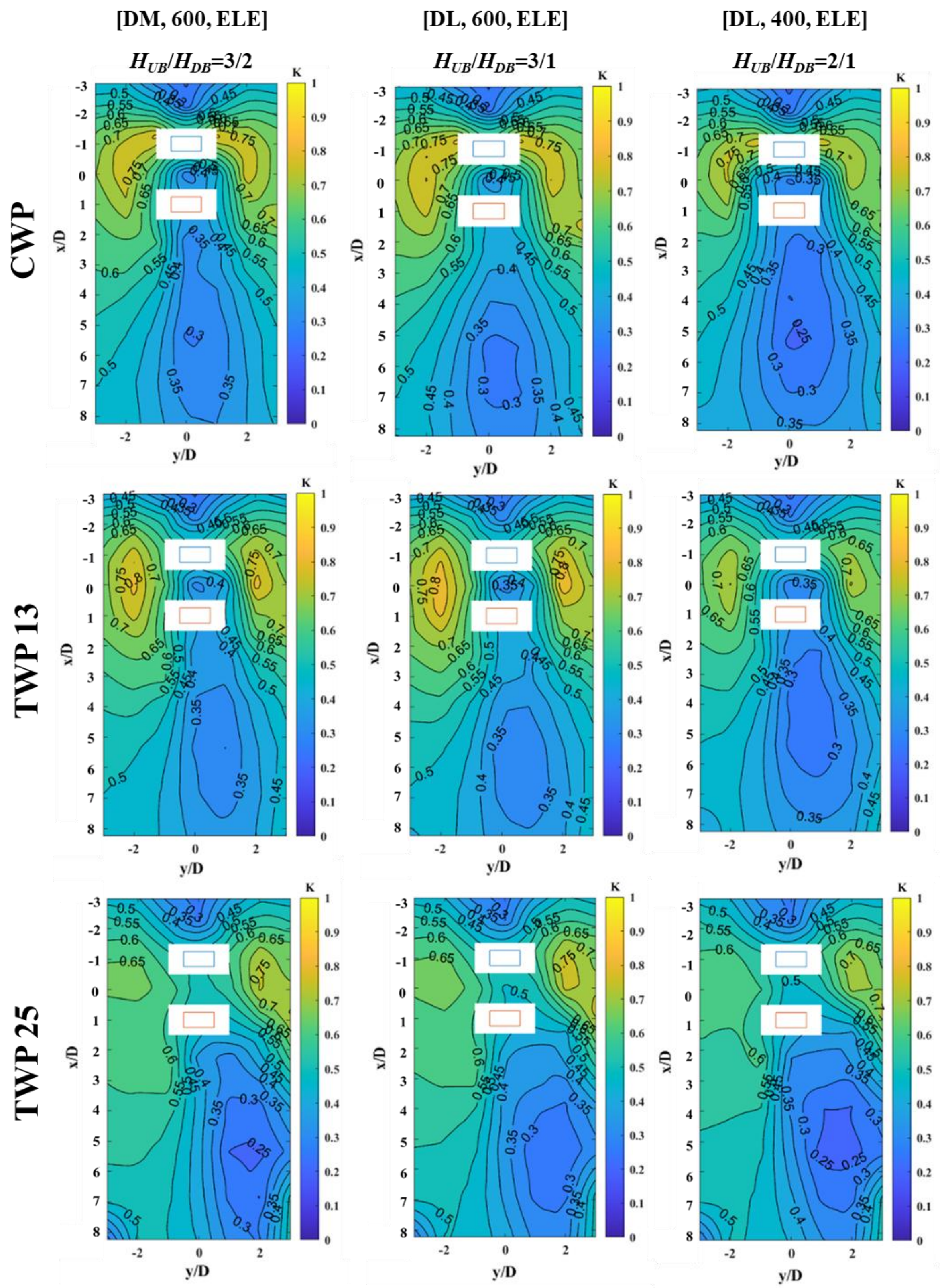

Figure 5.12. Distribution of *K* value near step-down tandem arrangement with non-identical building heights.

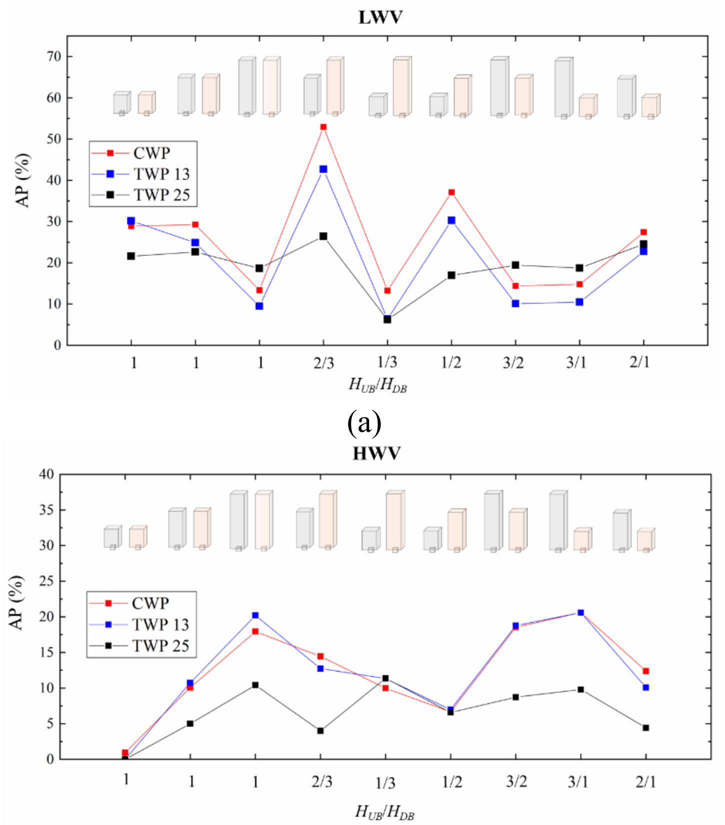

(a)

(b)

Figure 5.13. Area percentage of (a) Low wind velocity (K<0.3) and (b) High wind velocity (K>0.7) for two elevated buildings in tandem arrangement.

5.4.2.3 Variation of *K* values in the vicinity of two buildings with various elevated structure locations

The K distribution surrounding the two tandem buildings with various elevated structure locations is depicted in Figure 5.14 and Figure 5.15, where the upstream building remains non-elevated while the downstream building is elevated (LS cases). In contrast to the tandem arrangement of two elevated buildings (Figure 5.11), in the LS case, the USLWV tends to move further in the upstream direction due to the formation of a standing vortex at the front bottom of the upstream building and subsequent warping around the corners (Moonen et al., 2012). However, in the ELE case, when the flow hits the elevated columns, this phenomenon moves downstream, causing the USLWV region to move closer to the upstream building. The complete merging of the downstream building within the wake region of the upstream building results in a striking resemblance in flow patterns for both ELE and LS cases in the area behind the two tandem buildings. The wind environment modification near two buildings arranged in tandem, with the upstream building elevated and the downstream building non-elevated, is illustrated in Figure 5.15 (WS cases). A downstream near-field low wind velocity (DNLWV) area, characterized by reduced wind velocity in the vicinity of non-elevated downstream buildings, emerges and becomes increasingly prominent with taller downstream building heights, particularly for slender structures. This phenomenon is absent in cases involving elevated buildings (LS cases), suggesting that elevated structures effectively alleviate low wind velocity regions behind high-rise buildings, and the capacity of elevated buildings to enhance ventilation is also observed under TWPs. According to Figure 5.14 and Figure 5.15, the effects of TWPs on LS and WS cases with identical height are similar. It can be observed that wind twist has a more pronounced influence on shorter buildings, while the formation of the DSLWV region in the vicinity of two buildings exhibits dissimilarities under TWPs compared to CWP.

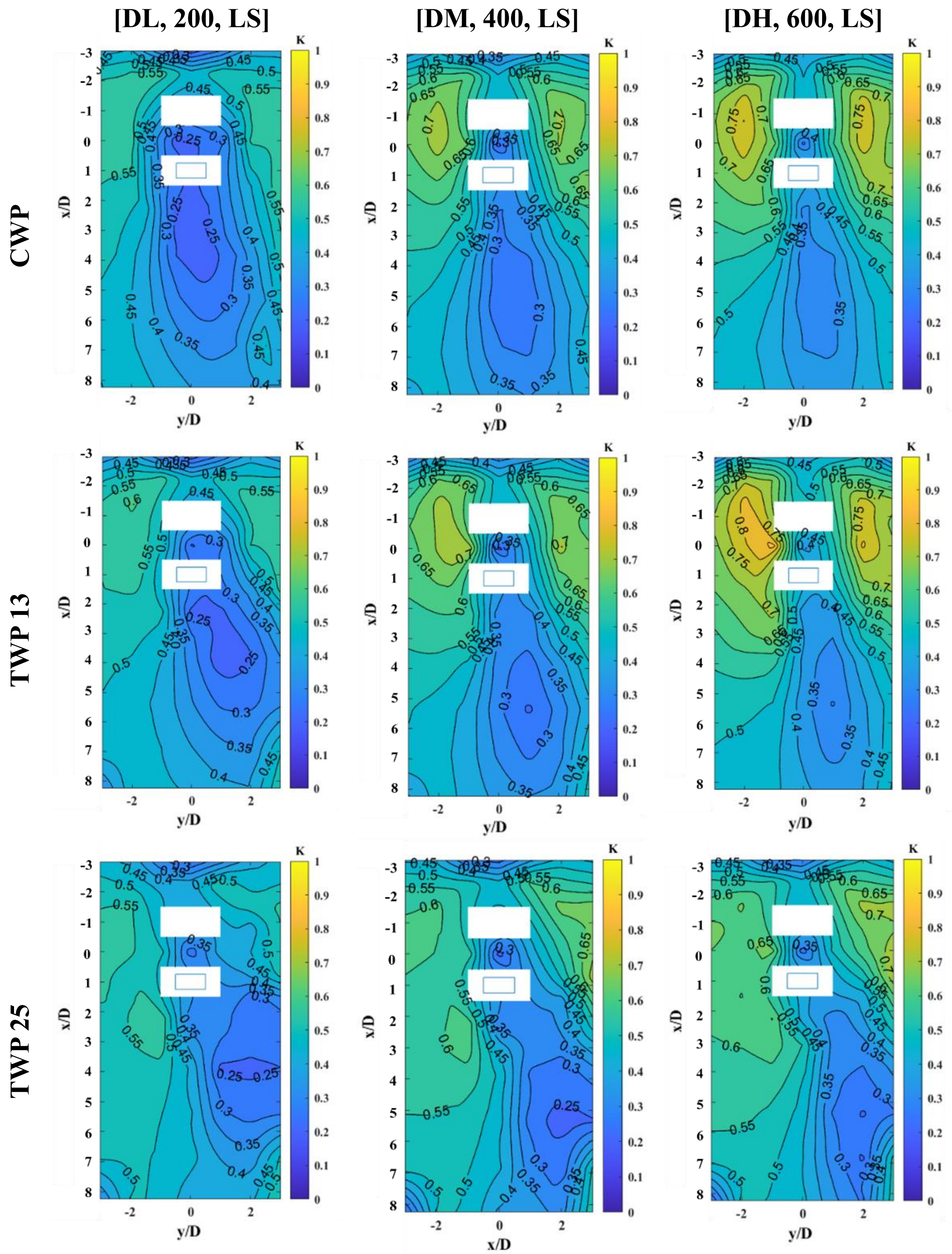

Figure 5.14. Distribution of *K* value near two buildings in tandem arrangement with the elevated structure in the downstream building.

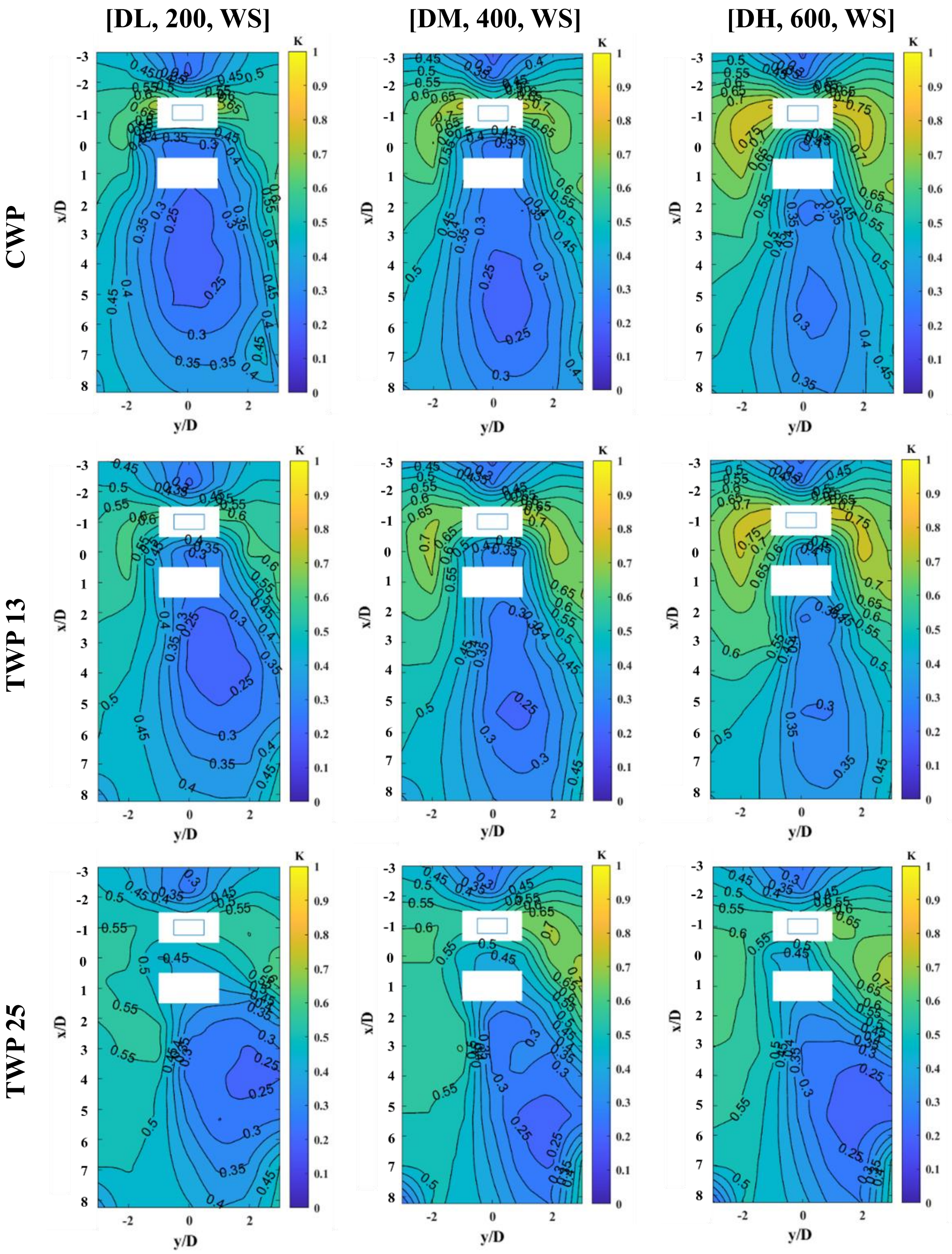

Figure 5.15. Distribution of *K* value near two buildings in tandem arrangement with the elevated structure in the upstream building.

The impact of the relative height difference between two buildings on LWV zones with varying elevated structure locations is illustrated in Figure 5.16. The relationship between *K* value and relative height differences exhibits three distinct patterns. They are: (1) Distinct LWV area percentages are observed for different elevated structure locations in the twisted wind flows. The LWV zones tend to be relatively smaller when the elevated structure is situated downstream, as opposed to upstream, in general. (2) LWV zone area percentages are higher in CWP than in TWPs, and (3) the percentage of LWV zones decreases as the relative height difference between two buildings increases; however, this phenomenon becomes less pronounced when both buildings have greater heights. The presence of a substantial NFLWV region behind the high-rise downstream building indicates a significant deterioration of PLWEs, as evidenced by the highest percentage of low wind velocity regions observed in proximity to this configuration. The area with the lowest LWV in CWP is observed for H_{UB}/H_{DB}=3/1, primarily due to the presence of a larger corner stream caused by the highest upstream building and the absence of a low-velocity region behind the downstream building due to its relatively smaller height. In addition, the LWV area percentage in CWP has distinct variations with the relative height difference. When the upstream building is a low-rise structure, modifying the relative height difference between two buildings proves highly effective in enhancing the wind environment; however, this approach loses its efficacy when dealing with a high-rise upstream building, as adjusting the relative height disparity has minimal impact on optimizing the wind conditions.

Apart from the twisting phenomenon of the flow field around the two buildings, TWPs exhibit a lower percentage of LWV area compared to CWP. For the WS case, the highest LWV area percentage recorded when H_{UB}/H_{DB} =2/3 is 27% and 18% in TWP 13 and TWP 25, respectively. TWP 25 generates nearly half of the LWV area percentage compared to CWP, primarily due to the rightward shift of the DSLWV region and an increased presence of areas with K>0.3 observed in the upstream building's left corner. The proportion of LWV area in TWP 25 exhibits reduced fluctuations as the upstream building height increases to medium or high-rise, suggesting a diminishing influence of twisted wind with taller buildings. The step-up building configuration is more prone to twisted wind effects compared to step-down building configurations, while TWP 25 demonstrates minimal variation across the test cases for step-down building configurations. The larger the twist angle, the lower the sensitivity of the building height difference to the LWV area. The region designed as the area of high wind velocity conditions (K>0.7) for various elevated structure locations is depicted in Figure 5.16. The relative height difference of the building exerts a more pronounced influence on the high-wind velocity region compared with the low-velocity region. When elevated structures are located downstream, a larger HWV area is generated compared to the case when elevated structures are located upstream. The highest HWV area is observed when the ratio of H_{UB} to H_{DB} is 3/1 in CWP for the LS case, constituting 30% of the overall area. The extensive formation of a shear layer is primarily attributed to the significant upstream building height, while the elevated building downstream effectively eliminates the low wind velocity region behind it. However, a comparatively lower HWV area with only 5% is generated by TWP 25, owing to reduced wind velocity magnitude on the left side of the building.

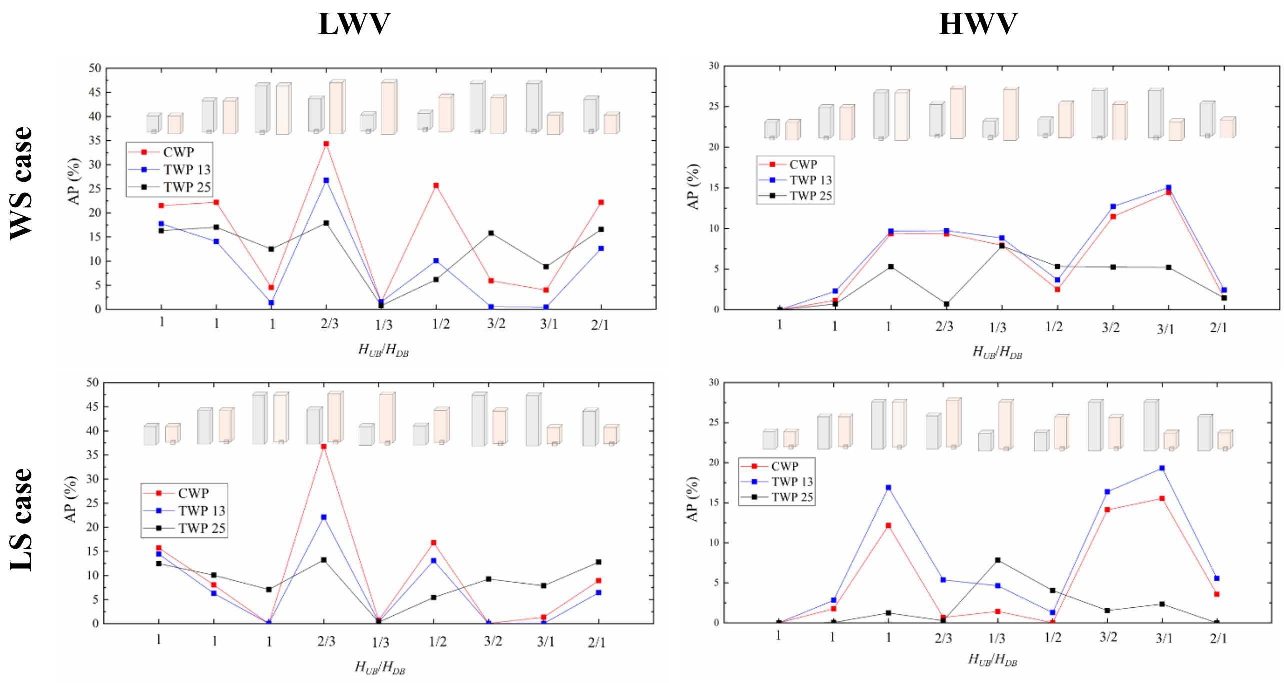

Figure 5.16. Variations of AP (%) in the low and high wind velocities across different relative height differences and elevated structure locations.

5.4.3 Variation of *K* values in the vicinity of two non-elevated buildings in tandem arrangement

5.4.3.1 Modification of mean wind velocity field

The distribution of *K* in two tandem identical buildings with increasing heights is illustrated in Figure 5.17. Due to the limited distance between the two tandem buildings, there was insufficient space for the complete development of vortices resulting from the detachment of the shear layer from the upstream building, thereby leading to vortex suppression. The downstream building was completely submerged within the wake region generated by the upstream building. Conventional wind profiles resulted in the formation of symmetric flow fields, where the shear layer was evenly separated on both the left and right sides. As the building height increases, there is a tendency for the downstream low wind velocity (DSLWV) area to move further away from the downstream building; however, an additional near-field low wind velocity (NFLWV) region emerges due to the increase in height. The corner stream exhibited an increase in wind velocities as well as an expansion in size with the growing building heights.

The presence of TWPs induced distinct flow separation compared with CWP, resulting in asymmetrical wind environments that tend to align with the direction of wind twist and extend further downstream. Specifically, the downstream area characterized by low wind velocities exhibited a rightward shift, accompanied by an expansion of the region influenced by twisted wind. A more pronounced twisting phenomenon was observed in cases where the building height was lower. Additionally, the left side of the corner stream experienced enlargement due to the oblique wind direction resulting from twisted wind and the separated shear layer on the left side directly merged into the deflected wake flow. In comparison to the flow field around a single building affected by twisted wind flows (Tse et al., 2017), the presence of a downstream building mitigated the impact of twisted wind flow on the PLWEs, resulting in reduced deviation angles and lessening the wake areas.

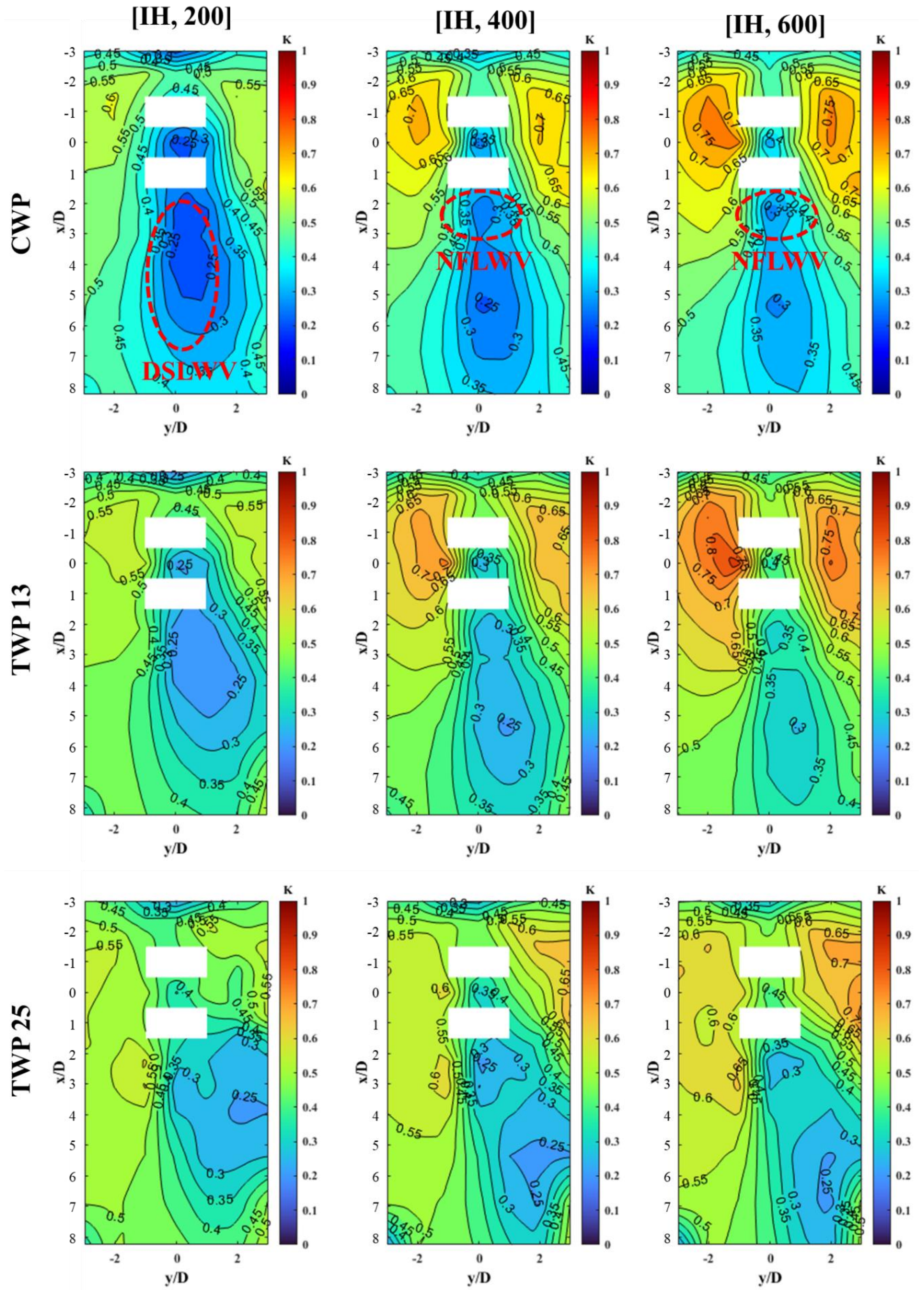

Figure 5.17. *K* value distribution for two identical-height tandem buildings under CWP and TWPs.

The distribution of K values around the two tandem step-up building configurations ($H_{UB}<H_{DB}$) is illustrated in Figure 5.18, with distinct differences from that of two tandem buildings with identical heights (Figure 5.17). The presence of the downstream building significantly altered the flow field compared to that of the isolated building (Tse et al., 2017), particularly when dealing with shorter or slender buildings exhibiting height disparities concerning the upstream building. The DSLWV area was observed in the case of (SU, 2/3), when the height of the upstream building was increased, a significant downwash flow from the upstream building resulted in an amplified corner stream beside the downstream building due to the enhanced shear layer effects. Consequently, this led to the formation of a pronounced low wind velocity region downstream. Under the influence of twist flow, the DSLWV region tended to shift towards the right side and experienced enhanced effects with twist angles. Another striking feature of the wind environment was the absence of the NFLWV region behind the downstream building due to the larger vertical height differences in the step-up building configuration. The flow field in front of the tall downstream building was modified by the presence of the low upstream building. In regions characterized by high wind velocities, unlike the corner stream where there is a high wind velocity at both ends of the upstream building, this area tends to migrate towards the passages between two buildings, resulting in the formation of two distinct regions with elevated wind velocities in the step-up building configuration. The velocity of these regions tended to increase proportionally with the height differences between the two buildings, suggesting a strong correlation between the wind velocity in the passage and the exposed area of the downstream building to the incoming wind. Under the influence of twisted wind, those two high wind velocity regions between the two buildings tended to shift to the right side, exhibiting a greater velocity difference between the right and left sides. Specifically, the K value between the right and left sides (ΔK) reached 0.6 when the ratio of H_{UB} to H_{DB} was 1:3 under TWP 25. The substantial discrepancy in velocities

within the building may induce pedestrians to perceive a significant variation in velocity over a limited distance, thereby impacting pedestrian comfort. The twisted wind also induced a deviation of the upstream low wind velocity region in the opposite direction to that of the twisted wind under TWP 25. The twist flow attacked the buildings at an oblique wind incident angle, resulting in a deflection of larger volumes of wind towards the right side of the building. Consequently, the high wind velocity on the right side exerts a tendency to displace the upstream low wind velocity region towards the left side. The K distribution around two tandem buildings with a step-down configuration is depicted in Figure 5.19, the flow field pattern exhibited a similar distribution to that of two tandem buildings with identical heights. Notably, the downstream movement of the DSLWV area was influenced by the height disparity between the two tandem buildings. The modification of the relative height difference between the two tandem buildings more pronounced effect on the PLWEs from the step-up building configuration than the step-down building configuration under both CWP and TWPs.

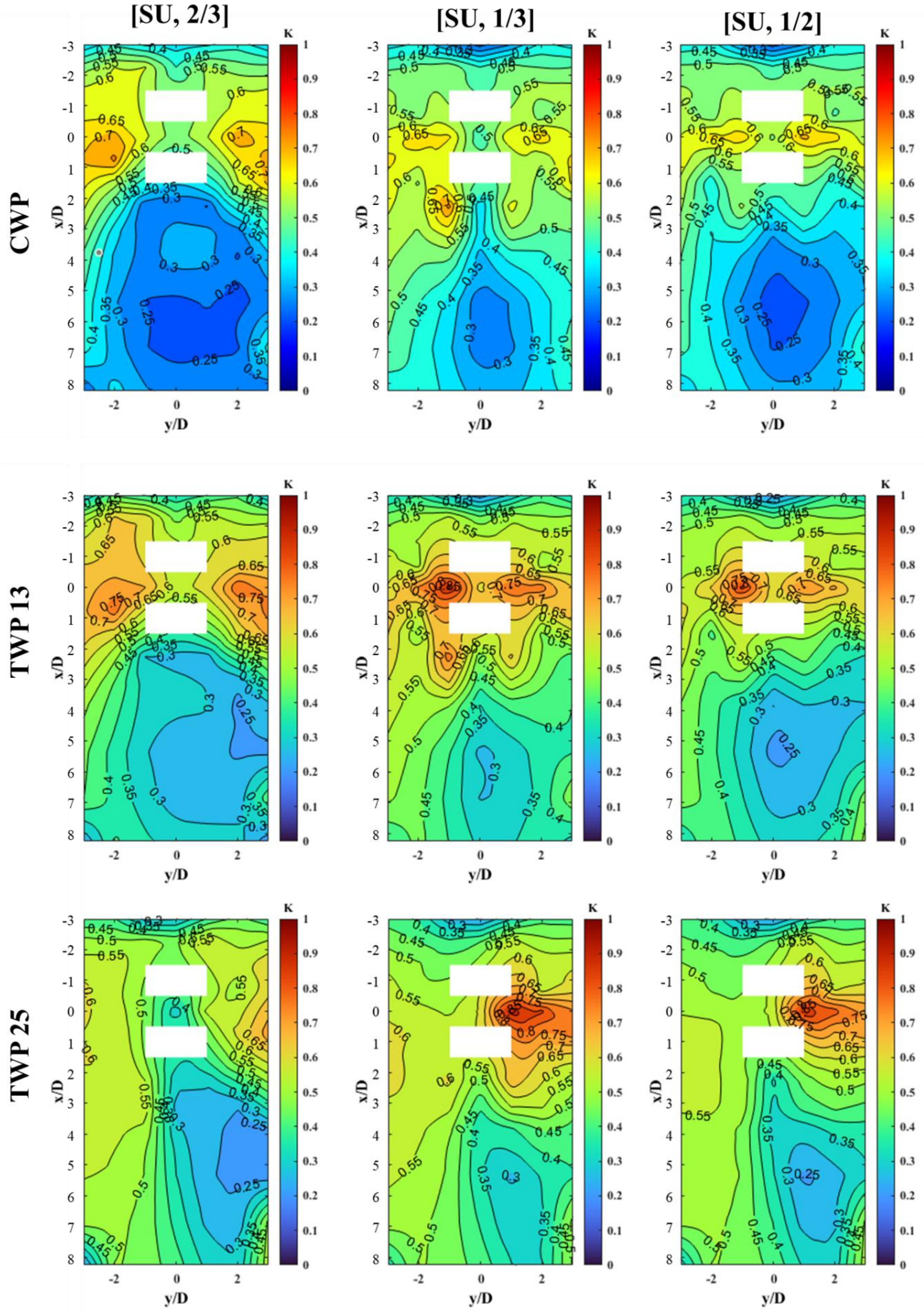

Figure 5.18. *K* value distribution surrounding two tandem buildings for step-up building configuration under CWP and TWPs.

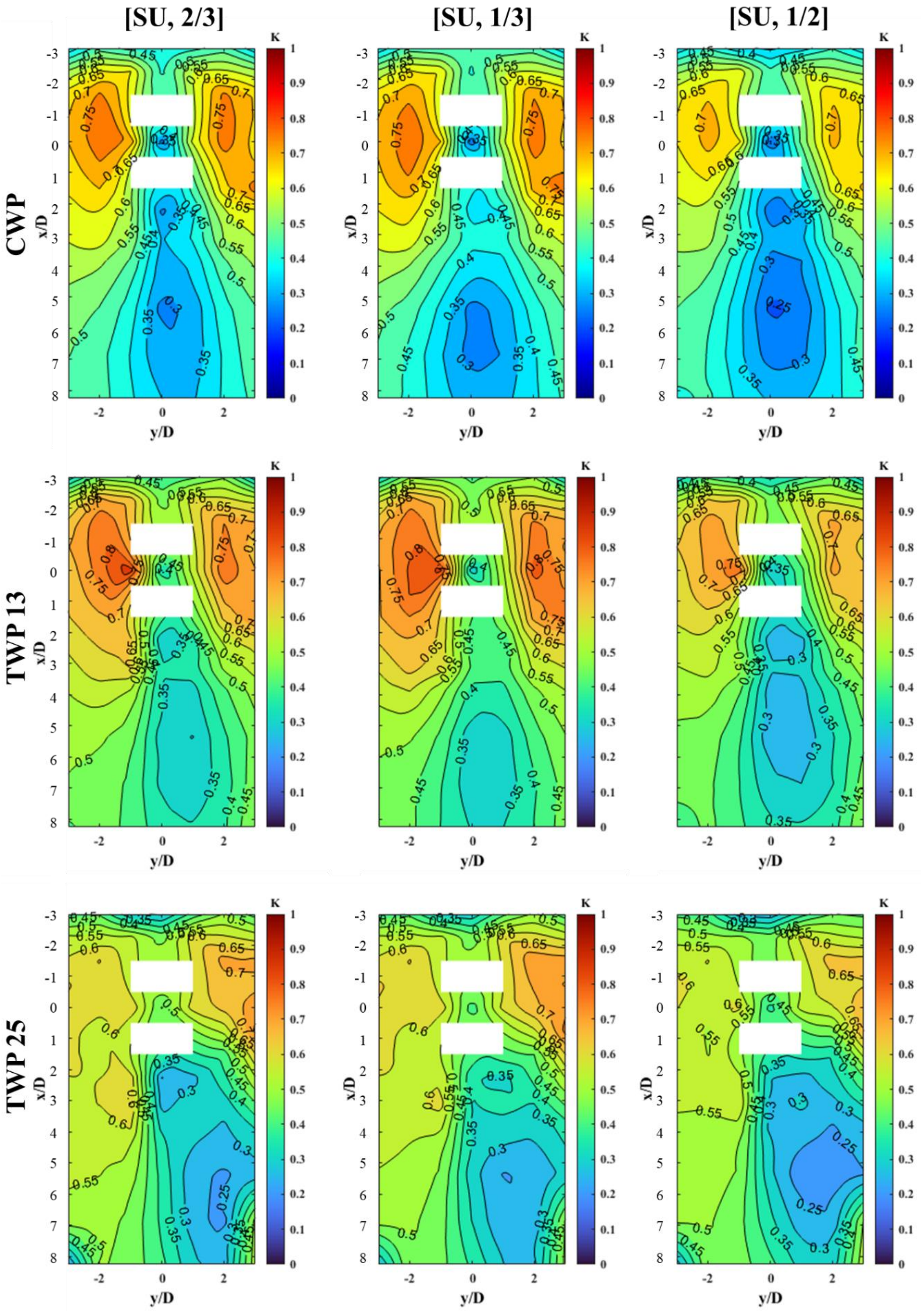

Figure 5.19. *K* value distribution surrounding two tandem buildings for step-down building configuration under CWP and TWPs.

5.4.3.2 Modification of gust wind velocity field

Gust wind velocity serves as an indicator of the maximum velocity that pedestrians may encounter due to the unsteady flow and is widely recognized as a source of wind discomfort (Vita et al., 2020; Melbourne, 1978; Zhong et al., 2022). Blocken et al. (2016) emphasized the necessity for a more comprehensive understanding of gust values at the pedestrian level to obtain accurate data for input into pedestrian-level wind safety criteria. The gust wind velocity is a more precise indicator for evaluating the mechanical effect on pedestrians compared to the mean wind velocity, and it plays a crucial role in assessing the safety of PLWEs. Understanding the impact of twisted wind flow on gust wind patterns enables city planners to predict PLWEs from both mean and gust wind velocity perspectives (Shirzadi and Tominaga, 2022). Gust Equivalent Mean (GEM) wind velocities proposed by Tsang et al. 2012 were utilized in this chapter to comprehensively evaluate both the mean and gust wind velocities. The gust wind velocities were determined by calculating the average of the maximum wind velocities recorded in each set of five independent samples. Considering the length scale L^*=1/200, and the velocity scale U^*=6.5/12=0.54, the time scale was estimated as $T^*=L^*/U^*=9.3\times 10^{-3}$. Each independent sample has a time duration of 24 seconds on the wind tunnel scale and 43 minutes on the prototype scale.

The GEM wind velocities (U_{GEM}) were normalized by the mean wind velocity at 150 m (U_{150}) in the prototype scale of the approaching flow, aiming to delineate regions that may cause discomfort to pedestrians by strong winds based on the criteria proposed by Lawson (Lawson, 1978) and Hong Kong's wind climate as an illustrative example. The threshold for maximum wind velocities at the pedestrian level causing discomfort to pedestrians was established as 10 m/s, with a 5% exceedance probability (Lawson, 1978). Considering the prevailing weather conditions in Hong Kong, where the wind velocity at a height of 150 m reaches approximately 13 m/s with a 5% exceedance probability (Tsang et al., 2012). Therefore, the estimated critical U_{GEM}/U_{150} value for Hong Kong is 0.77, suggesting that wind velocities exceeding this threshold are classified as high-gust wind velocity zones. The gust wind velocities that were converted were subsequently utilized to evaluate the areas characterized by high wind velocities based on the Equation (5.2). The critical U_{GEM}/U_{150} value in the wind tunnel was determined to be 1.47, areas where the U_{GEM}/U_{150} value exceeds 1.47 were considered as zones that may lead to pedestrian discomfort due to wind gusts.

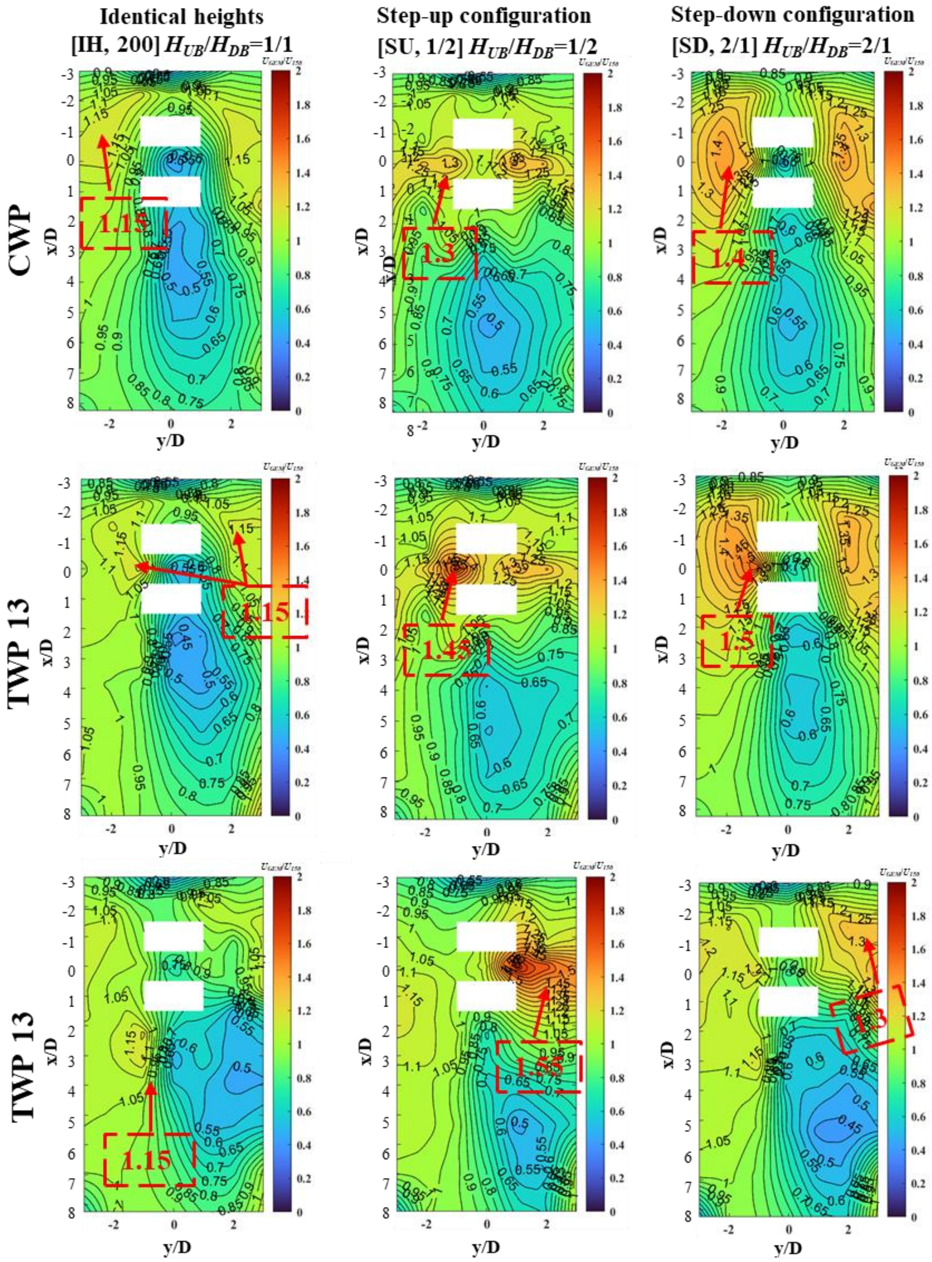

Figure 5.20. Effects of vertical height disparity between two tandem buildings on the normalized GEM wind velocity distribution under CWP and TWPs.

The normalized GEM wind velocity distribution under CWP and TWPs exhibited significant variations for varied building configurations (Figure 5.20). The twisted wind significantly influenced the spatial distribution of high-gust wind regions. Similarly to the distribution of mean wind velocity, under twisted wind, the maximum GEM wind velocity region exhibited a rightward twist. Under CWP, the maximum GEM wind velocity was observed at the corner of the upstream building. However, as the twist angle increased, this location shifted downstream on the left side of two tandem identical-height buildings. Furthermore, for the two tandem non-identical-height buildings, the location of maximum U_{GEM}/U_{150} is merged at the right side under TWP 25. The maximum U_{GEM}/U_{150} for all the test cases is listed in Table 5.6. The maximum U_{GEM}/U_{150} exhibited a larger magnitude under TWP 13 compared to CWP for all test cases, owing to the introduction of increased flow into the passage between the two buildings due to the smaller twist angle, resulting in an enhanced U_{GEM}/U_{150}. The deflection of flows to the right side increased with a further twist angle, resulting in a shift of the highest U_{GEM}/U_{150} area from the left to the right side with reduced magnitude. Therefore, except for the step-up building configuration, where the maximum U_{GEM}/U_{150} was observed at the passages between the two buildings and increases proportionally with the twist angle, TWP 25 exhibited a comparatively lower magnitude for its maximum U_{GEM}/U_{150} in comparison to CWP and TWP 13.

The vertical height differences between the two buildings tend to generate a higher gust wind region under TWPs, which has the potential to cause pedestrian discomfort due to strong winds. For instance, the maximum GEM wind velocity value for the step-up building configuration (SU, 1/3) increased from 1.3 to 1.55, respectively, when comparing CWP and TWP 25. The passage between two buildings under step-up building configurations exhibited a high GEM wind velocity region, which may lead to pedestrian discomfort due to the strong winds. Moreover, this area demonstrated a rightward twist and intensified magnitude under

TWP 25. The step-down configuration exhibited the largest high-gust wind region, attributed to the generation of high-velocity horseshoe vortices resulting from the downwash flow originating from the windward face of the building. However, the high-gust wind tended to be mitigated by the twisted wind resulting from a reduced shear layer intensity under TWP 25, which was decreased from 1.4 under CWP to 1.3 under TWP 25. The findings suggest that the presence of twisted wind may lead to potential pedestrian discomfort resulting from strong winds in high-rise buildings by augmenting the overall extent of areas with high wind velocities under small twist angles (TWP 13). However, for larger twist angles (TWP 25), the zones with high wind velocities were reduced, except for cases involving a step-up building configuration.

Table 5.6. Maximum U_{GEM}/U_{150} for non-elevated cases.

Case Name	H_{UB}/H_{DB}	**Maximum U_{GEM}/U_{150}**			**Remarks**
		CWP	**TWP 13**	**TWP 25**	
[IH, 200]	1/1	1.15	1.15	1.15	Two tandem identical-height buildings
[IH, 400]	1/1	1.4	1.45	1.25	
[IH, 600]	1/1	1.5	1.6	1.4	
[SU, 2/3]	2/3	1.4	1.45	1.45	Step-up building configuration
[SU, 1/3]	1/3	1.3	1.5	1.55	
[SU, 1/2]	1/2	1.3	1.45	1.55	
[SD, 3/2]	3/2	1.55	1.65	1.4	Step-down building configuration
[SD, 3/1]	3/1	1.55	1.6	1.45	
[SD, 2/1]	2/1	1.4	1.5	1.3	

5.4.3.3 Wind comfort assessment at pedestrian level

The area ratios for different wind comfort categories under weak wind conditions are illustrated in Figure 5.21, depicting two identical tandem buildings of increasing height. The twisted wind exerted a significant influence on both the regions of low wind velocity and high wind velocity zones, while no discernible variation was observed in the acceptable area. The low wind velocity region significantly decreased with the increasing height of buildings, and tandem buildings under TWPs occupied a larger proportion of the low wind velocity region compared to CWP due to the oblique phenomenon and increased blockage effect on incoming wind flow. This phenomenon was more pronounced at higher building heights.

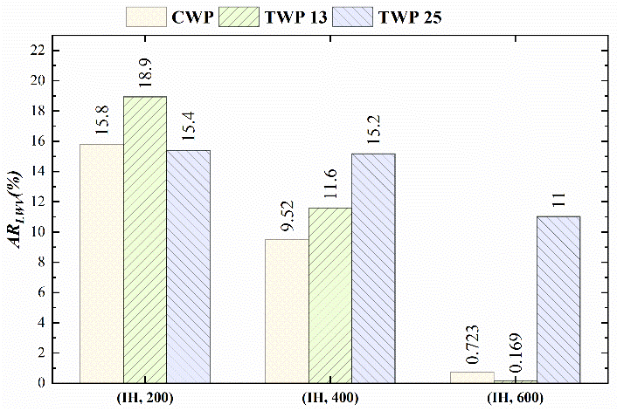

(a)

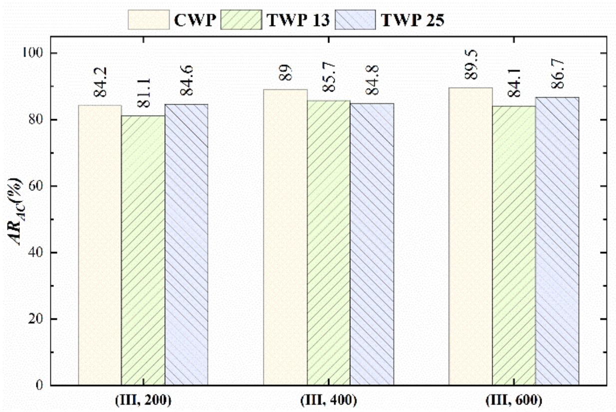

(b)

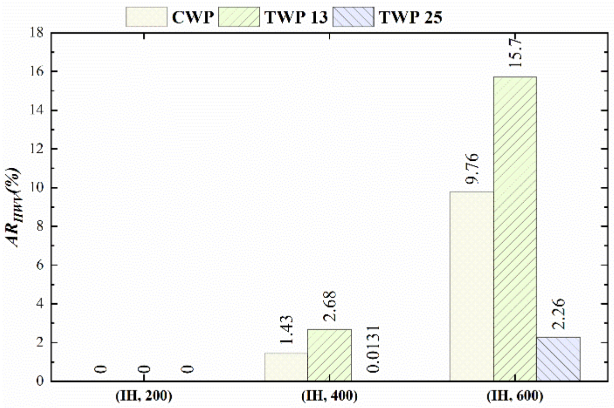

(c)

Figure 5.21. Area ratios for wind environments surrounding two tandem identical-height buildings for (a) Low wind velocity, (b) Acceptable, and (c) High wind velocity areas.

Figure 5.22 demonstrates area ratios of wind comfort classes calculated near two non-identical tandem buildings under weak wind conditions. Under CWP or TWPs, varying height disparity exhibits distinct wind comfort conditions. The step-down building configuration resulted in a smaller low wind velocity area compared to the step-up building configuration. For instance, when H_{UB}/H_{DB}=2/3, the low wind velocity (LWV) area occupied 35.2% of the interest precinct, whereas it only accounted for 0.82% of the interest precinct when H_{UB}/H_{DB}=3/2. The presence of the slender downstream building obstructs the incoming flows, causing the wind to be trapped in the passages between the two buildings and resulting in a significant area of reduced wind velocity behind the buildings. The minimal low wind velocity area was observed when the height ratio of H_{UB} to H_{DB} was 3:1 and 1:3, indicating that vertical height disparity plays a beneficial role in reducing the unfavorable wind environment, this effect was further enhanced with the larger differences in building heights. The impact of TWPs on the LWV area exhibited divergent trends for step-up and step-down building configurations. Specifically, TWP 25 resulted in a smaller LWV area for the step-up configuration, whereas the opposite trend was observed for the step-down configuration, with a greater LWV area compared to CWP.

The area classified as "Acceptable" exhibited minimal fluctuations across different H_{UB}/H_{DB} scenarios (Figure 5.22 (b)). The coverage of areas rated as "High wind velocity" regions (Figure 5.22 (c)) was maximized when H_{UB}/H_{DB}=3/1, owing to the significant expansion of the high wind velocity area resulting from the formation of a shear layer caused by the upstream building. However, the smaller "High wind velocity" regions were observed in the case of a step-up building configuration, as the gaps between buildings serve as breezy ways for entraining wind flows and reduce the formation of areas with high wind velocities. The step-up building configuration under TWPs tended to result in a larger area of high wind velocity due to the increased occurrence of high wind velocities between the two buildings on the right side. Conversely, in step-down building configurations, the high wind velocity area at the left corner of the upstream building was reduced due to the presence of twisted wind, and more flows were deflected to the right side, which led to smaller high wind velocity regions under TWP 25.

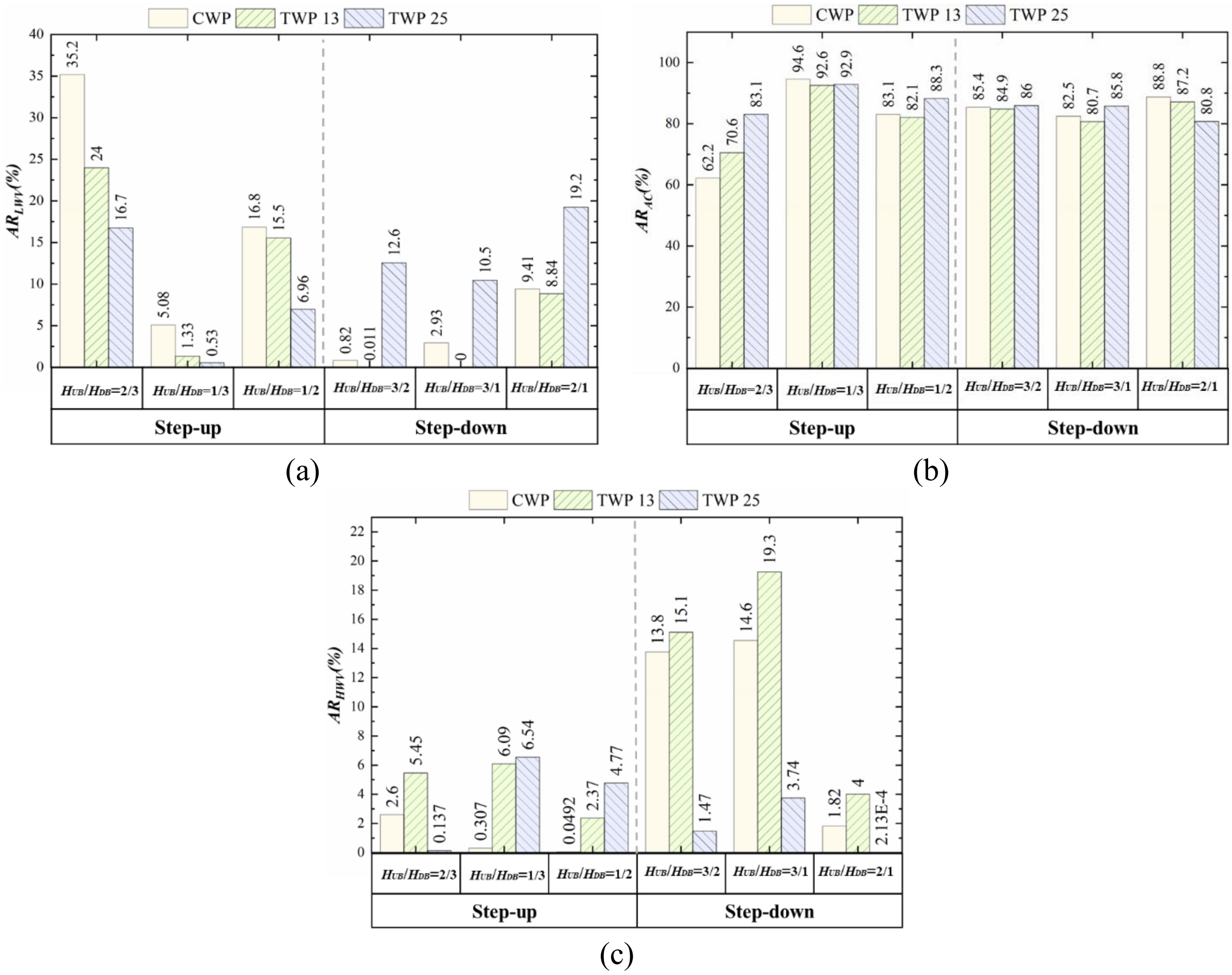

Figure 5.22. Area ratios for wind environments surrounding two tandem non-identical-height buildings for (a) Low wind velocity, (b) Acceptable, and (c) High wind velocity areas.

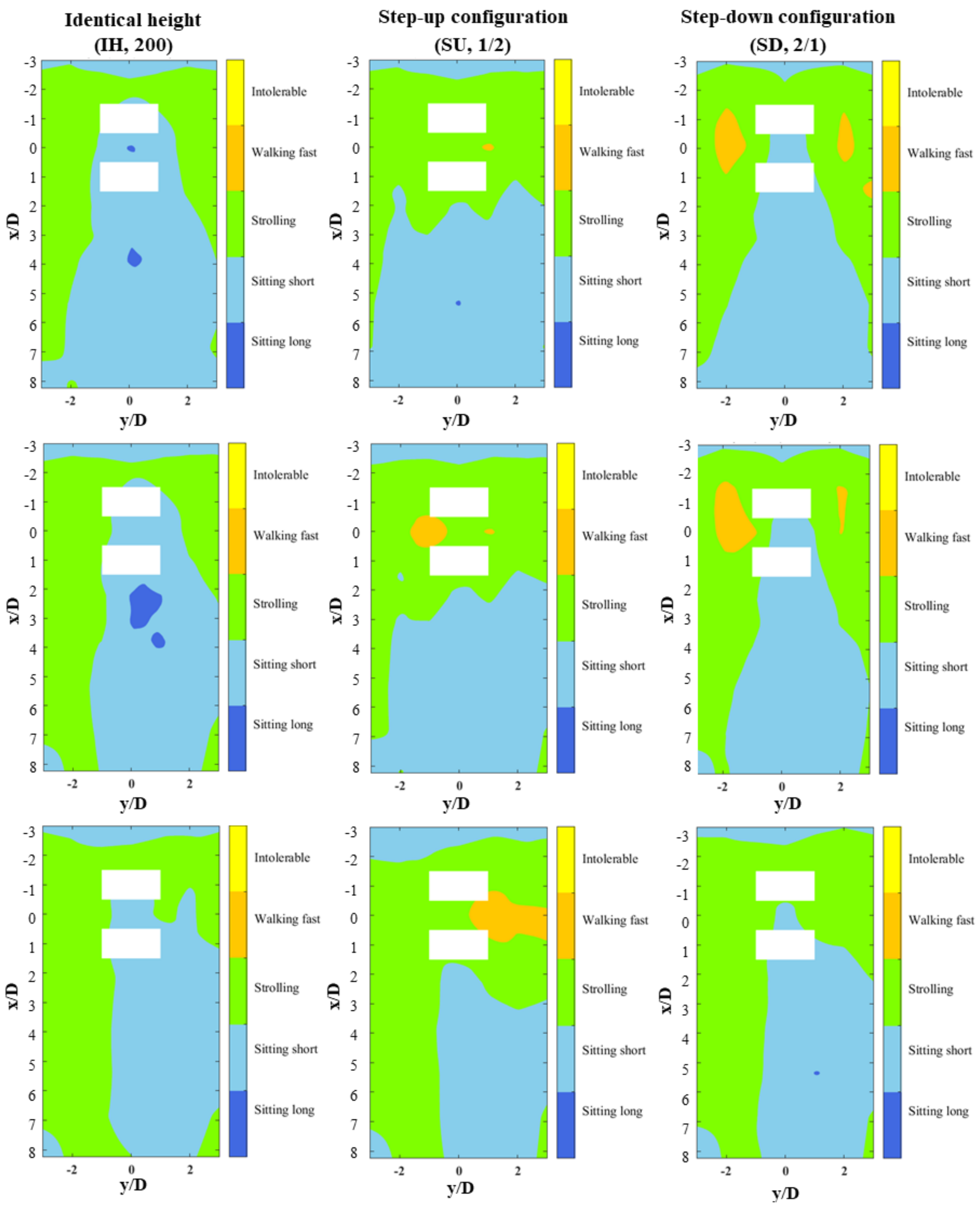

Figure 5.23. Distribution of wind comfort under windy wind conditions under CWP and TWPs.

The twisted wind enables the relocation of areas corresponding to different wind comfort categories under windy wind climates (Figure 5.23). The high wind velocities were generated by the pronounced separation layers formed at the corners of the upstream buildings, and the elevated wind velocities create an environment unsuitable for leisure activities such as "Sitting long" and "Sitting short". Varying vertical height disparities between two tandem buildings can be used to make urban planning decisions. For instance, identical-height tandem buildings and step-down building configurations are suitable for creating sheltered areas conducive to outdoor seating in the passage between the two buildings. Conversely, a step-up building configuration is more appropriate for enhancing street ventilation and providing additional space for recreational activities such as "Strolling" under CWP and TWPs. Winds in the wake region behind the two tandem buildings were less active and suitable for short-term sitting areas, and the twisted wind exerted on the two tandem identical-height buildings tends to induce a "Sitting short" area shift towards the right side and an expansion of the "Strolling" area on the left side. The step-down building configuration resulted in a significant area rated as "Walking fast" observed on the corner of the upstream building under CWP; however, this "Walking fast" area was replaced by a larger area classified as "Strolling" under TWP 25 due to the reduced intensity of the shear layer. In the case of a step-up building configuration. Under CWP, the region classified as "Walking fast" becomes almost imperceptible in the step-up building configuration, while a distinct "Walking fast" zone was observed on the right side of the passage between two buildings under TWP 25.

The area ratios of various wind comfort categories under windy wind conditions are illustrated in Figure 5.24. The increase in twist angle from TWP 13 to TWP 25 resulted in a significant expansion of the area rated as "Strolling", surpassing that observed under CWP conditions. This expansion enables individuals to engage in recreational activities under a windy climate, facilitated by the lateral entrained winds on the left side being transported to the right side through the passage between two buildings under TWPs. The relative height disparity between the two tandem buildings significantly influenced the surrounding wind comfort under both CWP and TWPs. Notably, the “Strolling” area exhibited its maximum extent when the ratio of H_{UB} to H_{DB} was 1:3. The step-down building configuration (H_{UB}>H_{DB}) exhibited a greater proportion of area classified as “Walking fast” compared to the step-up building configuration, owing to the amplified corner stream generated by the upstream building under CWP. The wind comfort in the tandem buildings showed minimal sensitivity to changes in twist angle up to 25 degrees, and no significant fluctuations were observed in the area ratios for all test cases under TWP 25.

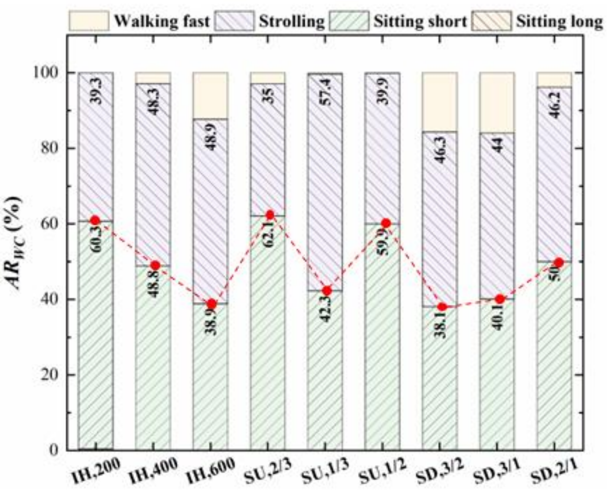

(a)

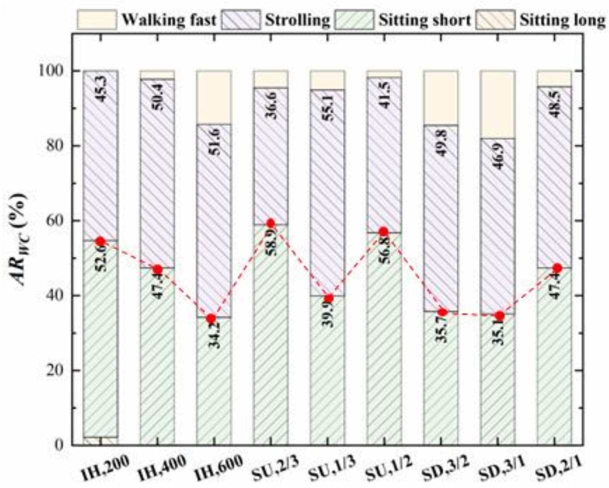

(b)

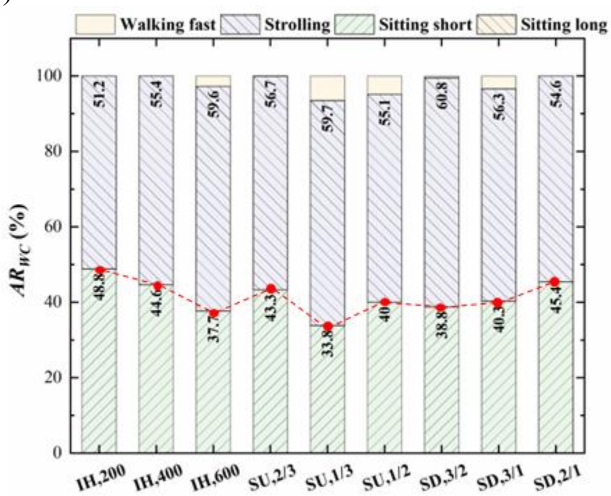

(c)

Figure 5.24. Area ratio of wind comfort categories under windy climate for all test cases under (a) CWP, (b) TWP 13, and (c) TWP 25.

5.4.4 The influence of twisted wind on deviation angles and wind velocity between two tandem buildings

The systematic examination of DFLWV zones involves defining the deviation angle (β) as the angle between the center axis of the building and a line connecting the geometric center of the DFLWV zones to the building's center. The calculated β values for building configurations with identical heights are listed in Table 5.7. The deviation of DFLWV zones exhibits an increasing trend with the twist angle; specifically, TWP 25 resulted in a larger deviation angle compared to TWP 13. The heights of buildings exert a substantial influence on the deviation angles. An evident reduction in the deviation angle becomes apparent with increasing building height, especially for low- to mid-rise structures. However, once a building surpasses 60 m in height, further increases do not yield substantial changes to the twist angle. The presence of an elevated building exerts a substantial impact on the flow field under both CWP and TWPs. Notably, the maximum deviation angle occurs when the elevated structure is positioned downstream, while positioning it upstream results in minimal deviation angles. The rationale behind this phenomenon lies in the fact that elevated buildings can effectively mitigate DFLNV and eliminate NFLWV areas (Figure 5.9), and the increased volume of airflows passing through the elevated area results in an intensified twisted wind effect on the flow field.

Table 5.7 Deviation angle (β) for two tandem identical-height buildings in CWP and TWPs.

Case Name	Deviation angle (β)			Remarks
	CWP	TWP 13	TWP 25	
[DL, 200, ELE]	0	19.9	27.7	Two tandem elevated buildings
[DM, 400, ELE]	0	10.5	17.1	
[DH, 600, ELE]	0	9.3	18.3	
[DL, 200, WS]	0	13.8	27.5	Elevated structure on the upstream building
[DM, 400, WS]	0	8.4	16.6	
[DH, 600, WS]	0	6.7	14.6	
[DL, 200, LS]	0	21.4	30.6	Elevated structure on the downstream building
[DM, 400, LS]	0	10.5	21.5	
[DH, 600, LS]	0	10.5	20.2	

The deviation angle (β) for two tandem non-identical-height buildings with elevated structures is listed in Table 5.8. The relative height difference between two tandem buildings plays a crucial role in modifying the surrounding wind environments under CWP and TWPs. The deviation angle of DFLWV zones in step-up building configurations decreases proportionally with the relative differences between the two buildings. For instance, in TWP 25, the deviation angle for H_{UB}/H_{DB} of 2/3 is 24.7° ; however, it reduces to 10.1° when H_{UB}/H_{DB} equals 1/3. The phenomenon can be observed irrespective of the location of the elevated structures. Furthermore, the smallest deviation angle was observed when the elevated structure is situated on the upstream building (WS case), which remains consistent in cases where two tandem buildings have identical heights. In contrast, the deviation angle exhibits minimal fluctuations across all cases with varying relative height differences in step-down building configurations. The obstruction caused by the tall upstream building impedes the incoming flow, thereby constraining the downstream flow field from being significantly influenced by twisted winds.

Table 5.8. Deviation angle (β) for two tandem non-identical-height buildings in CWP and TWPs.

Step-up building configurations

Case Name	Deviation angle (β)			H_{UB}/H_{DB}
	CWP	TWP 13	TWP 25	
[DH, 400, ELE]	0	13.5	24.7	2/3
[DM, 200, ELE]	0	9.3	12.2	1/2
[DH, 200, ELE]	0	7.2	10.1	1/3
[DH, 400, WS]	0	17.1	21	2/3
[DM, 200, WS]	0	8.6	11.6	1/2
[DH, 200, WS]	0	6.4	8.3	1/3
[DH, 400, LS]	0	21.1	25.7	2/3
[DM, 200, LS]	0	8.3	13.8	1/2
[DH, 200, LS]	0	6.2	11.5	1/3

Step-down building configuration

Case Name	Deviation angle (β)			H_{UB}/H_{DB}
	CWP	TWP 13	TWP 25	
[DM, 600, ELE]	0	8.7	17.2	3/2
[DL, 400, ELE]	0	8.2	17.5	2/1
[DL, 600, ELE]	0	6.1	16.2	3/1
[DM, 600, WS]	0	6.3	13.8	3/2
[DL, 400, WS]	0	4.5	14.5	2/1
[DL, 600, WS]	0	4.7	13	3/1
[DM, 600, LS]	0	8.1	19.8	3/2
[DL, 400, LS]	0	8.5	21.3	2/1
[DL, 600, LS]	0	5.4	17.2	3/1

The deviation angles for all non-elevated buildings are listed in Table 5.9. The deviation angles exhibited an increasing trend as the twist angles ranged from 13° to 25° across all building models. For shorter buildings, the twisted wind flow exhibited a more pronounced effect with larger deviation angles; for instance, under TWP 25, the deviation angle was 31.6°

for case [IH, 200], whereas it was only 19° for case [IH, 600]. The sensitivity of twisted wind flow to the height difference between two buildings was observed to exhibit variation, with a tendency for deviation angles to decrease as the height disparity between non-identical structures increases. Moreover, the step-down building configuration tended to yield a smaller deviation angle compared to the step-up building configuration.

Table 5.9. Deviation angle (β) for two tandem non-elevated buildings in CWP and TWPs.

Case Name	**Deviation angle β (°)**		**H_{UB}/H_{DB}**	**Remarks**
	TWP 13	**TWP 25**		
[IH, 200]	14.2	31.6	1/1	Two identical-height buildings
[IH, 400]	10.4	20.1	1/1	
[IH, 600]	7.9	19.0	1/1	
[SU, 2/3]	16.5	25.0	2/3	Step-up building configuration
[SU, 1/3]	9.4	12.8	1/3	
[SU, 1/2]	12.3	19.0	1/2	
[SD, 3/2]	7.5	18.8	3/2	Step-down building configuration
[SD, 3/1]	4.0	12.0	3/1	
[SD, 2/1]	6.3	19.5	2/1	

The parameter $K_{pcl,ave}$ is defined as the average K value along the passage center line at the pedestrian height between the two buildings for all cases (Li et al., 2015). Figure 5.25 illustrates the variation of $K_{pcl,ave}$ values with different height differences and elevated structure locations between two tandem buildings under CWP and TWPs. The $K_{pcl,ave}$ values for different H_{UB}/H_{DB} exhibit varying trends under CWP and TWPs, with an observed increase in velocities in the passages between two buildings as the twist angle increases. Specifically, the wind velocity between two tandem buildings is observed to increase significantly when the elevated structure is positioned upstream (WS cases) under TWPs, as compared to CWP. This phenomenon can be attributed to the amplified wind volume induced by TWPs through the elevated structure. However, this phenomenon remained undetectable for non-elevated buildings positioned upstream (LS cases), and the velocity in the inter-building gap is found to be lower for LS cases compared to WS and ELE cases under both CWP and TWPs. The step-up building configuration exhibits a higher $K_{pcl,ave}$ value compared to the step-down building configuration, whereas the step-down building configuration demonstrates similar levels of $K_{pcl,ave}$ value as the two tandem buildings with identical heights. For the non-elevated buildings in tandem arrangement (Figure 5.25 (d)), under CWP, the upstream building deflects the approaching winds, resulting in incomplete mobilization of airflows at the pedestrian level in the passage between the two buildings and creating regions with low wind velocity. The $K_{pcl,ave}$ values in both CWP and TWPs exhibited an increasing trend with the building heights for two identical-height buildings. The twisted wind tended to yield elevated $K_{pcl,ave}$ values due to the oblique wind direction at the ground level, resulting in a greater influx of flows into the passage between the two buildings. Step-up building configuration tended to induce the highest wind velocity in the passage between the two buildings when compared with step-down building configuration and a configuration where both buildings have identical heights. The $K_{pcl,ave}$ values increased as the relative height difference between the two buildings increased in the step-up building configuration, with the highest $K_{pcl,ave}$ value observed when H_{UB}/H_{DB}=1/3 due to the largest downwash flow caused by the downstream building. Conversely, the $K_{pcl,ave}$ values exhibited minimal sensitivity to relative height differences between the two buildings under both CWP and TWPs, demonstrating consistent $K_{pcl,ave}$ values for cases with a step-down configuration.

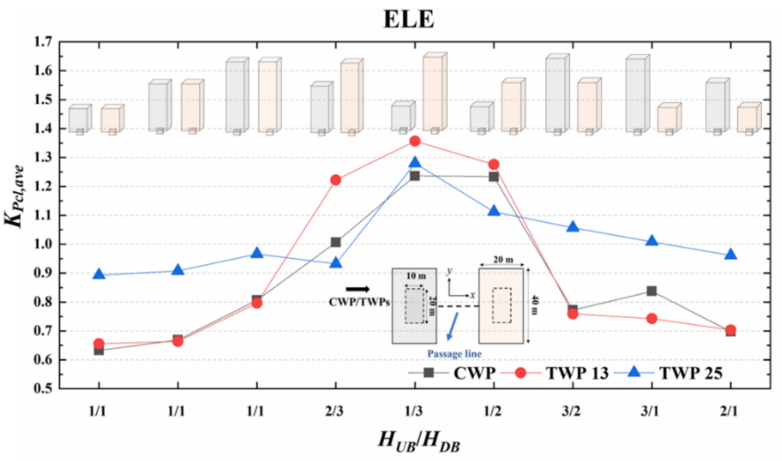
ELE
$K_{Pcl,ave}$
H_{UB}/H_{DB}
1/1 1/1 1/1 2/3 1/3 1/2 3/2 3/1 2/1
CWP/TWPs
10 m
20 m
40 m
Passage line
CWP TWP 13 TWP 25

(a)

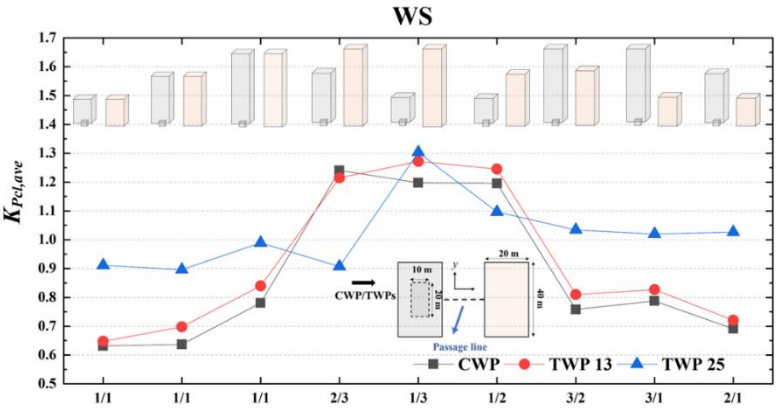
WS
$K_{Pcl,ave}$
1/1 1/1 1/1 2/3 1/3 1/2 3/2 3/1 2/1
CWP/TWPs
10 m
20 m
40 m
Passage line
CWP TWP 13 TWP 25

(b)

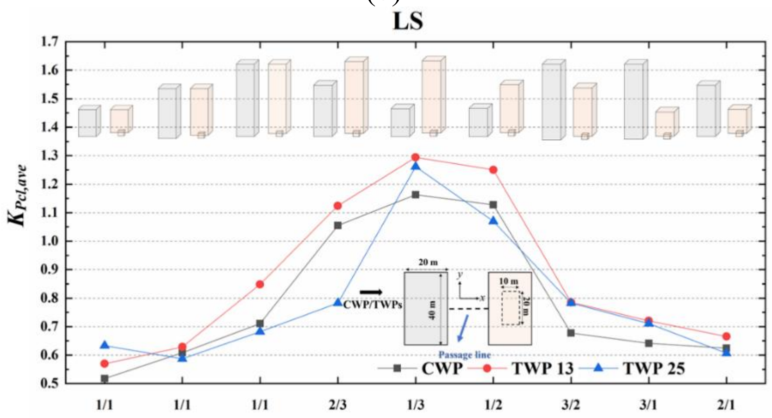
LS
$K_{Pcl,ave}$
1/1 1/1 1/1 2/3 1/3 1/2 3/2 3/1 2/1
CWP/TWPs
20 m
40 m
10 m
Passage line
CWP TWP 13 TWP 25

(c)

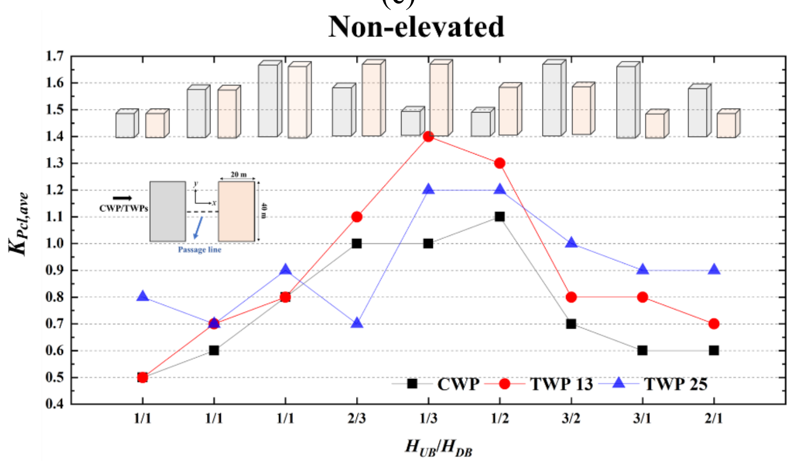
Non-elevated
$K_{Pcl,ave}$
H_{UB}/H_{DB}
1/1 1/1 1/1 2/3 1/3 1/2 3/2 3/1 2/1
CWP/TWPs
20 m
40 m
Passage line
CWP TWP 13 TWP 25

(d)

Figure 5.25. Variation of $K_{pcl,ave}$ value with height differences and elevated structure locations for (a) ELE, (b) WS, (c) LS, and (d) non-elevated cases.

5.4.5 Thermal comfort assessment under TWPs

The proportion of thermal comfort zones under weak wind conditions during both summer and winter across all scenarios is illustrated in Figure 5.26. As depicted in Figure 5.26 (a), the majority of the observed area fell within the "Very hot" category, while the rest were classified as "Hot" as a consequence of the reduced wind speed and elevated radiation temperature. For two tandem buildings of identical height, the thermal comfort zone classified as "Very hot" was found to expand with decreasing building height, potentially leading pedestrians to experience extreme heat stress during summer months. The pedestrians experience less heat stress when two tandem buildings exhibit disparity in heights. The step-down building configuration, in the meantime, exhibited superior thermal comfort with a reduced occurrence of "Very hot" thermal comfort zone compared to the step-up building configuration. Regarding the impact of twisted wind on thermal comfort zones, a greater extent of "Very hot" areas was observed under TWP 25 in comparison to cases under CWP. This implies that twisted wind tends to generate more unfavourable thermal comfort conditions, thereby discouraging outdoor activities for pedestrians during such weather conditions.

Figure 5.26 (b) describes the thermal comfort zones in winter for all cases. In this chapter, the "Neutral" thermal perceptions are assumed to be the most comfortable thermal comfort zones for pedestrians in winter, as PET=28℃ is considered the optimal temperature range for pedestrian activity according to Chen and Mak (2021). The size of "Neutral" exhibited a slight upward trend as the height of two tandem identical buildings increased. The areas of "Neutral" in the step-up building configuration were found to be smaller compared to those in the step-down building configuration. Among the three step-up building configurations, Case (SU, 1/3) demonstrated the smallest area classified as “Slightly warm” (45.3%), exhibiting the greatest vertical disparity between the two structures. This percentage was further reduced to 36.6% under TWP 25. The twisted wind effect tended to result in a larger proportion of areas rated as “Neutral” with reduced PET during winter compared to cases under CWP, and this effect was pronounced for step-up building configurations.

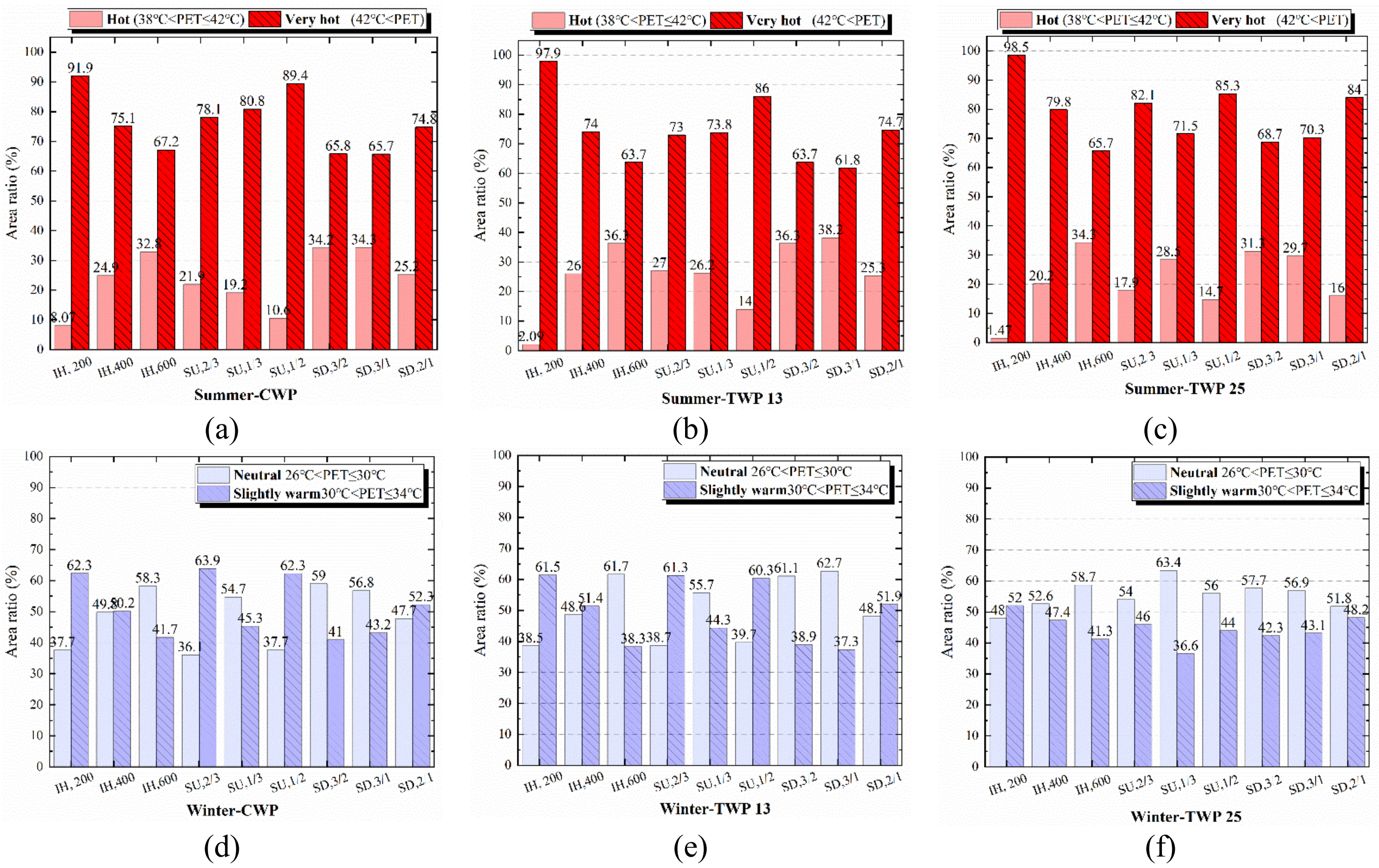

Figure 5.26. Area ratio of different thermal comfort zones in (a)-(c) Sunny day in summer and (d)-(f) Sunny day in winter.

5.5 Summary

The wind tunnel experiments were conducted in this capture on two tandem buildings (H_{UB}/H_{DB}) with varying relative height differences ranging from 3:1 to 0.33:1, while also considering different elevated structure locations through a total of over a hundred test cases. Two distinct twisted wind profiles were employed, featuring twist angles of 13° and 25°, respectively, to replicate two different ABL conditions. The wind environments under the twisted wind profiles (TWPs) were compared with those of the conventional wind profile (CWP), exhibiting similar wind velocity and turbulence intensity profiles. Kanomax velocity sensors were strategically deployed around the buildings to accurately measure the mean wind velocities at the pedestrian level. Subsequently, a meticulous analysis was conducted on these measured mean wind velocities to identify any modifications in the wind environment near two tandem buildings and ascertain any alterations in wind velocities. The key findings are summarized as follows:

(1) The flow field around the two tandem buildings is modified by twisted wind flows, resulting in the generation of an asymmetric wind environment characterized by the deviation of DFLWV and USLWV areas towards the direction of approaching twisted wind flow and a weakened corner stream on the left side. In the step-up building configuration, the primary vortex exhibited symmetry around the central axis under CWP conditions, while the outward flows towards the spanwise direction are found to be intensified due to the height difference between the two buildings. Similar observations have been reported in previous studies (Park et al., 2019; Li et al., 2020). The introduction of elevated structures leads to an increased collision intensity between the throughflow from the elevated structure and the downwash flow of the upstream building, thereby amplifying wind velocity in the building gaps. The stable primary vortex observed under CWP tends to exhibit a rightward inclination in flow fields under TWPs, subsequently exerting an influence on the corner stream of the downstream building. This fundamentally alters the distribution of the entire flow field, which diverges significantly from that observed in CWP.

(2) Experiment results demonstrate that adjusting the height disparity of elevated buildings presents a feasible approach to enhance the wind environment in regions characterized

by topography-induced twisted wind profiles. By utilizing step-up and step-down building configurations effectively, the local wind environment can be altered in a significant manner. Adding the downstream building height is more effective in mitigating LWV areas compared to increasing the height of the upstream building. The observed variation enhancement under TWPs with uneven building heights is consistent with those reported for CWP by Hang et al. (2012) and Tang et al. (2023).

(3) The step-up and step-down building configurations exhibit distinct sensitivities to the twisted wind. The impact of twisted wind on the wind field becomes increasingly prominent in the presence of height heterogeneity between two tandem buildings, resulting in an amplified discrepancy in wind velocities between the two ends of the building, accompanied by an observed larger deviation angle (β). For step-down configuration, the flow field surrounding two tandem buildings resembles that of identical height configurations, with a constant deviation angle (β) maintained across all variations in height differences within step-down building arrangements.

(4) The elevated structure significantly affects CS, DFLWV, and NFLWV areas under CWP and TWPs. When situated upstream, elevated buildings result in a corner stream with greater magnitude compared to non-elevated buildings. Conversely, when located downstream, it eliminates the NFLWV area as opposed to non-elevated structures and leads to the smaller DFLWV areas. A greater deviation angle (β) for DFLWV zones is observed when an elevated structure is located downstream, indicating that the elevated buildings are more susceptible to the twisted wind effect compared to non-elevated buildings.

(5) The impact of TWPs on the LWV area exhibits contrasting behavior for step-up and step-down building configurations. The twisted wind tends to reduce the regions of low wind velocity in step-up building configurations, while it tends to increase these regions

in step-down building configurations. For windy wind conditions, the sides of the two tandem buildings are categorized as “Strolling” and “Walking fast”, providing opportunities for recreational activities. These recreational areas tend to shift to the right side with a larger expanse. For step-up building configuration, the area within the passage between the two buildings is classified as “Strolling” and “Walking fast”, while it is classified as “Sitting short” for step-down building configuration and two tandem buildings with identical heights.

(6) The twisted wind has the potential to compromise thermal comfort in the vicinity of the two tandem buildings during summer while creating a more favourable thermal environment in winter. The area of more favourable thermal comfort is observed to increase with the height of two tandem identical buildings in summer. The step-down building configuration generates a smaller PET value than the step-up building configuration and demonstrates superior thermal comfort. The twisted wind effect tends to result in a higher proportion of the area being classified as “Neutral” with smaller PET values compared to under CWP during winter.

This chapter offers valuable recommendations for urban planners on implementing elevated structures in hilly urban areas prone to frequent twist flows. Our findings confirm that the presence of elevated structures enhances sensitivity to the twisted wind effect, leading to a greater deviation of DFLWV areas from the building center line. These flow modifications were not adequately captured in the wind environment considered in CWP, and for buildings without elevated structures. Neglecting these effects would result in an underestimation of both maximum pollutant concentration and its spatial distribution due to deviations in low wind velocity zones where pollutants are thoroughly mixed. The prediction of reduced high wind velocity areas under TWPs could prove valuable in mitigating unnecessary expenses associated with corrective measures taken against overestimated high-velocity areas around building corners, as per the conventional wind profile, thereby enabling better urban design for sustainable cities. This chapter also serves as a valuable source of inspiration for effectively utilizing the relative height difference between adjacent buildings to optimize the surrounding wind patterns and enhance thermal comfort. For instance, to improve wind conditions in the passage between two buildings, it is recommended that the upstream building be reconstructed at a lower height than the existing high-rise structure. However, in mountainous regions characterized by prevailing twisted winds, the high wind velocity zone may shift towards one end of the passages, potentially causing discomfort to pedestrians due to strong winds during extreme weather conditions. The results presented in this chapter are also expected to be valuable databases for future CFD simulations.

CHAPTER 6. Numerical evaluation of the effect of twisted wind on pedestrian comfort surrounding semi-open structures and influential factors under solar heating

6.1 Introduction

This chapter applied the steady RANS model with standard $k-\varepsilon$ models with discrete ordinate (DO) radiation to investigate the effects of twisted wind on wind and thermal comfort surrounding semi-opening structures. Additionally, various influential factors, such as elevation ratio (h/H), arcade width ratio (w/D), street canyon width (W/H), street canyon length (L/D), asymmetric height ratios (h_u/h_d), were investigated under both conventional wind profile (CWP) and twisted wind profile (TWP). Previous research on the impact of arcade design has primarily focused on conventional wind profiles, leaving a gap in understanding their applicability to regions where urban terrain significantly influences PLW and thermal comfort. The thermal effects around multiple buildings with arcade design and the thermally induced flow have not been taken into consideration in many previous studies. The investigation of the combined effects of arcade design parameters and twisted wind under solar radiation is therefore imperative. Furthermore, previous studies on twisted wind primarily focused on top entrainment (Tse et al., 2017); nevertheless, considering that street canyons have finite lengths, our concern lies in understanding the influence of lateral entrainment on flow structures within the street under TWPs. This chapter aims to evaluate the performance of arcade design under CWP and TWP, taking solar radiation into consideration. The objectives of the present chapter are outlined as follows: 1) to simulate the twisted wind flow field and evaluate the thermal environment under the influence of solar radiation; 2) to investigate the flow patterns in street canyon with arcade design, considering various design parameters under CWP and TWPs; 3) to assess the thermal comfort for various street canyon configurations featuring arcade structures under CWP and TWPs.

6.2 Methodology

6.2.1 Model description

The CFD simulation incorporates generic street canyon configurations with arcade design characterized by different design parameters (Table 6.1) (Chatzidimitriou and Yannas, 2017). The parametric studies encompassed variations in the elevation ratio (h/H), arcade width ratio (w/D), street canyon width and height ratios (W/H), street canyon length and depth ratios (L/D), and asymmetric height ratios between upstream and downstream structures (h_u/h_d) (Figure 6.1 (d)). To investigate the effects of different sidewalk area dimensions within the arcade design, various arcade elevation ratios (h/H) and width ratios (w/D) were examined (Wen et al., 2017). In addition to examining the influential factors of the arcade itself, this chapter also explored the effects of street canyon configurations such as street canyon width and height ratios (W/H), street canyon length and depth ratios (L/D), and asymmetric height ratios (h_u/h_d). The W/H of the canyons were carefully chosen for W/H=0.25, 0.75, 1.25, and 1.5 to faithfully replicate distinct flow regimes, encompassing skimming and wake interference in order to accurately simulate a wide range of urban canyon configurations (Ali-Toudert and Mayer, 2006; Oke, 1988). Li et al. (2024) used the wind tunnel experiment to investigate the flow field around two buildings arranged in tandem with a small side ratio (L/D). However, for high-rise buildings with a smaller side ratio, flow separation only occurs at the front corner, whereas for buildings with larger side ratios, flow separation simultaneously takes place at both leading and rear corners, resulting in more intricate flow motion (Lin et al., 2005). Therefore, assessing pedestrian comfort in the vicinity of buildings with a high L/D under TWP can be highly intricate and necessitates further investigation. The street length and depth ratios (L/D) were selected for 1, 3, 5, and 10 to represent the short, medium, and long street canyons (Li et al., 2021). The prevailing wind direction in Hong Kong is predominantly from the east (HKO, 2019), and thus, this chapter adopted this dominant wind direction for analysis.

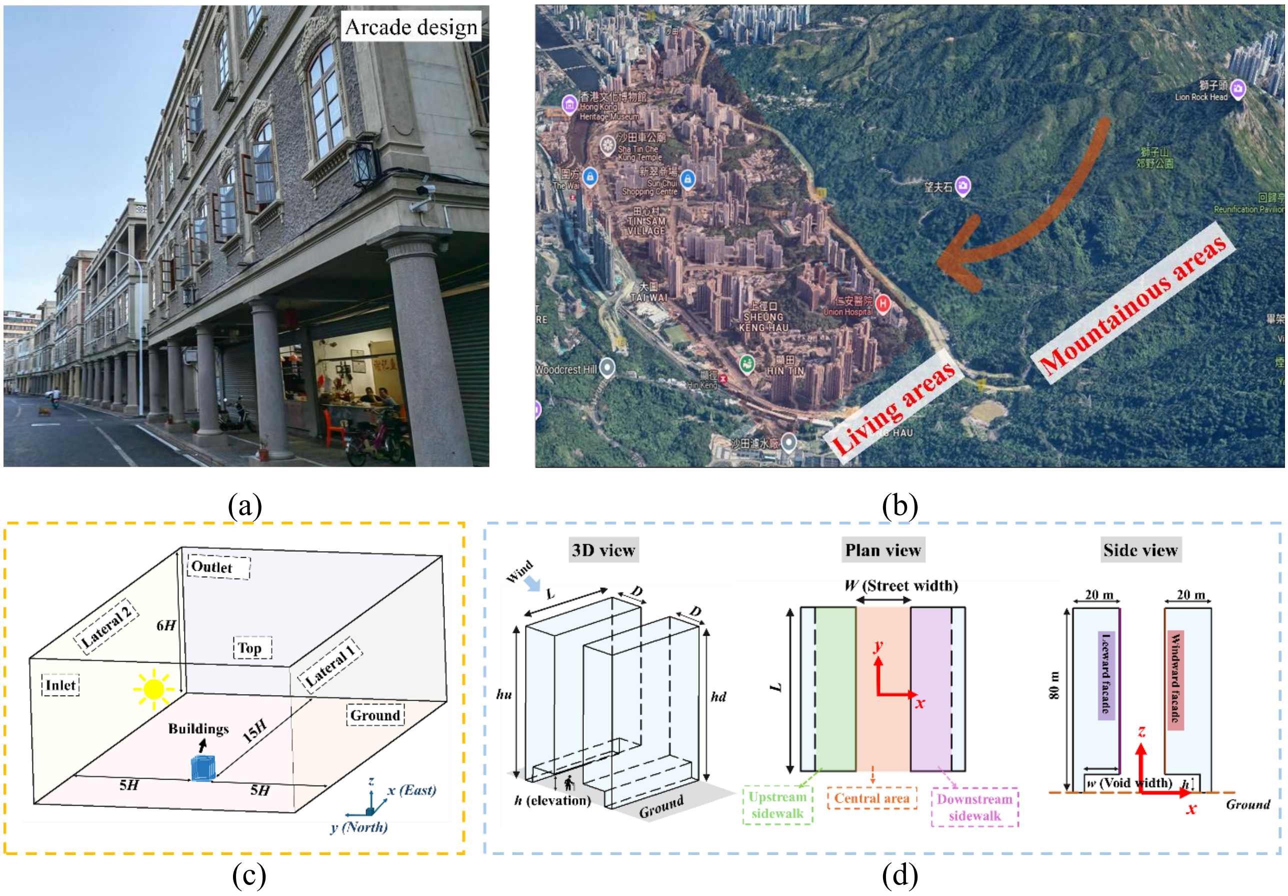

Figure 6.1. (a) Photographs depicting the arcade design in urban streets of Guangdong Province, China (Internet figure), (b) Residential areas near the mountains influenced by TWP, and Schematics of (c) boundary conditions and (d) geometric models and interest areas.

Table 6.1. Details of simulation cases.

Elevation ratio (*h*/*H*)	Arcade width ratio (*w*/*D*)	Street canyon width (*W*/*H*)	Street canyon length (*L*/*D*)	Asymmetric height ratios (h_u/h_d)	Parameter considered	Figure
0.05-0.2	0.5	0.25	3	1	*h*/*H*: 0.05, 0.1, 0.15, 0.2	Figure 6.8
0.1	**0.25-0.75**	0.25	3	1	*w*/*D*: 0.25, 0.5, 0.75	Figure 6.10 Figure 6.11
0.1	0.5	**0.25-1.5**	3	1	*W*/*H*: 0.25, 0.75, 1.25, 1.5	Figure 6.12
0.1	0.5	0.25	**1, 3, 5,10**	1	*L*/*D*: 1, 3, 5, 10	Figure 6.14
0.1	0.5	0.25	3	**0.5, 0.75, 1, 1.33, 2**	h_u/h_d: 0.5, 0.75, 1, 1.33, 2	Figure 6.16

6.2.2 CFD simulations

6.2.2.1 The inflow boundary conditions of CWP and TWPs

The CWP and TWP 25 were simulated in this chapter based on the wind profile generated in the wind tunnel experiment, all other details of the wind tunnel experiments investigating the flow field around tandem elevated buildings can be found in previous publications by the author (Li et al., 2024; Li et al., 2024). TWP 25 denotes the twisted wind profile where the maximum twist angle measured at ground level is 25 degrees, whereas CWP refers to the conventional wind profile. The domain inlet was set as the velocity-inlet boundary condition, and the measured wind profile, including the mean wind velocity (U/U_{ref}), was obtained from the wind tunnel experiment (Li et al., 2024) and expressed as the logarithmic function of height (Equation (6.1)). The twist in the wind direction can be explained by the Ekman Spiral effect due to the Earth's rotation, and the components of the wind velocity (*u* and *v*) can be described by the Equation (6.2) and Equation (6.3) (Ekman, 1905), the variation of the wind direction along the vertical height is characterized by the Equation (6.4). The twist angle profile was derived from the curve fitting of wind tunnel experimental results using the exponential equation for twist angle proposed by Tse et al., 2016, as shown in the Equation (6.5).

$$u_{(z)} = \frac{u^*_{ABL}}{\kappa}\ln(\frac{z+z_0}{z_0}) \quad (6.1)$$

$$u_{(z)} = u_g[1-e^{-z/h_E}\cos(\frac{z}{h_E})] - v_g e^{-z/h_E}\sin(\frac{z}{h_E}) \quad (6.2)$$

$$v_{(z)} = v_g[1-e^{-z/h_E}\cos(\frac{z}{h_E})] + u_g e^{-z/h_E}\sin(\frac{z}{h_E}) \quad (6.3)$$

$$\theta_{(z)} = \arctan(\frac{v_{(z)}}{u_{(z)}}) \quad (6.4)$$

$$\theta_{(z)} = \theta_0 \exp(\alpha_0 \times z / \beta_0) \quad (6.5)$$

where frictional velocity u^*_{ABL} =0.37 m/s; dynamic roughness height z_0 =0.00025 m; von Karman constant κ =0.4187 and the model constant C_μ=0.09; u_g and v_g are the gradient wind velocity components; h_E is the Ekman height ($h_E = \sqrt{2K/f}$), f is the Coriolis parameter, and K is the turbulence coefficient; $\theta_{(z)}$ is the twist angle along the vertical height; θ_0 is the yaw angle measured at the lowest height; The constants α_0 and β_0 , derived from the line fitted to the twist angle profile of the incident flow, were -10.9 and 9.2 respectively. The turbulence intensity profile ($I_{(z)}$) was obtained by fitting the wind tunnel data, and the inlet turbulence kinetic energy $k_{(z)}$ was derived from Equation (6.6) (Blocken et al., 2012). The inlet turbulence dissipation rate $\varepsilon_{(z)}$ can be calculated as in the Equation (6.7) based on the relationship between the $k_{(z)}$ and $\varepsilon_{(z)}$ proposed by Weerasuriya et al. (2018). The simulation was based on the horizontal homogeneous assumption ($\partial/\partial x = 0$ and $\partial/\partial y = 0$) and the vertical wind velocity $w = 0$, which has also been made in previous literature (Yang et al., 2009; Weerasuriya et al., 2018). Figure 6.2 (a) describes the incoming flow wind profile and twist angle profile in the wind tunnel experiment, and Figure 6.2 (b)-(f) shows the simulated inlet conditions in CFD.

$$k_{(z)} = \frac{3}{2}(I_{(z)}u_{(z)})^2 \tag{6.6}$$

$$\varepsilon_{(z)} = \sqrt{C_\mu}k_{(z)}\sqrt{(\frac{\partial u}{\partial z})^2 + (\frac{\partial v}{\partial z})^2} \tag{6.7}$$

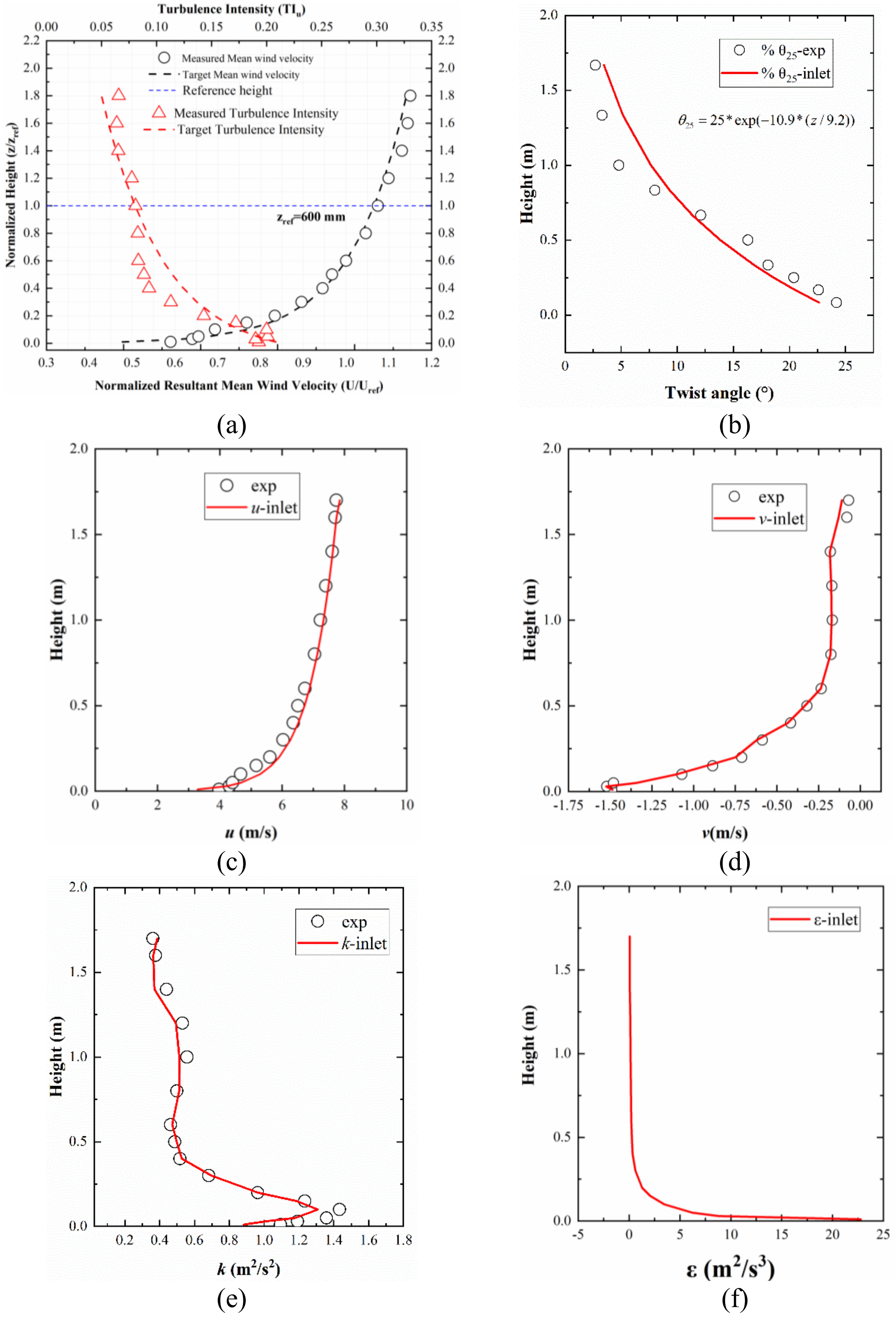

Figure 6.2. The inlet conditions for (a) Normalized resultant wind velocity and turbulence intensity profiles; (b) Twist angle profile; (c) Velocity at streamwise direction; (d) Velocity at lateral direction; (e) Turbulence kinetic energy, and (f) Turbulence dissipation rate in CFD simulation.

6.2.2.2 Computational domain and boundary conditions

The reduced scale ratio of 1:200 was employed in this chapter, which is consistent with the ratio adopted in the wind tunnel test (Li et al., 2024). The study conducted by Ai and Mak. (2014) highlights the potential of employing reduced-scale models with similarity criteria in CFD simulations for wind-related issues, enabling significant savings in computational resources without compromising accuracy. The computational domain extends to distances of 5 H_{max}, 5 H_{max}, and 15 H_{max} from the boundaries of the building models, respectively (Figure 6.1 (c)), adhering to the best practices of CFD simulations (Tominaga et al., 2008). The H_{max} is the larger of h_u and h_d, h_u and h_d are the heights of the upstream and downstream street canyon height. The simulation of CWP and TWP 25 involved the definition of three velocity inlets, with Table 6.2 presenting the corresponding boundary conditions utilized. The definition of ground roughness conditions incorporated the modification of sand-grain wall functions, adopting the suggested roughness height $k_s = 9.793 z_0 / C_s$ by Blocken et al. (2007). The domain was discretized into structured hexahedral cells, with a minimum grid size of 2 mm and a maximum expansion ratio of 1.17.

Table 6.2. Boundary conditions for the computational domain.

Location	Boundary type	Profiles
Inlet	Velocity inlet	CWP: $u_{(z)}$: Eq. (6.1); $k_{(z)}$: Eq. (6.6); $\varepsilon_{(z)}$: Eq. (6.7) TWP: $u_{(z)}$: Eq. (6.1); $v_{(z)}$:Eq. (6.4); $k_{(z)}$: Eq. (6.6); $\varepsilon_{(z)}$: Eq. (6.7)
Lateral 1	Velocity inlet under TWP, Symmetry under CWP	TWP: $u_{(z)}$: Eq. (6.1); $v_{(z)}$:Eq. (6.4); $k_{(z)}$: Eq. (6.6); $\varepsilon_{(z)}$: Eq. (6.7)
Lateral 2	Velocity inlet under TWP, Symmetry under CWP	TWP: $u_{(z)}$: Eq. (6.1); $v_{(z)}$:Eq. (6.4); $k_{(z)}$: Eq. (6.6); $\varepsilon_{(z)}$: Eq. (6.7)
Outlet	Outflow	$\frac{\partial}{\partial x}(u, v, w, k, \varepsilon) = 0$

Top	Free slip	$w=0$; $\frac{\partial}{\partial z}(u,v,w,k,\varepsilon)=0$
Ground	No-slip wall	Roughness height k_s=0.0004 Roughness constant C_s=9.793z_0/k_s

6.2.2.3 Radiation modelling

The radiation simulations were conducted at LSTs (local solar times) of 1500 LST (3 p.m.) during a summer day in Hong Kong (coordinates : $22^{\circ}18'$N, $114^{\circ}10'$E; date: June 15) with inlet temperatures of 29.1 °C for 3 p.m. (Li et al., 2020; Li et al., 2020). The solar radiation is capable of heating the outer surface of the building, thereby inducing upward natural convection flows adjacent to the wall (Mu et al., 2018). These flows have a significant impact on wind patterns and thermal comfort and should not be disregarded. To accurately predict the wall temperature of buildings, the Solar Calculator function in Ansys Fluent can be utilized to calculate the radiative heat fluxes resulting from solar radiation. Additionally, the Solar Ray Tracing function enables the prediction of direct illumination energy sources generated by incident solar radiation. Additionally, the discrete ordinates (DO) radiation model was employed to compute the radiation heat flux between the surfaces. The DO model transforms the radiative transfer equation (RTE) into a transport equation for radiation intensity in the spatial coordinates (Chui, 1993), and the governing equations of the DO model can be expressed as follows:

$$\nabla\cdot(I_r(\vec{r},\vec{s})\vec{s})+(a+\sigma_s)I_r(\vec{r},\vec{s})=an^2\frac{\sigma T_L{}^4}{\pi}+\frac{\sigma_s}{4\pi}\int_0^{4\pi}I_r(\vec{r},\vec{s}^{\,'})\Phi(\vec{s},\vec{s}^{\,'})d\Omega^{'} \tag{6.8}$$

Here, $\vec{r}$ and $\vec{s}$ are position and direction vectors respectively; $\vec{s}^{\,'}$ is the scattering direction vector; a is the absorption coefficient; n is the refractive index; σ_s is the scattering coefficient; σ is the Stefan-Boltzmann constant; I_r is the radiation intensity; T_L is the local temperature; Φ is the phase function and $\Omega^{'}$ is the solid angle. The heat transfer coefficient

(h_c) between the building faces and the ground is determined by $h_c = 5.7 + 3.8V_{air}$ (Yang et al., 2017), where V_{air} is the airflow velocity. The materials were specified as concrete for buildings, while the ground materials were designated as asphalt. For the building wall surfaces, the density, specific heat, thermal conductivity, and emissivity were set as 2400 kg/m^3, 750 J/kgK, 1.7 W/mK, and 0.7, respectively. For the ground, those properties were set at 2360 kg/m^3, 920 J/kgK, 0.75 W/mK, and 0.95, respectively.

6.2.2.4 Turbulence model and Solver settings

The steady RANS equations were employed to assess wind and thermal comfort in the presence of twisted winds. This assessment was based on the conservation equations of mass, momentum, and energy for the incompressible turbulence flow (Li et al., 2020; Hang et al., 2024, Launder, 1972). The corresponding governing equations are as Equations (6.9)-(6.13):

Mass conservation equation:

$$\frac{\partial(\rho u_i)}{\partial x_i} = 0 \tag{6.9}$$

Momentum and thermal transport equation:

$$\frac{\partial(\rho u_i u_j)}{\partial x_j} = -\frac{\partial p}{\partial x_j} + \frac{\partial}{\partial x_j}(\mu_o \frac{\partial u_i}{\partial x_j}) - \beta g \rho \Delta T_a \delta_{ij} \tag{6.10}$$

$$\frac{\partial(\rho u_i T_a)}{\partial x_i} = \frac{\partial}{\partial x_i}(\alpha T_a \frac{\partial T_a}{\partial x_i}) + \frac{Q_T}{c_P} + \frac{1}{c_P}(\frac{\partial q_{ri}}{\partial x_i}) \tag{6.11}$$

Turbulence kinetic energy (k) and dissipation rate (ε) equation:

$$u_i \frac{\partial k}{\partial x_i} = \frac{\partial}{\partial x_j}[(\mu + \frac{\mu_t}{\sigma_k})\frac{\partial k}{\partial x_j}] + \frac{1}{\rho}(P_k + P_b) - \varepsilon \tag{6.12}$$

$$u_i \frac{\partial \varepsilon}{\partial x_i} = \frac{\partial}{\partial x_j}[(\mu + \frac{\mu_t}{\sigma_\varepsilon})\frac{\partial \varepsilon}{\partial x_j}] + \frac{1}{\rho}C_1 \frac{\varepsilon}{k}(P_k + P_b) - C_2 \frac{\varepsilon^2}{k} \tag{6.13}$$

where u_i and u_j denotes the air velocity of the *i*-axis and *j*- axis components, respectively; p is the pressure and ρ is the density; μ is the kinetic viscosity; μ_t is the turbulent eddy viscosity and is defined as $\mu_t = C_\mu \dfrac{\rho k^2}{\varepsilon}$; δ_{ij} denotes the Kronecker delta; T_a denotes the air temperature and αT is the thermal diffusivity; Q_T and q_r is the heat production and the radiative heat flux respectively; C_p is the specific heat; P_k and P_b is the turbulence production term due to the mean velocity shear and buoyancy; C_1, C_2 and C_μ are the empirical constants at 1.44, 1.92, and 0.09 separately; σ_k and σ_ε are Parandtl numbers.

The standard $k-\varepsilon$ model has been validated for effectively characterizing turbulent flow phenomena, including airflow in urban areas influenced by thermal buoyancy forces (V. Yakhot, 1986). The successful modeling of the twisted wind profile by the standard $k-\varepsilon$ model has also been reported by Yuan et al. (2022). Although LES outperforms the steady RANS in modeling turbulence, the RANS method remains the predominant method employed in urban physics due to its accurate representation of mean quantities and computational efficiency (Toparlar et al., 2017). The governing equations were solved utilizing ANSYS Fluent 19.0, with pressure-velocity coupling accomplished via the implementation of the SIMPLEC algorithm. A second-order method was employed for pressure interpolation, along with second-order upwind schemes for handling convection terms in the governing equations. The residuals for the continuity, momentum, k, and ε were set as 10^{-4}, 10^{-6}, 10^{-6}, and $10^{-5,}$ respectively. The simulations are deemed to have converged when the residuals fall below the predefined threshold values. Furthermore, convergence is also verified in the **APPENDIX** by ensuring that the velocity and temperature values at monitoring points remain unchanged for more than 500 iterations.

6.2.3 Assessment for wind and thermal comfort

PLWEs were quantified using the mean wind velocity ratio (U/U_{ref}), which represents the ratio of mean wind velocity at the pedestrian-level height and the mean wind velocity at the reference heights similar to Chapter 3. In this chapter, a reference height of 200 m was assumed in accordance with the prototype (Du et al., 2017). The Physiological Equivalent Temperature (PET) was employed to evaluate the thermal comfort at the pedestrian level (Hang et al., 2024). The PET model, derived from the Munich Energy-balance model for individuals, incorporates both short-wave and long-wave radiation flux and is widely utilized in outdoor environments (Höppe, 1999). The RayMan model was employed to calculate the PET value based on the assumption of a male with a height of 1.7 m and a weight of 75 kg while considering a clothing level of 0.5 clo. The Sky View Factor (SVF) was calculated based on a virtual fish-eye image captured at the pedestrian level using SkyHelios (Ketterer et al., 2017). The mean radiant temperature (T_{mrt}) is 58.6 °C and 31.6 °C, and the relative humidity(%) is 86.7 and 83 for the podium and elevated area, based on the measurement results from Du et al. (2017). The thermal comfort sensation employed in this chapter was based on the climatic similarities between Hong Kong and Singapore, both characterized by hot and humid weather conditions, as listed in Table 6.3.

Table 6.3. PET value for different thermal sensations in Singapore (Yang et al., 2013).

PET (°C)	Thermal sensation
20-24	Slightly cool
24-30	Neutral
30-34	Slightly warm
34-38	Warm
38-42	Hot
>42	Very hot

6.3 CFD simulation verification and validation

Before validation, the grid sensitivity test was conducted, and three grid sizes were compared (Figure 6.3). These included the coarse grid (1,849,976 cells, the smallest cell size: 4 mm), medium grid (3,974,328 cells, the smallest cell size: 2 mm), and fine grid (5,031,558 cells, the smallest cell size: 1 mm) (Figure 6.3 (a) and (b)). To ensure grid independence, the grid convergence index (*GCI*) was employed between the medium and fine grid arrangements for validation, as shown in the Equation (6.14) (Roache, 1997). The *GCI* values for y=0.2 m, 0.1 m, and 0 m under CWP along the horizontal lines were recorded as 0.06%, 0.07%, and 0.06% respectively, while under TWP they were measured as 0.09%, 0.07%, and 0.07% respectively for y=0.1 m, 0 m, and 0.1 m. Therefore, the discrepancy between medium and fine meshes was negligible, the medium mesh was employed for subsequent simulations.

$$GCI = F_S \left| \frac{r^p (u_{i,grid1} - u_{i,grid2}) / U_{ref}}{1 - r^p} \right| \tag{6.14}$$

where F_s is the safety factor, r is the linear grid refinement, p is the formal order accuracy and u_i is the wind velocity under different grids, U_{ref} is the reference wind velocity at 1 m.

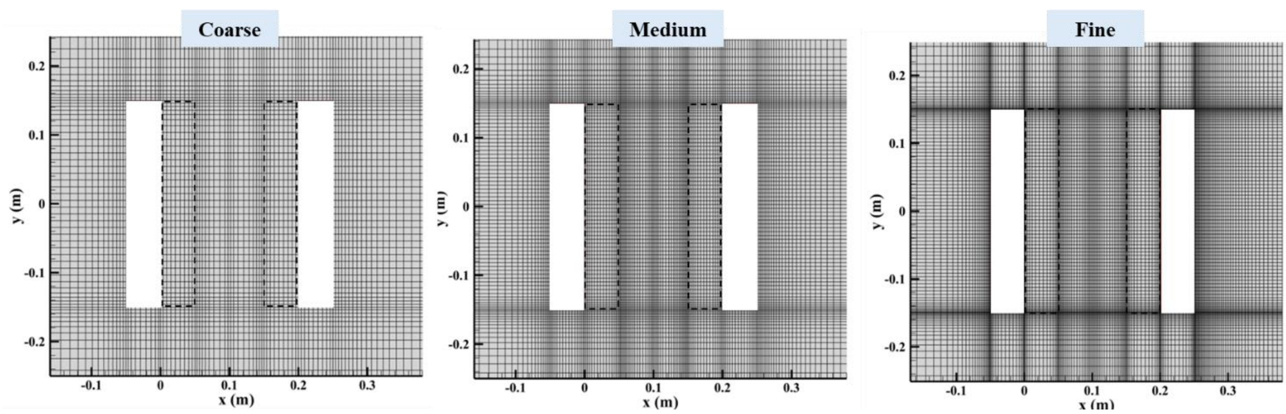

(a)

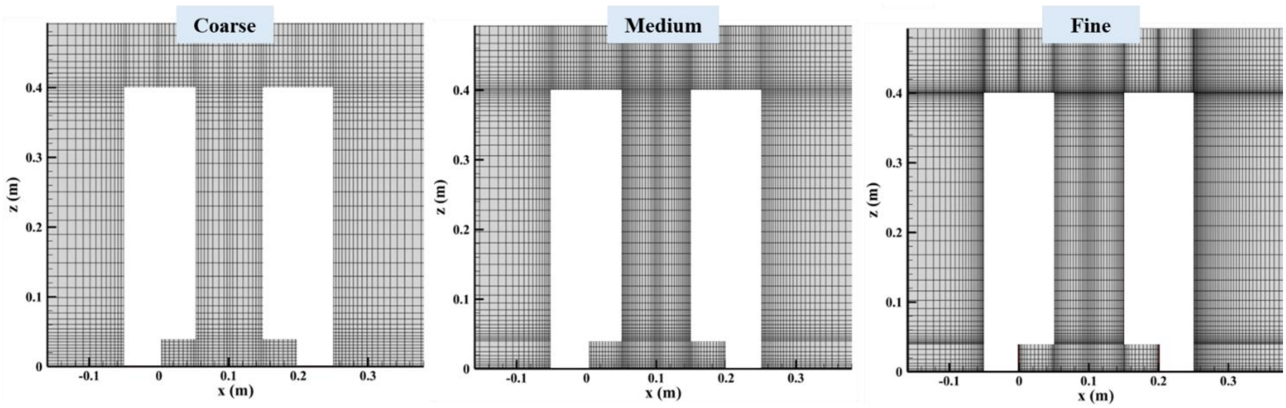
Coarse
Medium
Fine
z (m)
x (m)

(b)

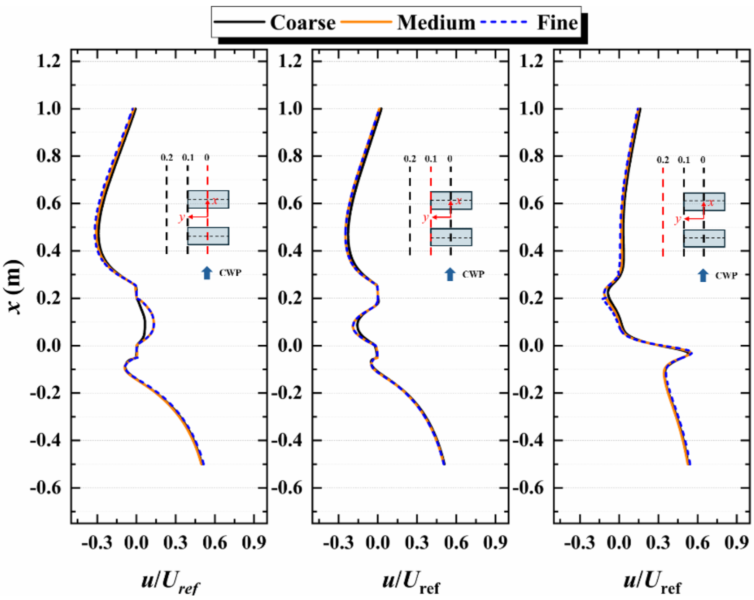
Coarse
Medium
Fine
x (m)
u/U_ref
CWP

(c)

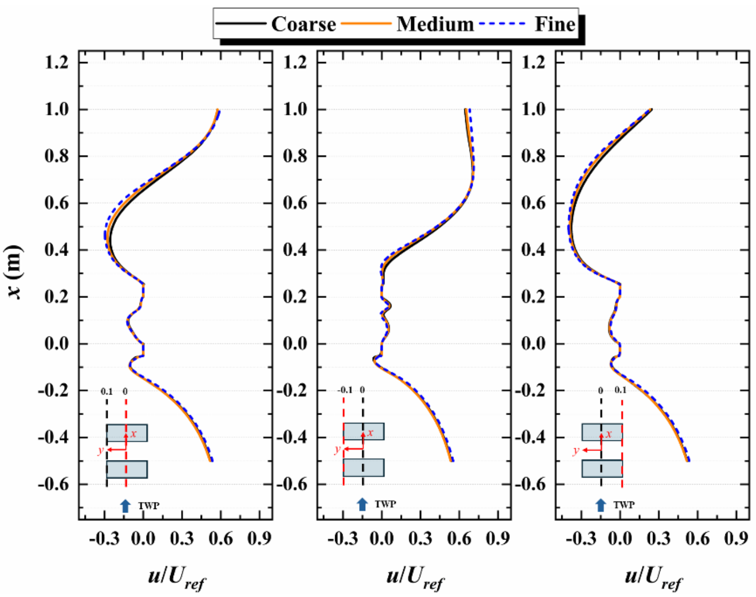
Coarse
Medium
Fine
x (m)
u/U_ref
TWP

(d)

Figure 6.3. Grid arrangement in (a) *x-y* plane, (b) *x-z* plane, and comparison of u/U_{ref} along three horizontal lines under (c) CWP and (d) TWP.

To evaluate the accuracy of CFD simulation results for tandem buildings subjected to CWP and TWP, the wind tunnel experiment results were employed as a benchmark for assessing the simulation results. The current numerical model for validating the isothermal airflow around two elevated buildings in tandem arrangement was validated against the wind tunnel measurements conducted in the authors' previous publications (Li et al., 2024). Two elevated buildings have identical main body heights of 0.17 m, accompanied by an elevated column height of 0.03 m, and are separated by a distance of 0.2 m (Figure 6.4 (a) and (b)). The twisted wind profile TWP 25 was accurately replicated by the twist vanes in the wind tunnel. The wind velocity at the pedestrian level (2 m in prototype scale) was measured using Kanomax sensors surrounding the buildings. The validation was conducted based on the two-dimensional velocity magnitude ($U = \sqrt{u^2 + v^2}$) at the pedestrian level (z=0.01 m) due to the limitations of the Kanomax sensors. The normalized mean wind velocity (U/U_{ref}) obtained from $k-\varepsilon$ turbulence model using standard (STD), realizable (RLZ), renormalized group (RNG) and $k-\omega$ SST (SST) models, as well as wind tunnel experiment results under CWP and TWP at measurement lines of x=-0.225 m, 0 m, 0.075 m, 0.31 m, 0.385 m, 0.535 m, are compared in Figure 6.4 (c) and (d).

The sensitivity of turbulence models in RANS was evaluated by comparing time-averaged streamlines and velocity magnitudes over a horizontal plane at the pedestrian level (Figure 6.5). Although the twisting of flows was predicted by all RANS models, significant deviations were observed in the wake region. Specifically, both the size and intensity of the circulation were underestimated (x=0.535 m) relative to the wind tunnel experiment results. This discrepancy arises due to the limitations of the steady RANS approach in accurately predicting vortex shedding in the wake region (Blocken, 2014). All RANS models tended to underestimate the twisting phenomenon of the flows compared to experimental results. Notably, the RNG model predicted a smaller wake area than the STD, RLZ, and SST models, which resulted in a greater underestimation of the twist angle relative to wind tunnel experiments. Similar phenomena were observed from Yuan et al. (2022), where the RNG model tends to predict a smaller wake length and twist angle compared with the other two turbulence models. Overprediction of the velocity by the RNG and SST models was also observed in the corner flow adjacent to the upstream building. The performance of the three turbulence models was quantitatively assessed by several validation metrics (Table 6.4), these metrics included the hit rate (q), the fraction bias (FB), the fraction of predictions within a factor of two of observations ($FAC2$), the Pearson correlation coefficient (R), and the normalized mean square error ($NMSE$). This chapter employed the criteria proposed by the literature (Hanna and Chang, 2012; I. Goricsán, 2011; Moonen and Allegrini, 2015): q>0.5, FB<1.5, $FAC2$>0.5, R>0.8, and $NMSE$<4. The standard $k-\varepsilon$ turbulence model satisfies all validation metrics under both CWP and TWP, demonstrating high R and FB values. Consequently, it was selected for the remaining CFD simulations in this chapter.

In addition, the air temperature and building wall temperature due to thermal effects and solar radiation were validated in the **APPENDIX**. For the validation of the wall temperature, the simulated wall temperatures exhibited good agreement with both the measurement data from Idczak et al. (2006) and the simulated data from Xu et al. (2023). This consistency confirms the reliability of the temperature simulations in the present chapter. For the validation of thermal comfort, the simulated wind velocity and air temperature data demonstrated alignment with the wind tunnel experiment results when the ground was heated.

Table 6.4. Metrics for validation of wind velocities by comparing CFD simulations and wind tunnel results under CWP and TWP 25.

		(a) CWP					**(b) TWP 25**				
	Metric	***q***	***FB***	***FAC2***	***R***	***NMSE***	***q***	***FB***	***FAC2***	***R***	***NMSE***
	***x*=-0.225 m**	0.86	-0.07	1	0.97	0.019	1	-0.09	1	0.92	0.02
	***x*=0 m**	0.57	0.125	0.71	0.96	0.055	0.86	0.00084	1	0.93	0.02
STD	***x*=0.075 m**	1	0.339	1	0.91	0.005	0.75	0.06	1	0.87	0.06
	***x*=0.31 m**	0.71	0.182	0.71	0.98	0.055	0.86	0.00015	1	0.97	0.02
	***x*=0.385 m**	0.57	0.113	0.71	0.96	0.081	0.71	0.03	0.86	0.92	0.06
	***x*=0.535 m**	0.57	0.131	0.86	0.97	0.063	0.57	0.076	0.57	0.97	0.13
	***x*=-0.225 m**	0.86	-0.05	1	0.97	0.013	1	-0.088	1	0.94	0.02
	***x*=0 m**	0.57	0.18	0.71	0.95	0.090	0.71	0.055	1	0.98	0.01
RLZ	***x*=0.075 m**	1	0.02	1	0.91	0.004	0.75	0.11	1	0.97	0.06
	***x*=0.31 m**	0.43	0.21	0.71	0.97	0.07	0.71	0.035	0.86	0.96	0.05
	***x*=0.385 m**	0.57	0.08	0.71	0.96	0.06	0.86	-0.07	1	0.99	0.01
	***x*=0.535 m**	0.29	0.18	0.57	0.97	0.09	0.57	0.02	0.86	0.98	0.06
	***x*=-0.225 m**	0.43	-0.003	1	0.97	0.016	1	-0.04	1	0.96	0.02
	***x*=0 m**	0.57	0.127	0.57	0.96	0.062	0.43	0.03	1	0.99	0.007
RNG	***x*=0.075 m**	0.75	-0.22	1	0.91	0.001	0.75	-0.044	1	0.21	0.006
	***x*=0.31 m**	0.43	0.06	0.71	0.88	0.07	0.29	-0.06	0.86	0.79	0.09
	***x*=0.385 m**	0.57	0.052	0.71	0.94	0.07	0.86	-0.06	1	0.99	0.01
	***x*=0.535 m**	0.29	0.19	0.29	0.99	0.07	0.57	0.15	0.71	0.99	0.08
	***x*=-0.225 m**	1	-0.998	1	0.97	0.015	1	-0.12	1	0.96	0.03
	***x*=0 m**	1	-0.08	1	0.98	0.015	0.86	-0.003	0.86	0.99	1.14
SST	***x*=0.075 m**	1	-0.03	1	0.91	0.001	1	-0.04	1	0.8	0.009
	***x*=0.31 m**	0.43	0.31	0.71	0.95	0.125	0.86	-0.11	1	0.97	0.03
	***x*=0.385 m**	0.57	-0.09	1	0.92	0.06	0.71	0.01	0.86	0.82	0.1
	***x*=0.535 m**	0.71	-0.103	0.96	0.96	0.044	0.57	0.05	0.57	0.97	0.1

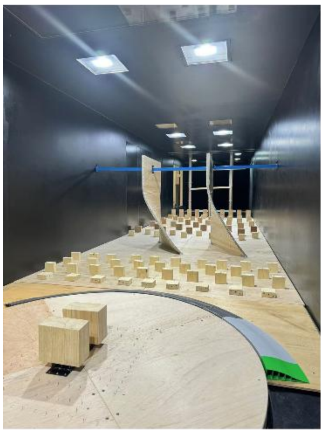

(a)

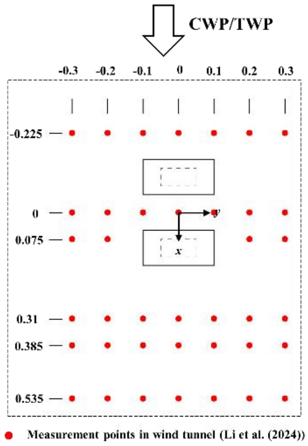
CWP/TWP
-0.3 -0.2 -0.1 0 0.1 0.2 0.3
-0.225
0
0.075
0.31
0.385
0.535
y
x
Measurement points in wind tunnel (Li et al. (2024))

(b)

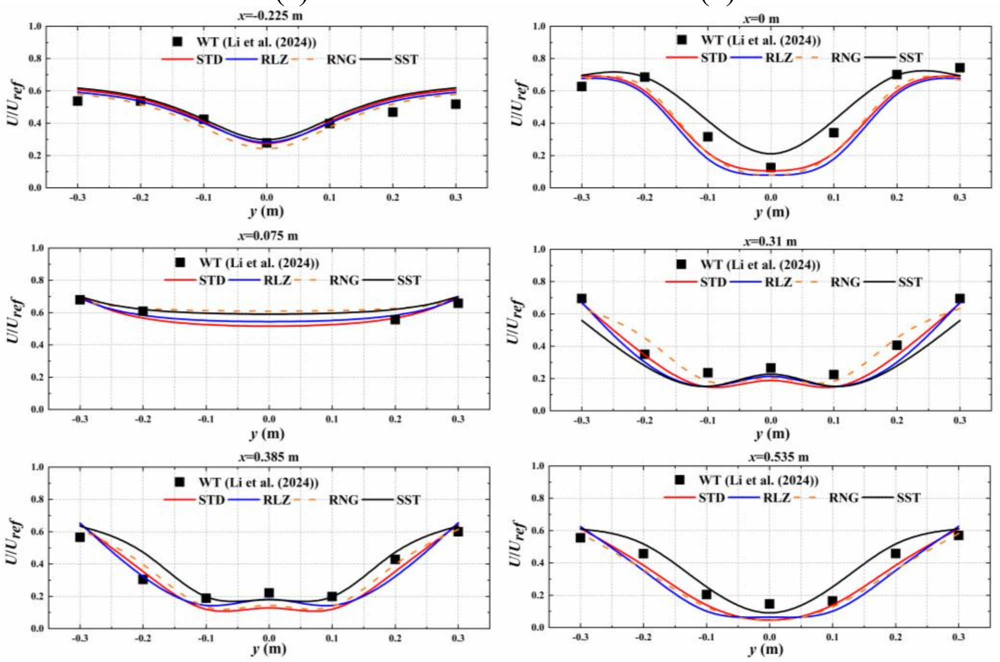
x=-0.225 m
x=0 m
x=0.075 m
x=0.31 m
x=0.385 m
x=0.535 m
WT (Li et al. (2024))
STD
RLZ
RNG
SST
U/Uref
y (m)

(c)

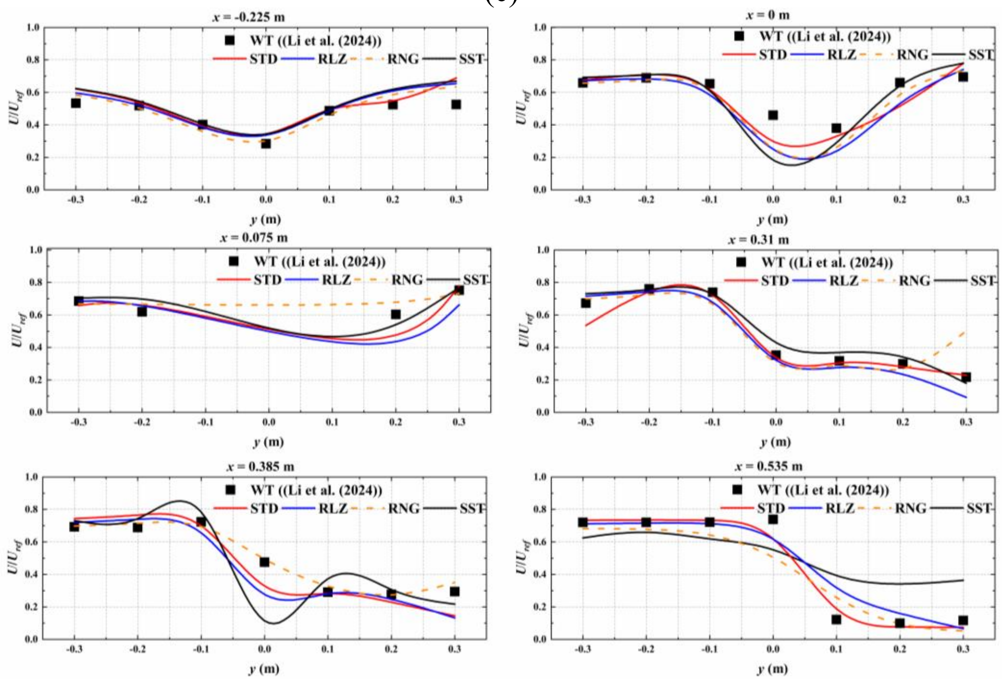
x = -0.225 m
x = 0 m
x = 0.075 m
x = 0.31 m
x = 0.385 m
x = 0.535 m
WT ((Li et al. (2024))
STD
RLZ
RNG
SST
U/Uref
y (m)

(d)

Figure 6.4. (a) Inside view of the wind tunnel experiment and schematics (Li et al., 2024) for (b) Wind tunnel test measurement points and comparison of U/U_{ref} values at different lines under (c) CWP and (d) TWP 25 with two identical-height buildings.

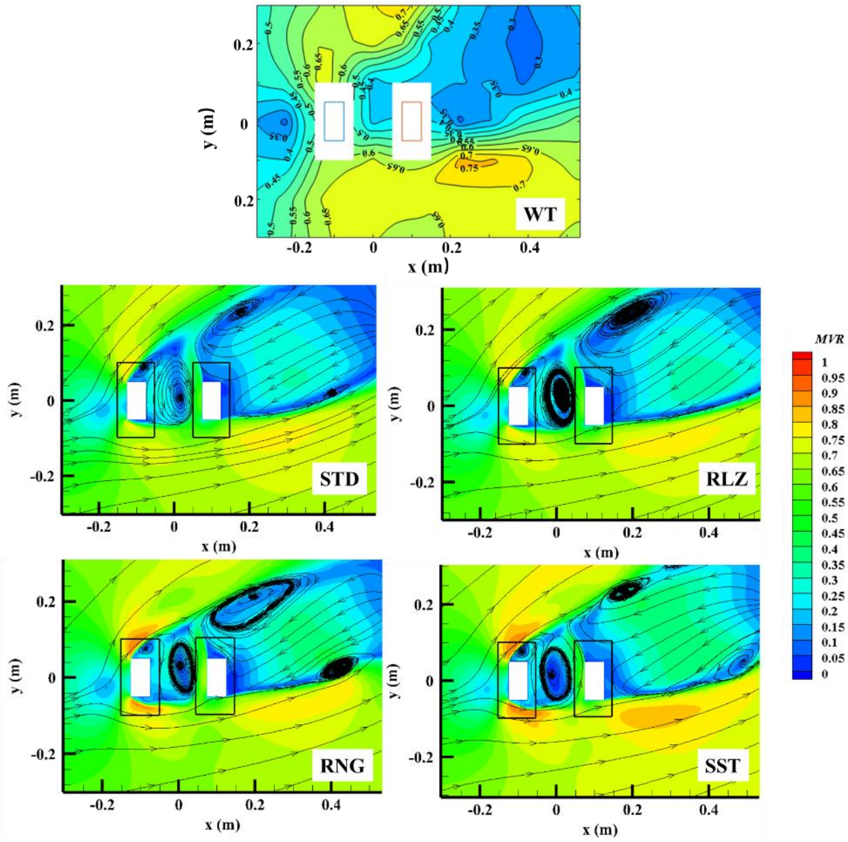

Figure 6.5. Comparison of wind velocity contour with streamlines under TWP over the horizontal plane at pedestrian level for different RANS turbulence models.

6.4 Results and discussion

6.4.1 Wind and temperature field without arcade design under CWP and TWP

The contours of normalized wind velocity at the pedestrian level (z=0.01 m) without the arcade design under CWP and TWP are depicted in Figure 6.6. This was achieved by normalizing the local wind velocity to a reference velocity at the pedestrian level. In order to quantitatively assess the effect of the twisted winds, the twisted angle of the wake region α is defined by the angle between the center line of the street canyon and a line connecting the center of the downstream low wind velocity areas and the center of the street canyon. Under CWP, the PLW flow was dominated by the outward flows and the along-street channeling flows towards the street ends, where a pair of corner vortices was formed due to the elongated afterbody of the street canyon. Specifically under TWP: (1) The shear layer under TWP exhibited asymmetry compared to the CWP scenarios, resulting in asymmetric vortex shedding along the streamwise direction; (2) The stagnation point deviated towards the side of the twisted wind direction, away from the center line; (3) The conical vortex experienced significantly weakening (see dotted red rounded rectangle 1 in Figure 6.6); (4) The separation line that divided the upwash and downwash flow moved upward under TWP (Figure 6.7 (b)), whereas it was situated near the middle height of the upstream building under CWP (Figure 6.7 (a)). The central vertical cross-section figures of the x-z plane (Figure 6.7(a)) demonstrate a distinct counterclockwise turbulence vortex downstream of the structure under CWP. The turbulence vortex, in contrast, was absent under TWP due to the spanwise vortex not only extending downstream at the central region but also deflecting towards the opposite direction of the incoming twisted wind (Figure 6.7 (b)). Accordingly, in contrast to the clockwise canyon vortex within the street canyon, which expanded with increasing W/H ratios and reattached to the windward surface of the downstream building, the clockwise canyon vortex under TWP occupied only half of the street width and did not grow larger as W/H increased. This led to a strong downwash flow caused by the twisted wind observed at the windward façade and gradually formed a new standing vortex in front of the downstream structure (Figure 6.7 (b)).

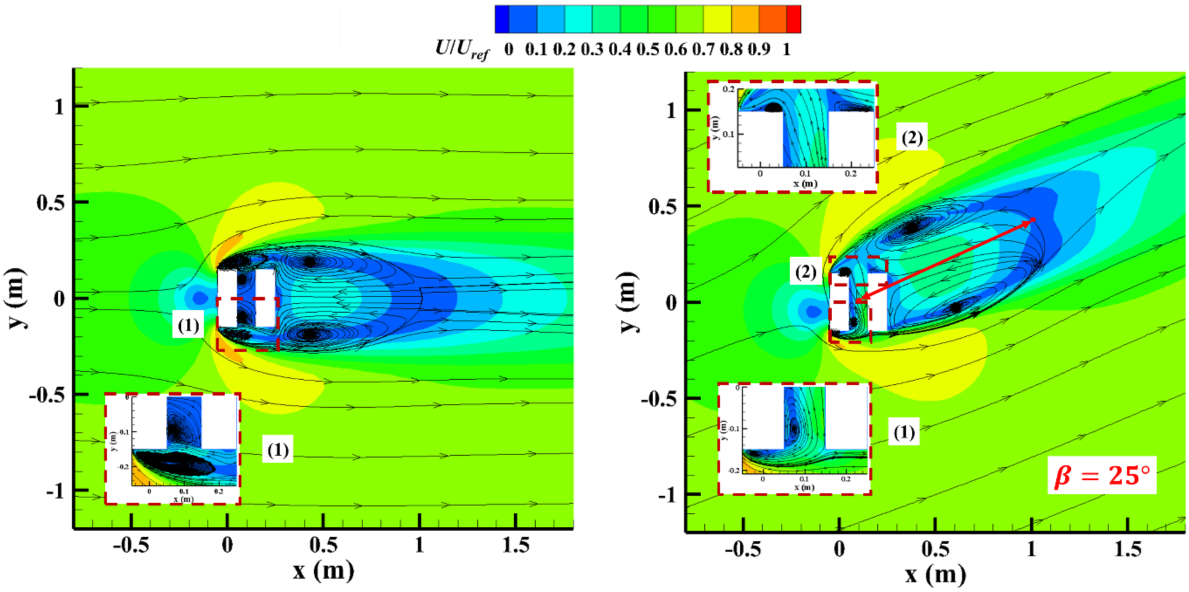

(a) (b)

Figure 6.6. Pedestrian-level U/U_{ref} distribution for street canyon without the arcade design with *W*/*H*=0.25 under (a) CWP and (b) TWP.

The presence of another weak vortex at the mid-level of the street canyon, with a *W*/*H* of 0.75 under TWP (see Figure 6.7 (b) rounded red rectangle), resulting in heat accumulation and a warmer temperature at half height compared to under CWP conditions. The air temperature contours under CWP and TWP are illustrated in Figure 6.7 (c) and (d). The dissipation of heat within the deep canyon structure (*W*/*H*=0.25) was hindered, making it difficult for heat to escape from the inner of the street canyon (Lin et al., 2020), and the air temperature exhibited a decrease in magnitude as the street width increased under both CWP and TWP conditions due to the reduced shading effect. Under CWP, a robust downwash airflow effectively sweeps along the leeward façade, thereby suppressing the upward buoyant plumes and consequently inhibiting air exchange within the deep canyon structure (*W*/*H*=0.25). The twisted wind induced an asymmetric temperature distribution within the street canyon, and the air temperature inside the street canyon decreased by approximately 1 °C when *W*/*H*=0.25 under TWP in comparison to CWP, with a more pronounced disparity observed at the lower level. This suggests that twisted wind possesses the potential to reduce air temperature in densely populated urban areas where the street width is comparable to or narrower than a single building width. The influence of twisted wind on the air temperature was not evident for *W*/*H* values exceeding 0.75. The intensified downwash flow in front of the windward facade induced by twisted wind tends to transport the cooler upper-level air temperature closer to the ground level and in proximity to the windward facade. The presence of another high-temperature region (indicated by the rounded red rectangle in Figure 6.7 (d)) can be related to the emergence of a newly merged vortex with low velocity upstream of the downstream structures (Figure 6.7 (b)).

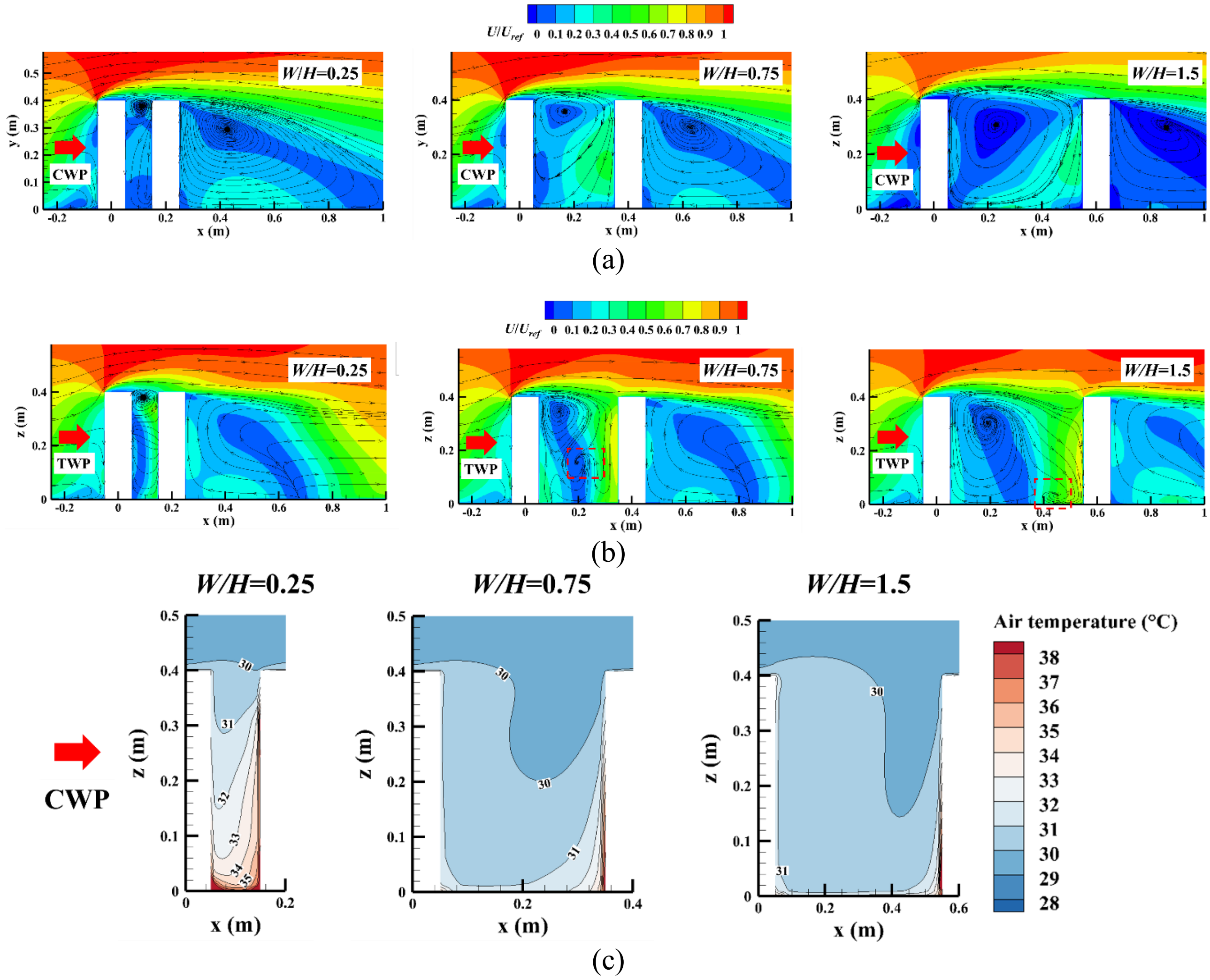

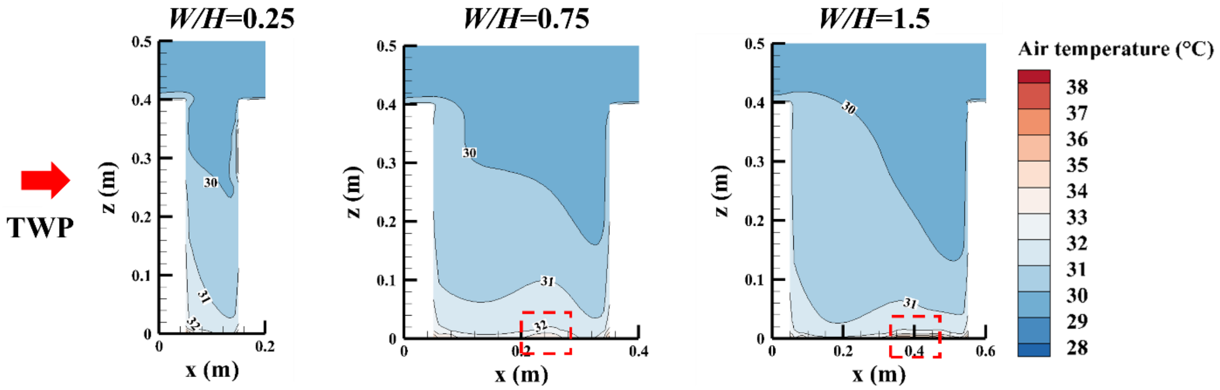

(d)

Figure 6.7. Pedestrian-level U/U_{ref} distribution with streamlines around street canyon without the arcade design under (a) CWP and (b)TWP, and the air temperature distribution at the central *x-z* plane under (c) CWP and (d) TWP for varied *W/H*.

6.4.2 Parametric study

6.4.2.1 Elevation ratios (*h/H*)

The impact of the elevation ratio (*h/H*) was investigated by varying the vertical void height of the arcade design under CWP and TWP while keeping other design parameters consistent. The contour of normalized wind velocity for different elevation ratios (0.05 and 0.2) under CWP and TWP is depicted in Figure 6.8 (a)-(d). The corner stream at the side of the upstream structure weakened in the arcade design under CWP, primarily due to the reduced side areas compared to the non-arcade design (Figure 6.6). The corner vortex moved into the inner areas of the street canyon under TWP, and the length of vortex intrusion in the street increased as the elevation ratio rose from 0.05 to 0.2, ranging from half to a full street length. The vortex core within the street canyon (indicated by the white dot) migrated downstream and approached the void in the arcade, converging towards the inner region of the street canyon. The twisting wind generated an asymmetrical distribution of wind velocity within the street canyon, wherein the downstream sidewalk areas exhibited significantly higher wind velocities compared to the velocity at the central areas and upstream sidewalks (Figure 6.8 (a)-(d)).

However, the wind velocity within the street canyon exhibited minimal variation across different elevation heights under both CWP and TWP (Figure 6.13 (a)).

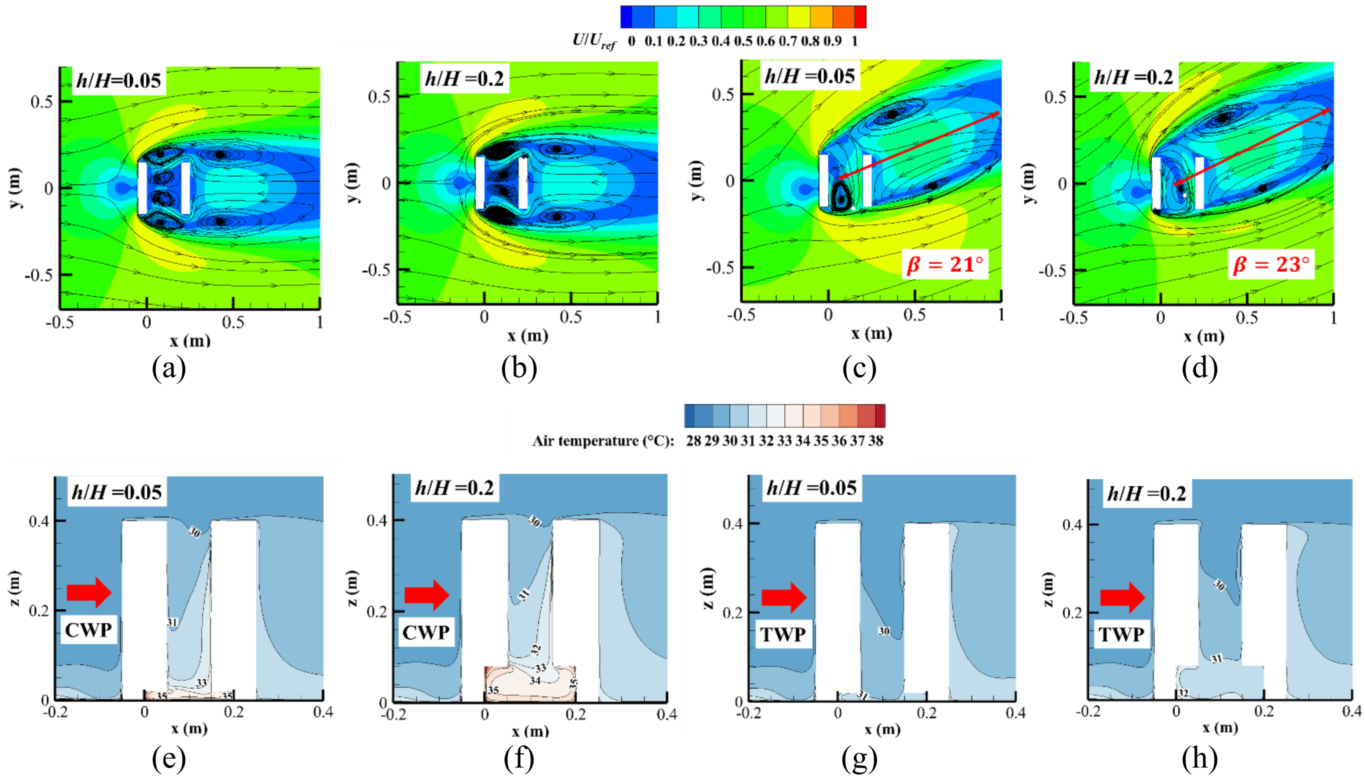

Figure 6.8. Pedestrian-level U/U_{ref} distribution with streamlines around two arcade structures under (a)-(b) CWP and (c)-(d) TWP and air temperature distribution at the central *x*-*z* plane under (e)-(f) CWP and (g)-(h) TWP for varied elevation ratios (*h*/*H*).

The air temperature distribution for different *h*/*H* at the central *x*-*z* plane under CWP and TWP is described in Figure 6.8 (e)-(h). The thermal patterns in non-isothermal conditions within a typical urban canyon exhibit a central vortex that extensively covers the street canyon, effectively entraining the warm air from the roof surfaces into the canyon (Hosseini et al., 2017). The introduction of the arcade design channels warm air into the upstream sidewalk areas, thereby effectively reducing the temperature in the central areas (Figure 6.7 (c) and Figure 6.8 (e)), and this phenomenon is more pronounced under CWP compared to under TWP. Under CWP, the air temperature distribution in the areas within the arcade design exhibited the highest air temperature due to the restricted ventilation, which was observed to be 2 °C higher than the central areas at an elevation ratio of 0.05 (Figure 6.8 (e)). With the increased elevated ratio from 0.05 to 2, the temperature at the lower part exhibited a rise due to the presence of weak flow and a relatively small vortex in the arcade section, impeding efficient heat transfer towards higher regions (Figure 6.8 (f)). Under TWP, the air temperature within the street canyon was significantly lower compared to under CWP (Figure 6.8 (g)-(h)). Notably, the air temperature at the windward façade exhibited an increase under CWP due to the direct solar radiation at 1500 LST; however, it shifted towards higher values near the leeward façade under TWP. This is because the influence of twisted wind results in a reduced downwash flow along the leeward façade in the vertical section, leading to a prevalence of upwash vortex within the street canyon while nearly eliminating the presence of downwash vortex. The upwash vortex facilitated the movement of warm air from the lower section of the street canyon towards the upper region, whereas the downwash vortex generated by the conventional wind profile tended to retain the warm air in its current position, thereby elevating the air temperature in the lower section of the street canyon. The area-averaged PET values of different zones for various h/H are depicted in Figure 6.9 (a). For the street canyon without the arcade design, the area-averaged PET value for the majority of the central area was over 41 °C under CWP, while a larger proportion of areas fell into the "Hot" category (38°C <PET<42°C) under TWP. The twisted wind tended to generate better thermal comfort at the downstream sidewalk areas compared to the cases under CWP. To be more precise, the area-averaged PET values at the downstream sidewalk areas exhibited a reduction of approximately 1 °C under TWP in comparison to CWP. The variation in thermal perception between the elevated area and the central area was more pronounced under TWP compared to CWP. The majority of the elevated areas in the arcade design were rated as "Slightly warm" (30 °C <PET<34 °C) as a result of the shading effect and elevated wind speeds. The impact of increasing the h/H ratio on air temperature was primarily observed in the central area, where the rise in arcade heights leads to higher PET values under CWP due to the enhanced entrapment of heated air within the street canyon. Conversely, increasing the arcade heights effectively mitigated high air temperature zones under TWP, while the impact on pedestrian comfort on both upstream and downstream sidewalk areas remained minimal.

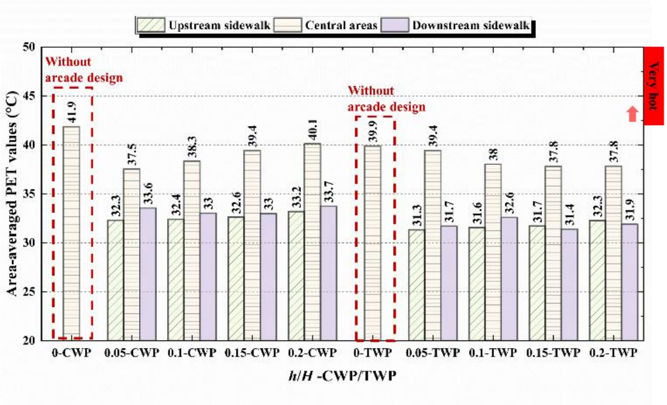

(a)

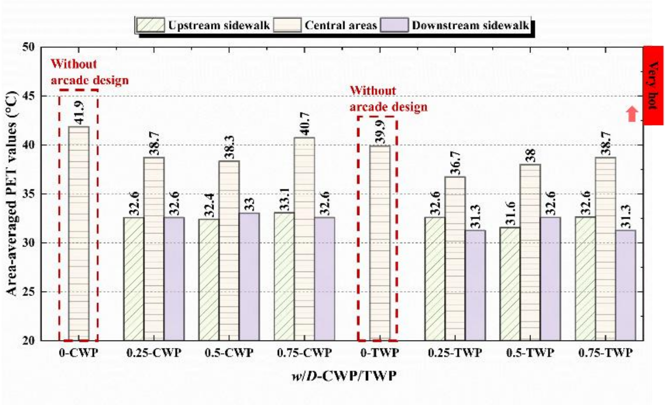

(b)

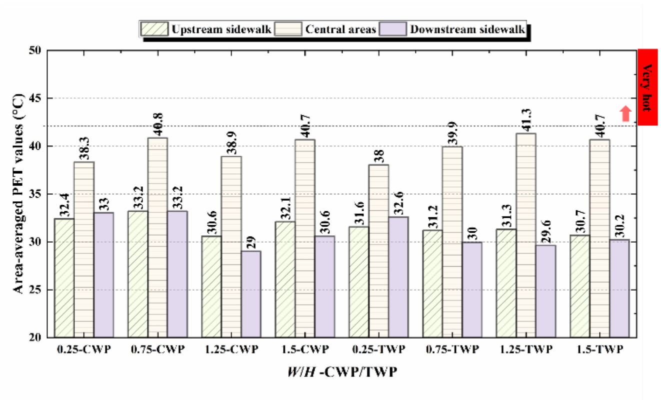

(c)

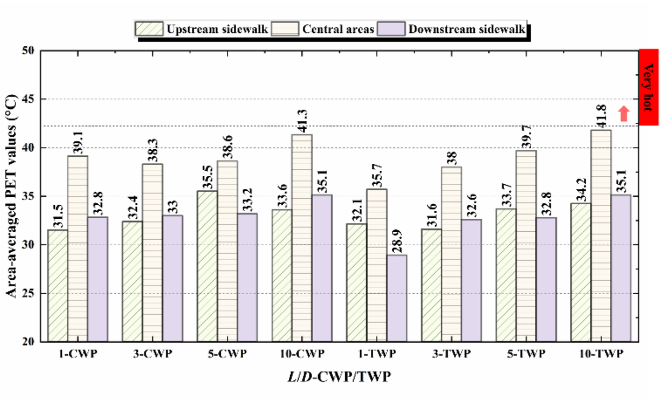

(d)

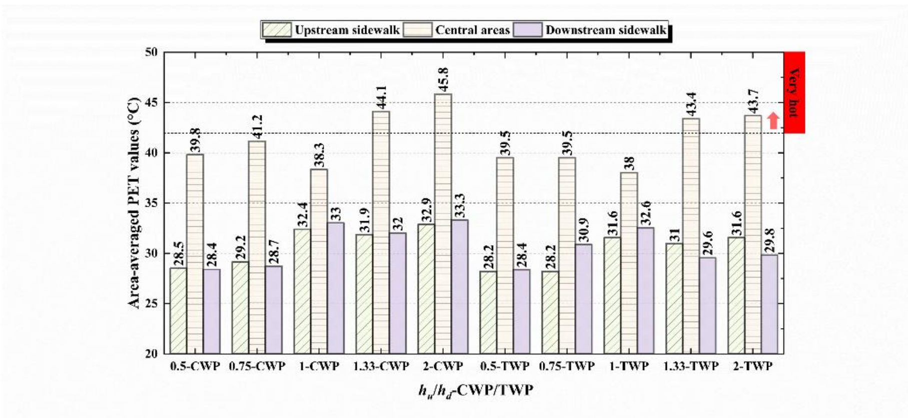

(e)

Figure 6.9. The area-averaged PET values under CWP and TWP for varied (a)*h*/*H*, (b) *w*/*D*, (c) *W*/*H*, (d) *L*/*D*, and (e) h_u/h_d.

6.4.2.2. Arcade width ratios (*w*/*D*)

The arcade width ratios (*w*/*D*) were examined at values of 0.25, 0.5, and 0.75 while maintaining constant arcade elevation ratios (*h*/*H*) and street canyon width (*W*/*H*) (Figure 6.10). Obviously, two corner vortices were observed adjacent to the upstream structures, while the vortices within the street canyon tend to approach closer to the downstream building and generate a pair of anti-clockwise vortices in the void beneath it as the arcade width ratios increase under CWP (Figure 6.10 (a)-(c)). Under TWP, the corner vortex moved into the central area of the street canyon, and the vortex core within the street remained stationary as the arcade width increased (indicated by the white dot) (Figure 6.10 (d)-(f)). The wind velocity exhibited an increase with decreasing arcade width inside the street canyon areas under CWP, consistent with previous findings in the literature (Hang et al., 2024). However, contrasting results were observed under TWP, where the wind velocity showed a significant increase with increasing arcade width. Notably, when the *w*/*D* was 0.75, the wind velocity was nearly twice as high compared to the *w*/*D* of 0.25 (Figure 6.13 (b)). The air temperature in the downstream sidewalk beneath the main building was found to decrease by 1-2 °C as the *w*/*D* increased from 0.25 to 0.75 under CWP conditions, thereby providing further evidence of the adverse impact of arcade width on thermal comfort (Figure 6.11 (a)-(c)). The present chapter newly reveals that arcade width also exerts adverse effects on thermal comfort under TWP. When the arcade width lessened, a comparatively lower air temperature was observed on the sidewalks of the downstream building compared to that in the upstream building (Figure 6.11 (d)-(f)). The formation of an anti-clockwise vortex within the street canyon caused by the twisted wind led to heightened wind velocities experienced at the sidewalk of the downstream building and promoted the expulsion of accumulated warm air from the void in the arcade design, where such warm air tended to accumulate under CWP.

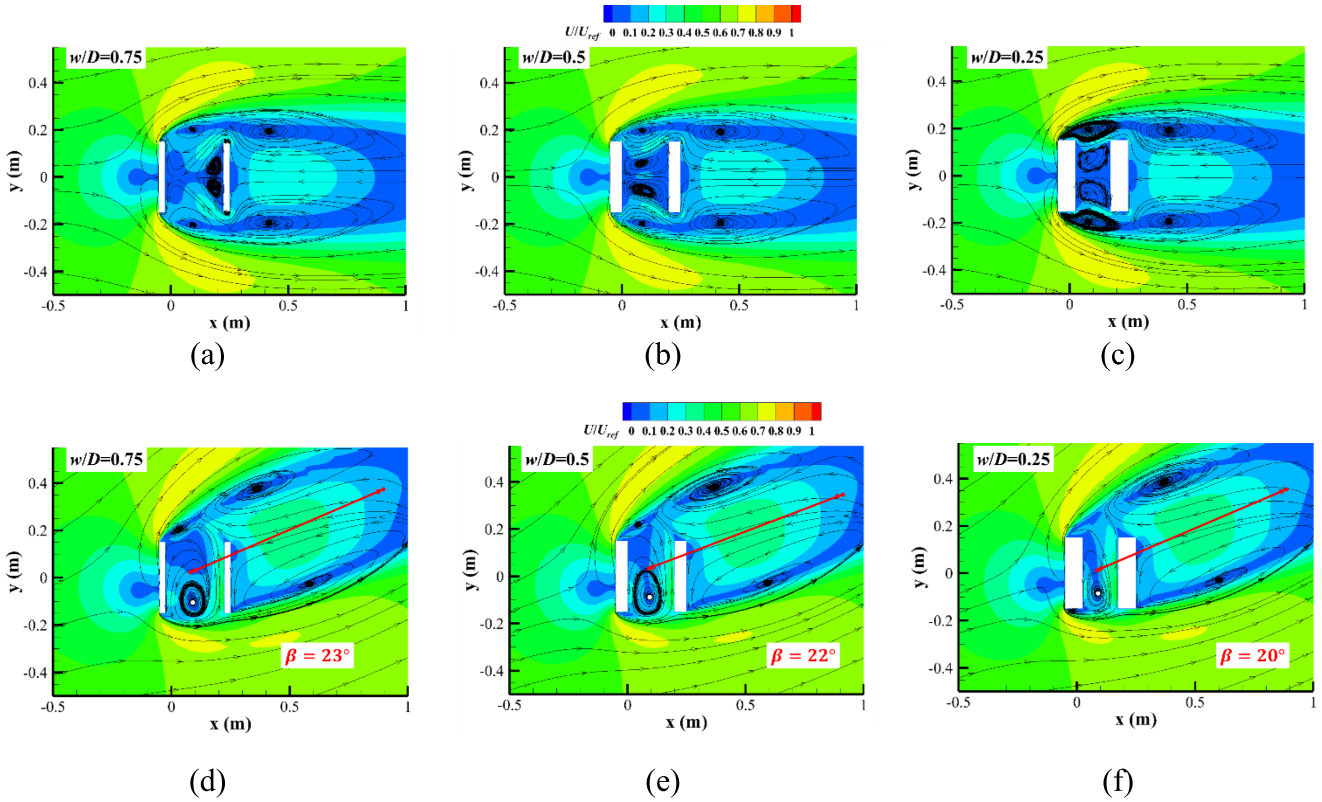

Figure 6.10. Pedestrian-level U/U_{ref} distribution with streamlines around two arcade structures with various arcade width ratios (w/D) under (a)-(c) CWP and (d)-(f) TWP.

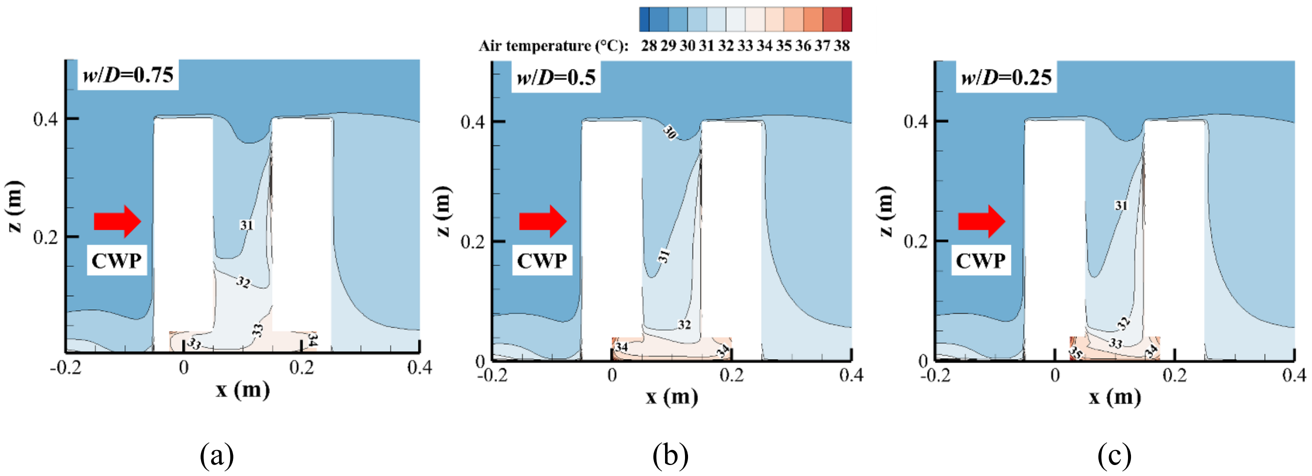

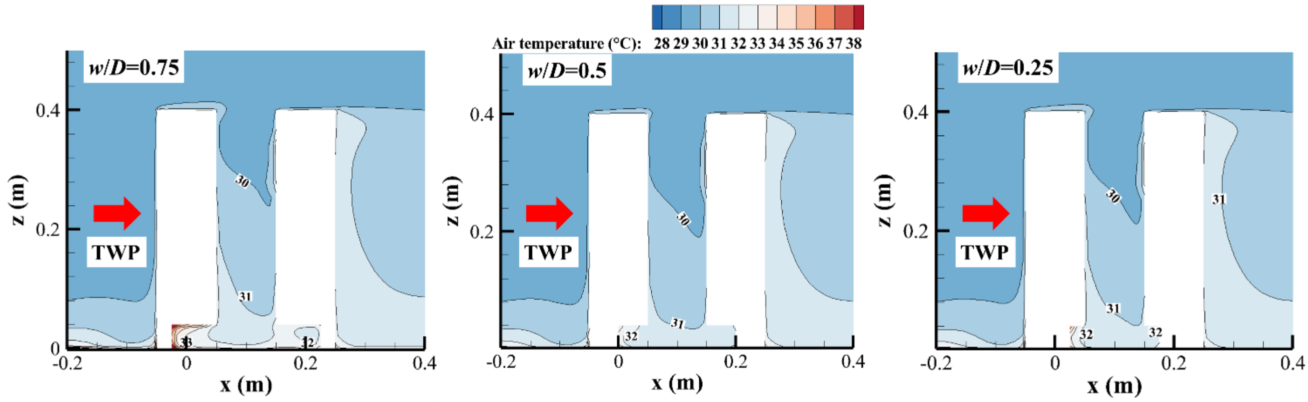

(d) (e) (f)

Figure 6.11. Air temperature distribution at the central *x-z* plane under (a)-(c) CWP and (d)-(f) TWP for varied *w*/*D*.

6.4.2.3 Street width and height ratios (*W*/*H*)

The impact of varying street canyon width ratios (*W*/*H*), ranging from 0.25 to 1.5, was investigated. Figure 6.12 illustrates the distribution of U/U_{ref} under different street canyon width ratios. In the regular urban canyons with a low *W*/*H*, the downstream building interacted with the vortex shedding of the upstream building. As a result, the wake vortex cannot be fully generated behind the upstream building (Figure 6.12 (a) and (d)), leading to the formation of a central vortex that induces a skimming flow regime (Hosseini et al., 2017). When the *W*/*H* ratio reached 1.5 (Figure 6.12 (c) and (f)), downstream structures exhibited behavior akin to that of an isolated free-standing model, and the horizontal street canyon vortices within the canyon were attenuated under CWP. The emergence of a novel vortex within the interstitial space between the two structures at the pedestrian level was observed under TWP, and its intensity increased with *W*/*H* values. As the street aspect ratios transition from narrow (*W*/*H*=0.25) to medium canyon (*W*/*H*=0.75 and 1.25), the U/U_{ref} exhibited a consistent increase across all regions under both CWP and TWP. Moreover, the discrepancy of U/U_{ref} between upstream and downstream sidewalk areas increased as *W*/*H* ratios rose under TWP while remaining relatively consistent under CWP. As the flow regimes transitioned to wake interference (*W*/*H*=1.5), the average U/U_{ref} value decreased under CWP while continuing to increase under TWP. This phenomenon demonstrates that the shift from skimming flow to wake interference flow results in an increase in low wind velocity areas under CWP due to the reduced flow interaction between the two buildings, whereas wind velocity increased under TWP due to enhanced wind flow interactions from the lateral side. The influence of twisted winds on the air temperature field was found to be less pronounced in street configurations with larger *W*/*H* values, this observation highlights the amplification of twisted wind effects in densely populated urban areas. The presence of twisted wind flow in the downstream buildings resulted in an improvement of thermal comfort for pedestrians at the arcade void areas, while the thermal stress was slightly higher under TWP compared to CWP in the central podium areas when *W*/*H*>0.75 (Figure 6.9 (c)). The findings suggest that standing in podium areas in wider streets with a twisted wind profile may exacerbate the discomfort caused by high temperatures. However, the arcade design offers optimal strategies for enhancing pedestrian thermal comfort in urban topologies with complex wind flow. Pedestrians experience reduced heat stress in arcade areas compared to podium areas under both CWP and TWP.

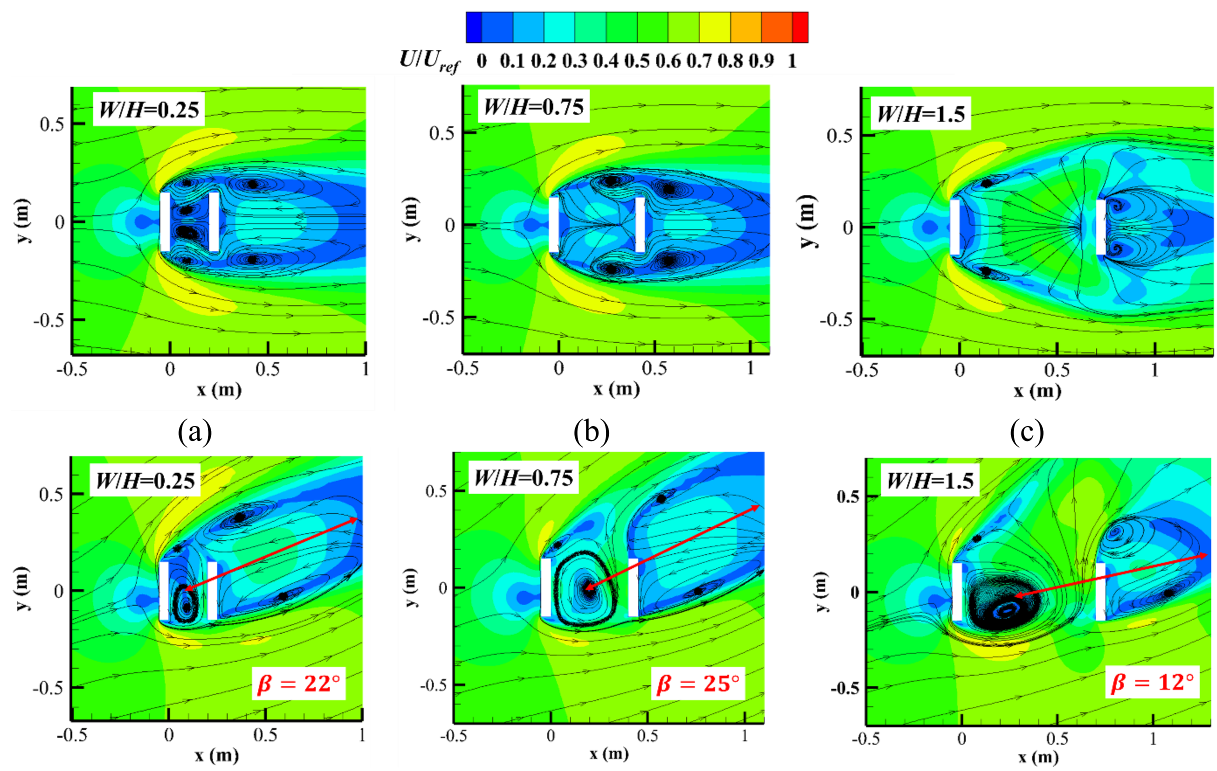

(d) (e) (f)

Figure 6.12. Pedestrian-level U/U_{ref} distribution with streamlines around two arcade structures with various street canyon widths (W/H) under (a)-(c) CWP and (d)-(f) TWP.

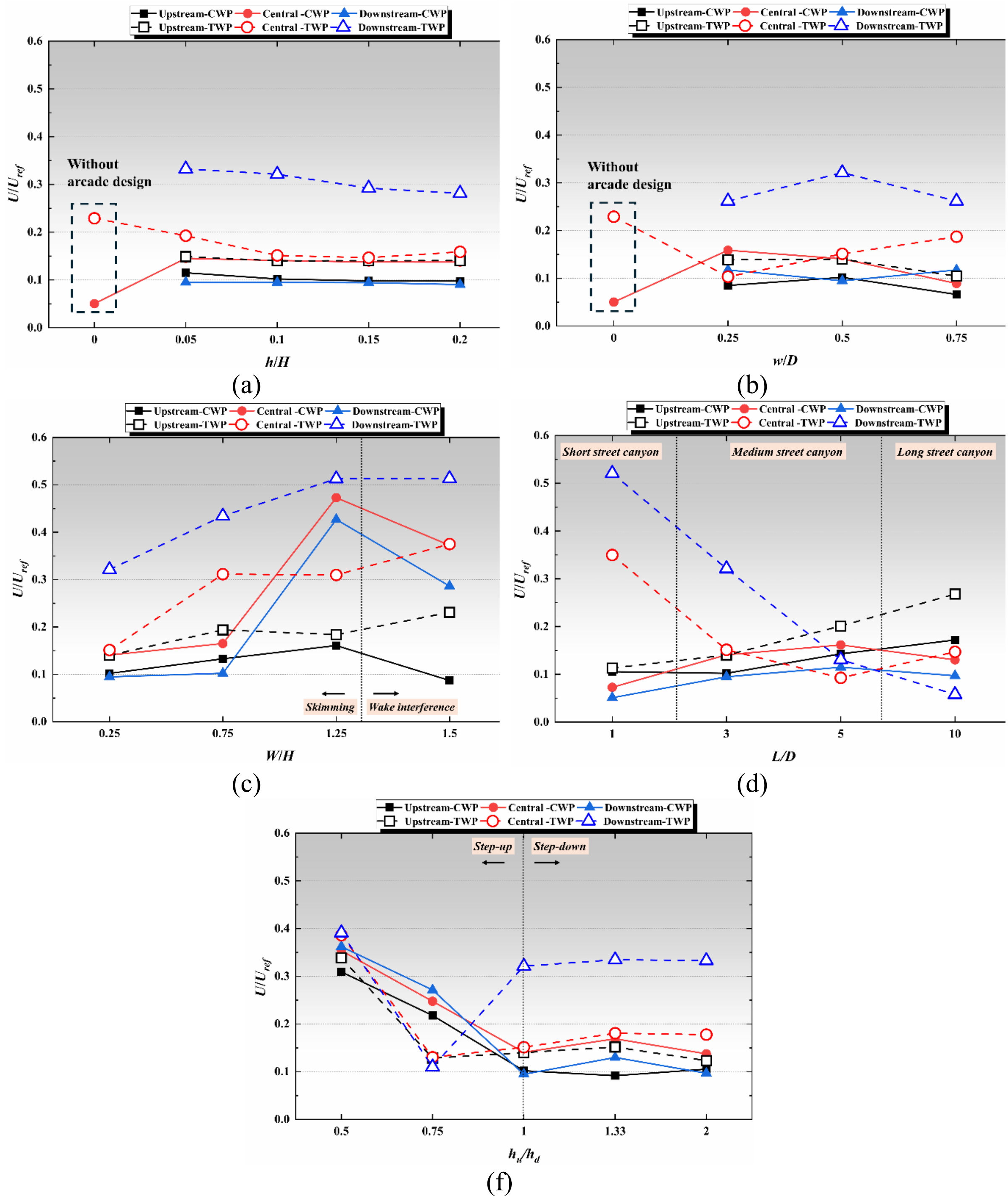

Figure 6.13. Area-averaged U/U_{ref} values under CWP and TWP for varied (a) h/H, (b) w/D, (c)W/H, (d) L/D, and (e) h_u/h_d.

6.4.2.4. Street length and depth ratios (*L*/*D*)

The effect of the lateral entrainment was investigated by varying the street length and depth ratios (*L*/*D*) at values of 1, 3, 5, and 10 while keeping other parameters constant. Figure 6.14 illustrates the pedestrian level U/U_{ref} value distributions for varied *L*/*D* values under CWP and TWP. For the short street canyon (*L*/*D*=1) (Figure 6.14 (a) and (e)), the flow separation occurred at the leading face, resulting in the formation of a canyon vortex due to the entrainment from the upper region, which was observed within the void downstream of the arcade structure. Besides, due to the small street length, no corner stream caused by lateral entrainment was observed. Under TWP, the canyon vortex in the short street canyon (*L*/*D*=1) was observed to exhibit a significant positive *y*-axis displacement with a pronounced deviation angle, as compared to the medium and long street canyons.

In medium street canyon (*L*/*D*=3 and 5) (Figure 6.14 (b)-(c) and (g)-(h)), under CWP, a new merged secondary corner vortex was observed adjacent to the downstream structure (refer to label (3) in Figure 6.14 (b)), resulting from the interaction between the street canyon vortex and the downstream vortex behind the street canyon, which was absent in the street canyon without the arcade design (Figure 6.6 (a)). The arcade design effectively reduced wind resistance from the lateral side by providing an open space, causing the corner vortex to slightly shift into the street canyon and compressing the size of the street canyon vortex. Under TWP, the intensified counterclockwise turbulence vortices on the oncoming twisted wind direction of the street canyon (refer to label (1) in Figure 6.14 (b)) interacted with the internal turbulence vortices within the street canyon (refer to label (2) in Figure 6.14 (b)), thereby displacing the regions of low wind velocity from the inner area towards the vicinity of the street canyon's edge on its opposite side of the oncoming twisted wind direction under TWP. In long street canyon (*L*/*D*=10) (Figure 6.14 (d) and (h)), under CWP, the corner vortices generated by the upstream structure, two symmetrical and flat vortices merged at the downstream sidewalk areas due to the interaction between the downwash flow from the upstream building and the recirculation flow at the arcade structure areas. As the *L*/*D* values increase, the street canyon vortex progressively shifts toward the downstream sidewalk areas, coinciding with the development of high-velocity inward flow at the upstream sidewalk areas, resulting in higher wind velocities in the upstream sidewalks compared to the downstream sidewalk areas (Figure 6.13 (e)). Under TWP, the interaction between the tilted vortex and the street canyon vortex results in the generation of a novel vortex within the long street canyon (refer to label (2) in Figure 6.14 (h)). The intensity of the downstream vortex on the oncoming twisted wind direction side was enhanced, and a portion of the downstream vortex re-entered the street canyon and interacted with the vortex within the street canyon, resulting in the formation of a substantial counterclockwise vortex (refer to label (3) in Figure 6.14 (h)). Although the twisted flow facilitated the corner eddies to penetrate toward the inner street-canyon area, the effects of arcade design became minor on the airflow due to the long street length. Moreover, while arcade design can effectively reduce temperatures in the central area, it tends to increase temperatures in sidewalk areas as street length increases. Therefore, it is recommended that city planners utilize arcade design in short and medium-length street canyons but avoid its use in long street canyons.

The air temperature distribution at different *x*-*z* sections for various *L*/*D* values is depicted in Figure 6.15. In a short street canyon (*L*/*D*=1), the air temperature remains relatively consistent across different *x*-*z* cross-sections, while the downstream sidewalk areas exhibited an elevated temperature of 33 °C under CWP. Conversely, under TWP conditions, this area experienced 2 °C lower air temperatures due to the high wind velocity induced by the substantial volume of airflow. The high air temperature region in the medium street canyon mitigated towards the downstream arcade structure, progressing from the inner to outer regions of the street canyon under CWP. The air temperature within the long street canyon (*L*/*D*=10) was generally higher than that in the medium and short street canyons under both CWP and TWP. The lower part of the street canyon exhibited higher temperatures than the upper part, while the arcade structure experienced elevated temperatures compared to those observed on the street. The inability to remove the heated warm air to the outer and upper regions of the street canyon accounts for this phenomenon in a long street canyon. The twisted wind significantly reduced the air temperature inside the street canyon at all cross-sections, particularly in the inner region of the canyon, where the air temperature was 1-2 °C lower under TWP compared to the CWP. The area-averaged PET values for different *L*/*D* ratios are depicted in Figure 6.9 (d). It is evident that the area-averaged PET values exhibited a clear increase with the lengthening of the street canyon, ranging from short to long in all three parts of the street canyon. Notably, the central areas of the long street canyon demonstrated the highest PET value (≥ 40 °C) under CWP. The impact of twisted wind on cooling was more pronounced in short street canyons, while its effect became increasingly minimal with the lengthening of the street canyon and eventually negligible in long street canyons. This was attributed to the fact that in a short street canyon with an aspect ratio (*L*/*D*=1) (Figure 6.14 (a) and (e)), the upstream and downstream buildings can be considered as isolated free-standing structures, resulting in a similar flow pattern for both upper and lower buildings, therefore significantly enhancing the wind velocity within the street canyon (Figure 6.13 (d)). In the case of a long street canyon, the corner stream was inclined and trapped within the street canyon under TWP conditions, thereby interacting with the turbulence vortex generated by the street and resulting in areas of low wind velocity (Figure 6.14 (d) and (h)). As a result, warm air became stagnant and trapped within the street canyon.

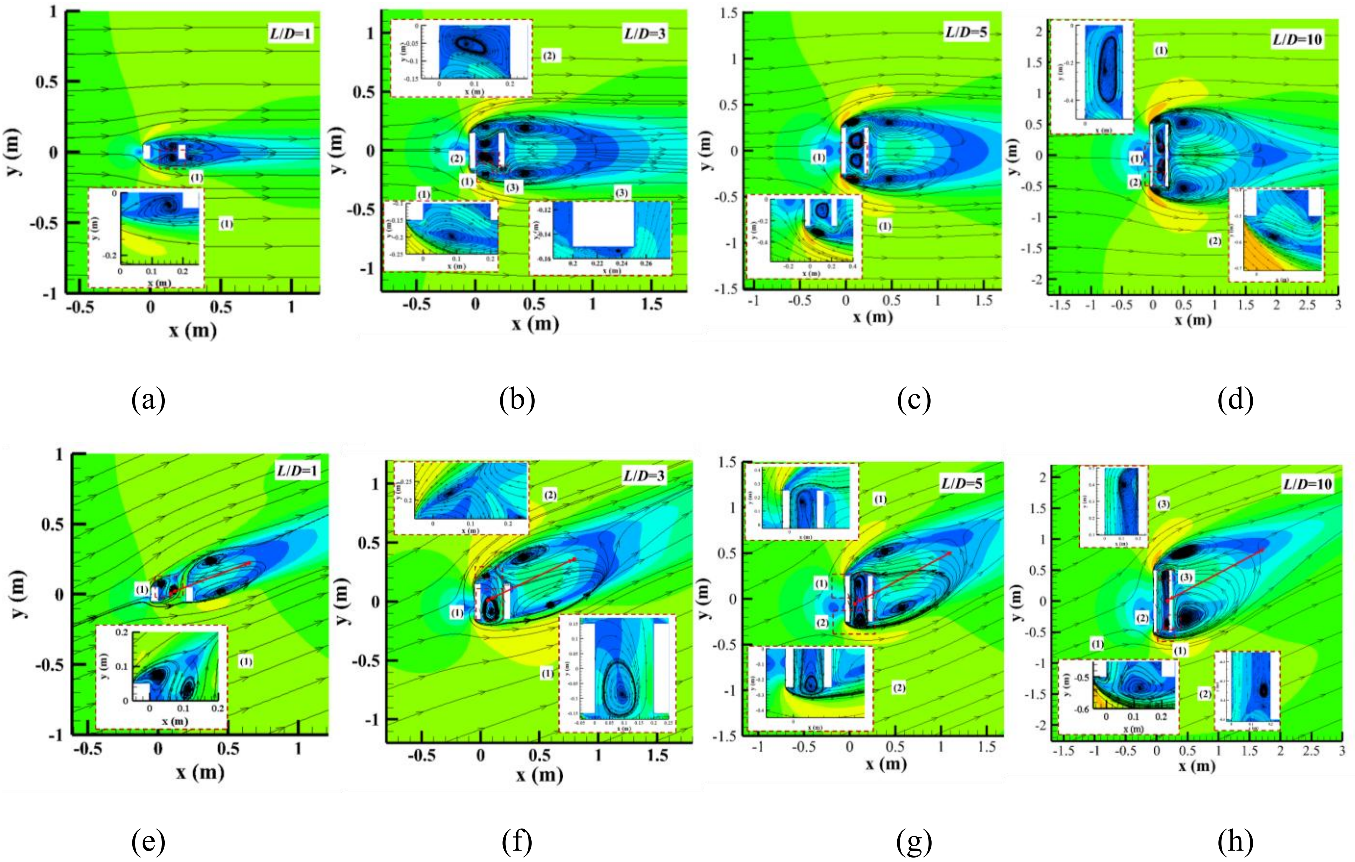

Figure 6.14. Pedestrian-level U/U_{ref} distribution with streamlines around two arcade structures with various street lengths (L/D) under (a)-(d) CWP and (e)-(h) TWP.

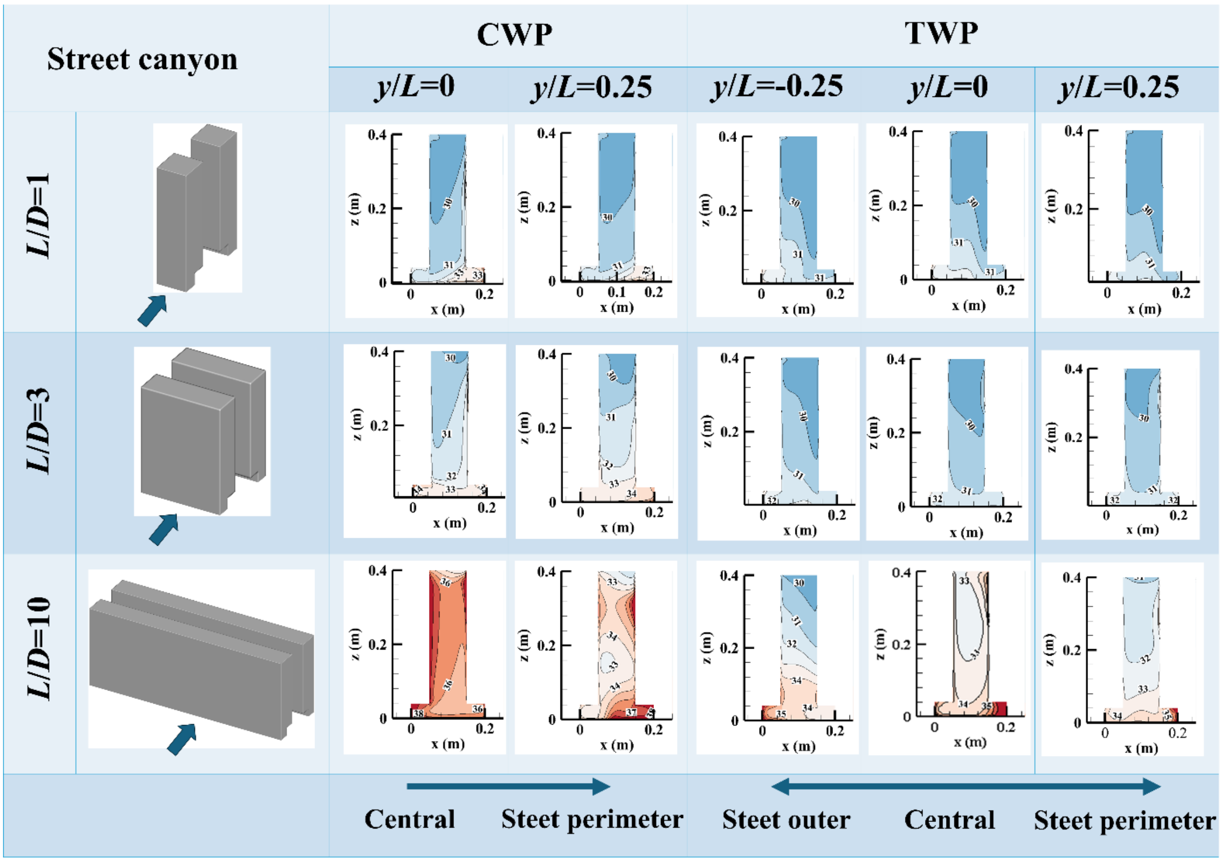

Figure 6.15. Air temperature contours at different *x*-*z* cross sections for different *L*/*D* values under CWP and TWP.

6.4.2.5. Asymmetric height ratios (h_u/h_d)

The investigation in this section focused on non-uniform street canyons with an arcade design under CWP and TWP, wherein the height ratio (h_u/h_d) between the upstream and downstream street canyons was varied from 0.5 to 2 (Figure 6.16). In the case of a step-up street canyon with an arcade design, the incoming flow directly impacted the upper section of the downstream buildings without obstruction. The upper flow was then redirected to the lower level, resulting in the formation of the turbulence vortices at the downstream sidewalk areas under CWP and TWP (Figure 6.16 (a) and (b)). A new merged turbulence vortices form at the upstream arcade sidewalk areas under TWP when h_u/h_d=0.75 (Figure 6.16 (d)), this phenomenon was due to the interaction between the weakened downwash flow and the recirculation flow in the downstream void under TWP. Within the step-down street canyon featuring an arcade design with h_u/h_d=1.33 under CWP (Figure 6.16 (g)), four turbulence vortices were observed: one beneath the main building in the upstream sidewalk areas, another within the street canyon itself, a third in the upper area between the up and downstream buildings, and a fourth was the downwash flow in the wake region of the street canyon. However, under TWP conditions (Figure 6.16 (h)), only one turbulence vortex was present in the upper area between the up and downstream buildings. This can be related to the weakened downwash flow caused by twist flow and dominance of the upwash vortex while eliminating the downwash vortex behind both buildings. Moreover, the wind velocities under TWP resulted in an intensified standing vortex with higher wind velocity located ahead of the upstream building compared to those observed under CWP.

The step-up street canyon (h_u<h_d) significantly enhanced the wind velocities within the street canyon under both CWP and TWP conditions ((Figure 6.16 (a)-(d)), owing to the intensified downwash flow at the front of the windward facade that introduces a greater influx of upper-level air towards the pedestrian level. The flow field under TWP exhibited a higher sensitivity to the height difference between upstream and downstream buildings, as evident by a decrease of U/U_{ref} from 0.4 to 0.1 compared to only a drop from 0.4 to 0.2 under CWP when h_u/h_d increased from 0.5 to 0.75 (Figure 6.13 (e)). The downwash flow in front of the windward façade was intensified, and the buoyancy-driven flow and wind-driven flow were in the same direction under CWP in the step-up street canyon ((Figure 6.16 (a) and (c)), thereby creating an assisting condition. For the step-down street canyon (h_u>h_d), the U/U_{ref} values exhibited minimal variation with changes in the height difference between the two structures (Figure 6.16 (e)). Hosseini et al. (2017) noted that the warming of the roof caused pollutants to accumulate on the leeward surface due to the direction of vortex rotation and low wind velocity. This phenomenon has also been observed in street canyons with arcade design under CWP. (Figure 6.16 (e)). However, under TWP, the updraft magnitude was enhanced as a result of downwash flow attenuation; the thermal effect was strong enough and led to the development of opposing buoyancy-driven and wind-driven flows (Figure 6.16 (h) and (j)), which increased wind velocity at the leeward surface and facilitated pollutant dispersion from the street canyon. This factor, combined with reduced solar radiation, contributed to lower area-averaged PET values in the central areas of the step-down street canyon compared to the step-up street canyon (Figure 6.9 (e)). However, the asymmetric street canyon elevated the air temperature in the central area when compared to a street canyon with identical heights, which was owing to the reduced shedding effects and increased solar radiation generated by the asymmetric configuration.

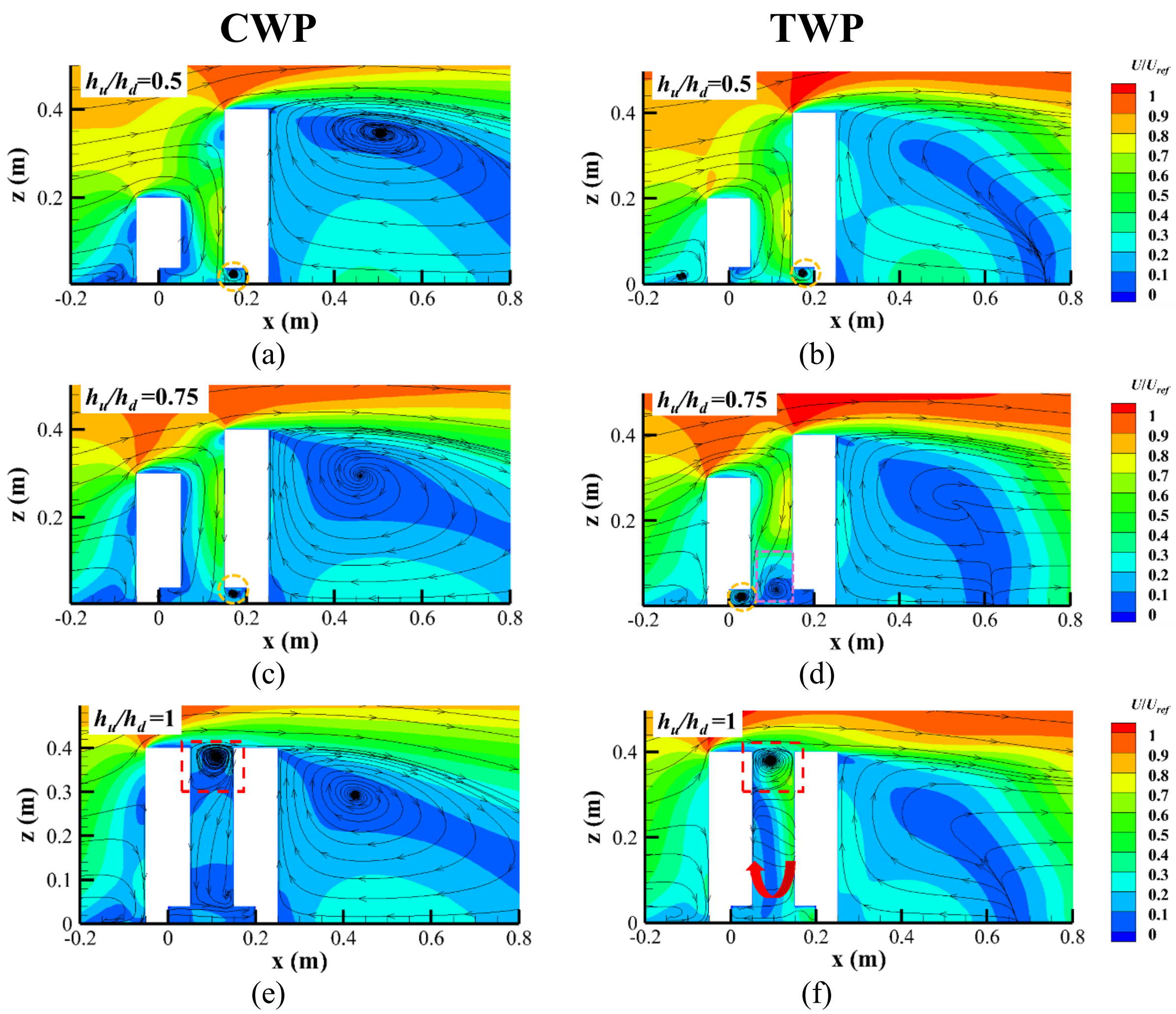

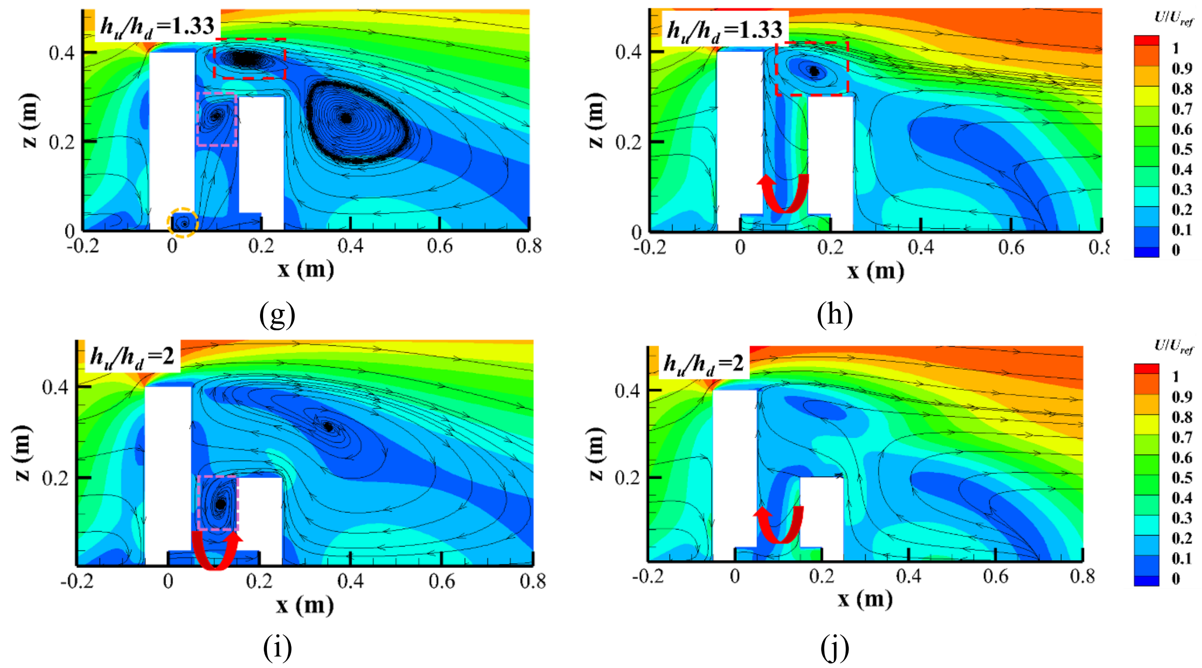

Figure 6.16. Contour plots of U/U_{ref} with streamlines at the center x-z plane under CWP and TWP with different h_u/h_d values: (a)-(b) h_u/h_d =0.5; (c)-(d) h_u/h_d =0.75; (e)-(f) h_u/h_d =1; (g)-(h) h_u/h_d =1.33 and (i)-(j) h_u/h_d =2.

6.5 Summary

The present chapter employs CFD simulation with standard $k-\varepsilon$ turbulence model and DO radiation model to investigate the impact of twisted wind on arcade design, considering various design parameters such as arcade heights and widths, street widths, and length, as well as the asymmetric height ratios. The accuracy of the simulation was ensured by comparing it with the wind tunnel experiments and field measurement results from the literature. The main conclusions drawn from this chapter are outlined below:

(1) The twisted wind has the potential to modify the thermal distribution within the street canyon, and its impact is particularly pronounced in densely populated urban areas with narrow street widths. Under CWP, direct solar radiation caused an increase in air temperature on the windward façade at 1500 LST. Conversely, under TWP, higher temperatures were observed on the leeward facade in the upper layer of the street

canyon due to weakened downwash flow. The significant updraft observed at the rear of the upstream building can be attributed to the inability of the weakened downwash flow to counteract the buoyancy force, thereby facilitating the vertical transport of warm air from the lower to the upper section of the street canyon.

(2) The arcade design presents a promising strategy for optimizing pedestrian thermal comfort in urban topologies with complex wind flow. Under the effects of the twisted wind, increasing the width of the arcade tended to result in an increase in the volume introduced into the street canyon and improved wind comfort. PET values under TWP were significantly lower compared to those under CWP, particularly in the downstream sidewalk areas. The corner vortex core shifted downstream and towards the inner area of the street as the arcade heights increased, while it remained stationary when increasing the arcade widths. This chapter revealed that, compared to local architectural modifications, the street configuration parameters exerted the most significant influence on the variation of air temperature at the pedestrian level under TWP.

(3) The cooling effect induced by the twisted winds was more pronounced in short street canyons with arcade design, whereas it diminished in medium and long street canyons. In a short canyon, the corner stream generated by the upstream structure flowed into the street canyon and extended towards the downstream structure. The inclined vortex shedding patterns were confined within the street canyon and interacted with turbulence vortices present in the central area in the medium and long street canyon. The PET values exhibited a positive correlation with the street length, specifically, the PET value increased by 2 °C under CWP and by 4 °C under TWP as the L/D increased from 1 to 10.

(4) The street canyon vortex extended across the entire width of the street as the W/H increased under CWP. However, under TWP, the size of the street canyon vortex

remained stable despite increasing *W*/*H*. This phenomenon led to a downwash flow in front of downstream structures and resulted in the merging of a new vortex when *W*/*H*>1.25. This newly observed vortex was related to regions of high air temperature under TWP, resulting in an amplification of air temperature under wider street canyons. The step-up building configuration demonstrated an augmentation in wind velocity compared to the step-down building configuration. Under TWP, the attenuation of downwash flow phenomena was enhanced in the step-down street canyon, where the buoyancy-driven flow and wind-driven flow acted in opposite directions and facilitated the transportation of warm air from the inside of the street canyon, this led to smaller PET values compared to those observed in a step-up street canyon. The vertical wind velocity in the wake areas was found to be lower under twisted wind conditions compared to those under CWP. The absence of vertical eddies may adversely affect PLWEs and reduce the efficiency of air pollutant removal.

CHAPTER 7. Conclusions and recommendations

7.1 Summary of main contributions

This thesis presents a systematic investigation into the effects of urban open and semi-open designs, including elevated and arcade designs, on wind and thermal comfort, as well as their performance under twisted wind conditions in high-density urban environments. This thesis contributes to a better understanding of the application of urban open designs under various atmospheric boundary conditions, with the aim of promoting the development of locally thermally comfortable outdoor environments. Specifically, Chapter 3 presents the experimental results on pedestrian-level gust wind flow and comfort around irregular elevated buildings within simplified building arrays. The findings are valuable for urban planners determining building orientations that align with prevailing wind directions and can be useful for validating CFD results. Chapter 4 addresses the research gaps concerning the effects of elevated sections on time-averaged flow quantities and turbulent statistics and evaluates the applicability of various turbulence modelling approaches for simulating the flow field around elevated buildings. The findings offer insights into the utilization of elevated buildings from a turbulence perspective, as well as the prediction accuracy of RANS and LES in capturing mean and gust wind velocities around elevated buildings. The results encourage architects and urban planners to effectively utilize elevated sections to enhance urban ventilation and to adopt favorable curved building orientations aligned with prevailing wind directions for improved airflow. Specific strategies should be developed for different curved structure orientations. Furthermore, designers can use the elevation strategically to minimize strong downwash and improve wind comfort at building entrances or public spaces on the windward side and avoid placing sensitive pedestrian spaces, playgrounds, or outdoor seating directly downstream of the elevated buildings, or use landscaping and windbreaks to mitigate increased turbulence. Chapter 5 presents the results of the PLWEs surrounding two tandem non-identical height elevated buildings under the influence of twisted wind flows, this chapter offers valuable recommendations for urban planners on implementing elevated structures in hilly urban areas prone to frequent twisted flows. Our findings confirm that the presence of elevated structures enhances sensitivity to the twisted wind effect, leading to a greater deviation of DFLWV areas from the building center line. Chapter 6 presents the results of the impact of twisted wind on pedestrian comfort around semi-open structures, as well as influential factors under solar heating, based on numerical simulations. These findings can offer valuable insights into the effectiveness of arcade designs in enhancing PLW and thermal comfort in hilly areas.

7.2 Summary of main findings

This thesis investigates the turbulent flow structures around elevated buildings and the impacts of twisted winds on wind and thermal comfort in the vicinity of such buildings with wind tunnel experiments, Steady RANS approach, LES, and RayMan modeling. The research work is summarized below, with the key findings highlighted:

7.2.1 Pedestrian-level gust wind flow and comfort around irregular elevated buildings within simplified urban arrays

Irregular elevated buildings demonstrated a higher concentration of accelerated areas in the lateral and rear regions of the central elevated building due to the pronounced flow separation at the upwind corner and the formation of corner streams along the side of these distinctive architectural forms. The central elevated building led to an increase in *MVR* and *GVR* region, and this chapter shows compelling experimental evidence demonstrating that elevated buildings possess the capacity to augment wind velocity, even in the presence of surrounding structures.

Implementing aerodynamic modifications proves advantageous in controlling areas with extreme wind discomfort. The architectural elements of concavity and convexity have significant effects on wind patterns, the diverging flow transported a larger volume of high-velocity upstream airflow towards the downstream building when the wind hits the convex part of the elevated building. The Arc-shaped elevated building exhibited a greater "Intolerable" area than V- and Rectangular-shaped building cases.

7.2.2 Mean and turbulent wind characteristics around a high-rise elevated building with curved cross-sections

RANS models exhibit limited accuracy in predicting mean wind velocity in the side and wake regions of buildings, as evidenced by discrepancies with wind tunnel data, yet demonstrate satisfactory performance in the upstream region. In the elevated region, where vortices formed due to reverse and backflow from the elevated column, RANS models failed to reproduce vortex V_d in the downstream elevated section and vortex Nd behind the building, with only the SST model accurately capturing these features. Additionally, RANS models overestimated the length of jet flow between elevated columns by 1.5 to 2 times compared to experimental data. LES can accurately reproduce mean wind velocity and reasonably estimate rms velocity components around elevated buildings. It also shows superior performance in predicting high TKE regions, especially downstream. The time step choice is critical for estimating both mean wind velocity and TKE. Large time steps may underestimate near-building TKE, yet LES remains more accurate than RANS models despite not fully resolving all turbulence structures.

The vortex shedding frequency near elevated buildings shows a wider range, indicating more complex interactions between flow separation and vortex shedding. The elevated section generates a new upstream vortex (V_u), which reduces backflow and weakens the horseshoe vortex in front of the building. This decreases turbulent downwash, leading to less pronounced PSD peaks in the windward areas. The formation of a downstream vortex (V_d) in the elevated region reduces reverse flow, weakens the near-ground vortex (N_d), and increases the height of the downstream stagnation point (Z_{dsp}).

High-rise elevated buildings significantly enhance the instantaneous streamwise flow while reducing mean wind fluctuations, which suggests greater lateral entrainment of low-velocity flows near the building. The increased u component indicates that these buildings draw high-velocity streamwise flows into their wake regions, thereby reducing wake size. Elevated structures weaken TKE on the side due to reduced corner stream magnitude but increase TKE downstream as jet flow from the column collides with downwash flows. Although the mean wind velocity is higher at convex building surfaces, TKE peaks at concave areas, indicating that high turbulence can occur in low-velocity zones due to enhanced turbulence intensity.

7.2.3 Pedestrian-level wind environment surrounding two tandem non-identical height elevated buildings under the influence of twisted wind flows

Twisted wind flows alter the flow field around two tandem buildings, creating an asymmetric wind environment marked by a shift in DFLWV and USLWV zones toward the direction of the incoming twisted flow and a weakened corner stream on the left side. In the step-up configuration, the primary vortex remains symmetric under CWP conditions, but spanwise outward flows intensify due to the height difference between the buildings. Under TWPs, the primary vortex tilts rightward compared to its stable position under CWP, affecting the downstream corner stream and significantly altering the overall flow field distribution. Experimental results show that adjusting the height difference between elevated buildings can effectively improve wind conditions in areas affected by topography-induced twisted wind profiles. Step-up and step-down configurations significantly modify the local wind environment. Raising the downstream building height is more effective than increasing the upstream height in reducing LWV areas.

Step-up and step-down building configurations respond differently to twisted wind. Height differences between tandem buildings amplify the wind velocity disparity at both ends of the structures and increase the deviation angle under twisted wind conditions. In contrast, for step-down configurations, the flow field remains similar to that of buildings with equal heights, maintaining a consistent deviation angle regardless of height variation. When placed upstream, they produce stronger corner streams than non-elevated buildings. When downstream, they eliminate the NFLWV area and reduce DFLWV zones. A larger DFLWV deviation angle is observed in downstream elevated configurations, indicating greater sensitivity to twisted wind effects compared to non-elevated buildings.

Twisted wind conditions may degrade thermal comfort in the vicinity of two tandem buildings during summer. During the summer season, an increase in building height expands the spatial extent of favourable thermal environments. The step-down configuration produces lower PET values and demonstrates superior thermal comfort performance relative to the step-up configuration. In winter, twisted wind leads to a greater proportion of areas categorized as "Neutral" with reduced PET values when compared to CWP conditions.

7.2.4 The effect of twisted wind on pedestrian comfort surrounding semi-open structures and influential factors under solar heating

Twisted wind has the potential to alter the thermal distribution within street canyons, with particularly significant effects observed in densely populated urban areas characterized by narrow street widths. The strong updraft behind the upstream building results from the weakened downwash failing to counteract buoyancy, which enhances vertical transport of warm air from the lower to upper parts of the street canyon. Under TWP, the attenuation of downwash flow was more pronounced in the step-down street canyon, where buoyancy-driven and wind-driven flows acted in opposing directions, promoting the transport of warm air out of the canyon interior. This resulted in lower PET values compared to those observed in the step-up configuration. The absence of vertical eddies may negatively impact PLWEs and diminish the efficiency of air pollutant dispersion.

The arcade design offers an effective approach for improving pedestrian thermal comfort in urban areas with complex wind flow patterns. Pedestrian thermal comfort, as indicated by PET values, was substantially improved under TWP compared to CWP, with the most pronounced enhancement observed in downstream sidewalk zones. The cooling effect generated by twisted winds was more evident in short street canyons featuring arcade designs, while it decreased progressively in medium- and long-length canyons. PET values demonstrated a positive correlation with street length; specifically, the PET value increased by 2 °C under CWP and by 4 °C under TWP as the L/D ratio rose from 1 to 10.

7.3 Recommendations for future research

Despite the achievements attained in the present study, certain limitations remain that warrant further investigation in future research:

(1) For the irregular elevated building investigations, the parametric study solely encompasses specific building shapes; future research endeavours will encompass additional parameters such as street layout, height of buildings, and supporting pillars. For the simulations, a typical Arch-shaped high-rise elevated building was considered. However, in real urban areas, there are more irregularly shaped buildings. Future studies will focus on extending the simulation to incorporate other building shapes. In addition, the wind tunnel experiment was performed with only one planar area ratio, it is anticipated that further CFD simulations will be conducted to predict pedestrian-level wind patterns associated with planar area ratios in future studies.

(2) For the twisted wind investigation, due to the time and cost constraints, this study only simulated two distinct twist angles (13° and 25°) to represent two different wind

conditions. However, it is important to note that real-life topography-induced wind profiles tend to exhibit greater complexity. Therefore, future studies should explore additional twist angles to provide a more comprehensive understanding of these intricate wind patterns. Additionally, the simulated tandem building configuration cannot fully represent the wide range of building configurations found in real-life scenarios. Hence, further research should consider other parameters.

(3) The entire process in the twisted wind study is based on mean wind velocity at the pedestrian level; therefore, a series of CFD simulations should be expected to predict the wind flow interference at the vertical plane in future investigations. This study encompasses a diverse range of velocity fields, which can serve as valuable resources for validating CFD simulations. Moreover, the temporal fluctuations of wind velocity were not taken into account; future studies should incorporate considerations for wind turbulence.

(4) For the effect of twisted wind on arcade design, even though the simulated TWP in the CFD simulations provides a general framework for analyzing pedestrian comfort in urban environments, it falls short of fully replicating real-world conditions. Future research should utilize realistic terrain models to incorporate more detailed topographic effects, such as actual terrain slopes. Second, the current study exclusively examined arcade designs featuring semi-open structures. Other arcade configurations incorporating peripheral columns or shear walls may substantially influence pedestrian wind and thermal comfort under CWP and TWP, owing to increased disturbances in wind flows.

REFERENCES

A. Peña S. E. G., R. Floors. (2014). The Turning of the Wind in the Atmospheric Boundary Layer. *In Journal of Physics: Conference Series*. 524, 012118.

Abd Elraouf R., Elmokadem A., Megahed N., Abo Eleinen O., Eltarabily S.(2022). The Impact of Urban Geometry on Outdoor Thermal Comfort in a Hot-Humid Climate. *Building and Environment*. 225. https://doi.org/10.1016/j.buildenv.2022.109632.

Addepalli B.,Pardyjak E. R.(2013). Investigation of the Flow Structure in Step-up Street Canyons—Mean Flow and Turbulence Statistics. *Boundary-Layer Meteorology*. 148(1), 133-155. https://doi.org/10.1007/s10546-013-9810-5.

Ai Z. T., Mak C. M.(2014). Potential Use of Reduced-Scale Models in Cfd Simulations to Save Numerical Resources: Theoretical Analysis and Case Study of Flow around an Isolated Building. *Journal of Wind Engineering and Industrial Aerodynamics*. 134, 25-29. https://doi.org/10.1016/j.jweia.2014.08.009.

Ai Z. T., Mak C. M.(2015). Large-Eddy Simulation of Flow and Dispersion around an Isolated Building: Analysis of Influencing Factors. *Computers & fluids*. 118, 89-100. https://doi.org/10.1016/j.compfluid.2015.06.006.

Ali-Toudert F., Mayer H.(2006). Numerical Study on the Effects of Aspect Ratio and Orientation of an Urban Street Canyon on Outdoor Thermal Comfort in Hot and Dry Climate. *Building and Environment*. 41(2), 94-108. https://doi.org/10.1016/j.buildenv.2005.01.013.

Amorim J. H., Rodrigues V., Tavares R., Valente J., Borrego C.(2013). Cfd Modelling of the Aerodynamic Effect of Trees on Urban Air Pollution Dispersion. *Sci Total Environ*. 461-462, 541-551. https://doi.org/10.1016/j.scitotenv.2013.05.031.

Antoniou N., Montazeri H., Neophytou M., Blocken B.(2019). Cfd Simulation of Urban Microclimate: Validation Using High-Resolution Field Measurements. *Sci Total Environ*. 695, 133743. https://doi.org/10.1016/j.scitotenv.2019.133743.

AS. NZS 1170.2.(2002). Australian/New Zealand Standard, Structural Design Action Parts 2: Wind Actions. *Standards Australia & Standards New Zealand, Sydney*.

ASCE.(1999). American Society of Civil Engineers (Asce) Manuals and Reports on Engineering Practice. *Virginia*. No. 67: Wind tunnel studies of buildings and structures.

Biao L., Cunyan J., Lu W., Weihua C.,Jing L.(2019). A Parametric Study of the Effect of Building Layout on Wind Flow over an Urban Area. *Building and Environment*. 160. https://doi.org/10.1016/j.buildenv.2019.106160.

Blocken B.(2014). 50 Years of Computational Wind Engineering: Past, Present and Future. *Journal of Wind Engineering and Industrial Aerodynamics*. 129, 69-102. https://doi.org/10.1016/j.jweia.2014.03.008.

Blocken B.(2015). Computational Fluid Dynamics for Urban Physics: Importance, Scales, Possibilities, Limitations and Ten Tips and Tricks Towards Accurate and Reliable Simulations. *Building and Environment*. 91, 219-245. https://doi.org/10.1016/j.buildenv.2015.02.015.

Blocken B., Janssen W. D.,van Hooff T.(2012). Cfd Simulation for Pedestrian Wind Comfort and Wind Safety in Urban Areas: General Decision Framework and Case Study for the Eindhoven University Campus. *Environmental Modelling & Software*. 30, 15-34. https://doi.org/10.1016/j.envsoft.2011.11.009.

Blocken B., Stathopoulos T., Carmeliet J.(2007). Cfd Simulation of the Atmospheric Boundary Layer: Wall Function Problems. *Atmospheric Environment*. 41(2), 238-252. https://doi.org/10.1016/j.atmosenv.2006.08.019.

Blocken B., Stathopoulos T., van Beeck J. P. A. J.(2016). Pedestrian-Level Wind Conditions around Buildings: Review of Wind-Tunnel and Cfd Techniques and Their Accuracy for Wind

Comfort Assessment. *Building and Environment*. 100, 50-81. https://doi.org/10.1016/j.buildenv.2016.02.004.

Bottema M.(2000). A Method for Optimisation of Wind Discomfort Criteria. *Build Environ*. 35, 1-18.

Caciolo M., Stabat P., Marchio D.(2012). Numerical Simulation of Single-Sided Ventilation Using Rans and Les and Comparison with Full-Scale Experiments. *Building and Environment*. 50, 202-213. https://doi.org/10.1016/j.buildenv.2011.10.017.

Chatzidimitriou A., Yannas S.(2017). Street Canyon Design and Improvement Potential for Urban Open Spaces; the Influence of Canyon Aspect Ratio and Orientation on Microclimate and Outdoor Comfort. *Sustainable Cities and Society*. 33, 85-101. https://doi.org/10.1016/j.scs.2017.05.019.

Chen G., Mei S.-J., Hang J., Li Q., Wang X.(2025). Urans Simulations of Urban Microclimates: Validated by Scaled Outdoor Experiments. *Building and Environment*. 272. https://doi.org/10.1016/j.buildenv.2025.112691.

Chen L., Mak C. M.(2021). Integrated Impacts of Building Height and Upstream Building on Pedestrian Comfort around Ideal Lift-up Buildings in a Weak Wind Environment. *Building and Environment*. 200. https://doi.org/10.1016/j.buildenv.2021.107963.

Chen L., Mak C. M.(2021). Numerical Evaluation of Pedestrian-Level Wind Comfort around "Lift-up" Buildings with Various Unconventional Configurations. *Building and Environment*. 188. https://doi.org/10.1016/j.buildenv.2020.107429.

Chen L., Mak C. M., Hang J., Dai Y.(2024). Influence of Elevated Walkways on Outdoor Thermal Comfort in Hot-Humid Climates Based on on-Site Measurement and Cfd Modeling. *Sustainable Cities and Society*. 100. https://doi.org/10.1016/j.scs.2023.105048.

Chen Z., Li D., Li S., Bai J., Fu X., Li C. Y., Wang H., Fu Y.,Tse K. T.(2023). Experimental and Numerical Investigation on the Aerodynamics of Isolated High-Rise Building and

Phenomenology of Twisted Wind Field. *Engineering Applications of Computational Fluid Mechanics*. 17(1). https://doi.org/10.1080/19942060.2023.2264351.

Chew L. W., Norford L. K.(2018). Pedestrian-Level Wind Speed Enhancement in Urban Street Canyons with Void Decks. *Building and Environment*. 146, 64-76. https://doi.org/10.1016/j.buildenv.2018.09.039.

Chui E. H. a. R., G.D. (1993). Computation of Radiant Heat Transfer on a Nonorthogonal Mesh Using the Finite-Volume Method., *Numerical Heat Transfer*. 23(3), 269-288.

Courant, R., Friedrichs, K., & Lewy, H.(1967). On the Partial Difference Equations of Mathematical Physics. . *IBM Journal of Research and Development.* 11 2, 215-234.

da Silva B. L., Chakravarty R., Sumner D., Bergstrom D. J.(2020). Aerodynamic Forces and Three-Dimensional Flow Structures in the Mean Wake of a Surface-Mounted Finite-Height Square Prism. *International Journal of Heat and Fluid Flow*. 83. https://doi.org/10.1016/j.ijheatfluidflow.2020.108569.

Dai Y., Mak C. M., Ai Z.,Hang J.(2018). Evaluation of Computational and Physical Parameters Influencing Cfd Simulations of Pollutant Dispersion in Building Arrays. *Building and Environment*. 137, 90-107. https://doi.org/10.1016/j.buildenv.2018.04.005.

Deevi B., Chundeli F. A.(2020). Quantitative Outdoor Thermal Comfort Assessment of Street: A Case in a Warm and Humid Climate of India. *Urban Climate*. 34. https://doi.org/10.1016/j.uclim.2020.100718.

Du Y., Mak C. M., Huang T.,Niu J.(2017). Towards an Integrated Method to Assess Effects of Lift-up Design on Outdoor Thermal Comfort in Hong Kong. *Building and Environment*. 125, 261-272. https://doi.org/10.1016/j.buildenv.2017.09.001.

Du Y., Mak C. M., Kwok K., Tse K.-T., Lee T.-c., Ai Z., Liu J.,Niu J.(2017). New Criteria for Assessing Low Wind Environment at Pedestrian Level in Hong Kong. *Building and Environment*. 123, 23-36. https://doi.org/10.1016/j.buildenv.2017.06.036.

Du Y., Mak C. M.,Li Y.(2019). A Multi-Stage Optimization of Pedestrian Level Wind Environment and Thermal Comfort with Lift-up Design in Ideal Urban Canyons. *Sustainable Cities and Society*. 46. https://doi.org/10.1016/j.scs.2019.101424.

Du Y., Mak C. M., Liu J., Xia Q., Niu J., Kwok K. C. S.(2017). Effects of Lift-up Design on Pedestrian Level Wind Comfort in Different Building Configurations under Three Wind Directions. *Building and Environment*. 117, 84-99. https://doi.org/10.1016/j.buildenv.2017.03.001.

Du Y., Mak C. M., Tang B.-s.(2018). Effects of Building Height and Porosity on Pedestrian Level Wind Comfort in a High-Density Urban Built Environment. *Building Simulation*. 11(6), 1215-1228. https://doi.org/10.1007/s12273-018-0451-y.

Durgin F. H.(1992). Pedestrian Level Wind Studies at the Wright Brothers Facility. *J. Wind Eng. Ind. Aerodyn*. 44(1-3), 2253-2264.

Ekman V. W.(1905). On the Influence of the Earth's Rotation on Ocean-Currents.

Engineers A. S. o. C.(2012). Wind Tunnel Testing for Buildings and Other Structures. *American Society of Civil Engineers*.

Fan M., Chau C. K., Chan E. H. W.,Jia J.(2017). A Decision Support Tool for Evaluating the Air Quality and Wind Comfort Induced by Different Opening Configurations for Buildings in Canyons. *Sci Total Environ*. 574, 569-582. https://doi.org/10.1016/j.scitotenv.2016.09.083.

Fang T. Y., Shui T., Liu J., Wang H., Zhang L., Khaletski V.(2019). Wind Tunnel Study on the Pedestrian-Level Wind Comfort in Residential Areas of Harbin. *E3S Web of Conferences*. 136. https://doi.org/10.1051/e3sconf/201913604097.

Fanger P. O.(1970). Thermal Comfort: Analysis and Applications in Environmental Engineering. *McGraw-Hill, New York*. 244.

Feng C., Gu M., Zheng D.(2019). Numerical Simulation of Wind Effects on Super High-Rise Buildings Considering Wind Veering with Height Based on Cfd. *Journal of Fluids and Structures*. 91. https://doi.org/10.1016/j.jfluidstructs.2019.102715.

Fiala D., Havenith G., Brode P., Kampmann B.,Jendritzky G.(2012). Utci-Fiala Multi-Node Model of Human Heat Transfer and Temperature Regulation. *Int J Biometeorol*. 56(3), 429-441. https://doi.org/10.1007/s00484-011-0424-7.

Flay R. G. J., King A. B., Revell M., Carpenter P., Turner R., Cenek P., Safaei Pirooz A. A.(2019). Wind Speed Measurements and Predictions over Belmont Hill, Wellington, New Zealand. *Journal of Wind Engineering and Industrial Aerodynamics*. 195. https://doi.org/10.1016/j.jweia.2019.104018.

Fluent.(2013). Ansys Fluent Theory Guide. *In. Canonsburg, PA: ANSYS Inc.*

Franke J., et al.(2011). The Cost 732 Best Practice Guideline for Cfd Simulation of Flows in the Urban Environment: A Summary. *International Journal of Environment and Pollution*. 44 1-4, 419-427.

Freidooni F., Sohankar A., Rastan M. R., Shirani E.(2021). Flow Field around Two Tandem Non-Identical-Height Square Buildings Via Les. *Building and Environment*. 201. https://doi.org/10.1016/j.buildenv.2021.107985.

Fu Y., Li C. Y., Zhao Z., Zhang B., Tse K. T., Mak C. M., Chen Z.*, et al.*(2024). Energetic and Dynamic Characterization of Pollutant Dispersion in Varied Building Layouts through an Augmented Analysis Procedure. *Physics of Fluids*. 36(3). https://doi.org/10.1063/5.0190268.

Gagge A. P., Fobelets, A.P. and Berglund, L.(1986). A Standard Predictive Index of Human Response to the Thermal Environment.

Gao H., Liu J., Lin P., Li C., Xiao Y.,Hu G.(2022). Pedestrian Level Wind Flow Field of Elevated Tall Buildings with Dense Tandem Arrangement. *Building and Environment*. 226. https://doi.org/10.1016/j.buildenv.2022.109745.

Grimmond C. S. B., Oke T. R.(1999). Aerodynamic Properties of Urban Areas Derived from Analysis of Surface Form. *Journal of Applied Meteorology*. 38(9), 1262-1292. https://doi.org/10.1175/1520-0450(1999)038.

Gromke C., Buccolieri R., Di Sabatino S.,Ruck B.(2008). Dispersion Study in a Street Canyon with Tree Planting by Means of Wind Tunnel and Numerical Investigations – Evaluation of Cfd Data with Experimental Data. *Atmospheric Environment*. 42(37), 8640-8650. https://doi.org/10.1016/j.atmosenv.2008.08.019.

Gu Z.-L., Zhang Y.-W., Cheng Y.,Lee S.-C.(2011). Effect of Uneven Building Layout on Air Flow and Pollutant Dispersion in Non-Uniform Street Canyons. *Building and Environment*. 46(12), 2657-2665. https://doi.org/10.1016/j.buildenv.2011.06.028.

H. Wu T. S.(1994). Further Experiments on Irwin's Surface Wind Sensor. *Journal of Wind Engineering and Industrial Aerodynamics*. 53 (3), 441-452.

H. Wu T. S.(1994). Further Experiments on Irwin's Surface Wind Sensor. *J. Wind Eng. Ind. Aerodyn*. 53(3), 441-452.

Hang J., Li Q., Du Y., Feng J., Hua J., Zhao B.(2024). Effects of Arcade Design on Wind and Thermal Environment inside an Idealized 2d Urban Canyon with Realistic Solar Heating. *Building and Environment*. 254. https://doi.org/10.1016/j.buildenv.2024.111329.

Hang J.,Li Y.(2010). Ventilation Strategy and Air Change Rates in Idealized High-Rise Compact Urban Areas. *Building and Environment*. 45(12), 2754-2767. https://doi.org/10.1016/j.buildenv.2010.06.004.

Hang J.,Li Y.(2011). Age of Air and Air Exchange Efficiency in High-Rise Urban Areas and Its Link to Pollutant Dilution. *Atmospheric Environment*. 45(31), 5572-5585. https://doi.org/10.1016/j.atmosenv.2011.04.051.

Hang J., Li Y., Sandberg M., Buccolieri R.,Di Sabatino S.(2012). The Influence of Building Height Variability on Pollutant Dispersion and Pedestrian Ventilation in Idealized High-Rise

Urban Areas. *Building and Environment*. 56, 346-360. https://doi.org/10.1016/j.buildenv.2012.03.023.

Hang J., Luo Z., Sandberg M., Gong J.(2013). Natural Ventilation Assessment in Typical Open and Semi-Open Urban Environments under Various Wind Directions. *Building and Environment*. 70, 318-333. https://doi.org/10.1016/j.buildenv.2013.09.002.

Hanna S., Chang J.(2012). Acceptance Criteria for Urban Dispersion Model Evaluation. *Meteorology and Atmospheric Physics*. 116(3-4), 133-146. https://doi.org/10.1007/s00703-011-0177-1.

Hassan S., Molla M. M., Nag P., Akhter N., Khan A.(2021). Unsteady Rans Simulation of Wind Flow around a Building Shape Obstacle. *Building Simulation*. 15(2), 291-312. https://doi.org/10.1007/s12273-021-0785-8.

HKO.(2019). *Statistical Data of Weather Information in Hong Kong*.

Holger Koss H.(2006). On Differences and Similarities of Applied Wind Comfort Criteria. *Journal of Wind Engineering and Industrial Aerodynamics*. 94(11), 781-797. https://doi.org/10.1016/j.jweia.2006.06.005.

Höppe P.(1999). The Physiological Equivalent Temperature–a Universal Index for the Biometeorological Assessment of the Thermal Environment. *International journal of Biometeorology* 43 2, 71-75.

Höppe P.(1999). The Physiological Equivalent Temperature – a Universal Index for the Biometeorological Assessment of the Thermal Environment. *International Journal of Biometeorology*. 43, 71-75.

Hosseini S. H., Ghobadi P., Ahmadi T., Calautit J. K.(2017). Numerical Investigation of Roof Heating Impacts on Thermal Comfort and Air Quality in Urban Canyons. *Applied Thermal Engineering*. 123, 310-326. https://doi.org/10.1016/j.applthermaleng.2017.05.095.

Huang T., Niu J., Xie Y., Li J.,Mak C. M.(2020). Assessment of “Lift-up” Design’s Impact on Thermal Perceptions in the Transition Process from Indoor to Outdoor. *Sustainable Cities and Society*. 56. https://doi.org/10.1016/j.scs.2020.102081.

I. B. Celik Z. N. C., and I. Yavuz. (2005). Index of Resolution Quality for Large Eddy Simulations. *J. Fluids Eng*. 127 (5), 949-958.

I. Goricsán M. B., M. Balogh, K. Czáder, A. Rákai, C. Tonkó.(2011). Simulation of Flow in an Idealised City Using Various Cfd Codes. *Int. J. Environ. Pollut*. 44(1-4), 359-367.

Idczak M., Mestayer P., Rosant J.-M., Sini J.-F., Violleau M.(2006). Micrometeorological Measurements in a Street Canyon During the Joint Atreus-Picada Experiment. *Boundary-Layer Meteorology*. 124(1), 25-41. https://doi.org/10.1007/s10546-006-9095-z.

Irwin H. P. A. H.(1981). A Simple Omnidirectional Sensor for Wind-Tunnel Studies of Pedestrian-Level Winds. *Journal of Wind Engineering and Industrial Aerodynamics*. 7 (3), 219-239.

J.V.Seguro, Lambert T. W.(2000). Modern Estimation of the Parameters of the Weibull Wind Speed Distribution for Wind Energy Analysis. *Journal of Wind Engineering and Industrial Aerodynamics*. 85, 75-84.

Jeong H., Lee S., Kwon S.-D.(2018). Blockage Corrections for Wind Tunnel Tests Conducted on a Darrieus Wind Turbine. *Journal of Wind Engineering and Industrial Aerodynamics*. 179, 229-239. https://doi.org/10.1016/j.jweia.2018.06.002.

Ji Y., Song J.,Shen P.(2022). A Review of Studies and Modelling of Solar Radiation on Human Thermal Comfort in Outdoor Environment. *Building and Environment*. 214. https://doi.org/10.1016/j.buildenv.2022.108891.

Juan Y.-H., Yang A.-S., Wen C.-Y., Lee Y.-T.,Wang P.-C.(2017). Optimization Procedures for Enhancement of City Breathability Using Arcade Design in a Realistic High-Rise Urban Area. *Building and Environment*. 121, 247-261. https://doi.org/10.1016/j.buildenv.2017.05.035.

K.B. Shah J. H. F.(1997). A Fluid Mechanicians View of Wind Engineering: Large Eddy Simulation of Flow Past a Cube Obstacle. *J. Wind Eng. Ind. Aerod*. 67-68, 211-224.

Ketterer C., Gangwisch M., Frohlich D.,Matzarakis A.(2017). Comparison of Selected Approaches for Urban Roughness Determination Based on Voronoi Cells. *Int J Biometeorol*. 61(1), 189-198. https://doi.org/10.1007/s00484-016-1203-2.

Lai D., Liu W., Gan T., Liu K., Chen Q.(2019). A Review of Mitigating Strategies to Improve the Thermal Environment and Thermal Comfort in Urban Outdoor Spaces. *Sci Total Environ*. 661, 337-353. https://doi.org/10.1016/j.scitotenv.2019.01.062.

Lateb M., Masson C., Stathopoulos T., Bédard C.(2013). Comparison of Various Types of K–E Models for Pollutant Emissions around a Two-Building Configuration. *Journal of Wind Engineering and Industrial Aerodynamics*. 115, 9-21. https://doi.org/10.1016/j.jweia.2013.01.001.

Launder B. E., Spalding, D.B.(1972). Lectures in Mathematical Model of Turbulence., *Academic Press, London.*

Lawson T.(1978). The Wind Content of Built Environment. *Journal of Wind Engineering and Industrial Aerodynamics*. 3, 93-105.

Li B., Luo Z., Sandberg M., Liu J.(2015). Revisiting the 'Venturi Effect' in Passage Ventilation between Two Non-Parallel Buildings. *Building and Environment*. 94, 714-722. https://doi.org/10.1016/j.buildenv.2015.10.023.

Li W., Mak C. M.,Cai C.(2025). Numerical Evaluation of the Effect of Twisted wind on Pedestrian Comfort Surrounding Semi-Open Structures and Influential Factors under Solar Heating. *Building Simulation*. 18, 1409-1433. https://doi.org/10.1007/s12273-025-1262-6.

Li W., Mak C. M., Cai C., Fu Y., Tse K. T.,Niu J.(2024). Wind Tunnel Measurement of Pedestrian-Level Gust Wind Flow and Comfort around Irregular Lift-up Buildings within

Simplified Urban Arrays. *Building and Environment*. 256. https://doi.org/10.1016/j.buildenv.2024.111487.

Li W., Mak C. M., Fu Y., Cai C., Tse K. T.,Niu J.(2024). The Impact of Twisted Wind on Pedestrian Comfort around Two Non-Identical-Height Buildings in Tandem Arrangement: A Wind Tunnel Study. *Building and Environment*. 262. https://doi.org/10.1016/j.buildenv.2024.111847.

Li W., Mak C. M., Fu Y., Cai C., Tse K. T., Niu J., Wong S. H. Y.(2024). Pedestrian-Level Wind Environment Surrounding Two Tandem Non-Identical Height Elevated Buildings under the Influence of Twisted Wind Flows. *Sustainable Cities and Society*. https://doi.org/10.1016/j.scs.2024.105641.

Li Z., Zhang H., Juan Y.-H., Wen C.-Y., Yang A.-S.(2022). Effects of Building Setback on Thermal Comfort and Air Quality in the Street Canyon. *Building and Environment*. 208. https://doi.org/10.1016/j.buildenv.2021.108627.

Li Z., Zhang H., Wen C.-Y., Yang A.-S., Juan Y.-H.(2020). Effects of Frontal Area Density on Outdoor Thermal Comfort and Air Quality. *Building and Environment*. 180. https://doi.org/10.1016/j.buildenv.2020.107028.

Li Z., Zhang H., Wen C.-Y., Yang A.-S., Juan Y.-H.(2020). Effects of Height-Asymmetric Street Canyon Configurations on Outdoor Air Temperature and Air Quality. *Building and Environment*. 183. https://doi.org/10.1016/j.buildenv.2020.107195.

Li Z., Zhang H., Wen C.-Y., Yang A.-S., Juan Y.-H.(2021). The Effects of Lateral Entrainment on Pollutant Dispersion inside a Street Canyon and the Corresponding Optimal Urban Design Strategies. *Building and Environment*. 195. https://doi.org/10.1016/j.buildenv.2021.107740.

Lin C., Ooka R., Kikumoto H., Sato T.,Arai M.(2021). Cfd Simulations on High-Buoyancy Gas Dispersion in the Wake of an Isolated Cubic Building Using Steady Rans Model and Les. *Building and Environment*. 188. https://doi.org/10.1016/j.buildenv.2020.107478.

Lin M., Hang J., Li Y., Luo Z.,Sandberg M.(2014). Quantitative Ventilation Assessments of Idealized Urban Canopy Layers with Various Urban Layouts and the Same Building Packing Density. *Building and Environment*. 79, 152-167. https://doi.org/10.1016/j.buildenv.2014.05.008.

Lin N., Letchford C., Tamura Y., Liang B., Nakamura O.(2005). Characteristics of Wind Forces Acting on Tall Buildings. *Journal of Wind Engineering and Industrial Aerodynamics*. 93(3), 217-242. https://doi.org/10.1016/j.jweia.2004.12.001.

Lin Q., Yang Q.,Tamura Y.(2025). Piv Study on Characteristics of Pedestrian-Level Fluctuating Wind Speeds around Square Buildings with Different Heights. *Building and Environment*. 267. https://doi.org/10.1016/j.buildenv.2024.112271.

Lin T. P.,Matzarakis A.(2008). Tourism Climate and Thermal Comfort in Sun Moon Lake, Taiwan. *Int J Biometeorol*. 52(4), 281-290. https://doi.org/10.1007/s00484-007-0122-7.

Lin Y., Ichinose T., Yamao Y.,Mouri H.(2020). Wind Velocity and Temperature Fields under Different Surface Heating Conditions in a Street Canyon in Wind Tunnel Experiments. *Building and Environment*. 168. https://doi.org/10.1016/j.buildenv.2019.106500.

Liu J., Niu J.(2016). Cfd Simulation of the Wind Environment around an Isolated High-Rise Building: An Evaluation of Srans, Les and Des Models. *Building and Environment*. 96, 91-106. https://doi.org/10.1016/j.buildenv.2015.11.007.

Liu J., Niu J., Du Y., Mak C. M., Zhang Y.(2019). Les for Pedestrian Level Wind around an Idealized Building Array—Assessment of Sensitivity to Influencing Parameters. *Sustainable Cities and Society*. 44, 406-415. https://doi.org/10.1016/j.scs.2018.10.034.

Liu J., Niu J., Mak C. M., Xia Q.(2017). Detached Eddy Simulation of Pedestrian-Level Wind and Gust around an Elevated Building. *Building and Environment*. 125, 168-179. https://doi.org/10.1016/j.buildenv.2017.08.031.

Liu J., Niu J., Xia Q.(2016). Combining Measured Thermal Parameters and Simulated Wind Velocity to Predict Outdoor Thermal Comfort. *Building and Environment*. 105, 185-197. https://doi.org/10.1016/j.buildenv.2016.05.038.

Liu J., Zhang X., Niu J., Tse K. T.(2019). Pedestrian-Level Wind and Gust around Buildings with a 'Lift-up' Design: Assessment of Influence from Surrounding Buildings by Adopting Les. *Building Simulation*. 12(6), 1107-1118. https://doi.org/10.1007/s12273-019-0541-5.

Liu W., Zhang Y., Deng Q.(2016). The Effects of Urban Microclimate on Outdoor Thermal Sensation and Neutral Temperature in Hot-Summer and Cold-Winter Climate. *Energy and Buildings*. 128, 190-197. https://doi.org/10.1016/j.enbuild.2016.06.086.

Liu Z., Zheng C., Wu Y., Flay R. G. J., Zhang K.(2019). Investigation on the Effects of Twisted Wind Flow on the Wind Loads on a Square Section Megatall Building. *Journal of Wind Engineering and Industrial Aerodynamics*. 191, 127-142. https://doi.org/10.1016/j.jweia.2019.06.003.

Liu Z., Zheng C., Wu Y.,Song Y.(2018). Investigation on Characteristics of Thousand-Meter Height Wind Profiles at Non-Tropical Cyclone Prone Areas Based on Field Measurement. *Building and Environment*. 130, 62-73. https://doi.org/10.1016/j.buildenv.2017.12.001.

Lombardo F. T.(2021). History of the Peak Three-Second Gust. *Journal of Wind Engineering and Industrial Aerodynamics*. 208. https://doi.org/10.1016/j.jweia.2020.104447.

Longo S.(2012). Wind-Generated Water Waves in a Wind Tunnel: Free Surface Statistics, Wind Friction and Mean Air Flow Properties. *Coastal Engineering*. 61, 27-41. https://doi.org/10.1016/j.coastaleng.2011.11.008.

Melbourne W.(1978). Criteria for Environmental Wind Conditions. *Journal of Wind Engineering and Industrial Aerodynamics*. 3, 241-249.

Melbourne W. H.(1971). Problem of Wind Flow at the Base of Tall Buildings. *In 2nd Int. Conf. on Wind Effects on Buildings and Structures.*

Melbourne W. H.(1978). Criteria for Environmental Wind Conditions. *Journal of Wind Engineering and Industrial Aerodynamics*. 241-249.

Memon R. A., Leung D. Y. C., Liu C.-H.(2010). Effects of Building Aspect Ratio and Wind Speed on Air Temperatures in Urban-Like Street Canyons. *Building and Environment*. 45(1), 176-188. https://doi.org/10.1016/j.buildenv.2009.05.015.

Mendenhall B. R.(1967). A Statistical Study of Frictional Wind Veering in the Planetary Boundary Layer. *Atmospheric science paper*. 116.

Mendenhall B. R.(1967). Statistical Study of Frictional Wind Veering in the Planetary Boundary Layer., *Ph.D. Dissertation, Colorado State University, Fort Collins, CO, USA*.

Menter F.(1993). Zonal Two Equation K-W Turbulence Models for Aerodynamic Flows. *In 23rd fluid dynamics, plasmadynamics, and lasers conference*. 2906.

Middel A., AlKhaled S., Schneider F. A., Hagen B., Coseo P.(2021). 50 Grades of Shade. *Bulletin of the American Meteorological Society*. 102(9), E1805-E1820. https://doi.org/10.1175/bams-d-20-0193.1.

Moemenbellah-Fard M. S., Noori S.(2020). Discrete Ordinate and P1-Based Approximations of Heater Transparency on Radiation-Convection of Four Separate Gases in Factory Setting. *Building Simulation*. 13(3), 647-663. https://doi.org/10.1007/s12273-020-0604-7.

Mohammadi M., Tien P. W.,Calautit J. K.(2023). Numerical Evaluation of the Use of Vegetation as a Shelterbelt for Enhancing the Wind and Thermal Comfort in Peripheral and Lateral-Type Skygardens in Highrise Buildings. *Build Simul*. 16(2), 243-261. https://doi.org/10.1007/s12273-022-0943-7.

Moonen P., Allegrini J.(2015). Employing Statistical Model Emulation as a Surrogate for Cfd. *Environmental Modelling & Software*. 72, 77-91. https://doi.org/10.1016/j.envsoft.2015.06.007.

Moonen P., Defraeye T., Dorer V., Blocken B., Carmeliet J.(2012). Urban Physics: Effect of the Micro-Climate on Comfort, Health and Energy Demand. *Frontiers of Architectural Research*. 1(3), 197-228. https://doi.org/10.1016/j.foar.2012.05.002.

Mu D., Gao N., Zhu T.(2018). Cfd Investigation on the Effects of Wind and Thermal Wall-Flow on Pollutant Transmission in a High-Rise Building. *Build Environ*. 137, 185-197. https://doi.org/10.1016/j.buildenv.2018.03.051.

Murakami S.(1993). Comparison of Various Turbulence Models Applied to a Bluff Body. *J. Wind Eng. Ind. Aerod*. 46-47, 21-36.

N. Isyumov, Davenport A. G.(1975). The Ground Level Wind Enviornment in Built-up Areas. *In Proc. 4th Int. Conf. on Wind Effects on Buildings and Structures*. 403-422.

Nicoud F D. F.(1999). Subgrid-Scale Stress Modelling Based on the Square of the Velocity Gradient Tensor., *Flow, Turbulence and Combustion*. 62, 183-200.

Niegodajew P., Procházka P., Uruba V., Elsner W.,Gnatowska R.(2024). Effect of the Angle of Attack on the Flow around Two Non-Identical-Height Square Buildings in Tandem Arrangement. *Building and Environment*. 248. https://doi.org/10.1016/j.buildenv.2023.111076.

Niu J., Liu J., Lee T.-c., Lin Z., Mak C., Tse K.-T., Tang B.-s., Kwok K. C. S.(2015). A New Method to Assess Spatial Variations of Outdoor Thermal Comfort: Onsite Monitoring Results and Implications for Precinct Planning. *Building and Environment*. 91, 263-270. https://doi.org/10.1016/j.buildenv.2015.02.017.

Okaze T., Kikumoto H., Ono H., Imano M., Ikegaya N., Hasama T., Nakao K., *et al.*(2021). Large-Eddy Simulation of Flow around an Isolated Building: A Step-by-Step Analysis of Influencing Factors on Turbulent Statistics. *Building and Environment*. 202. https://doi.org/10.1016/j.buildenv.2021.108021.

Oke T. R.(1988). Street Design and Urban Canopy Layer Climate. *Energy Build*. 11, 103–113.

Park S.-J., Kim J.-J., Choi W., Kim E.-R., Song C.-K.,Pardyjak E. R.(2019). Flow Characteristics around Step-up Street Canyons with Various Building Aspect Ratios. *Boundary-Layer Meteorology*. 174(3), 411-431. https://doi.org/10.1007/s10546-019-00494-9.

Peng Y., Gao Z., Buccolieri R., Shen J.,Ding W.(2021). Urban Ventilation of Typical Residential Streets and Impact of Building Form Variation. *Sustainable Cities and Society*. 67. https://doi.org/10.1016/j.scs.2021.102735.

Prohasky D., and Simon Watkins. (2014). Low Cost Hot-Element Anemometry Verses the Tfi Cobra. *In 19th Australasian Fluid Mechanics Conference*.

Qu Y., Milliez M., Musson-Genon L.,Carissimo B.(2012). Numerical Study of the Thermal Effects of Buildings on Low-Speed Airflow Taking into Account 3d Atmospheric Radiation in Urban Canopy. *Journal of Wind Engineering and Industrial Aerodynamics*. 104-106, 474-483. https://doi.org/10.1016/j.jweia.2012.03.008.

Reiminger N., Vazquez J., Blond N., Dufresne M.,Wertel J.(2020). Cfd Evaluation of Mean Pollutant Concentration Variations in Step-Down Street Canyons. *Journal of Wind Engineering and Industrial Aerodynamics*. 196. https://doi.org/10.1016/j.jweia.2019.104032.

Ribeiro K. F. A., Justi A. C. A., Novais J. W. Z., Santos F. M. d. M., Nogueira M. C. d. J. A., Miranda S. A., Marques J. B.(2022). Calibration of the Physiological Equivalent Temperature (Pet) Index Range for Outside Spaces in a Tropical Climate City. *Urban Climate*. 44. https://doi.org/10.1016/j.uclim.2022.101196.

Roache P. J.(1997). Quantification of Uncertainty in Computational Fluid Dynamics. *Annu. Rev. Fluid Mech*. 29, 123-160.

Sanz-Andres A.,Cuerva A.(2006). Pedestrian Wind Comfort: Feasibility Study of Criteria Homogenisation. *Journal of Wind Engineering and Industrial Aerodynamics*. 94(11), 799-813. https://doi.org/10.1016/j.jweia.2006.06.004.

Sheng R., Perret L., Calmet I., Demouge F., Guilhot J.(2018). Wind Tunnel Study of Wind Effects on a High-Rise Building at a Scale of 1:300. *Journal of Wind Engineering and Industrial Aerodynamics*. 174, 391-403. https://doi.org/10.1016/j.jweia.2018.01.017.

Shih T. H., Liou, W.W., Shabbir, A., Yang, Z., and Zhu, J.(1995). A New K-ϵ Eddy Viscosity Model for High Reynolds Number Turbulent Flows., *Computers & fluids*. 24 3, 227-238.

Shirzadi M.,Tominaga Y.(2022). Cfd Evaluation of Mean and Turbulent Wind Characteristics around a High-Rise Building Affected by Its Surroundings. *Building and Environment*. 225. https://doi.org/10.1016/j.buildenv.2022.109637.

Shu Z. R., Li Q. S., He Y. C., Chan P. W.(2018). Observational Study of Veering Wind by Doppler Wind Profiler and Surface Weather Station. *Journal of Wind Engineering and Industrial Aerodynamics*. 178, 18-25. https://doi.org/10.1016/j.jweia.2018.05.001.

Sin C. H., Cui P. Y., Jon K. S., Luo Y., Shen J. W.,Huang Y. D.(2023). Evaluation on Ventilation and Traffic Pollutant Dispersion in Asymmetric Street Canyons with Void Decks. *Air Qual Atmos Health*. 16(4), 817-839. https://doi.org/10.1007/s11869-023-01314-3.

Soligo M. J.(1993). Pedestrian Comfort Including Wind and Thermal Effects. *3rd Asia-Pacific Symp. on Wind Engineering.* . 961-966.

Sudirman M., van Hooff T., Gillmeier S., Blocken B.(2025). Validation Study of Cross-Ventilation in a Realistic Building Geometry: Rans, Sas and Les. *Building and Environment*. 269. https://doi.org/10.1016/j.buildenv.2024.112354.

T.Stathopoulos R. S.(1986). Wind Environmental Conditions in Passages between Buildings. *Journal of Wind Engineering and Industrial Aerodynamics*. 24, 19-31.

T.V. Lawson, Penwarden A. D.(1975). The Effects of Wind on People in the Vicinity of Buildings. *In Proceedings 4th international conference on wind effects on buildings and structures.*, 604-622.

Tang L., Liu H., Zheng C.(2023). Effects of Twisted Wind Flow on the Mean Wind Load Characteristics of Super High-Rise Buildings with Different Heights. *Journal of Building Engineering*. 75. https://doi.org/10.1016/j.jobe.2023.106972.

Tang Y.-F., Wen Y.-B., Chen H., Tan Z.-C., Yao Y.-H.,Zhao F.-Y.(2023). Airflow Mitigation and Pollutant Purification in an Idealized Urban Street Canyon with Wind Driven Natural Ventilation: Cooperating and Opposing Effects of Roadside Tree Plantings and Non-Uniform Building Heights. *Sustainable Cities and Society*. 92. https://doi.org/10.1016/j.scs.2023.104483.

Taylor G. I.(1916). Skin Friction of the Wind on the Earth's Surface. *Proceedings of the Royal Society of London. Series A, Containing Papers of a Mathematical and Physical Character*. 92(637), 196-199.

To A. P., Lam, K.M.(1995). Evaluation of Pedestrian-Level Wind Environment around a Row of Tall Buildings Using a Quartile Descripter., *Journal of Wind Engineering and Industrial Aerodynamics*. 54-55, 527-541.

Tominaga Y.(2015). Flow around a High-Rise Building Using Steady and Unsteady Rans Cfd: Effect of Large-Scale Fluctuations on the Velocity Statistics. *Journal of Wind Engineering and Industrial Aerodynamics*. 142, 93-103. https://doi.org/10.1016/j.jweia.2015.03.013.

Tominaga Y., Mochida A., Murakami S., Sawaki S.(2008). Comparison of Various Revised K–E Models and Les Applied to Flow around a High-Rise Building Model with 1:1:2 Shape Placed within the Surface Boundary Layer. *Journal of Wind Engineering and Industrial Aerodynamics*. 96(4), 389-411. https://doi.org/10.1016/j.jweia.2008.01.004.

Tominaga Y., Mochida A., Yoshie R., Kataoka H., Nozu T., Yoshikawa M.,Shirasawa T.(2008). Aij Guidelines for Practical Applications of Cfd to Pedestrian Wind Environment around Buildings. *Journal of Wind Engineering and Industrial Aerodynamics*. 96(10-11), 1749-1761. https://doi.org/10.1016/j.jweia.2008.02.058.

Tominaga Y.,Shirzadi M.(2021). Wind Tunnel Measurement Dataset of 3d Turbulent Flow around a Group of Generic Buildings with and without a High-Rise Building. *Data Brief*. 39, 107504. https://doi.org/10.1016/j.dib.2021.107504.

Tominaga Y.,Shirzadi M.(2021). Wind Tunnel Measurement of Three-Dimensional Turbulent Flow Structures around a Building Group: Impact of High-Rise Buildings on Pedestrian Wind Environment. *Building and Environment*. 206. https://doi.org/10.1016/j.buildenv.2021.108389.

Tominaga Y., Stathopoulos T.(2009). Numerical Simulation of Dispersion around an Isolated Cubic Building: Comparison of Various Types of K–Ɛ Models. *Atmospheric Environment*. 43(20), 3200-3210. https://doi.org/10.1016/j.atmosenv.2009.03.038.

Tominaga Y., Stathopoulos T.(2012). Cfd Modeling of Pollution Dispersion in Building Array: Evaluation of Turbulent Scalar Flux Modeling in Rans Model Using Les Results. *Journal of Wind Engineering and Industrial Aerodynamics*. 104-106, 484-491. https://doi.org/10.1016/j.jweia.2012.02.004.

Tominaga Y., Stathopoulos T.(2013). Cfd Simulation of near-Field Pollutant Dispersion in the Urban Environment: A Review of Current Modeling Techniques. *Atmospheric Environment*. 79, 716-730. https://doi.org/10.1016/j.atmosenv.2013.07.028.

Toparlar Y., Blocken B., Maiheu B., van Heijst G. J. F.(2017). A Review on the Cfd Analysis of Urban Microclimate. *Renewable and Sustainable Energy Reviews*. 80, 1613-1640. https://doi.org/10.1016/j.rser.2017.05.248.

Toparlar Y., Blocken B., Vos P., van Heijst G. J. F., Janssen W. D., van Hooff T., Montazeri H.,Timmermans H. J. P.(2015). Cfd Simulation and Validation of Urban Microclimate: A Case Study for Bergpolder Zuid, Rotterdam. *Building and Environment*. 83, 79-90. https://doi.org/10.1016/j.buildenv.2014.08.004.

Tsang C. W., Kwok K. C. S., Hitchcock P. A.(2012). Wind Tunnel Study of Pedestrian Level Wind Environment around Tall Buildings: Effects of Building Dimensions, Separation and

Podium. *Building and Environment*. 49, 167-181. https://doi.org/10.1016/j.buildenv.2011.08.014.

Tse K. T., Weerasuriya A. U., Kwok K. C. S.(2016). Simulation of Twisted Wind Flows in a Boundary Layer Wind Tunnel for Pedestrian-Level Wind Tunnel Tests. *Journal of Wind Engineering and Industrial Aerodynamics*. 159, 99-109. https://doi.org/10.1016/j.jweia.2016.10.010.

Tse K. T., Weerasuriya A. U., Zhang X., Li S., Kwok K. C. S.(2017). Pedestrian-Level Wind Environment around Isolated Buildings under the Influence of Twisted Wind Flows. *Journal of Wind Engineering and Industrial Aerodynamics*. 162, 12-23. https://doi.org/10.1016/j.jweia.2017.01.002.

Tse K. T., Weerasuriya A. U., Zhang X., Li S. W., Kwok K. C. S.(2017). Effects of Twisted Wind Flows on Wind Conditions in Passages between Buildings. *Journal of Wind Engineering and Industrial Aerodynamics*. 167, 87-100. https://doi.org/10.1016/j.jweia.2017.04.011.

Tse K. T., Zhang X., Weerasuriya A. U., Li S. W., Kwok K. C. S., Mak C. M., Niu J.(2017). Adopting 'Lift-up' Building Design to Improve the Surrounding Pedestrian-Level Wind Environment. *Build Environ*. 117, 154-165. https://doi.org/10.1016/j.buildenv.2017.03.011.

Uehara K., Murakami, S., Oikawa, S., & Wakamatsu, S.(2000). Wind Tunnel Experiments on How Thermal Stratification Affects Flow in and above Urban Street Canyons. *Atmospheric Environment*. 34(10), 1553-1562

V. Yakhot S. A. O.(1986). Renormalization Group Analysis of Turbulence. I. Basic Theory. *J. Sci. Comput.* . 1, 3-51. https://doi.org/ https://doi.org/10.1007/BF01061452.

van Druenen T., van Hooff T., Montazeri H.,Blocken B.(2019). Cfd Evaluation of Building Geometry Modifications to Reduce Pedestrian-Level Wind Speed. *Building and Environment*. 163. https://doi.org/10.1016/j.buildenv.2019.106293.

Vita G., Shu Z., Jesson M., Quinn A., Hemida H., Sterling M., Baker C.(2020). On the Assessment of Pedestrian Distress in Urban Winds. *Journal of Wind Engineering and Industrial Aerodynamics*. 203. https://doi.org/10.1016/j.jweia.2020.104200.

Wang J., You R.(2024). Evaluating Different Categories of Turbulence Models for Calculating Air Pollutant Dispersion in Street Canyons with Generic and Real Urban Layouts. *Journal of Wind Engineering and Industrial Aerodynamics*. 255. https://doi.org/10.1016/j.jweia.2024.105948.

Wang Y., Zhong K., Zhang N., Kang Y.(2014). Numerical Analysis of Solar Radiation Effects on Flow Patterns in Street Canyons. *Engineering Applications of Computational Fluid Mechanics*. 8(2), 252-262. https://doi.org/10.1080/19942060.2014.11015511.

Weerasuriya A. U., Hu Z. Z., Zhang X. L., Tse K. T., Li S., Chan P. W.(2018). New Inflow Boundary Conditions for Modeling Twisted Wind Profiles in Cfd Simulation for Evaluating the Pedestrian-Level Wind Field near an Isolated Building. *Build Environ*. 132, 303-318. https://doi.org/10.1016/j.buildenv.2018.01.047.

Weerasuriya A. U., Tse K. T., Zhang X., Kwok K. C. S.(2018). Integrating Twisted Wind Profiles to Air Ventilation Assessment (Ava): The Current Status. *Build Environ*. 135, 297-307. https://doi.org/10.1016/j.buildenv.2018.03.024.

Wen C.-Y., Juan Y.-H.,Yang A.-S.(2017). Enhancement of City Breathability with Half Open Spaces in Ideal Urban Street Canyons. *Building and Environment*. 112, 322-336. https://doi.org/10.1016/j.buildenv.2016.11.048.

Wen Y. B., Huang Z. R., Tang Y. F., Li D. R., Zhang Y. J.,Zhao F. Y.(2022). Air Exchange Rate and Pollutant Dispersion inside Compact Urban Street Canyons with Combined Wind and Thermal Driven Natural Ventilations: Effects of Non-Uniform Building Heights and Unstable Thermal Stratifications. *Sci Total Environ*. 851(Pt 1), 158053. https://doi.org/10.1016/j.scitotenv.2022.158053.

Willemsen E., Wisse J. A.(2007). Design for Wind Comfort in the Netherlands: Procedures, Criteria and Open Research Issues. *Journal of Wind Engineering and Industrial Aerodynamics*. 95(9-11), 1541-1550. https://doi.org/10.1016/j.jweia.2007.02.006.

Xia Q., Liu X., Niu J., Kwok K. C. S.(2015). Effects of Building Lift-up Design on the Wind Environment for Pedestrians. *Indoor and Built Environment*. 26(9), 1214-1231. https://doi.org/10.1177/1420326x15609967.

Xiaomin X., Zhen H., Jiasong W.(2006). The Impact of Urban Street Layout on Local Atmospheric Environment. *Building and Environment*. 41(10), 1352-1363. https://doi.org/10.1016/j.buildenv.2005.05.028.

Xu F.,Gao Z.(2022). Frontal Area Index: A Review of Calculation Methods and Application in the Urban Environment. *Building and Environment*. 224. https://doi.org/10.1016/j.buildenv.2022.109588.

Xu F., Zhang J.,Gao Z.(2023). The Effect of Building Surface Cool and Super Cool Materials on Microclimate in Typical Residential Neighborhoods in Nanjing. *Sustainable Cities and Society*. 98. https://doi.org/10.1016/j.scs.2023.104838.

Yakhot V., Orszag, S.A.(1986). Renormalization Group Analysis of Turbulence. I. Basic Theory. *Journal of Scientific Computing*. 1, 3-51.

Yakhot V. a. O., S.A.(1986). Renormalization Group Analysis of Turbulence. I. Basic Theory. *Journal of scientific computing*. 1 1, 3-51.

Yan B., Ding W., Zhou X., Guo K., Ren H., Li X., Yang Q.(2023). Experimental Study on the Aeroelastic Response of a Square Supertall Building Considering Twisted Wind Effect. *Engineering Structures*. 283. https://doi.org/10.1016/j.engstruct.2023.115923.

Yan B., Li Y., Li X., Zhou X., Wei M., Yang Q.,Zhou X.(2022). Wind Tunnel Investigation of Twisted Wind Effect on a Typical Super-Tall Building. *Buildings*. 12(12). https://doi.org/10.3390/buildings12122260.

Yang A.-S., Juan Y.-H., Wen C.-Y.,Chang C.-J.(2017). Numerical Simulation of Cooling Effect of Vegetation Enhancement in a Subtropical Urban Park. *Applied Energy*. 192, 178-200. https://doi.org/10.1016/j.apenergy.2017.01.079.

Yang J., Yang Y., Sun D., Jin C., Xiao X.(2021). Influence of Urban Morphological Characteristics on Thermal Environment. *Sustainable Cities and Society*. 72. https://doi.org/10.1016/j.scs.2021.103045.

Yang S., Wang L., Stathopoulos T.,Marey A. M.(2023). Urban Microclimate and Its Impact on Built Environment – a Review. *Building and Environment*. 238. https://doi.org/10.1016/j.buildenv.2023.110334.

Yang W., Wong N. H., Zhang G.(2013). A Comparative Analysis of Human Thermal Conditions in Outdoor Urban Spaces in the Summer Season in Singapore and Changsha, China. *Int J Biometeorol*. 57(6), 895-907. https://doi.org/10.1007/s00484-012-0616-9.

Yang Y., Gu M., Chen S., Jin X.(2009). New Inflow Boundary Conditions for Modelling the Neutral Equilibrium Atmospheric Boundary Layer in Computational Wind Engineering. *Journal of Wind Engineering and Industrial Aerodynamics*. 97(2), 88-95. https://doi.org/10.1016/j.jweia.2008.12.001.

Yuan C.,Ng E.(2012). Building Porosity for Better Urban Ventilation in High-Density Cities - a Computational Parametric Study. *Build Environ*. 50, 176-189. https://doi.org/10.1016/j.buildenv.2011.10.023.

Yuan Y., Yan B., Zhou X., Yang Q., Huang G., He Y., Yan J.(2022). Rans Simulations of Aerodynamic Forces on a Tall Building under Twisted Winds Considering Horizontal Homogeneity. *Journal of Building Engineering*. 54. https://doi.org/10.1016/j.jobe.2022.104628.

Yuan Y., Yan B., Zhou X., Yang Q., Wei M., He Y., Zhou X., Li X.(2023). Twisted-Wind Effect on the Aerodynamic Force Acting on Varying Side-Ratios Tall Buildings. *Journal of Wind Engineering and Industrial Aerodynamics*. 240. https://doi.org/10.1016/j.jweia.2023.105481.

Zhang S., Kwok K. C. S., Liu H., Jiang Y., Dong K., Wang B.(2021). A Cfd Study of Wind Assessment in Urban Topology with Complex Wind Flow. *Sustainable Cities and Society*. 71. https://doi.org/10.1016/j.scs.2021.103006.

Zhang X., Gao Y., Tao Q., Min Y.,Fan J.(2023). Improving the Pedestrian-Level Wind Comfort by Lift-up Factors of Panel Residence Complex: Field-Measurement and Cfd Simulation. *Building and Environment*. 229. https://doi.org/10.1016/j.buildenv.2022.109947.

Zhang X., Tse K. T., Weerasuriya A. U., Kwok K. C. S., Niu J., Lin Z., Mak C. M.(2018). Pedestrian-Level Wind Conditions in the Space Underneath Lift-up Buildings. *Journal of Wind Engineering and Industrial Aerodynamics*. 179, 58-69. https://doi.org/10.1016/j.jweia.2018.05.015.

Zhang X., Tse K. T., Weerasuriya A. U., Li S. W., Kwok K. C. S., Mak C. M., Niu J.,Lin Z.(2017). Evaluation of Pedestrian Wind Comfort near 'Lift-up' Buildings with Different Aspect Ratios and Central Core Modifications. *Build Environ*. 124, 245-257. https://doi.org/10.1016/j.buildenv.2017.08.012.

Zhang X., Weerasuriya A. U., Tse K. T.(2020). Cfd Simulation of Natural Ventilation of a Generic Building in Various Incident Wind Directions: Comparison of Turbulence Modelling, Evaluation Methods, and Ventilation Mechanisms. *Energy and Buildings*. 229. https://doi.org/10.1016/j.enbuild.2020.110516.

Zhang X., Weerasuriya A. U., Zhang X., Tse K. T., Lu B., Li C. Y., Liu C. H.(2020). Pedestrian Wind Comfort near a Super-Tall Building with Various Configurations in an Urban-Like Setting. *Build Simul*. 13(6), 1385-1408. https://doi.org/10.1007/s12273-020-0658-6.

Zheng X., Yang J.(2021). Cfd Simulations of Wind Flow and Pollutant Dispersion in a Street Canyon with Traffic Flow: Comparison between Rans and Les. *Sustainable Cities and Society*. 75. https://doi.org/10.1016/j.scs.2021.103307.

Zhong J., Liu J., Xu Y., Liang G.(2022). Pedestrian-Level Gust Wind Flow and Comfort around a Building Array–Influencing Assessment on the Pocket Park. *Sustainable Cities and Society*. 83. https://doi.org/10.1016/j.scs.2022.103953.

Zhou L., Hu G., Tse K. T., He X.(2021). Twisted-Wind Effect on the Flow Field of Tall Building. *Journal of Wind Engineering and Industrial Aerodynamics*. 218. https://doi.org/10.1016/j.jweia.2021.104778.

APPENDIX

CFD validation of the wall temperature

The accuracy of the solar radiation simulation was ensured by comparing it with the field measurement data obtained by Idczak et al. (2006). The microclimate conditions in a street canyon were measured at Guerville ($48^{\circ}56'$N, $1^{\circ}44'$W), France on a sunny day (28 July). The wind velocity, temperature, atmospheric pressure, and relative humidity were recorded within the three parallel street canyons formed by four rows of buildings. The dimensions of the buildings were 18.3 m in length, 5.2 m in height, and 2.4 m in width respectively, with a street width of 2.1 m and the street axis forming an angle of 54° with the north (Fig. A). The CFD validation cases were conducted with an inlet temperature of 19.2 °C and 28.3 °C for 0800 LST and 1600 LST respectively. The wind direction exhibited near-parallel alignment with the street axis, measuring at 1.6 m/s and 2.1 m/s for 0800 LST and 1600 LST. The wall temperatures at z/H=0.21 and 0.84 on the southern surface of the second street canyon were compared with experimental results (Idczak et al., 2006) and Xu et al.'s findings (Xu et al., 2023) (Table. A).

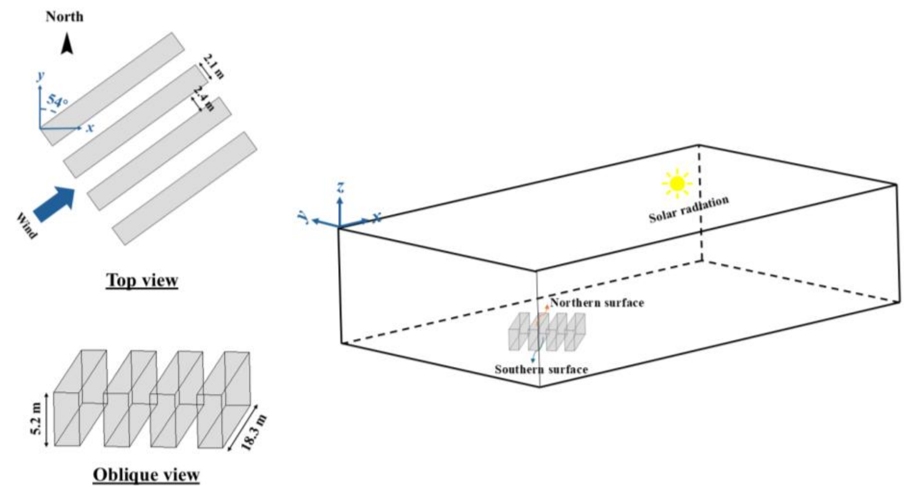

Fig. A. Physical models for solar radiation validation.

Table. A. Comparison between the wall temperature between CFD and on-site measurement.

Position	**On-site measurement**		Xu et al., 2023		**Present research**	
	0800 LST	**1600 LST**	**0800 LST**	**1600 LST**	**0800 LST**	**1600 LST**
***x*/*H*=0.21**	21.4	29.2	20.3	29.8	21.7	29.5
***x*/*H*=0.84**	24.9	28.9	23.9	29.5	23.8	28.6

CFD validation of the thermal effect

The accuracy of the CFD in predicting thermal comfort was validated using the experimental results conducted by Uehara. (2000). The experimental model consists of an array of buildings, with 14 rows and 7 columns. Each building has dimensions of 0.1 × 0.1 × 0.1 m^3, with a spacing of 0.1 between each row and 0.05 m between each column. The thermal stratification was induced by heating the floor (T_f) to 79 °C, while the incoming floor temperature (T_a) was maintained at 20 °C (Fig. B (a)). The inlet velocity profile was defined with frictional velocity u^*=0.12 m/s and roughness length of 0.0033 m (Uehara, 2000). In the on-site measurement, the bulk Richardson number $R_b = \frac{gH(T_a - T_f)}{(T_a + 273) \times U_H}$ is -0.21, U_H is the mean wind velocity at the top of the street canyon (0.96 m/s). The wind velocity in the streamwise direction and temperature at the monitoring points, spanning from ground level to the top of the street canyon, located at the center of rows five and six were compared with experimental findings. The simulated normalized wind velocity and air temperature were compared with the experimental data obtained from the vertical section (z/H=0-2) (Fig. B (b) and (c)). The simulated velocity and temperature data are in good agreement with the experimental results, and the error is within 5%, indicating that the CFD simulated results are credible.

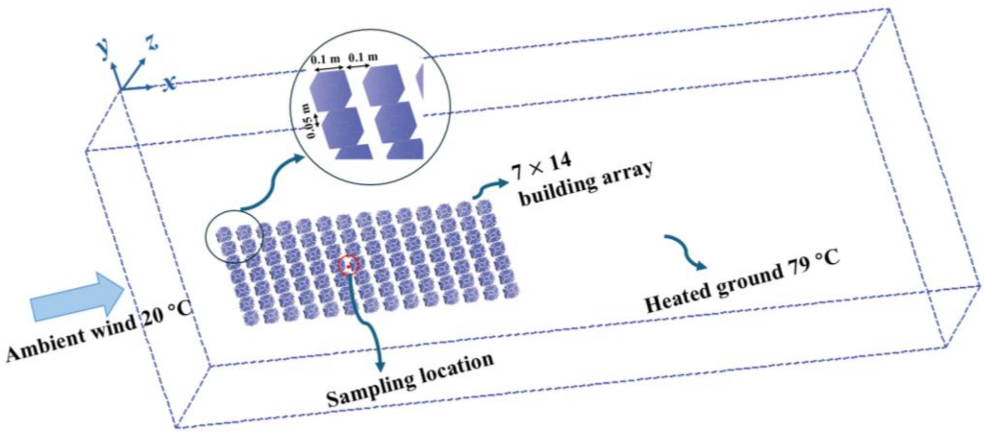

(a)

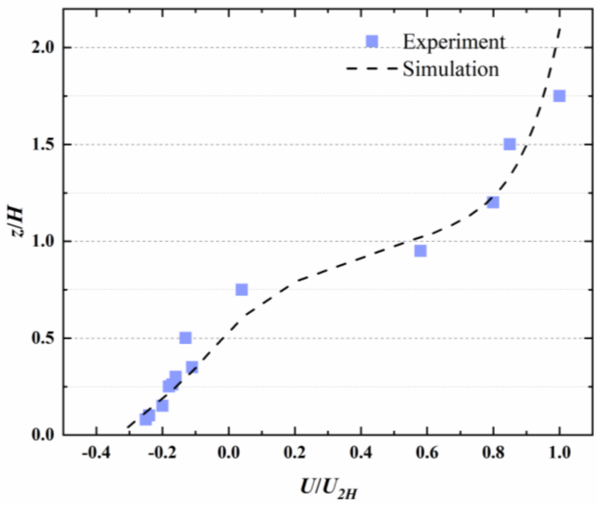

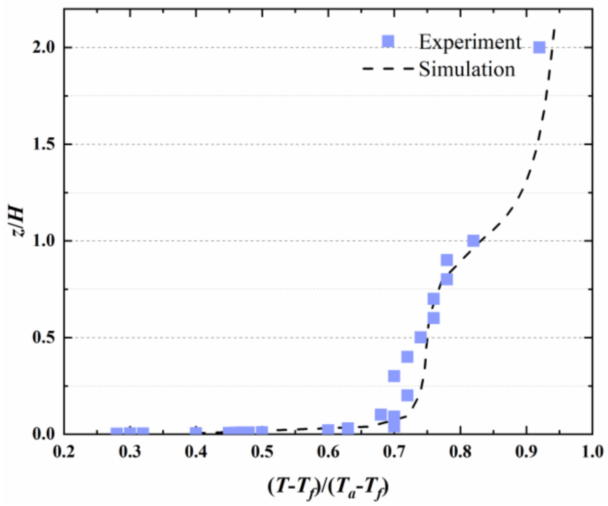

(b) (c)

Fig. B. (a) Physical models for thermal comfort validation and Comparison of CFD results with experimental data (Uehara, 2000) for (b) Normalized wind velocity and (c) Normalized temperature.

Convergence monitoring for temperature

The temperature convergence was verified using convergence monitoring plots for temperatures at three designated monitoring points located upstream, at the center, and downstream of the street canyon with arcade design under TWP (Fig. C).

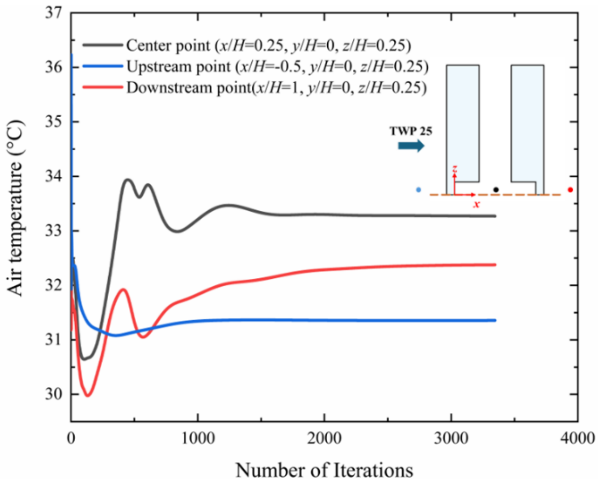

Fig. C. Convergence monitoring for air temperature and the locations of the monitor points.